Efficient Terahertz (THz) generation from some indigenously grown organic nonlinear crystals and designing of band pass filters for spectroscopy of high energy materials

A thesis submitted to

University of Hyderabad

Towards partial fulfillment for the degree of

Doctor of Philosophy

in

Physics

By

Ganesh Damarla
(13ACPA01)

हैदराबाद विश्वविद्यालय
University of Hyderabad

प्रतिष्ठित संस्थान
INSTITUTION OF EMINENCE

Under the supervision of

Prof. Anil Kumar Chaudhary

Advanced Centre of Research in High Energy Materials (ACRHEM)

School of Physics, University of Hyderabad

Hyderabad 500046, Telangana, India.

July 2020

A thesis entitled

Efficient Terahertz (THz) generation from some indigenously grown organic nonlinear crystals and designing of band pass filters for spectroscopy of high energy materials

Submitted to

University of Hyderabad

Towards partial fulfillment for the degree of

Doctor of Philosophy

in

Physics

By

Ganesh Damarla (13ACPA01)

Supervisor: **Prof. Anil Kumar Chaudhary**

Advanced Centre of Research in High Energy Materials (ACRHEM)

School of Physics, University of Hyderabad,

Hyderabad 500046, Telangana, India.

July 2020

Dedicated to Amma-Nanna

&

Kosanam Bhaskar Kumar

&

Prof. Khanindra Pathak

Declaration

I, **Ganesh Damarla(13ACP01)**, hereby declare that the work reported in this thesis entitled **"Efficient Terahertz (THz) generation from some indigenously grown organic nonlinear crystals and designing of band pass filters for spectroscopy of high energy materials"** is original and has been carried out by me under the supervision of **Dr. Anil Kumar Chaudhary**, Professor in ACRHEM (School of Physics), University of Hyderabad, Hyderabad, Telangana, India, as per the Ph.D. ordinances of the University, which is also free from plagiarism. I further declare that this work has not submitted for the award of a research degree of any other University. I hereby agree that my thesis can be deposited in Shodhganga/INFLIBNET.

A report on plagiarism statistics from the University Librarian is enclosed.

D. Ganesh.

(Ganesh Damarla)

Reg. No: 13ACPA01

A Chaudhary 17.07.2020

Prof. Anil Kumar Chaudhary

Thesis Supervisor,
ACRHEM,
School of Physics,
University of Hyderabad.

Dr. Anil Kr. Chaudhary
Professor (Physics)
Advanced Centre of Research in
High Energy Materials (ACRHEM),
UNIVERSITY OF HYDERABAD
HYDERABAD-500 046. T.S. INDIA.

Dr. A. K. Chaudhary
Professor
Tel.: + 91-40-23138807
Fax: + 91-40-23012800
E-mail: akcphys@gmail.com

ACRHEM
University of Hyderabad,
Prof. C. R. Rao Road,
Gachibowli,
Hyderabad – 500 046,
Telangana, India.

Certificate

This is to certify that the thesis entitled **"Efficient Terahertz (THz) generation from some indigenously grown organic nonlinear crystals and designing of band pass filters for spectroscopy of high energy materials"** being submitted to the University of Hyderabad by **Ganesh Damarla** (Reg. No. **13ACPA01**), for the award of the degree of **Doctor of Philosophy in Physics**, is a record of bonafide work carried out by him under my supervision and is free of plagiarism.

The thesis has not been submitted previously in part or in full to this or any other University or Institution for the award of any degree or diploma.

17.07.2020

Prof. Anil Kumar Chaudhary
(Supervisor)

Dr. Anil Kr. Chaudhary
Professor (Physics)
Advanced Centre of Research in
High Energy Materials (ACRHEM),
UNIVERSITY OF HYDERABAD
HYDERABAD-500 046. T.S. INDIA.

Director
ACRHEM

Director
ACRHEM

Dean
School of Physics

DEAN
School of Physics
University of Hyderabad
HYDERABAD - 500 046.

CERTIFICATE

This is to certify that the thesis entitled **"Efficient Terahertz (THz) generation from some indigenously grown organic nonlinear crystals and designing of band pass filters for spectroscopy of high energy materials"** submitted by **Ganesh Damarla** bearing registration number **13ACPA01** in partial fulfillment of the requirements for award of **Doctor of Philosophy in physics at ACRHEM, School of physics, University of Hyderabad** is a bonafide work carried out by him under my supervision and guidance. This thesis is free from plagiarism and has not been submitted previously in part or in full to this or any other University or Institution for award of any degree or diploma.

Further, the student has the following publications before submission of the thesis for adjudication:

1. **G. Damarla, A. K. Chaudhary, and M. Venkatesh, "Study of Water Loss in the Rose Petals Using Terahertz Spectroscopy," in** *WRAP 2017 - Workshop on Recent Advances in Photonics*).
2. **G. Damarla, M. Venkatesh, and A. K. Chaudhary, "Temperature**-dependent terahertz spectroscopy and refractive index measurements of aqua-**soluble and plastic explosives,"** *Appl. Opt.*, 2018,
3. **D. Ganesh***et al.*, **"Time**-Domain Terahertz Spectroscopy and Density Functional Theory Studies of Nitro/Nitrogen-Rich Aryl-**Tetrazole Derivatives,"** *ACS Omega*, 2020, doi: 10.1021/acsomega.8b03383.
4. **Ganesh Damarla,** Karthick Subramani, M. Venkatesh , Thirupugalmani Karunanithi, A. K. Chaudhary, rahadeeswaran S . **"THz generation and spectroscopy of BNA crystals a growth solvent dependence study "communicated**
5. **Ganash Damarla,** Hanna J Maria, A.K. Chaudhary, and S. Thomas. Study of optical and diffusion properties of fillers on the strength of CIIR/NR hybrid natural rubber using time domain terahertz spectroscopy. **(Communicated)**

Also, made presentations in the following conferences:

1. **Delivered an oral presentation entitled "Temperature dependent Terahertz Spectroscopy of Aqueous** soluble and **Insoluble Explosives" in HEMCE 2017 held at HEMRL, PUNE, India.**
2. **Presented a poster entitled "Terahertz Time domain spectroscopy of 5**-(Choloromethyl)-**1H tetrazole Derivatives" in** UFS-2017, held at University of Hyderabad, Hyderabad, India. **(Awarded as best poster)**
3. **Presented a poster entitled "**Terahertz Time Domain Spectroscopy of Aqua-soluble and Plastic Explosives" in NLS-2016 held at held at KIIT- Bhubaneshwar, Odisha, India.
4. **Presented a poster entitled "**Time domain Terahertz spectroscopy for the determination of vibrational modes and refractive indices of Tetrazole-N-**(Hetro) Aryl Derivatives"** in NLS-2017, held at BARC Mumbai, India.
5. **Presented a poster entitled "**THz generation and spectroscopy of BNA crystals a growth solvent dependence study" in NLS-2018, held at RRCAT, INDORE, India.

The following courses have taken as the part of the course work:

Course No.	Course offered at	Title of the Course	Credits	Pass/Fail
MT453	SEST	Modeling and simulation	4	Pass
AC807	ACRHEM	Research Methodology	4	Pass
AC808	ACREHM	Non-linear Optics	4	Pass
PD801	SEST	Surface engineering	4	Pass

17.07.2020

Supervisor
Dr. Anil Kumar Chaudhary,
Professor,
ACRHEM, University of Hyderabad,
Hyderabad, India.

Dr. Anil Kr. Chaudhary
Professor (Physics)
Advanced Centre of Research in
High Energy Materials (ACRHEM),
UNIVERSITY OF HYDERABAD
HYDERABAD-500 046. T.S. INDIA.

Director
ACRHEM,
University of Hyderabad,
Hyderabad,
India.

Director
ACRHEM

Dean
School of Physics,
University of Hyderabad,
Hyderabad,
India.

DEAN
School of Physics
University of Hyderabad
HYDERABAD - 500 046

Acknowledgements

I Thank my supervisor **Prof. A. K. Chaudhary** for his exceptional guidance, motivation carrying out this research work. It is my pleasure to thank the present director, **Dr V. Kameswara Rao,** and former directors of ACRHEM for their support in all aspects towards completion of this work. I also thank the Dean, School of Physics (SoP), UoH, for the academic support.

I sincerely thank my doctoral committee members **Prof. Soma Venugopal Rao** and **Prof G. Manoj Kumar** for their invaluable suggestions in and out of the doctoral committee meetings. I am indebted to Prof. Ganapathy Subramanian Vaitheeswaran sir for his support during my initial stage of research. I thank Prof. P. Pream kiran sir for his lucid teachings. I would also thank Dr. Harsha sir for on and off line discussions.

I would like to thank Defence Research and Development Organization (DRDO), India for providing me the financial support (through ACRHEM) all through my PhD.

I thank all the teaching staff of ACRHEM and SoP, SEST for conducting the classes and explaining the nitty-gritty things in the core subjects. I would also like to thank all the non-teaching staff of ACRHEM and SoP for their co-operation as when required.

I thank Prof. S. Brahadeeswaran, Prof. Dibakar Roy Chowdhury, Dr. S. Karthick, Subya da, Deepak, for helping me. I would like to thank my seniors Dr M. Venkatesh, Dr. K. S. Rao, for several fruitful discussions, which helped me in clarifying many doubts that I encountered in understanding the experimental observations from you people.

I acknowledge Dr Ashwin kumar, Dr M V Nanada Kishore, Dr Vinoth Lakshmi Narayanan, Dr Sachin, Dr E Manikanta, Dr Sai Shiva gaaru, Dr, P Venkateshwarulu, and Dr T Vikranth, Mr Anubham Shiva, K Lalitha Niharika for being with me during this journey. I also thank Miss Ankita Chaudahry, IMA (International Relations), Kerala Central University, Thirvannathpuram, for helping in thesis proof reading.

I am unambiguously grateful to my loving family for their love and prayers. I am indebted to my Father Mr Panakala Rao, Mother Mrs Indira venu. Special thanks to my sister Mrs **Jayanaga Durga** because of whom I did my research work being away from home. I also thank my brother-in-law Mr. B. Subba rao, my nephews B. Sairam Manohar, Master B. Trilochan sai their unconditional love, endless support, encouragement giving me strength to achieve my ambitions. I would like to express my sincere gratitude to my brother, Mr **Sri Rama Krishna Battu,** who inculcated the

seed (worm) of doing PhD in my mind and his encouragement and support directly, indirectly.

I would like to thank my friends/roommates Rajendhar, Chandu, Kalam, Naga, Naresh for their help in carrying out this research work, sharing their joy and my pain in these years. Without their company and help these years would have been much tougher. I would also like to thank my colleagues Samuel Jackson, N. Linga murthy, KK, J. Yellu, Miss M.S. Bharathi, and all others juniors for their support.

I also thank my graduation friends K. Bhaskaracahri, DR. Chv Prakash, Moram Vishnu, Dr. Vemuri Nageshwarao, Dronavalli Bhanu, Potluri Deepthi, Dr. Suman Patteti for their motivation and support throughout my education career. I can not forget my happy days of teaching with Optometry(SMST) students Aakanksha Varadi (Bidda), P. Sri kavya, B.Sreya, Sowmya, Suchi, Priyanka, H. Meena, isak, G Pranay Madhu, Tim, Aadiya prabharakan, H. Jose, Comrade Soha, khadir, Arif, H. Entajul.

Finally, I would like to thank the mother earth, almighty God for his blessings throughout my entire life.

"*when you want something, all the universe conspires in helping you to achieve it*"

-Paulo Coelho

Abbreviations

Fs/fs	Femtosecond
Ps/ps	Picosecond
RSD	Relative Standard Deviation
SNR	Signal To Noise Ratio
FWHM	Full Width at Half Maximum
RDX	1, 3, 5-Trinitroperhydro-1, 3, 5-Triazine
HMX	1, 3, 5, 7-Tetranitro-1, 3, 5, 7-Tetrazocane
TNT	2-Methyl-1, 3, 5-Trinitrobenzene
CL-20	Hexanitrohexaazaisowurtzitane
AN	Ammonium Nitrate
DNT	2, 4- Dinitrotoluene
HEMs	High Energy Materials
IEDs	Improvised Explosive Devices
BBO	β-barium borate
BNA	N-benzyl-2-methyl-4-nitroaniline
BPD	Balanced photo diodes
CW	Continuous wave
DAST	4-N, N- Dimethylamino -4' - N'-methyl-stilbazolium toyslate
EO	Electro optic
EOS	Electro optic sampling
FFT	Fast Fourier transform
GaAs	Gallium arsenide
LT	Low temperature
PC	Photoconductive
PCA	Photoconductive antennas
PCS	Photoconductive sampling
PDE	Photo Dember effect
SI	Semi insulating
TDS	Time domain spectroscopy
THz	Terahertz
TRTS	Time resolved THz spectroscopy
ZnTe	Zinc telluride
CST	Computer Simulation Technology
FD	Frequency Domain.
FDTD	Finite Difference Time Domain
THzTDS	Terahertz Time-Domain Spectroscopy
CST-MWS	Computer Simulation Technology MicroWave Studio

CHAPTER 1 : Introduction

The region lying between the infrared and microwave spectrum of electromagnetic radiation having frequency range of 0.1 - 10 X 10^{12} is known as terahertz (THz) band [1]. It has unique properties such as high absorption in water, high reflective to metals, and transmission through packing materials. In addition, it has wide spectral features associated with vibration of bonds in a molecule, semiconductors intra-band transitions, vibrational and rotational transitions of organic molecules [1–4]. Furthermore, it is non-ionizing and non-destructive in radiation because of their low photon energy (order of meV) [4,5]. Due to aforesaid properties, it has wide range of applications and opens a new channel of research in various fields.

THz spectroscopy is an efficient technique for identification of material's polymorphic structures as compared to X-ray diffraction and Raman spectroscopy techniques [6]. X-ray diffraction is limited to large crystalline structures whereas Raman spectroscopy induces phase change in material during measurements. These limitations can be overcome using THz spectroscopy. The THz time resolved spectroscopy (TRTS) is useful in studying the dynamic properties of materials [7]. TRTS has several advantages over other known techniques such as time-resolved luminescence, transient absorption and four wave mixing in determination of material's dynamical properties. It is helpful in determining the carrier dynamics of direct and indirect bandgap materials, while luminescence technique is restricted to only direct band gap materials [8]. It can also probe the material properties evolving with frequencies whereas four wave mixing and transient grating are unable to determine the frequency dependent properties. Moreover, it can be used to study the intraband relaxation as well as interband recombination dynamics of excited carriers in materials on ultrafast time scales [9]. As compared to X-ray imaging, THz imaging has several advantages such as increased in image contrast, chemical identification, and reduced risk of radiation exposure [10]. Additionally, THz radiation finds potential applications in the areas of defense security, astronomy, biomedical science, telecommunications etc. [5,11–18].

The distinct properties and innumerable applications of THz radiation has motivated us to carry out research on generation, detection, and characterization of THz radiation from different materials. There are several challenges associated with the detection of THz radiation in real time measurements. One of the most common reason is the absorption due to presence of water molecules in the atmosphere that restricts the use of THz radiation in detection, spectroscopy and imaging to shorter distances [19–21]. This limitation can be overcome by increasing the

sensitivity of THz detector, selection of frequency in air windows and increasing the emission efficiency (or using powerful THz sources). Hence, there is need to develop high power sources and sensitive detectors in THz domain. Our main objective is to generate efficient THz radiation using different types of optical techniques in some selected organic and semiconductor nonlinear materials. Finally, the generated radiation is employed in spectroscopy of HEMs and other organic materials.

THz radiation can be generated and detected using different types of electronic and optical techniques [22–25]. Among them, optical rectification, photoconductive switching, and focusing of ultra-short pulses in air and semiconductor surfaces are some of the widely used generation techniques [26,27,36,28–35]. The photoconductive and electro optic sampling are some of the prominent coherent detection techniques. Bolometer, Pyrometer and Golay cells are some of the incoherent detection devices. In this thesis, we have employed ultra-short pulses based optical techniques for generation, detection of THz radiation from some selected nonlinear organic and semiconductor materials [37].

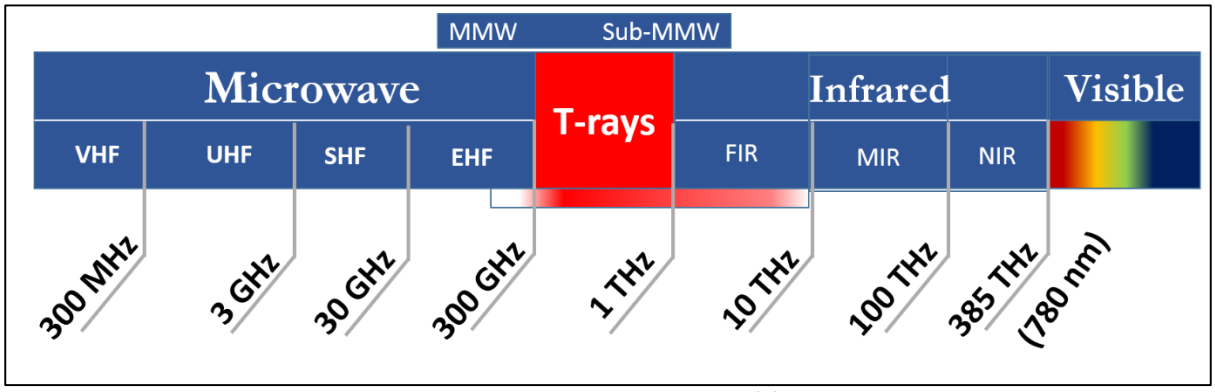

Figure 1.1. Electromagnetic spectrum – THz neighbors

THz radiation is spread over the spectral region, commonly known as the far-infrared region. However, it occupies the position between microwave and IR (optical) of the electromagnetic (EM) radiation. In terms of frequency, it is between 100 GHz to 10THz range. Figure 1.1 Shows the EM spectrum in terms of frequency. THz frequency has low energy and non- ionizing in nature that makes THz-TDS an attractive and non-destructive technique.

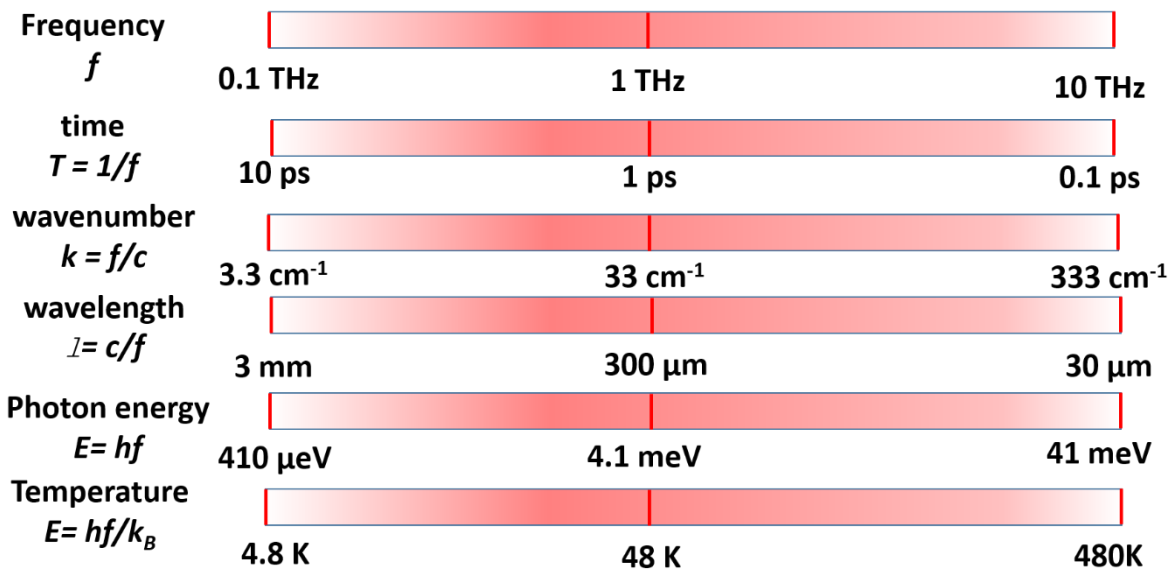

Figure 1.2. Terahertz plotted in the units of frequency, wavelength, wavenumber, photon energy, equivalent temperature.

Figure 1.2 presents the detailed classification of in terms of wavelength and energy (eV). For example, 33.33 cm^{-1} wavenumber is equal to 300 µm wavelength correspond to photon energy of 4.1 meV [38]. THz wavelength and energy covers the wide range of rotational -vibrational transitions of molecules, which includes both intra intermolecular and intra molecular, motions of molecules bonded by hydrogen and torsional motion of attached functional groups. Visible and NIR photon energy is of the order of few eVs which is very much less than THz photon energy (4.1 meV), even band gap energies of semiconducting materials are one thousand times higher than the terahertz energy. Thus it is so improbable that the sample would ionize dissociate under the influence of THz radiation.

For the sack of generating THz radiation and scaling of optical and electronic devices needs special approach which includes proper information of lifetime of charge carriers, resistivity, band gap, phonon band, transmission, refractive index, absorption coefficients, damage threshold and easy to grow good quality non hygroscopic materials. Therefore, the selection of optical material is one of the most important tasks. Alternatively, it is not a judicious way to employ all types of optical materials as a source of terahertz generation. In addition, several researcher groups have put attention to develop other new techniques like free electron lasers, synchrotrons and narrowband QCL (quantum cascade lasers) for wideband THz generation. However, use of ultrafast pulsed lasers in generation of THz radiation is part of a coherent technique with good Signal-to-noise ratio(SNR).

1.1 Terahertz Generation and Detection from different types of optical non-linear materials

1.1.1 Terahertz Sources

Terahertz radiations is generated from different types of optical devices such as, ultrafast photoconductive switching of antennas, optical rectification in nonlinear crystals, CO_2 lasers, two color mixing in air plasma, semiconductor substrates etc. Based on a few important factors like incident laser power, spectral bandwidth, pulse duration and we opted to select photoconductive(PC) antennas and Crystals as a THz source and detector [39,40].

1.1.1.a Details of Photoconductive antennas (PC)

A Photoconductive antenna is made of SIGaAs /LTGaAs semiconductors. It consists of two parallel metal electrodes separated by a very small gap (5-10 microns) on a semiconductor substrate [41,42]. The two metal electrodes are biased using external voltage (~10 V) creating a very high electric field. When ultrafast laser pulses are of the order 100 fs, their energy typically is near to the bandgap and incident in the gap of semiconductor materials that help to generate photo charge carriers. These freely generated photo charge carriers get accelerated under the influence of biasing field causing transient photocurrent J(t). This, time-dependent current produced due to acceleration of charge carriers emits radiation falling in Terahertz range given by the following equation [43,44]

$$\vec{E}(r,t) = \frac{1}{4\pi\varepsilon_0 c^3 r^3} . \vec{r} \times \left(\vec{r} \times \frac{d\ \vec{j}(t)}{dt} \right) \quad [1]$$

However, carrier lifetime, effective mass, breakdown of materials limits the bandwidth and power of THz radiation emitted. In addition to semiconductor material, the designing aspects such as separation gap between metal electrode or plates, type of electrode shape, also plays a key crucial in THz emission. A variety of designs like Dipole, Bow-tie, Strapline also have been used. Antennas having large gap require high bias voltages that limits the bandwidth of generation, so small gaps are preferred to get high bandwidth and vice versa in case of power is concerned. In the present study we have used an inter-digital photoconductive antenna (BATTOP iPCA-21-05-300-800-h) depicted in Figure 1.3 iPCA consists of multiple strips at

constant gaps and with array of antennas. Laser beam diameter of ~1 mm was allowed to fall on iPCA, a micro lens array was used to focus the incident Laser beam into the gaps of electrodes array that leads to maximum utilization of laser energy falling on the antenna surface [45].

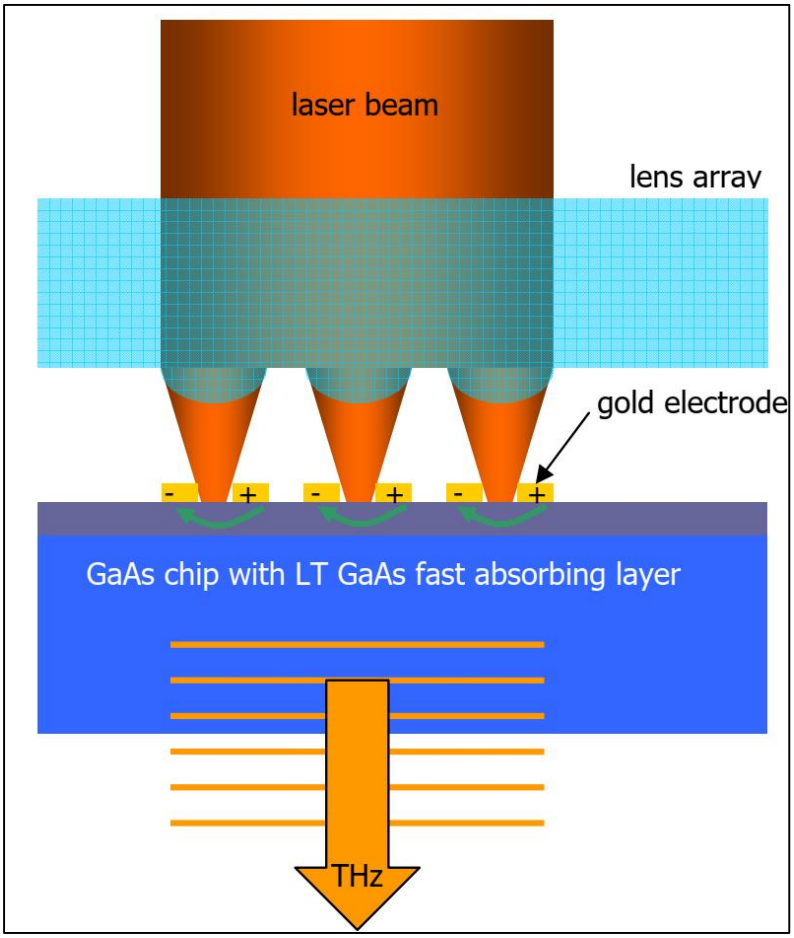

Figure 1.3. PCA antenna structure

It was noticed that 2 μW of THz power was emitted from the antenna using 100 mW power from incident laser. The antenna can sustain up to 500 mW of incident laser power and radiates between 0.1 – 3 THz range.

1.1.1.b Terahertz Generation through optical rectification

Terahertz generation from Photoconductive antenna/switches requires incident energy of radiation of the order of bandgap of semiconductor material whereas THz generation from nonlinear crystals has no such limitations. THz generation from optical rectification is a robust and simple technique. In conventional electronics the process of conversion of AC current into DC current is known as rectification. Similarly, in a nonlinear crystal a varying electric field

component of optical signal induces a DC polarization, this phenomenon is called Optical rectification [46–48]. In Dielectric medium, the applied electric filed ($\vec{E}$) and induced polarization ($\vec{P}$) are linearly related but when electric field strength is high compared as to atomic field (~ 105 to 108 V/m), the relation is no longer linear. If the medium is transparent for small electric fields it can be treated as a source of linear susceptibility as the number of photons increases, its intensity increases and nonlinear effects come into the picture which can be represented as Taylor expansion of the polarization

$$\vec{P}_i = \varepsilon_0 \left(\chi_{ij}\varepsilon_j + \chi^{(2)}{}_{ijk}\varepsilon_j\varepsilon_k + \chi^{(3)}{}_{ijk}\varepsilon_j\varepsilon_k\varepsilon_l + ...\right) \quad [2]$$

Where χ1 is the linear susceptibility and χ2, χ2 are the second and third order nonlinear susceptibilities respectively. Optical rectification is a second order process, if E(t) is the electric field component of applied optical electric field component also assuming it contains two frequency components ω_1 and ω_2,

$$E(t) = E_1 e^{-jw_1 t} + E_2 e^{-jw_2 t} + C.C. \quad [3]$$

The second-order polarization is directly proportional to

$$P^2(t) \propto \chi^2\left[E_1^2 e^{-2jw_1 t} + E_2^2 e^{-2jw_2 t} + 2E_1E_2e^{-j(w_1+w_2)t} + 2E_1E^*{}_2 e^{-j(w_1-w_2)t} + C.C.\right] + 2\chi^2\left[E_1E^*{}_1 + E_2E^*{}_2\right] \quad [4]$$

where C.C. represents the complex conjugate of all the components. The resultant frequency components of the polarization enclose Second Harmonic(SH), Sum Frequency E (ω_1+ ω_2) (SFG), difference frequency E(ω_1-ω_2) (DFG) of E_1 and E_2. Optical rectification is a special case of comment corresponding to E (ω_1-ω_2) generates the DC polarization whose duration lies in sub picoseconds when exited with ultrafast pulses.

Essentially, the generated THz is related to derivative of second order polarization.

$$E_{THz}(t) \propto \frac{\partial^2 P^2(t)}{\partial t^2} \quad [5]$$

Hence the generated THz is related to second order derivative of the pulse [49]. THz frequencies can be considered as DFG with all the spectral components of the laser pulse. Figur:1.4 a) represents the slowly varying envelope approximation of Gaussian pulse and Fig. (1-4) b) is the

shape of second order derivative of pulse. However, the detected shape of THz pulse need not be in

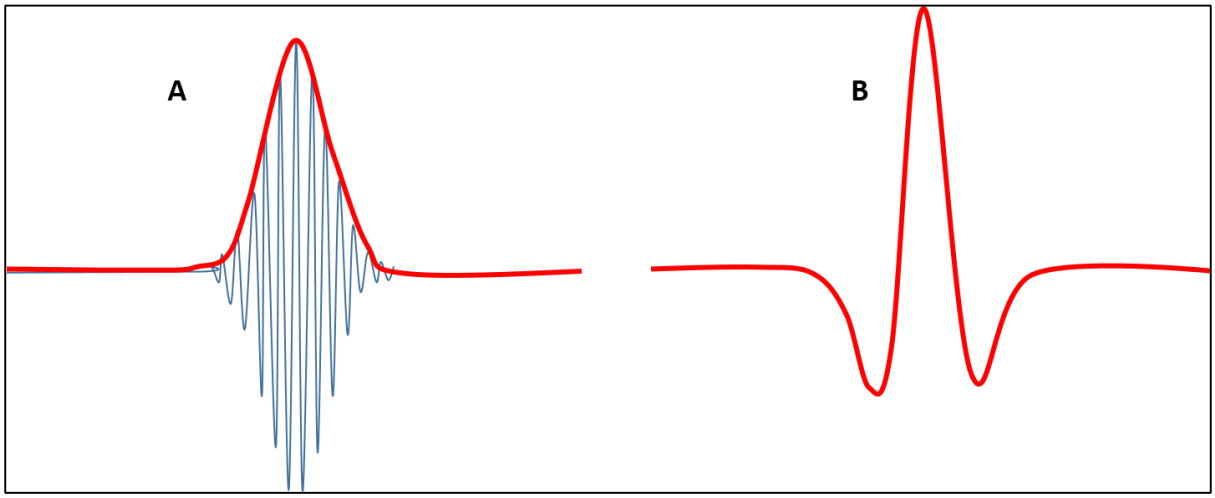

Figur:1.4. Optical pulse (blue) brings a polarization density of Gaussian shape (red) b) Generated Terahertz pulse from polarization

the form of Figur:1.4 because pulse shape modification is caused by properties of detection medium such as absorption and dispersion. In addition, the group velocity dispersion and refractive indices are also the function of frequency. When a laser pulse travels from the nonlinear medium, due to dispersion its group refractive index is different from actual optical refractive index of the generated terahertz. As a result, they propagate with different velocities. The efficient THz generation can be achieved, if generated THz is in phase with optical pulse, this is called velocity matching condition. The effective interaction distance traveled by optical pulse and THz is known as coherence length and is calculated using following equations

$$L_c = \frac{\lambda_{THz}}{2(n_{group} - n_{THz})} \qquad [6]$$

Where n_{group} is given by:

$$n_{group} = n_{optical} - \frac{\partial n_{optical}}{\partial \lambda_{optical}} \lambda_{optical} \qquad [7]$$

Here $\lambda_{optrical}$, $n_{optical}$ are the wavelength and refractive indices of pump beam.

1.1.2 THz wave detectors

The generated THz radiation is detected by different types of mechanism and detectors. Mainly, there are three type of detectors used for THz detection, 1). photo-conductive detection (PC

Sampling), 2). Electro-optic detection (EO sampling). 3) Pyro detector. In first two techniques, probe pulses are scanned in time-gated manner for detection of generated THz signal. LTGaAs/SIGaAs semiconductors are used in PC sampling technique, whereas E-O sampling is a nonlinear crystal based technique that works on the principle of Pockels effect. In the present thesis, we have employed both these techniques along with incoherent pyro techniques for the detection of power of THz radiation.

1.1.2.a Photo-conductive detection

The working principle of photo-conductive sampling is different from the process of THz generation using nonlinear crystal. In this process, designed antenna on the semiconductor substrate is illuminated by both probe beam and generated THz beam simultaneously as shown in the Figure 1.5. The optical probe pulse generates free electron-hole pair in the photoconductive antenna material. In the absence of THz the charge carriers generated by probe pulse recombine without moving to electrodes of the antenna, so no photocurrent is generated. The charge carriers are swept by electric field vector of incident THz radiation produces photocurrent [50,51].

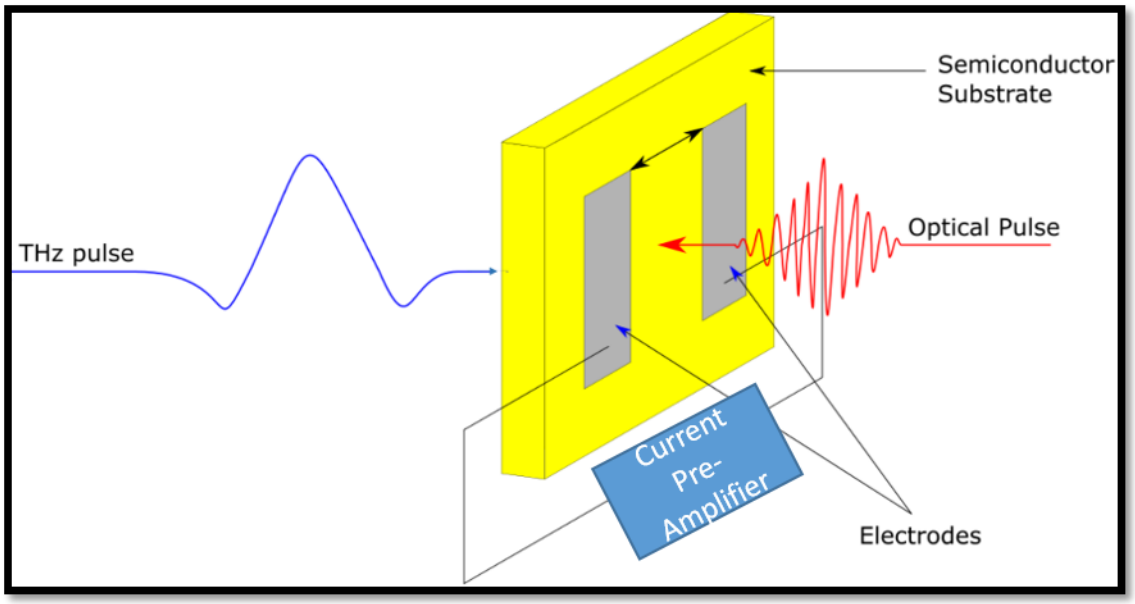

Figure 1.5. THz detection using PC sampling

As the time span of carrier lifetime is shorter than terahertz pulse the measured photocurrent is function of THz amplitude at a particular instant of time, so this method is called as photoconductive sampling. The photocurrent is recorded with the help of Pico ammeter coupled

with lock-in amplifier. By synchronizing probe pulse and THz pulse the profile of the THz is recorded.

1.1.2.b Electro-optic detection

Femtosecond short pulses from the same laser are used for both THz generation(pump) and detection(probe) purposes. The generated THz beam from pump pulse is directed with the help of 8 numbers of parabolic mirrors (OAPM) sets are used for collection of generated THz radiation and focusing it on the detector. The transmitted THz beam through the sample is focused on a non-linear ZnTe crystal for detection. The probe beam passes via the ZnTe crystal to detect the THz radiation. By changing the delay time of the visible probe pulses and THz to the ZnTe crystal, the generated THz beam is directed to combination of quarter wave plate, Wollaston prism, balance photodiode [52,53]. The optical signal is converted into electrical signal which is weak in nature. Therefore, preamplifier coupled with lock-in -amplifier is used for removing the noise and amplifying and averaging of signals arriving in the same phase. In the end, it is dispatched to the computer for recording of time domain signal. The role of quarter wave in absence and presence of THz radiation. Figure 1.6 (a)

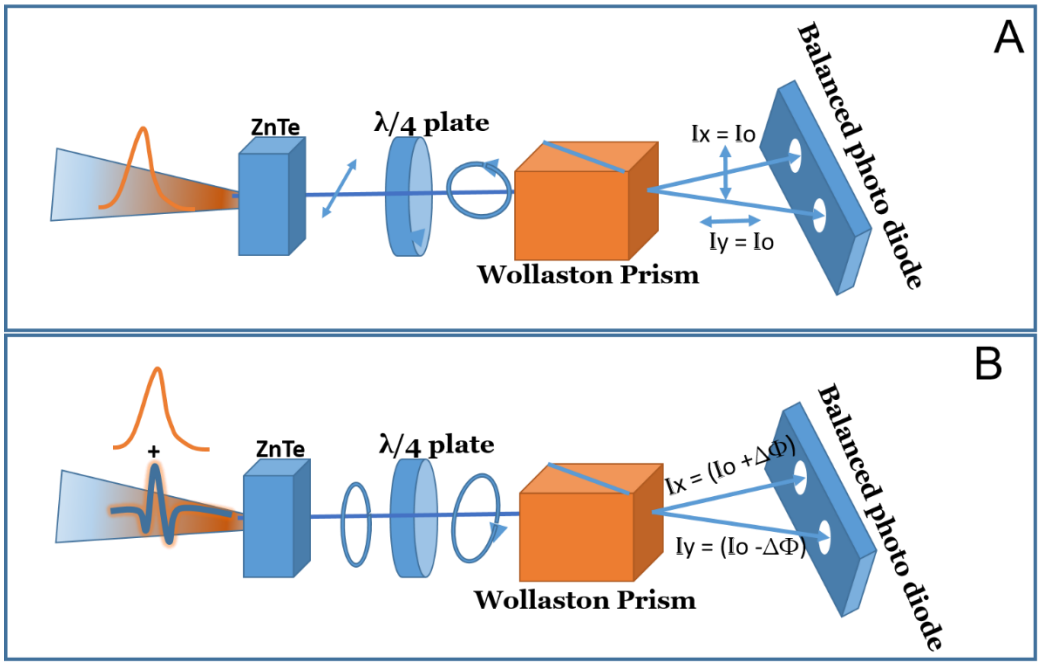

Figure 1.6. THz detection using Electro-optic sampling.

In the absence of THz signal, the polarization of optical probe beam remains unaltered after passing through the ZnTe and quarter wave converts the plane polarized light in to circular polarized light and Wollaston prism splits the circular polarized into two equal but cross

polarized parts. As a result, detector remains in balance position and output signal is zero. However, as shown in Figure 1.6 (b) in presence of THz, due to E-O effect the ZnTe crystal rotates the polarization of probe beam into circular polarized and quarter wave plate converts the circularly polarized light into elliptical polarized and Wollaston prism splits elliptical polarized probe beam into two unequal parts and now photodetector gets unbalanced and output electric signal which is also the signature of generated THz is recorded by the computer. the quantity of change within the polarization is proportional to the field energy of the THz radiation

1.2 Data collection

The lock-in amplifier gathers records from feature generator and the balanced photodiode and transfers to the statistics acquisition software developed the usage of Labview software program [54]. The software program allows variant in segment and amplitude of THz signal with admire to the put off time between pump and probe beam. At zero delay, we can see noise free amplified time domain signature peak of THz signal is recorded.

1.3 THz Applications

Terahertz part of electromagnetic spectrum is now widely explored for recording of characteristic signature of explosives, pharmaceutical, etc. [55–57]. However, majority of explosives are organic polymers but due to presence of different functional groups and orientation and rotational vibrational modes. As a result, they provide their signature in different THz region [58–60]. THz spectroscopy has several advantages over common spectroscopic techniques.

In addition, THz can be used for both qualitatively and quantitatively identification of molecules very accurately. According to Beer-Lambert law the absorption is proportional to concentration of substance under study. THz spectroscopic techniques can also be used for identification and detection of explosives mixed in soil. The mechanical strength of rubber polymers with organic and inorganic fillers can also be evaluated. It has potential application in food quality assessment and water and toxic chemical transfer in vegetables and fruits.

THz imaging by time domain spectroscopy is another fascinating area of research particularly in case of imaging of historical artefacts, biological samples and explosives and drugs under concealed condition. In this technique the desired object is illuminated with THz radiation. By measuring the temporal delay in the reflected signal the mapping of image will be carried out.

The refractive index of each layer of the paint material is different causes delay in the reflected signal. THz radiation is completely harmless so T- ray imaging can be treated as good alternative to the X-ray imaging which is ionizing in nature [61].

In this thesis, we mainly focused on the generation, detection and time domain spectroscopy of THz radiation from different types of sources such as photoconductive (PC) antennas, organic and semiconductor non-linear crystals. A multipurpose experimental setup which can be modified to perform THz generation, spectroscopy, TRTDS. In addition, the radiation emitted from these sources was compared with previously reported results. Apart from this, THz radiation was used to investigate the absorption properties of High energy materials and effect of temperature on spectral properties was studied. Finally, the designing and fabrication of band-pass filters in THz was carried out. These filters were used to perform the spectroscopy at different bands. The present thesis is organized as follows:

In case of non-linear crystals, the characteristics of emitted THz radiation were studied as a function of laser parameters and crystal growth conditions. The emitted THz amplitude and bandwidth from different non-linear crystals were compared. The effect of growth solvent on nonlinear properties of the crystal has investigated.

The time domain spectroscopy of emerging secondary high energy materials was carried in pellet form. The results were compared with Density functional theatrical studies. The effect of temperature on shifting of absorption peaks, change in the refractive indices was deliberated.

Metal mesh bandpass filter were designed and fabricated using CST microwave studio, UV lithography process. They were tested THz spectrophotometer was designed using Low temperature gallium arsenide (LT-GaAs) PC antennas, pyroelectric detector. These band-pass filters were used for measuring the absorption properties at selected frequencies.

The thesis comprises seven chapters, which describe aforementioned studies. The organization of the thesis is provided in the following.

Chapter 1: Introduction

In this chapter, we briefly discussed the fundamentals of THz radiation and its properties. The description of various sources and detectors of THz radiation are included. This chapter also discusses the fundamental mechanisms responsible for THz generation from PC antennas, semiconductors and non-linear crystals. A short description on detection techniques such as PC sampling, electro optic sampling is also incorporated. Furthermore, a brief introduction to THz

time domain spectroscopy, plasmonics in THz rage was discussed. This chapter concludes with brief discussion on the THz applications.

Chapter 2: Experimental details

This chapter mainly focuses on the details of laser systems, devices and optical components employed for THz generation, detection and spectroscopic applications. The details of laser assets used for the experiments and ultrafast pulse characterization methods which includes intensity autocorrelation are explained. The experimental setup used for THz spectroscopy in reflection and transmission mode. In addition to above, incoherent method of Pyroelectric detection for the measuring of Terahertz power is discussed. Computer Simulation Technology Microwave Studio (CST-MWS).

Chapter 3: Evolution of some nonlinear crystals for THz generation

This chapter discusses the effect of laser parameters and growth process on THz generation, detection and its enhancement from different types of non-linear crystals. The THz emission and efficiency of generated THz varies with nature of solvents. Terahertz generation and detection using coherent and incoherent technique from different type of nonlinear crystals and effect of precursor growth solvent on nonlinear properties of crystals. Different types of organic and inorganic crystals were studied to generate THz using femtosecond pulses of 800 nm wavelength. We present the Terahertz absorption coefficients, refractive indices in relation with phase matching connections. Optimized conditions for the efficient THz generation from crystals and a comparison with the reported literature are discussed. The THz generation capability of another indigenously grown organic crystal named BNA (N-benzyl-2-methyl-4-nitro aniline), which is grown in four different solvents is studied using 140 fs laser pulses. We employed BNA, OH1, LAP, for the study.

Chapter 4: Terahertz Spectroscopy and Density Functional Theory Studies of Nitro/Nitrogen-Rich Aryl-Tetrazole Derivatives

This chapter presents have a look at of THz-TDS covers the spectral vicinity of 0.1- 2.5 THz or 5-100 cm-1, which has low photon power and non-ionizing portion of the electromagnetic spectrum. Spectra are recorded in a time-area configuration where broad-band pulse of THz electromagnetic radiation passes via a sample and detected using the EO sampling approach. This methodology gives a direct dimension of the time-of-flight of THz radiation from the sample and, evaluation of consequences infers direct way to measure interactions among the transmitting THz and the sample. This chapter describes the THz-TDS study of newly

synthesized aryl-tetrazoles derivatives. The effect of functional groups attached to tetrazole moiety on the energetic properties is discussed. The THz-TDS experimental results are compared with DFT studies at molecular (using G-09) and single crystal level (using plane wave pseudopotential(PAW) method). The obtained vibrational frequencies and linear optical properties are found to have good agreement with the experimental data in THz regions and UV-Visible.

Chapter 5: Temperature-Dependent Terahertz Spectroscopy of Explosives

This chapter reports the temperature dependent time domain terahertz spectroscopy(TDS) of the premium aqua-soluble and plastic explosives RDX, TNT, $NH4NO_3$, and between 0.1 and 2 THz. The temperature dependent spectroscopic study changed into completed between 30°C and 200°C in a specially designed oven. The signature peaks of TNT and RDX at 1.60 and 0.82 THz, respectively. It indicates sizable redshift, while the NH_4NO_3 molecule indicates small shift. The observed excessive-temperature-based totally Redshift phenomenon is just the opposite of the blue shift pronounced at low(cryogenic) temperatures. In addition, the temperature-based absorption coefficient information of these molecules aid the change inside the awareness of the NO_2 molecule that's inconsistent with our institution suggested primarily based on photoacoustic spectroscopy. The temperature established refractive indices of these molecules among 0.1 and 2 THz were calculated. subsequently, to apprehend the sensitivity of the spectrometer signature height of RDX with recognize to the decrease inside the weight attention of RDX within the Teflon matrix is studied

Chapter 6: Designing and fabrication of band pass filters for THz spectroscopy

This chapter deals with designing of bandpass filters in THz region using CST microwave studio at different frequency with sharp bandwidths on silicon, polyimide substrate. Metallic hole array on a dielectric substrate technique used to achieve band pass action. The fabrication was carried out using UV lithography process. The filters were tested in THz spectrometer. These bandpass filters used to study the spectroscopy of high energy materials.

Chapter 7: Conclusions and Future-scope

This Chapter summarizes the thesis work and discusses the destiny scope on explorations of optical materials for THz enhancement and their subject packages.

1.4 References

1. A. Debayle, L. Gremillet, L. Bergé, C. Köhler, R. M. Woodward, and T. Elsaesser, "Analytical model for THz emissions induced by laser-gas interaction " Strong terahertz pulse generation by chirped laser pulses in tenuous gases," New J. Phys. Opt. Express, **22**, pp. 13691-13709 (2014).

2. Y. S. Lee, *Principles of Terahertz Science and Technology* (2009).

3. X. C. Zhang and J. Xu, "Chapter 2 - Generation and detection of terahertz waves," in *Introduction to THz Wave Photonics* (2010).

4. B. Ferguson and X. C. Zhang, "Materials for terahertz science and technology," Nat. Mater. (2002).

5. H. Park, J.-H. Son, and C.-B. Ahn, "Enhancement of terahertz reflection tomographic imaging by interference cancellation between layers," Opt. Express, **24**, 7028-7036 (2016).

6. P. F. Taday, I. V. Bradley, D. D. Arnone, and M. Pepper, "Using Terahertz pulse spectroscopy to study the crystalline structure of a drug: A case study of the polymorphs of ranitidine hydrochloride," J. Pharm. Sci, **92**(4):831-8 (2003).

7. Y. C. Shen, P. C. Upadhya, E. H. Linfield, and A. G. Davies, "Temperature-dependent low-frequency vibrational spectra of purine and adenine," Appl. Phys. Lett. **82**, 2350–2352 (2003).

8. M. C. Beard, G. M. Turner, and C. A. Schmuttenmaer, "Transient photoconductivity in GaAs as measured by time-resolved terahertz spectroscopy," Phys. Rev. B - Condens. Matter Mater. Phys., **62**, 15764 (2000).

9. J. H. Strait, P. A. George, M. Levendorf, M. Blood-Forsythe, R. Rana, and J. Park, "Measurements of the Carrier Dynamics and Terahertz Response of Oriented Germanium Nanowires," Nano Lett, **9**, 8, 2967–2972 (2009).

10. M. Jazbinsek, U. Puc, A. Abina, and A. Zidansek, "Organic crystals for THz photonics," Appl. Sci., **9**(5), 882 (2019).

11. Y. C. Shen, T. Lo, P. F. Taday, B. E. Cole, W. R. Tribe, and M. C. Kemp, "Detection and identification of explosives using terahertz pulsed spectroscopic imaging," Appl. Phys. Lett, **86**, 241116 (2005).

12. Y. C. Shen, "Terahertz pulsed spectroscopy and imaging for pharmaceutical applications: A review," Int. J. Pharm, **417**, 48-60 (2011).

13. J. F. Federici, B. Schulkin, F. Huang, D. Gary, R. Barat, F. Oliveira, and D. Zimdars, "THz imaging and sensing for security applications—explosives, weapons and drugs," Semicond. Sci. Technol. **20**, S266–S280 (2005).

14. D. M. Mittleman, R. H. Jacobsen, and M. C. Nuss, "T-ray imaging," IEEE J. Sel. Top. Quantum Electron. **2**, 679–692 (1996).

15. P. H. Siegel, "Terahertz technology in biology and medicine," IEEE Trans. Microw. Theory Tech., **52**, 2438 - 2447 (2004).

16. J. W. Waters, "Submillimeter-Wavelength Heterodyne Spectroscopy and Remote Sensing

of the Upper Atmosphere," Proc. IEEE, **80**, 1679 - 1701 (1992).

17. J. Federici and L. Moeller, "Review of terahertz and subterahertz wireless communications," J. Appl. Phys, **107**, 111101 (2010).

18. T. Kleine-Ostmann and T. Nagatsuma, "A review on terahertz communications research," J. Infrared, Millimeter, Terahertz Waves, **32**, 143–171 (2011).

19. H. B. Liu, H. Zhong, N. Karpowicz, Y. Chen, and X. C. Zhang, "Terahertz spectroscopy and imaging for defense and security applications," in *Proceedings of the IEEE* , **95**, 1514 - 1527 (2007).

20. X. C. Zhang, "Air photonics: Tera - Mid infrared radiation," NATO Sci. Peace Secur. Ser. B Phys. Biophys. (2011).

21. M. R. Leahy-Hoppa, J. Miragliotta, R. Osiander, J. Burnett, Y. Dikmelik, C. McEnnis, and J. B. Spicer, "Ultrafast laser-based spectroscopy and sensing: Applications in LIBS, CARS, and THz spectroscopy," Sensors, **10**(5):4342-72 (2010).

22. A. Singh and S. S. Prabhu, "Microlensless interdigitated photoconductive terahertz emitters," Opt. Express, **23**, 1529-1535 (2015).

23. P. C. Upadhya, W. Fan, A. Burnett, J. Cunningham, A. G. Davies, E. H. Linfield, J. Lloyd-Hughes, E. Castro-Camus, M. B. Johnston, and H. Beere, "Excitation-density-dependent generation of broadband terahertz radiation in an asymmetrically excited photoconductive antenna," Opt. Lett, **32**(16):2297-9 (2007).

24. P. R. Smith, D. H. Auston, and M. C. Nuss, "Subpicosecond Photoconducting Dipole Antennas," IEEE J. Quantum Electron,**24**, 255 - 260 (1988).

25. A. Rice, Y. Jin, X. F. Ma, X. C. Zhang, D. Bliss, J. Larkin, and M. Alexander, "Terahertz optical rectification from 〈110〉 zinc-blende crystals," Appl. Phys. Lett, **64**, 1324 (1994).

26. X. C. Zhang and D. H. Auston, "Optoelectronic measurement of semiconductor surfaces and interfaces with femtosecond optics," J. Appl. Phys, **71**, 326 (1992).

27. G. H. Welsh, N. T. Hunt, and K. Wynne, "Terahertz-pulse emission through laser excitation of surface plasmons in a metal grating," Phys. Rev. Lett, **98**(2):026803 (2007).

28. P. C. M. Planken, M. C. Nuss, I. Brener, K. W. Goossen, M. S. C. Luo, S. L. Chuang, and L. Pfeiffer, "Terahertz emission in single quantum wells after coherent optical excitation of light hole and heavy hole excitons," Phys. Rev. Lett, **28**;69(26):3800-3803 (1992).

29. L. Ozyuzer, A. E. Koshelev, C. Kurter, N. Gopalsami, Q. Li, M. Tachiki, K. Kadowaki, T. Yamamoto, H. Minami, H. Yamaguchi, T. Tachiki, K. E. Gray, W. K. Kwok, and U. Welp, "Emission of coherent THz radiation from superconductors," Science **80** (2007).

30. E. Beaurepaire, G. M. Turner, S. M. Harrel, M. C. Beard, J. Y. Bigot, and C. A. Schmuttenmaer, "Coherent terahertz emission from ferromagnetic films excited by femtosecond laser pulses," Appl. Phys. Lett, **84**, 3465 (2004).

31. D. J. Cook and R. M. Hochstrasser, "Intense terahertz pulses by four-wave rectification in air," Opt. Lett, **25**, 1210-1212 (2000).

32. X. Xie, J. Dai, and X. C. Zhang, "Coherent control of THz wave generation in ambient air," Phys. Rev. Lett, **96**, 075005 (2006).

33. J. Shen, X. Fan, Z. Chen, M. F. Decamp, H. Zhang, and J. Q. Xiao, "Damping modulated

terahertz emission of ferromagnetic films excited by ultrafast laser pulses," Appl. Phys. Lett, **101**, 072401 (2012).

34. L. Cong, S. Tan, R. Yahiaoui, F. Yan, W. Zhang, and R. Singh, "Experimental demonstration of ultrasensitive sensing with terahertz metamaterial absorbers: A comparison with the metasurfaces," Appl. Phys. Lett. , **106**, 031107(2015).

35. Y. Yang, R. Singh, and W. Zhang, "Anomalous terahertz transmission in bow-tie plasmonic antenna apertures," Opt. Lett, **36**, 2901-2903 (2011).

36. A. Nahata, A. S. Weling, and T. F. Heinz, "A wideband coherent terahertz spectroscopy system using optical rectification and electro-optic sampling," Appl. Phys. Lett, **69**(16), (1996).

37. Y. C. Shen, P. C. Upadhya, E. H. Linfield, H. E. Beere, and A. G. Davies, "Ultrabroadband terahertz radiation from low-temperature-grown GaAs photoconductive emitters," Appl. Phys. Lett, **83**, 3117 (2003).

38. K. J. Button, *Infrared and Millimeter Waves V15: Millimeter Components and Techniques* (Academic Press, 1986).

39. M. E. Barnes, D. McBryde, S. A. Berry, P. C. Gow, G. J. Daniell, H. E. Beere, D. A. Ritchie, and V. Apostolopoulos, "Terahertz emission from lateral surge currents and suppression of dipoles under a metal mask," in *International Conference on Infrared, Millimeter, and Terahertz Waves, IRMMW-THz* (2013).

40. S. Hargreaves, K. Radhanpura, and R. A. Lewis, "Generation of terahertz radiation by bulk and surface optical rectification from crystal planes of arbitrary orientation," Phys. Rev. B - Condens. Matter Mater. Phys, **80**, 195323 (2009).

41. K. Sakai and M. Tani, "Introduction to terahertz pulses," Top. Appl. Phys, **97**:1-30 (2005).

42. A. M. Weiner, *Ultrafast Optics* (2009).

43. P. Gu and M. Tani, "Terahertz radiation from semiconductor surfaces," Top. Appl. Phys, **20**, 4518 (2005).

44. J. N. Heyman, N. Coates, A. Reinhardt, and G. Strasser, "Diffusion and drift in terahertz emission at GaAs surfaces," Appl. Phys. Lett, **83**, 5476 (2003).

45. S. G. Park, K. H. Jin, M. Yi, J. C. Ye, J. Ahn, and K. H. Jeong, "Enhancement of terahertz pulse emission by optical nanoantenna," ACS Nano, **27**;6(3):2026-31 (2012).

46. A. Schneider, M. Neis, M. Stillhart, B. Ruiz, R. U. A. Khan, and P. Günter, "Generation of terahertz pulses through optical rectification in organic DAST crystals: theory and experiment," J. Opt. Soc. Am. B, **23**, 822-1835 (2006).

47. M. Bass, P. A. Franken, J. F. Ward, and G. Weinreich, "Optical rectification," Phys. Rev. Lett, **9**, 446 (1962).

48. X. C. Zhang, X. F. Ma, Y. Jin, T. M. Lu, E. P. Boden, P. D. Phelps, K. R. Stewart, and C. P. Yakymyshyn, "Terahertz optical rectification from a nonlinear organic crystal," Appl. Phys. Lett, **18**, 1369-1371 (1992).

49. K. Ravi, W. R. Huang, S. Carbajo, E. A. Nanni, D. N. Schimpf, E. P. Ippen, and F. X. Kärtner, "Theory of terahertz generation by optical rectification using tilted-pulse-fronts," Opt. Express, **23**, 5253-5276 (2015).

50. P. U. Jepsen, R. H. Jacobsen, and S. R. Keiding, "Generation and detection of terahertz pulses from biased semiconductor antennas," J. Opt. Soc. Am. B, **13**, 2424-2436 (1996).

51. S. Kono, M. Tani, and K. Sakai, "Ultrabroadband photoconductive detection: Comparison with free-space electro-optic sampling," Appl. Phys. Lett, **79**, 898 (2001).

52. Q. Wu and X. C. Zhang, "Ultrafast electro-optic field sensors," Appl. Phys. Lett, **68**, 1604 (1996).

53. I. E. Ilyakov, G. K. Kitaeva, B. V. Shishkin, and R. A. Akhmedzhanov, "Laser pulse amplitude changes induced by terahertz waves under linear electro-optic effect," Appl. Phys. Lett, **104** (15), 151107 (2014).

54. I. Tools, "Getting Started with LabVIEW," Building (2001).

55. J. Qin, Y. Ying, and L. Xie, "The detection of agricultural products and food using terahertz spectroscopy: A review," Appl. Spectrosc. Rev, **48**, 439-457 (2013).

56. U. Puc, A. Abina, A. Jeglič, A. Zidanšek, I. Kašalynas, R. Venckevičius, and G. Valušis, "Spectroscopic Analysis of Melatonin in the Terahertz Frequency Range," Sensors (Basel), **23**;18(12):4098 (2018).

57. D. Nguyen, Y. Hernandez, F. Dortu, A. Dispa, P. Hubert, and E. Ziemons, "Terahertz hyper-spectral imaging of lab-prepared versus commercial paracetamol tablets and potential applications," in (2018).

58. R. Beigang, S. G. Biedron, S. Dyjak, F. Ellrich, M. W. Haakestad, and M. Walczakowski, "Comparison of terahertz technologies for detection and identification of explosives," in *Terahertz Physics, Devices, and Systems VIII: Advanced Applications in Industry and Defense* , 9102 (2014).

59. E. M. Witko, T. M. Korter, J. Wilkinson, W. Ouellette, and J. Lightstone, "Terahertz spectroscopy of energetic materials," in *Terahertz Physics, Devices, and Systems V: Advance Applications in Industry and Defense* (2011).

60. V. A. Trofimov, S. A. Varentsova, M. Szustakowski, and N. Palka, "Efficiency of the detection and identification of ceramic explosive using the reflected THz signal," in *Terahertz Physics, Devices, and Systems VI: Advanced Applications in Industry and Defense* (2012).

61. U. Puc, A. Abina, M. Rutar, A. Zidanšek, A. Jeglič, and G. Valušis, "Terahertz spectroscopic identification of explosive and drug simulants concealed by various hiding techniques," Appl. Opt, **54**, 4495-4502 (2015).

CHAPTER 2 : Experimental techniques

This Chapter Comprises the details of different types of experimental and simulation techniques used for analysis and evaluation of optical materials in THz domain. It consists of information about the laser sources used for the experiments and intensity autocorrelation. The mechanism of terahertz generation, detection and its artefacts are discussed in detailed. In addition, incoherent technique for THz detection using Pyroelectric detector is also discussed. Finally, the use of mechanism of FDTD solver workflow Computer Simulation Technology Microwave Studio (CST-MWS) for designing of frequency selective surfaces is discussed.

2.1 Ultrafast laser sources

All the experiments carried out were performed on following Laser sources

1. Coherent Chameleon Ultra-II (Oscillator)
2. Coherent LIBRA (Amplifier)

2.1.1 Chameleon Ultra-II (oscillator)

Coherent Chameleon Ultra-II laser is compact, tunable form visible (680 nm) to NIR (1080 nm) region, and laser pulses having of duration ~140 fs at repetition rate of 80 MHz. The average power of pulse at 800 nm is 4 mW. Major parts of laser are laser head, power supply, Chiller, miniature-recirculating unit (MRU). The Schematic of Laser includes Verdi, Verdi pumped ultrafast (VPUF) laser head, and power track mirrors as shown in the Figure 2.1. Verdi laser comprises Neodymium vanadate (Nd: YVO_4) as gain medium and pumped by fiber optic in dual end pump geometry. A type-I cut non-critically phase matched LBO crystal is used for second harmonics generation maintained at 150 ^{0}C. The Pump power track (PPT) mirrors mounted on piezo operated in feedback loop electric transducers (PZT) guides the Pump 532(nm) beam coming from Verdi leaser into VPUF. Inside VPUF a cavity, power track mirrors (CPT) align the Laser pump beam into cavity.

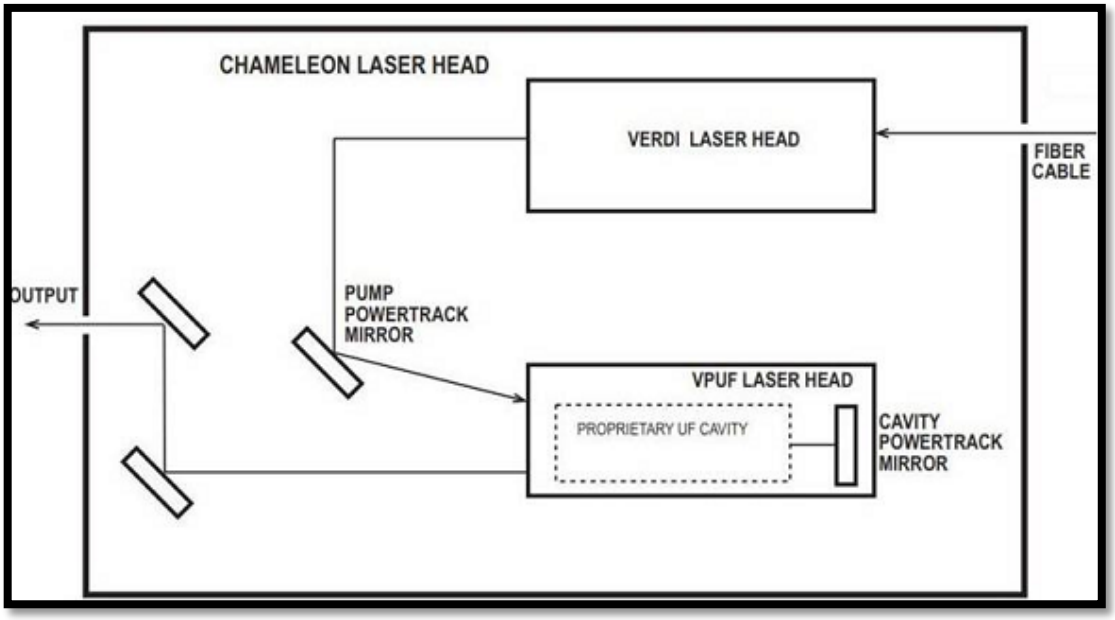

Figure 2.1. Chameleon Ultra II Laser Head (image adopted from coherent manual)

The temperature of the baseplate inside UPUF is maintained at 20 °C by circulating pre-mixed solution using chiller situated outside. Ti:sapphire is used as gain medium which emits ultrashort femtosecond pulses using Kerr Lens Mode locking technique. Kerr lensing is a phenomenon in which refractive index of medium varies as a characteristic intensity Chameleon laser tunability is achieved by changing the cavity length.

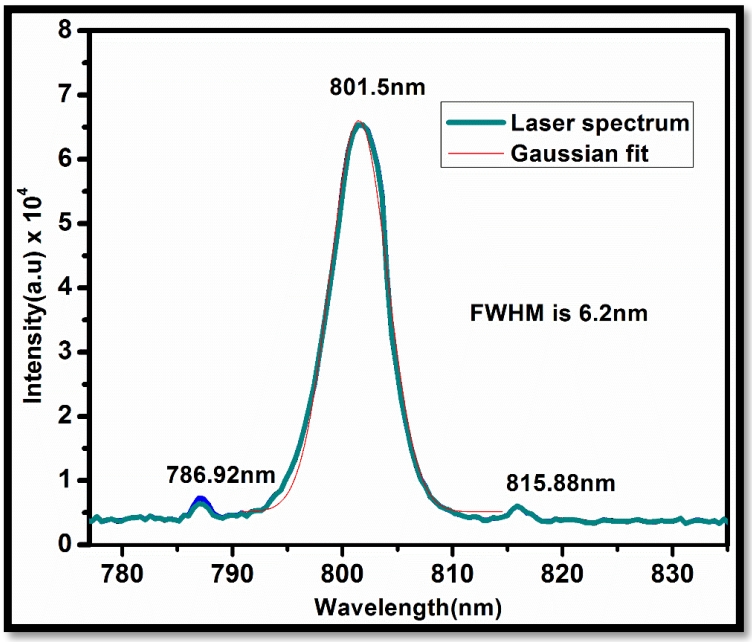

Figure 2.2. Output spectrum of Laser at 800 nm

MRU is used for conditioning, cleaning and maintaining the humidity inside the laser system. An in-built spectrometer is attached to Laser head for monitoring the wavelength emitted from the laser. A simple GUI provided by manufactures displays the output and controlling operation.

The Chameleon oscillator emits the maximum output power at 800 nm, at line width (Δλ) ~ 6.2 nm at FWHM. Figure 2.2 shows the output spectrum of at 800 nm recorded using Maya 2000 Pro spectrometer.

2.1.2 Coherent LIBRA (amplifier)

Coherent LIBRA is a compact oscillator cum regenerative amplifier laser system. Its major components are Optical bench assembly, synchronization & delay generator (SDG), Power supply to Vitesse and evolution, chiller. The optical bench assembly comprises four modules, they are (a)Vitesse seed laser (b) Evolution pump laser, (c) and (d) Regenerative amplifier (RA) along with stretcher and compressor.

2.1.2.a Vitesse seed laser

The schematic of Vitesse is identical to Chameleon laser except for cavity power track mirrors as show in Figure 2.3. Vitesse is a Ti: sapphire oscillator laser pumped by a green coloured diode laser (Coherent Verdi) with a power of 2-5 W. Verdi includes vanadate (gain medium), LBO (second harmonic crystal), an Etalon, two pump mirrors, two cavity end mirrors and an astigmatic compensator as shown in the Figure 2.3.

Neodymium Yttrium Orthovanadate (Nd:YVO_4), generates a wavelength of 1064 nm. Lithium triborate (LBO) NLO crystal generates second harmonic of 1064 nm (i.e. 532 nm, green color allowing efficient absorption via the Ti:sapphire crystal. LBO crystal is maintained at 148 °C with the aid of resistive heater. The Etalon is placed in the cavity to avoid the unwanted modes of getting locked. The vitesse is proficient in emitting 50 fs pulse width with power of 150 mw having 60 nm bandwidth at 80 MHz repetition rate. Femtosecond pulses are generated using Kerr lens mode-locking Technique. The Kerr effect is a nonlinear phenomenon in which crystal medium experiences different refractive indices for different intensities.

$$n = n_0 + n_2 I \tag{1}$$

Here n_0 and n_2 are the linear and intensity dependent refractive indices receptively.

If the intensity distribution of EM field in the incident laser beam is not uniform, then higher intensity based refractive index will be needing more focusing action. This phenomenon is called Kerr lensing Effect. Due to Kerr lensing effect, only higher intensity modes are allowed to build in the cavity. As a result, the spectral bandwidth of output laser pulses will increase and

temporally shorter pulses are produced. The generated ultrashort femtosecond pulse directed to amplifier to increase the intensity of laser beam. Amplifier consists of 1. Pulse stretcher, 2. Regenerative amplifier (RA), 3. Pulse compressor.

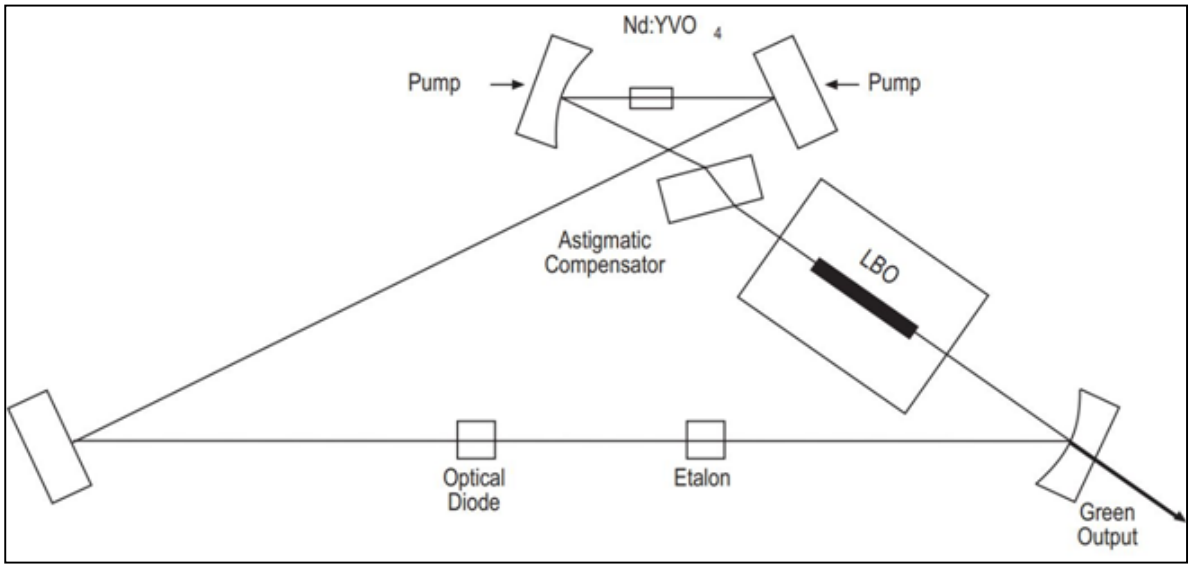

Figure 2.3. Verdi laser head schematic (image adopted from coherent Manual)

2.1.2.b Optical pulse compressor and stretcher

Optical path flowed in pulse compressor and stretcher shown in Figure 2.4. The stretcher (and compressor) has grating(SG) which changes the velocity of blue frequency components of beam faster than red frequency so that the pulse undergoes positive chirping (similarly negatively chirped in compressor). The input pulses fall on grating(SG) which scatters the beam and sends to the SM3 mirror. The SM3 introduces vertical displacement in the optical path and reflects towards mirror (SM4) where it hits back below the point of first incidence. The Reflected beam again directed to grating. This time beam propagates toward the lower mirror of the vertical (SM5-6) retro-reflector. After upper retro mirror SM6 beam follows same path (SG-SM3-SM4-SM3-SG) for four times. The straight-up height is re achieved after the fourth pass and is directed to SM7 mirror, which directs to regenerative amplifier. The compressor does exactly reverse action produced by a stretcher. The Amplified pulses from RA reaches to compress grating (CG) and follows the path CG-CM2-CM3-CG-CM4-CM-5-CG-CM3-CM-2-CG-Output port (CM4, CM5 are the vertical retro mirrors). Beam profiles after each pass are shown Fig. (2-4).

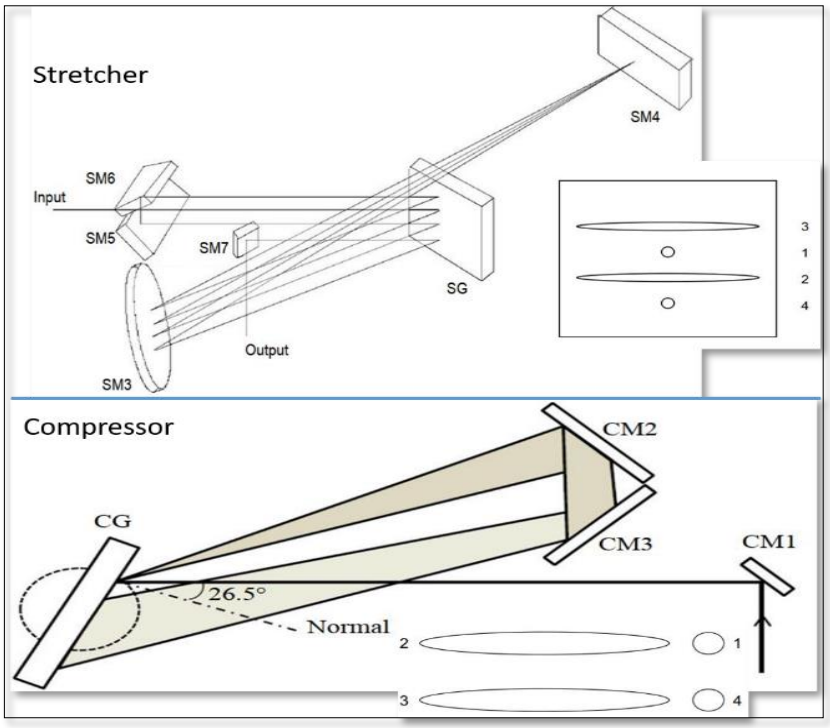

Figure 2.4. Optical layout of stretcher and compressor of LIBRA amplifier (image adopted from coherent Manual)

2.1.2.c Regenerative Amplifier

Regenerative amplifier (RA) is a multiple pass amplifier consists of a Ti:sapphire crystal fed with an Evolution (Nd:YLF) as a gain medium which is pumped by AlGaAs (Aluminium Gallium Arsenide) diode laser arrays, of 527 nm wavelength at 1 KHz repetition rate. The Optical arrangement of RA is depicted in the Figure 2.5. The amplification process begins after excitation of Evolution. The stretched pulses with S- polarization (vertical) are directed to the Ti: sapphire rod and reflected to end mirror RM2 and into RA cavity. Since the repetition rate of seed, pulse is different from prepetition rate of the amplifier most of the pulses do not get amplified. To avoid that, in Libra the injection as well as ejection of pulses is controlled by Pockels cell (PC).

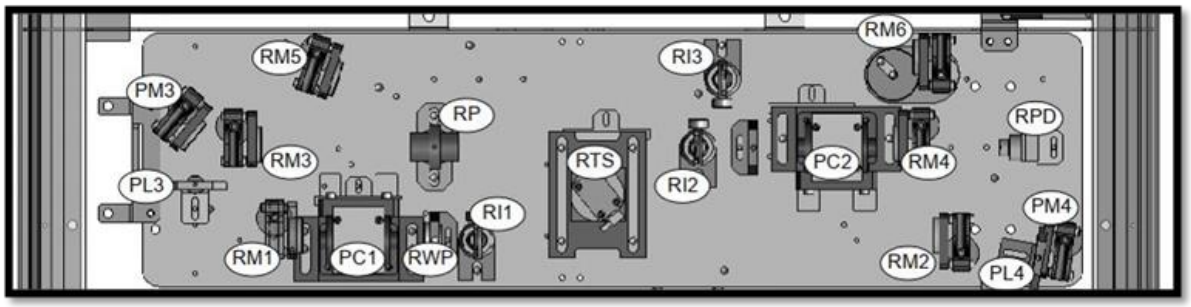

Figure 2.5. Schematic of Regulative Amplifier (image adopted from coherent Manual)

When voltage is applied to the Pockels cell, it behaves like a quarter-wave plate. For double pass, a total rotation of 90° is achieved. The amplification occurs as follows. In the first step, pulse entered into the cavity go for double pass though RWP and converts into a P- polarized. Now, this pulse passes through multiple round trips (~15) between PC1 and PC2 to get amplification in the gain medium. When voltage is applied to PC2, the amplified pulse gets back to S polarization and reflects from RP towards RM5.

2.1.2.d Synchronization and Delay generator (SDG Elite)

The regenerative amplifier needs an accurate harmonization of source, Amplifier pump (Evolution), and Pockels cells which regulate the entering and leaving of pulses. The SDG Elite provides adjustable delay for Pockels cell with respect to input seed and pump pulses. All the delays can be operated at pump frequency or it's inters in form of submultiples.

Table 2-1 Specification of Different lasers

Specifications	Chameleon Ultral-II (Oscillator)	Vitesse(Oscillator)	Libra (Amplifier)
Pulse width	~ 140 fs	~50 fs	~35 fs
Maximum Output power	4 W @ 800 nm	300 mW	4 W
Repetition rate	80 MHz	80 MHz	1 KHz
Polarization	Horizontal	Horizontal	Horizontal
Beam diameter	~(1.2 ±0.2) mm	~(1±0.25) mm	~14 mm

Different Coherent laser sources use in experiments and corresponding specifications are tabulated in Table 2-1 [1–3].

2.2 Measurement of pulse width of ultrashort pulses

It is a challenging task to measure the pulse width of a sub-picosecond or femtosecond pulse with the help of photo diode. The difficulty occurs due to the response time is far higher than temporal width of pulse leads to violation of basic thumb rule which states that least count of yardstick must be smaller than being measured. The available fastest photodiode has limited response time about 10 ps, but generated pulse rise time is of the order of 0.2 picoseconds.

Therefore, it is difficult to measure ultrashort pulses having pulse duration below 200 fs with electronics and there is no direct method to measure the duration of laser pulse below sub-picoseconds [4–9].

The solution to the problem is to use the ultrashort pulse itself to measure the pulse width interfering. This technique is called autocorrelation and it is easy and most affordable technique. Apart from this technique we will use different state-of-the-art techniques like frequency resolved optical gating (FROG), spectral phase interferometry for direct electric-field reconstruction (SPIDER), Streak camera, and so on., the various existing strategies autocorrelation is the best technique to degree the pulse duration of ultrafast pulse [9–12]. However, phase information of the pulse is not obtained in this technique. Autocorrelation setup is a modified version of Michelson interferometer in which two beams were allowed to interfere in a nonlinear medium, resulted second harmonic is recorded [13,14]. Figure 2.6 depicts the autocorrelation setup.

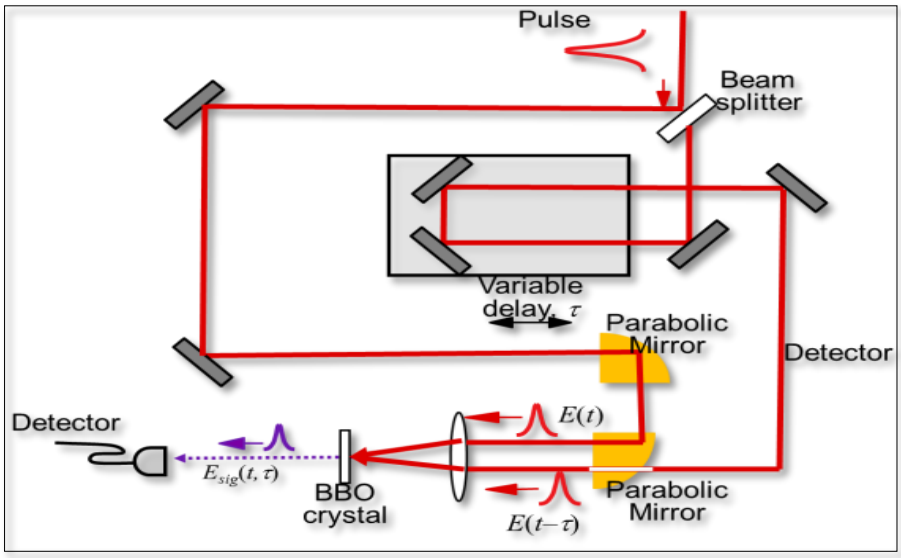

Figure 2.6. Experimental setup for autocorrelation experiment.

The incident laser beam is divided into two parts i.e. I(t+τ), I(t) of different intensity using a beam splitter. The variation in the delay between two beams was achieved by allowing reflected part of pulse through a linear translation stage. Two beams are focused on β-Barium Borate (BBO) crystal and the strength of emitted SHG blue light signal by varying time delay is measured using Energy meter. The generated signal appears in between the two fundamental (800 nm) beams as shown in Figure 2.7.

The strength of produced SHG is related to overlap of pulses inside the medium. A second harmonic Autocorrelation signal appears at the center of two fundamental beams. The strength of the generated SHG depends upon the overlap of pulses inside the nonlinear medium (BBO).

$$AC(\tau) = \frac{\int_{-\infty}^{\infty} I(t)I(t+\tau)dt}{\int_{-\infty}^{\infty} I(t)I(t)dt} \quad (2)$$

However, when ultrashort pulse travels through the dispersive medium with different refractive indices such a BK7 glass, BBO also even during its travel it undergoes dispersion resulting variation in the group velocity in the spectral components of the pulse [15].

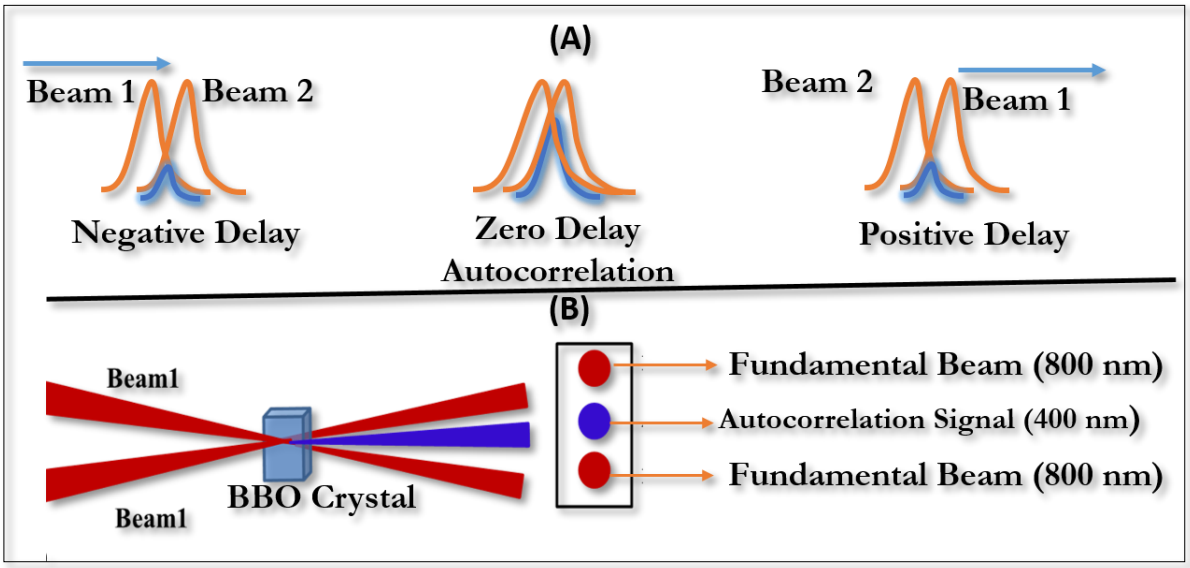

Figure 2.7.(A) Temporal evolution of autocorrelation signal. Here red and blue pulses represent fundamental and second harmonic respectively. Beam2 remain fixed while beam1 traverses beam 1. The intensity of the AC signal increases as the overlap of fundamental beam

This is called group velocity dispersion (GVD). The GVD causes temporal differences in the spectral components of pulses known as frequency chirping [16,17]. Figure 2.8 depicts the autocorrelation data obtained for LIBRA amplifier and Chameleon Oscillator after performing Gaussian fit. We obtained the FWHM to be 131.5431 fs, 205 fs respectively. The relationship between FWHM of measured intensity autocorrelation (Δt ac) of the pulse and the FWHM of laser pulse duration (Δt_p) for Gaussian shape is given below

$$\Delta t_p = \Delta t_{ac} \times 0.707 \quad (2)$$

A Gaussian pulse remains as Gaussian in the medium but stretches as it travels a distance L. Temporal broadening can be calculated by using eq. (3)

$$B = \left\{1 + \left[\frac{4 \ln 2 \times GVD \times L}{\Delta t_{in}^{\ 2}}\right]^2\right\}^{0.5} \quad (3)$$

The valves of second order dispersion coefficient or GVD at 800 nm for BBO and BK-7 glass were 74.735 fs2 /mm and 45 fs2 / mm respectively. Calculated value of B for BBO and BK-7 are 1.012 and 1.0270 by substituting B value in formula [18, 15, 19].

$$B = \frac{\Delta t_{out}}{\Delta t_{in}} \quad (4)$$

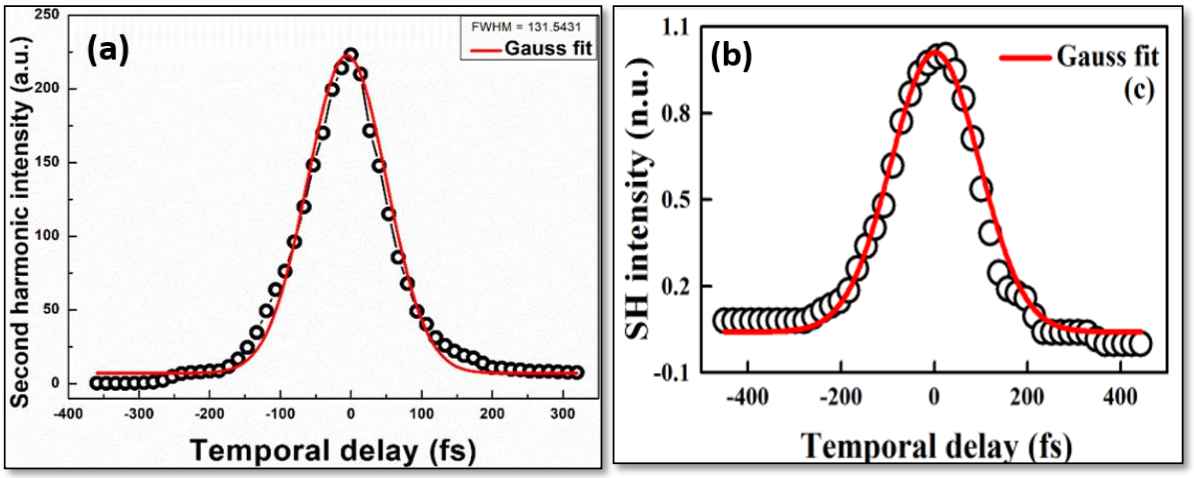

Figure 2.8: Intensity autocorrelation Signal a) Libra b) coherent chameleon Ultra-II

Estimated pulse durations of LIBRA and Chameleon laser pulse are 89 fs, 145 fs respectively by intensity autocorrelation. Figure 2.9 represents the intensity autocorrelation signal. The two Bright beams show the fundamental beams and center blue spot is the generated autocorrelation signal at zero dely.

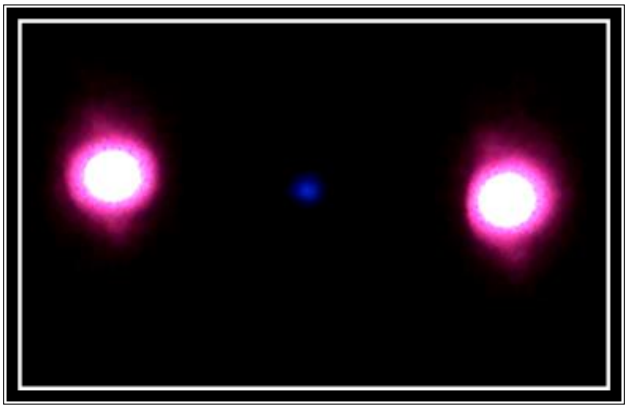

Figure 2.9. The image of Intensity autocorrelation.

2.3 Terahertz Experimental setup details

This section mainly focusses on the Various Terahertz generation and detection techniques used. Most part of the thesis deals with generation and detections with antenna, nonlinear

crystals or vice versa [18–21]. Figure 2.10 shows the multipurpose experimental setup which can be modified to one of the flowing.

1. Terahertz time domain spectrometer (Transmission and Reflection mode).
2. Terahertz Generation and Detection.
3. Optical pump Terahertz probe spectrometer

Table 2-2: THz sources and detractors used in present thesis

S.no	THz Source	Detection system
1	ZnTe (2 mm, cut<110>) (Inorganic crystals)	1. Electro optic sampling 2. PC sampling 3. Pyroelectric detection
2.	BNA, OH1, LAP (Organic crystals)	1. PC sampling 2. Pyroelectric detection
3	PC antenna(strip-line, gap~5μm, length~20μm	1. Electro optic sampling 2. PC sampling

Schematic illustrates the optical layout of a THz generation and pump-probe setup. Mode-locked Ti: sapphire polarized laser pulses with 140 fs duration, 4000 mW average power and central wavelength of 800nm at 80 MHz repetition rate. The laser beam first passed through attenuator (combination of half wave plate followed by a brewster window) was split into two parts by 90:10 beam splitters (BS1). The reflected (90) beam is further split into two parts falls by allowing to fall on a 30:70 beam splitter (BS2). The reflected part sent to a retro alignment on a Thor lab linear translation stage (Model No. NRT 100/M). The pump beam was chopped by mechanical a chopper (C) and focused on THz source (NLO crystal/ PC antenna) using a 50 cm convex lens(L1). Four half axis parabolic mirrors PM1, PM2, PM3, PM4 having diameter 50 mm and focal length 150 mm were employed in f - 2f- 2f - 2f – f form to focus and collimate generated THz. Usually, sample kept between PM2 and PM3. PM4 focuses the THz radiation on the ZnTe crystal where it gets mixed with probe beam. The transmitted part from BS1 used as probe for the detection. Delay variation between two beams was achieved by allowing reflected part of pulse through a linear translation stage (Model No. NRT 150/M) followed by Electro optic sampling (described in chapter 1) used for terahertz detection. Lock-in amplifier (Model No.SR 830) was used to enhance the SNR synchronized with motorized chopper rotating at 1.568 kHz.

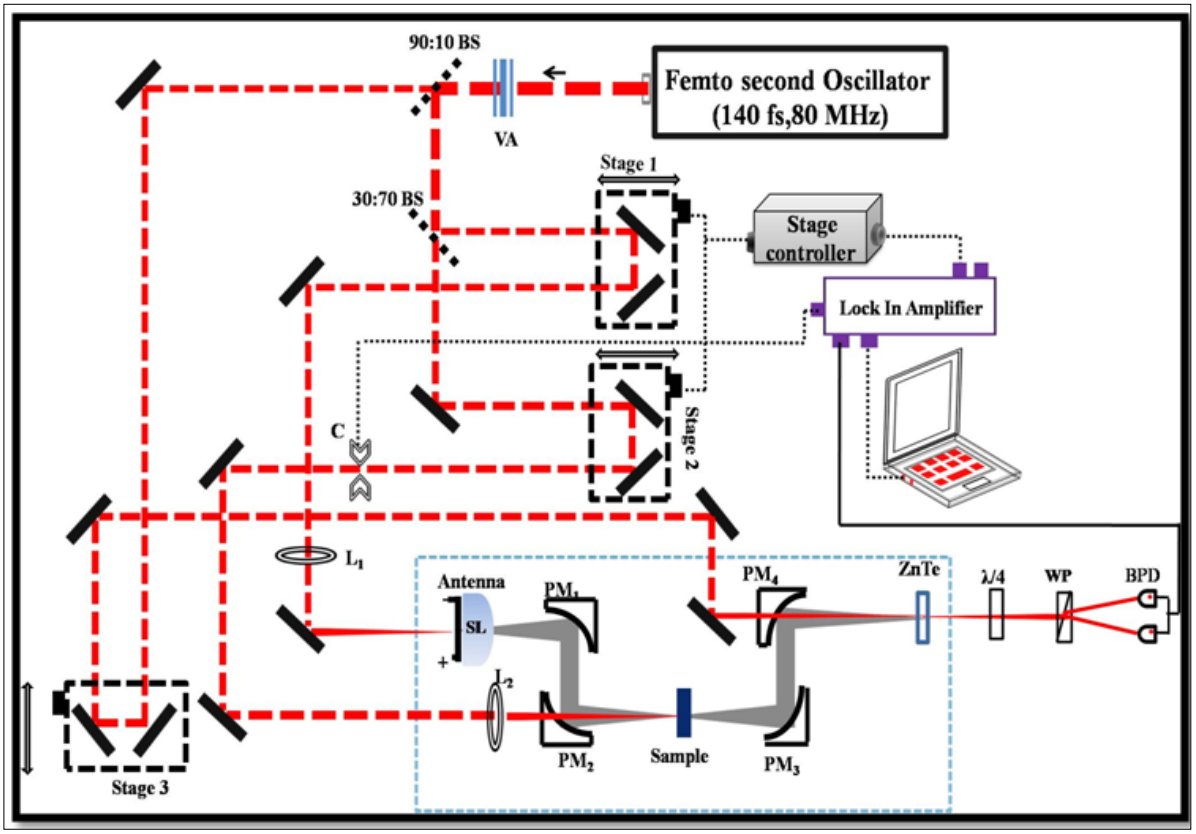

Figure 2.10. Multipurpose Experimental Setup highlighting the schematic of coherent THz detection based TRTS, TDS system and THz generation and detection using nonlinear crystal or antenna (L-lens, C-mechanical chopper, PM- parabolic mirror).

Transmitted part from BS2 used for sample excitation (by keeping a BBO crystal the path 400 nm pump) as an optical pump for optical pump THz probe(TRTS) experiments. The optical path lengths of all the three beams, i.e. THz generation Pump, Sample excitation pump (TRTS), probe are adjusted to zero delay at detector ZnTe crystal, this was achieved by putting a BBO crystal.

Figure 2.11 depicts the Zero delays signals obtained by all the three beams. (Left to right) First blue autocorrelation signal corresponds to THz generation Pump and probe. The second bright blue spot is the signal for (middle and right) THz generation Pump and Sample excitation pump, there is another blue (dominated by middle not clear in this picture) corresponds to left and right i.e. between probe and sample excitation pump.

Figure 2.11. Zero delay obtained among all three interacting beams.

So the experimental setup shown in the Figure 2.10 can modified to all the four possible combinations of generation and detection interchanging the positions of crystals and PC antenna. In the present thesis by keeping the detection sensitivity and signal to noise ratio in mind we have employed generation using crystals and detection using PC antenna (photoconductive sampling) for the study of different types of organic crystals [22–26]. Generation using PC antenna and detection using crystals (EO sampling) for terahertz time domain spectroscopy [27–29].

2.3.1 Crystals based generation and detection using PC antenna

The modified experimental arrangement for the detection of THz radiation from NL crystal using PCS is illustrated in Figure 2.12 which was obtained by the following modifications to setup shown in Figure 2.10.

1. The sample excitations pump (Reflected part of BS1) used as pump for THz generation.
2. By replacing ZnTe crystal with a PC antenna for PC sampling detection.

THz pulses produced from NLO crystal sources was collimated and focused by P1 and P2 parabolic mirrors on to the PC antenna. The PC antenna output was joined to low noise current preamplifier that was fed to voltage input channel of lock-in amplifier for measuring the strength of THz induced voltage [20,30–32]. The output of lock-in amplifier and delay between pump and probe beam stage were connected to the computer. The THz waveforms were recorded with respect to stage delay using program written and executed with Lab-VIEW software.

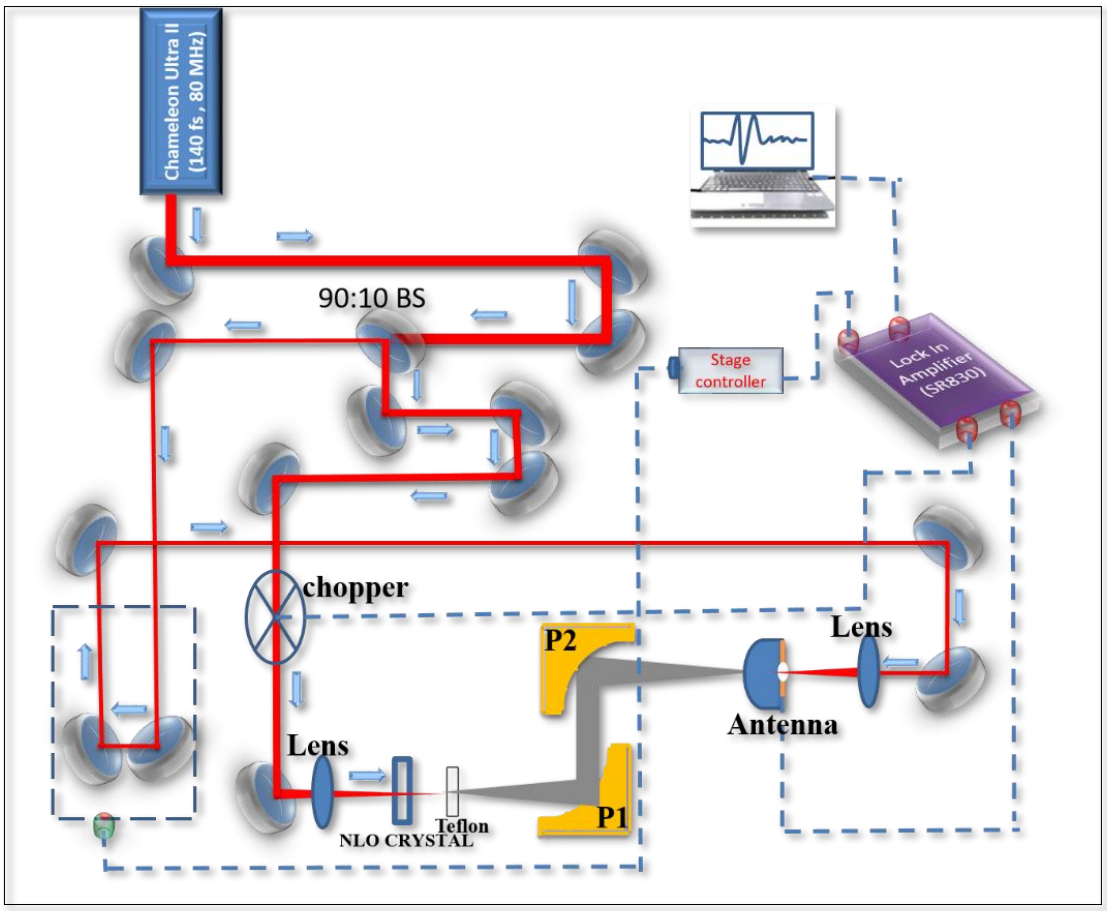

Figure 2.12. Experimental schematic of THz generation by crystals and detection using PC antenna

NLO crystals are robust, they can be used in amplifier laser systems as well as oscillator lasers. PC antennas are not suitable for amplifier systems as their damage threshold is low [33].

2.3.2 Modified THz spectroscopy Setup

THz spectroscopy was performed in two modes namely 1. Transmission mode 2. Reflection mode.

2.3.2.aTransmission mode

Figure 2.13 (a) shows the transmission mode THz spectrometer. The laser beam falls on 90:10 beam splitter (BS). The reflected portion of laser beam from BS was focused on to the antenna by using a plano-convex lens having focal length 60cm.

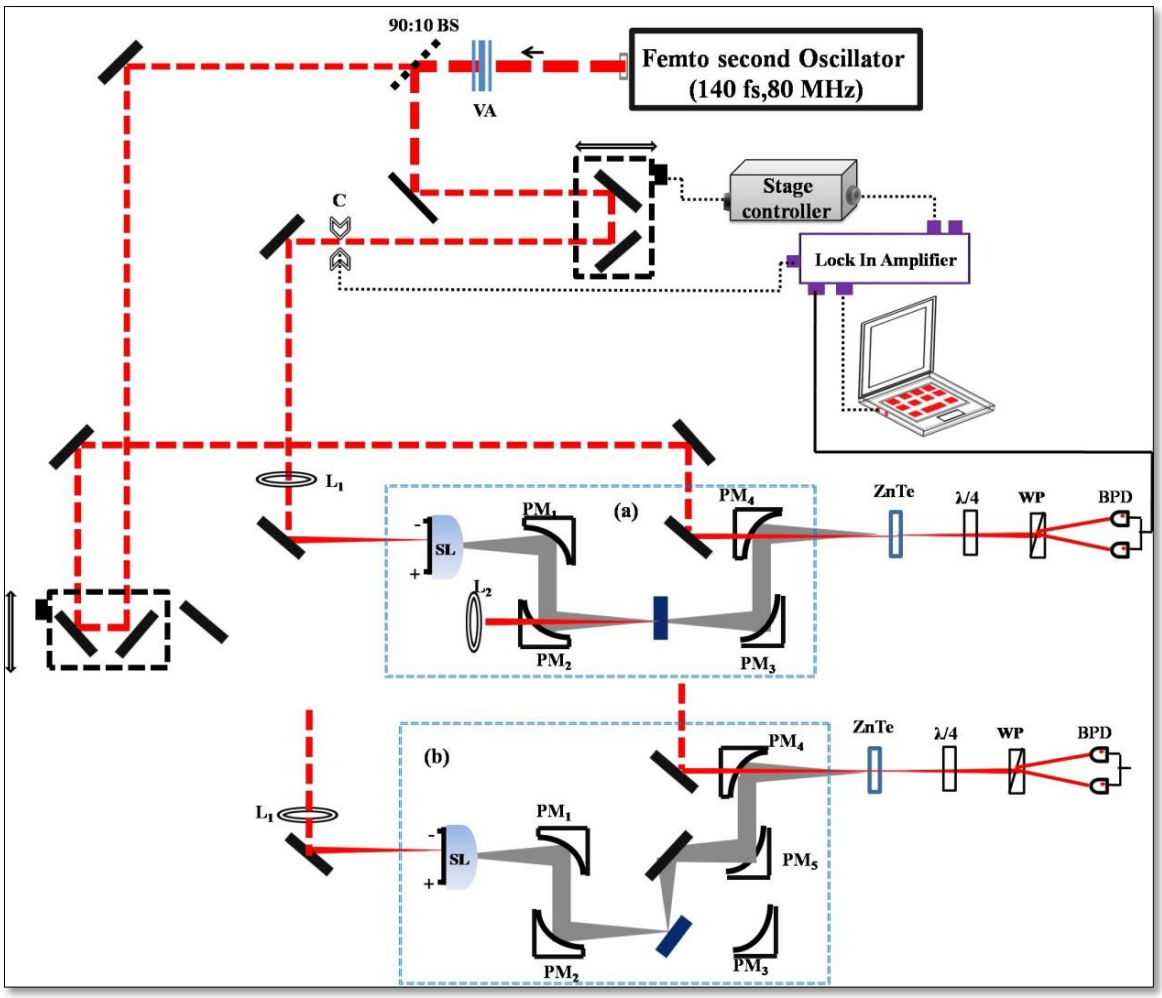

Figure 2.13. Experimental schematic of THz time domain spectrometer (a) Transmission type spectrometer (b) Reflection type spectrometer (Where VA-Variable attenuator, SL-Hyper hemispherical silicon lens, BS- beam splitter, L1 & L2- Plano Convex Lens, ZnTe-Zinc Telluride crystal).

Upon illumination on Photoconductive antennas (strip-line, gap~5μm, length~20μm), it emits THz radiation using the phenomenon of photoconduction. The four half axis parabolic mirrors (PM1, PM2, PM3, PM4) are having diameter (D) = 50 mm and focal length = 150 mm were used to collimate and focus THz radiation on to the THz detector i.e., ZnTe. The optical path length of transmitted part of beam splitter is varied with respect to pump beam by using linear Translation stage (Thor lab NRT100) at a reference of crystal. The probe beam is focused by using a Plano convex lens having focal length of 30 cm on crystal. The generated THz from antenna is detected by using standard optical rectification technique. The output of balanced photo diodes is hooked up to lock in Amplifier (model no.SR830). The data acquisition program used for recording the output changed into automated the use of Lab-view software. The time domain profile of THz signal is recorded by changing the delay between optical probe beam w.r.t

THz pulse at antenna. The Lab-View platform is used for developing a data acquisition program for recording and saving the data.

2.3.2.b Reflection mode

Figure 2.13 (b) depicts the THz time domain spectrometer in transmission mode. In this mode, explosive materials are mounted on a sample holder at zero angles and transmitted THz radiation is focused on to the detector by PM4 parabolic mirror. Figure 2.14 depicts THz time domain spectrometer in reflection mode. In this mode sample is oriented to 450 angle and reflected THz radiation is focused on to THz detector by using PM5, PM4 mirrors.

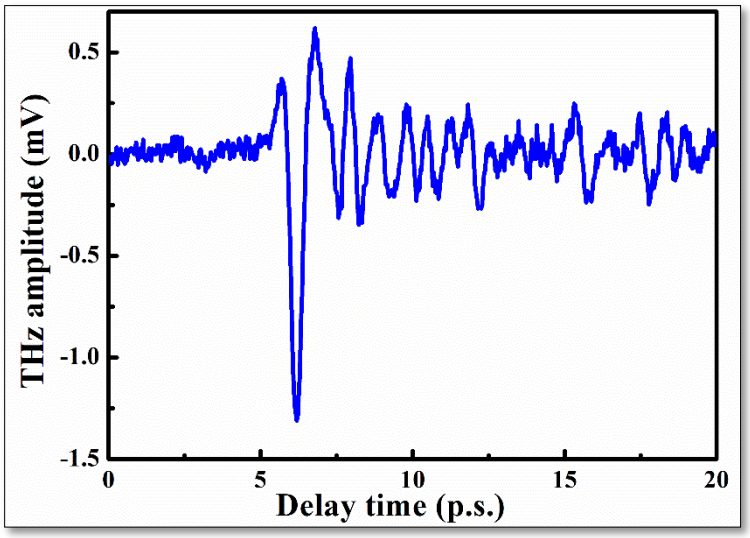

Figure 2.14. Time domain signal of a PTFE pellet recorded in reflection mode

In addition to parabolic mirrors, two-inch gold coated mirror is used in reflection type spectrometer to redirect THz radiation on to the PM5 parabolic mirror [34,35].

2.4 Pyroelectric incoherent detection method for the measuring of Terahertz power

The schematic of Terahertz detection using Pyroelectric detector is shown in Figure 2.15. The amplified laser pulses with 800 nm wavelength, 35 fs pulse width allowed to incident on nonlinear crystal. The generated terahertz from crystal. A Teflon sheet and a HRFZ silicon wafer to filter the unconverted pump beam, only allows THz radiation to pass through a Winston cone connected to the body of Pyroelectric(PED) to collect terahertz and focus on detector. Lithium tantalite ($LiTaO_3$) acts as the absorbing material in a Pyroelectric detector.

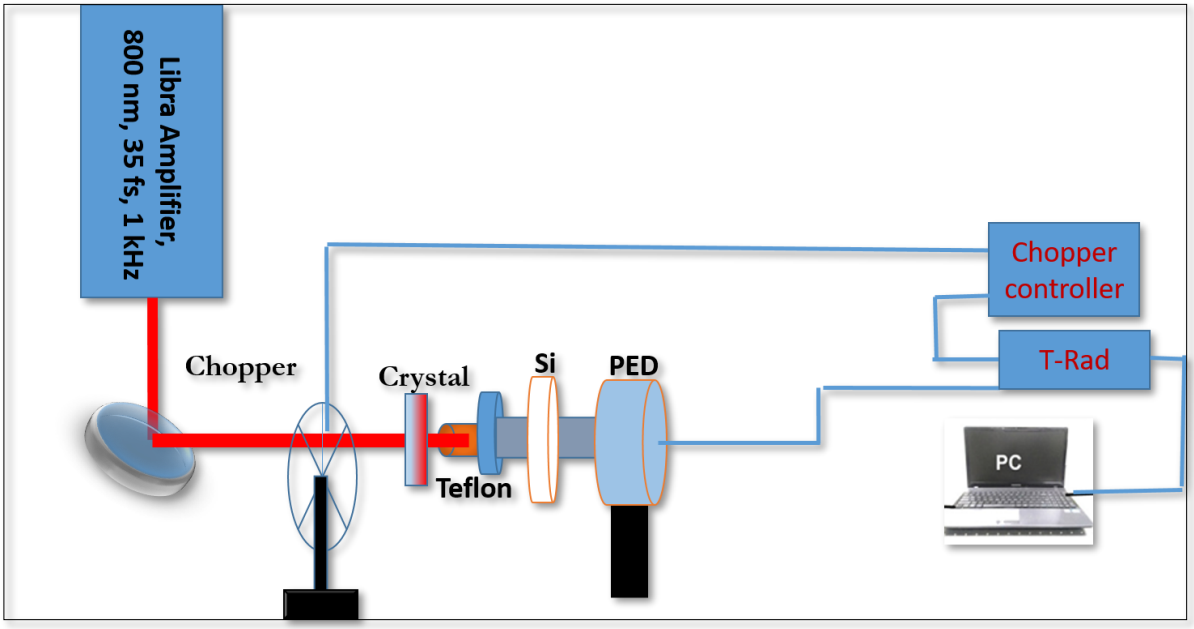

Figure 2.15. Experimental layout of THz generation using Crystal and detection by pyroelectric detector

When thermal radiation falls on the detector cause, temperature dependent spontaneous polarization which results generation of charge. This charge moves to electrodes connected to pyroelectric crystal to compensate the modifications in surface charge and spontaneous polarization. The change in the amount of current is function of change in temperature of the crystal, which mainly is governed by on magnitude of THz radiation falling on it. The output of detector connected to T-RAD-USB (lock-in-Amplifier) synchronized with a chopper rotating with frequency of 23.31 Hz (Model no.SDC-500).

2.5 Terahertz Time Domain Spectroscopy

2.5.1 Working Principle

The working principle of terahertz time-domain spectroscopy (THz-TDS) is sampling of fast transient slowly by coherent detection [36]. In general, any THz-TDS experimental arrangement made up of a THz source and sensor with an optical delay. In this process laser pulse is divided into two parts in which the high intensity part is used for the THz generation in the source and to gate the detector as shown in Figure 2.16 The pulse width of the pump and the time of integration of the detector are less than that of THz pulse. The detector samples the THz pulse with small temporal gates a function of delay Δt. The delay achieved by moving of retro mirrors mounted on a Lenoir translation stage. So higher frequencies can be measured. By varying the

path length between pump and probe pulse, the electric field can be detected. moreover, laser repetition rate is very high than the reciprocal of the pulse width, so most of the detectors becomes insensitive. If THz pulse is exists during that time the detector gives signal and rest of time it produces electronic noise/neutral signal based on the nature of detector.

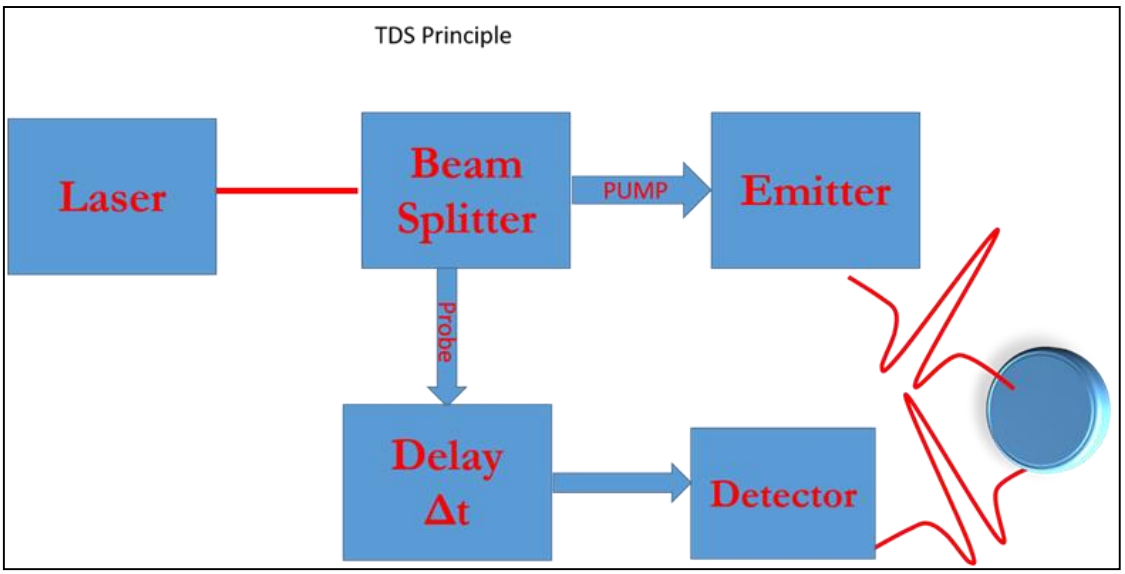

Figure 2.16. Schematic diagram of the THz time domain spectroscopy experiment

2.5.2 Pulse Propagation and Data Processing

In contention to the previous section in time-domain spectroscopy (THz-TDS) a slowly changing THz pulse (0.5 -1 ps) is sampled at different positions of pulse using a time-gated ultrashort optical probe pulse as shown in Figure 2.17.

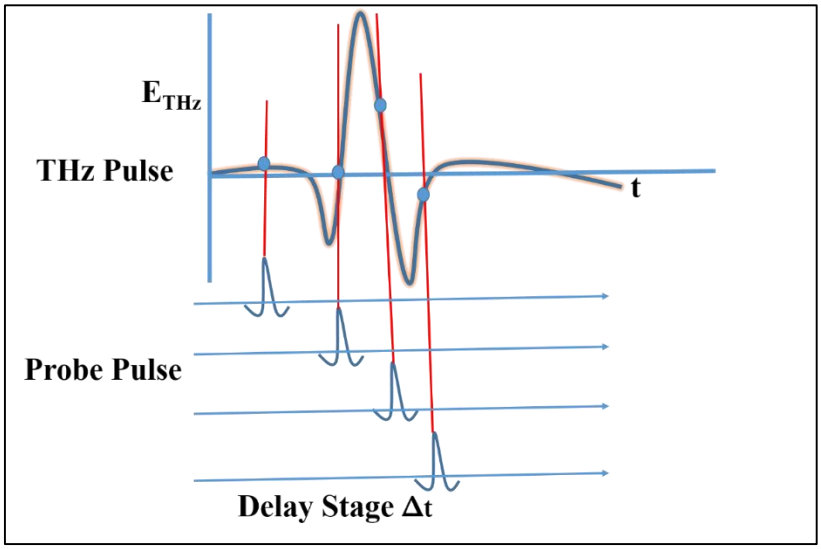

Figure 2.17. Working principle of THz TDS

An optical delay line delays the femtosecond optical pulse (probe) temporally with respect to THz pulse generated with the aid of the THz. The balance photodiode records the photocurrent in detector is measured using lock-in amplifier which considerably improves the signal-to-noise ratio. The modulation is achieved by positioning an optical chopper in pump beam or from a TTL trigger of a function generator. i.e. Voltage applied to antenna, which is used as a reference for lock in amplifier.

2.5.3 Data processing

In THz time domain spectroscopy electric fields are detected, Fourier transformation can give the temporal information to frequency amplitude together with phase information and intensity. The recorded time domain data points must be equally separated for the calculation of Fast-Fourier-Transform (FFT). This can be achieved either by moving the delay stage (on which retro reflecting mirrors present) in discreet distances (stepwise). The temporal step distance, Δt and the spectral resolution $\Delta\nu$ and number of data points N are mathematically related by

$$\Delta\upsilon = \frac{1}{N\Delta t} \tag{5}$$

2.6 Comparison between Terahertz spectroscopy and IR spectroscopy

Molecular spectroscopy has been an important tool to understanding of bonding mechanism in molecule, identification of various modes etc. UV-Visible spectroscopy is associated with electronic translation whereas IR spectroscopy deals with bending and stretching of bonds in molecule. A special type of spectroscopy technique in THz region of electromagnetic spectrum has a got great attention due it versatility in recent past. Both THz and the far-infrared region of the electromagnetic spectrum offers vital information about the physical and chemical processes. In this range both FTIR and THz TDS have their respective benefits however, THz Spectroscopy has got few additional features competed to IR spectroscopy. Experimental arrangement for THz time-domain spectroscopy(TDS) consists of ultrashort laser, a THz detector, a THz source, parabolic mirrors used to focus and collimating THz radiation, a motorized translation stage, a lock-in amplifier, and a data recording system. FTIR spectrometer comprises an incoherent high-pressure mercury arc lamp, a FIR beam splitter, optical for

focusing of IR beam and collimating, a thermal sensor, a motorized delay line filter, and finally a data acquisition system.

Table 2-2 lists some of the important comparisons between THz time-domain spectroscopy and far-IR Fourier transform spectroscopy [37,38]

Parameter	FTIR spectroscopy	THz spectroscopy
1. Dynamic range of power (< 3 THz)	~300	10^8
2. Bandwidth	0.1-200 THz	1-3 THz
3. Time taken for Data acquisition	Few minutes	Few minutes
4. Uniqueness	Broader spectrum	Time gated Coherent pulse
5. SNR	1 : 100	1 : 10000
6. Temporal resolution	Nanosecond	Picosecond
7. Frequency resolution	0.1 cm^{-1}	0.1 cm^{-1}
8. Peak Power	1×10^{-7} μW	1×10^{-3} μW
9. Measurable	Intensity	Electric field and phase

Despite many similarities, FTIR and THz time-domain spectroscopy they are two quite different techniques. The sign to noise ratio(SNR) of THz –TDS has better than FTIR at frequency under three THz (100 cm^{-1}) while the communicate is authentic at over 5 THz (167 cm^{-1}). Furthermore, the time-gated coherent nature of THz-TDS makes it appropriate for few applications, for example nonlinear THz emission spectroscopy, high temperature processes, and time resolved THz spectroscopy.

2.7 Data Analysis in THz spectroscopy

First, the sample reference is subjected to terahertz followed by the sample to record the temporal profiles. Then we perform the FFT to obtain corresponding frequency domain spectra. Terahertz pulse in frequency domain is represented by THz electric field $E_{Sample}(\upsilon)$ transmitted from the sample and $E_{\text{Referance}}(\upsilon)$ for reference. The transmitted electric field includes features of the combination of source and detector as well as the optics like mirrors and lenses. Moreover, humidity of air will show a strong absorption lines. Therefore, normally a reference is recorded without a sample or an identical PTFE pellet to avoid all system parameters besides the changes induced by the sample to be tested. The ratio of these two fields gives the sample's transmission

The Fourier transformed signal can be represented

$$E(\upsilon) = \int_{-\infty}^{\infty} E(t)e^{-i\upsilon t}dt \quad (7)$$

The transmission is signal by given by

$$H(\upsilon) = \frac{E_{Sample}(\upsilon)}{E_{\text{Re } ferance}(\upsilon)} = T(\upsilon)e^{i\phi(\upsilon)} \quad (8)$$

Where $T(\upsilon)$ is Amplitude and $\phi(\upsilon)$ is the phase. The phase will be unwrapped to calculate the refractive index and extinction coefficient. For optically thick sample the formula used for the absorption coefficient (α) of sample is expressed as

$$\alpha = -\frac{1}{d}\ln\left(\frac{E_{THz\text{-}Sam}(\upsilon)}{E_{THz\text{-}Ref}(\upsilon)}\right) \quad (9)$$

Where, d – Effective thickness of pellet, ω is THz frequency. The effective thickness of sample is given by

$$d = \frac{m}{\rho}\frac{4}{\pi D^2} \quad (10)$$

where, m- Weight of the sample, ρ – density of material, D – diameter of sample. Density (ρ) and the calculated effective thicknesses (l) of sample.

Refractive index of material in THz region is given by

$$n(\upsilon) = 1 + \frac{c \times (\phi_s(\upsilon) - \phi_r(\upsilon))}{2\pi\upsilon d} \quad (11)$$

Here $n(\upsilon)$ frequency dependent refractive index, c is velocity of light, $\phi_s(\upsilon), \phi_r(\upsilon)$ are the phase obtained after performing FFT of sample and reference respectively.

2.8 Simulations using CST Microwave Studio

CST-MWS (Computer Simulation Technology Microwave Studio) used as simulation software for the modeling of the frequency selective surfaces(FSS) and simulated their plasmonics resonance [39–41]. CST Studio is a standard motive electromagnetic solver works on Finite

Integration approach(in shape) evolved by Weiland in 1977 [42]. FIT solves electromagnetic Maxwell's equations in integral form which is opposite to Finite Difference Time Domain (FDTD) solvers which are done by differential form [41,43,44].

$$\oint_{\partial A} \vec{E}.d\vec{s} = -\int_{A} \frac{\partial \vec{B}}{\partial t}.d\vec{A} \quad \oint_{\partial A} \vec{\mathrm{H}}.d\vec{s} = -\int_{A} \left(\frac{\partial \vec{B}}{\partial t} + \vec{J} \right).d\vec{A}$$
$$\oint_{\partial V} \vec{\mathrm{D}}.d\vec{A} = -\int_{V} \rho dV \quad \oint_{\partial A} \vec{\mathrm{B}}.d\vec{A} = 0 \qquad \textbf{(12)}$$

The FSS/Bandpass filter can be modeled as metallic(Au) surface covered over a dielectric substrate (Teflon/Silicon). After Designing the shape using the CST 3D layout GUI, the stricture is difficult to meshing. Two orthogonal grids are fashioned for fixing the magnetic and electric powered fields ($\vec{E}$, $\vec{B}$) and corresponding vectors ($\vec{D}$, $\vec{H}$). The material properties are defining the members of the family among electric displacement and electric powered field ($\vec{D}$= $\epsilon\vec{E}$) and their magnetic equivalents ($\vec{B}$= $\mu\vec{H}$). those equations are called Maxwell's Grid Equations.

FSS are generally modelled using two particular type of solvers:

1. Transient solvers
2. Frequency domain solver.

The variance between those two types of solvers is that their treatment of time derivatives in Maxwell's equations. The transient solver treats the time derivatives as time variations and solves for temporal evolution of fields the usage of a leapfrog scheme. The advantage of this form of method is that a version could be solved for a wide frequency band in a single computation but this approach is time eating for massive mesh limits. It best works for hexahedral mesh. The Frequency area (FD) solver technique is useful for narrow band structures. unit cell boundaries and Periodic type of Problems solved using this method. The FD solver is based on Maxwell's Grid Equations in the time harmonic case ($\partial/\partial t \rightarrow i\omega$). The general-purpose FD solver can be used composed with hexahedral or tetrahedral grids. The general-purpose solver along with a module is specialized for calculation of S-parameter in resonant structures like bandpass filters. This type of solver is tremendously fast compared to rest of simulation methods.

2.9 Frequency Domain Solver Workflow

The Frequency domain solver specifically useful while the running region of hobby extraordinarily low frequency, i.e., the scale of the structure could be very much less than the

wavelength. The bandpass filter resonance frequency is expanded or tuned in an entire model by using the solver. The solver can hastily deliver a close to-area and some distance area allocations and S-parameters. This form of solver is typically desired because it calculates all S-parameters for each the polarizations in a single simulation run. The simulations work-flow r in frequency domain solver provided by the CST manual is shown below [39].

Set the units (Length = μm, Frequency = THz, Time = ps) and frequency range of interest→ Model and construct the structure → Set the boundary conditions →Assign source and listener ports → Create the meshing →Run the solver → Analyse your output (S-parameters, electric field patterns and currents).

2.9.1 Analysis of Results: S-parameters

Scattering parameters(S-parameters) normally used in steady state microwave engineering to designate the linear response of a circuit element in a two port network system. CST-MWS models given structure as a two-port network Figure 2.18 for the calculation of S-parameters from which the reflection and transmission for various modes obtained.

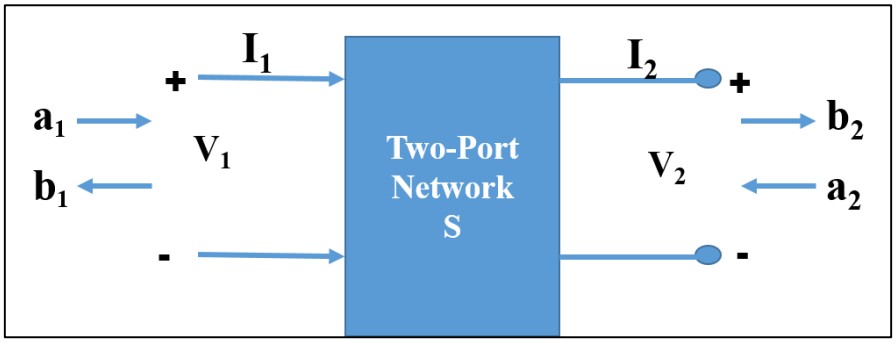

Figure 2.18. Schematic showing a two-port network for scattering parameters.

For a given -port network, the relation between the incoming waves a_1 and a_2 and outgoing waves b_1 and b_2 is given by using the following equation

$$\begin{pmatrix} b_1 \\ b_2 \end{pmatrix} = \begin{pmatrix} S_{11} & S_{12} \\ S_{21} & S_{22} \end{pmatrix} \begin{pmatrix} a_1 \\ a_2 \end{pmatrix} \quad \textbf{(13)}$$

The factors of S-matrix are referred as S-parameters. For a given microwave circuits, the S-parameters are typically calculated by using placing the 2-port network in a transmission line linked to a VNA (vector community analyser) [45]. One of the input ports is hooked up to the

supply and the other is attached to load. The dimension of S-parameters is finished by using joining to a matched load(impedance). From maximum energy transfer theorem, none of the pondered waves coming from the load (a_2 = zero) possible. The S-matrix equations are given by using

$$\begin{aligned} b_1 &= S_{11}\, a_1 + S1_2 \;\; a_2 = S_{11}\, a_1 \Longrightarrow S_{11} = (b_1/a_1) \\ b_2 &= S_{21}\, a_1 + S_{22}\, a_2 = S_{21}\, a_1 \Longrightarrow S_{21} = (b_2/a_1) \end{aligned} \tag{14}$$

where, S_{12} and S_{11} are the transmission and reflection coefficients. By exchanging the load connections and generator, we can record S_{22} and S_{21} giving the reflection and transmission coefficients from port 2. In most of the simulations excitation from a single port is measured. Most customarily, attained S-parameters are the equivalent for each kind of excitation. To evaluate with the experimental spectra for bandpass filters, the absolute value of the complicated S-parameters is vital. Fabrication and Lithography techniques used for Band pass filters will be will be discussed in chapter 6.

2.10 References

1. S. S. Dhillon, M. S. Vitiello, E. H. Linfield, A. G. Davies, M. C. Hoffmann, J. Booske, C. Paoloni, M. Gensch, P. Weightman, G. P. Williams, E. Castro-Camus, D. R. S. Cumming, F. Simoens, I. Escorcia-Carranza, J. Grant, S. Lucyszyn, M. Kuwata-Gonokami, K. Konishi, M. Koch, C. A. Schmuttenmaer, T. L. Cocker, R. Huber, A. G. Markelz, Z. D. Taylor, V. P. Wallace, J. Axel Zeitler, J. Sibik, T. M. Korter, B. Ellison, S. Rea, P. Goldsmith, K. B. Cooper, R. Appleby, D. Pardo, P. G. Huggard, V. Krozer, H. Shams, M. Fice, C. Renaud, A. Seeds, A. Stöhr, M. Naftaly, N. Ridler, R. Clarke, J. E. Cunningham, and M. B. Johnston, "The 2017 terahertz science and technology roadmap," J. Phys. D. Appl. Phys. (2017).
2. S. Du, K. Yoshida, Y. Zhang, I. Hamada, and K. Hirakawa, "Terahertz dynamics of electron–vibron coupling in single molecules with tunable electrostatic potential," Nat. Photonics, **12**, 608–612 (2018).
3. C. Bosshard, "Third-Order Nonlinear Optics in Polar Materials," Nonlinear Optical Effects and Materials, 7-161 (2000).
4. R. SILBEY, "Chapter I-1 - The Structure and Properties of the Organic Solid State," in *Nonlinear Optical Properties of Organic Molecules and Crystals*, D. S. Chemla and J. Zyss, eds. (Academic Press, 1987), 3–20.
5. D. G. Parker, P. G. Say, A. M. Hansom, and W. Sibbett, "110 ghz high-efficiency photodiodes fabricated from indium tin oxide/gaas," Electron. Lett, **23**, 527 - 528 (1987).
6. A. Finch, Y. Liu, H. Niu, W. Sibbett, W. E. Sleat, D. R. Walker, Q. L. Yang, and H. Zhang, "Development And Evaluation Of A New Femtosecond Streak Camera," in *18th Intl Congress on High Speed Photography and Photonics* (1989).
7. A. Takahashi, M. Nishizawa, Y. Inagaki, M. Koishi, and K. Kinoshita, "New femtosecond streak camera with temporal resolution of 180 fs," in *Generation, Amplification, and Measurement of Ultrashort Laser Pulses* (1994).
8. *Femtosecond Laser Pulses* (1998).
9. H. G. Bach, "Ultrafast efficient photodiodes exceeding 100 GHZ bandwidth (invited)," in *Conference Proceedings - International Conference on Indium Phosphide and Related Materials* (2007).
10. R. Trebino, *Frequency-Resolved Optical Gating: The Measurement of Ultrashort Laser Pulses* (2000).
11. R. Trebino, K. W. DeLong, D. N. Fittinghoff, J. N. Sweetser, M. A.

Krumbügel, B. A. Richman, and D. J. Kane, "Measuring ultrashort laser pulses in the time-frequency domain using frequency-resolved optical gating," Rev. Sci. Instrum, **68**, 3277 (1997).

12. M. Wollenhaupt, A. Assion, and T. Baumert, *Springer Handbook of Lasers and Optics - Femtosecond Laser Pulses: Linear Properties, Manipulation, Generation and Measuremen*, *Springer Handbook of Lasers and Optics*,*937-983* (2007).
13. K. H. Hong, J. H. Sung, Y. S. Lee, and C. H. Nam, "Temporal characterization of chirped femtosecond laser pulses," Opt. Commun, **37**(5),1141 (2002).
14. M. Raghuramaiah, A. K. Sharma, P. A. Naik, P. D. Gupta, and R. A. Ganeev, "A second-order autocorrelator for single-shot measurement of femtosecond laser pulse durations," Sadhana - Acad. Proc. Eng. Sci, **26**, 603–611 (2001).
15. M. Rosete-Aguilar, F. C. Estrada-Silva, N. C. Bruce, C. J. Román-Moreno, and R. Ortega-Martínez, "Calculation of temporal spreading of ultrashort pulses propagating through optical glasses," Rev. Mex. Fis, **54**(2) 141–148 (2008).
16. R. J. Lanzafame and J.-C. D. and W. Rudolph, *Ultrashort Laser Pulse Phenomena: Fundamentals, Techniques, and Applications on a Femtosecond Time Scale*, ***25****(1), 58* (2007).
17. A. M. Weiner, *Ultrafast Optics* (2009).
18. P. R. Smith, D. H. Auston, and M. C. Nuss, "Subpicosecond Photoconducting Dipole Antennas," IEEE J. Quantum Electron,**24**, 255 - 260 (1988).
19. P. J. Hale, J. Madeo, C. Chin, S. S. Dhillon, J. Mangeney, J. Tignon, and K. M. Dani, "20 THz broadband generation using semi-insulating GaAs interdigitated photoconductive antennas," Opt. Express, **22**, 26358-26364 (2014).
20. X. C. Zhang and J. Xu, "Chapter 2 - Generation and detection of terahertz waves," in *Introduction to THz Wave Photonics* (2010).
21. M. Hoffmann, "Novel Techniques in THz-Time-Domain-Spectroscopy A comprehensive study of technical improvements to THz-TDS," (2006).
22. M. Nakajima, Y. Oda, and T. Suemoto, "Competing terahertz radiation mechanisms in semi-insulating InP at high-density excitation," Appl. Phys. Lett, **85**(14):2694-2696 (2004).
23. A. Krotkus, "Semiconductors for terahertz photonics applications," J. Phys. D. Appl. Phys, **43**, 27 (2010).
24. K. Radhanpura, S. Hargreaves, and R. A. Lewis, "Bulk and surface field-

induced optical rectification from (11N) zincblende crystals in a quasireflection geometry," Phys. Rev. B - Condens. Matter Mater. Phys, **83** (12), 125322-1-125322-6. (2011).

25. G. H. Welsh, N. T. Hunt, and K. Wynne, "Terahertz-pulse emission through laser excitation of surface plasmons in a metal grating," Phys. Rev. Lett, **98**, 026803 (2007).
26. E. Beaurepaire, G. M. Turner, S. M. Harrel, M. C. Beard, J. Y. Bigot, and C. A. Schmuttenmaer, "Coherent terahertz emission from ferromagnetic films excited by femtosecond laser pulses," Appl. Phys. Lett, **84**, 3465 (2004).
27. C. Winnewisser, P. Uhd Jepsen, M. Schall, V. Schyja, and H. Helm, "Electro-optic detection of THz radiation in LiTaO3, LiNbO3 and ZnTe," Appl. Phys. Lett, **70**, 3069 (1997).
28. Y. Takahashi, H. Adachi, T. Taniuchi, M. Takagi, Y. Hosokawa, S. Onzuka, S. Brahadeeswaran, M. Yoshimura, Y. Mori, H. Masuhara, T. Sasaki, and H. Nakanishi, "Organic nonlinear optical DAST crystals for electro-optic measurement and terahertz wave generation," J. Photochem. Photobiol. A Chem, **183**, 247-252 (2006).
29. N. S. Daghestani, S. Persheyev, M. A. Cataluna, G. Ross, and M. J. Rose, "THz generation from a nanocrystalline silicon-based photoconductive device," Semicond. Sci. Technol, **26**, 7 (2011).
30. X. C. Zhang and J. Xu, *Introduction to THz Wave Photonics* (2010).
31. J. Choi, W. S. Kwon, K. S. Kim, and S. Kim, "Nondestructive Material Characterization in the Terahertz Band by Selective Extraction of Sample-Induced Echo Signals," J. Nondestruct. Eval, **34**, 269 (2015).
32. V. Apostolopoulos and M. E. Barnes, "THz emitters based on the photo-Dember effect," J. Phys. D. Appl. Phys, **47**, 37 (2014).
33. Y. S. Lee, *Principles of Terahertz Science and Technology* (2009).
34. P. U. Jepsen, U. Møller, and H. Merbold, "Investigation of aqueous alcohol and sugar solutions with reflection terahertz time-domain spectroscopy," Opt. Express,**15**, 14717-14737 (2007).
35. S. Nishizawa, K. Sakai, M. Hangyo, T. Nagashima, M. W. Takeda, K. Tominaga, A. Oka, K. Tanaka, and O. Morikawa, "Terahertz time-domain spectroscopy," Top. Appl. Phys. (2005).
36. D. Grischkowsky, S. Keiding, M. van Exter, and C. Fattinger, "Far-infrared time-domain spectroscopy with terahertz beams of dielectrics and semiconductors," J. Opt. Soc. Am. B **7**, 2006 (1990).
37. P. Y. Han, M. Tani, M. Usami, S. Kono, R. Kersting, and X. C. Zhang, "A direct comparison between terahertz time-domain spectroscopy and far-

infrared Fourier transform spectroscopy," J. Appl. Phys, **89**, 2357 (2001).

38. F. Huang, J. Federici, D. Gary, R. Barat, and D. Zimdars, "Noninvasive study of explosive materials by time domain spectroscopy and FTIR," in *AIP Conference Proceedings* (2005).
39. "CST Microwave studio," IEEE Microw. Mag. (2008).
40. G. A. E. Vandenbosch, "Computational Electromagnetics in Plasmonics," in *Plasmonics - Principles and Applications*, **47**, 777-780 (2012).
41. J. Schneider, "Understanding the Finite-Difference Time-Domain Method," Artech House antennas Propag. Libr. (2005).
42. T. Weiland, "Discretization Method for the Solution of Maxwell's Equations for Six-Component Fields.," AEU-Archiv fur Elektron. und Ubertragungstechnik, **32** , 65-87 (1977).
43. K. S. Yee, "Numerical Solution of Initial Boundary Value Problems Involving Maxwell's Equations in Isotropic Media," IEEE Trans. Antennas Propag,**14**, 302 - 307 (1966).
44. D. M. Sullivan, *Electromagnetic Simulation Using the FDTD Method* (2010).
45. P. Policy, "RF network analyzer basics tutorial," Spectrum (2010).

CHAPTER 3 : Evolution of Some nonlinear crystals for Terahertz Generation

This chapter deals with THz generation from various types of nonlinear crystals via detection using coherent and incoherent techniques. Different types of organic crystals such as BNA, OH1, LAP, were studied to generate efficient THz radiation using 800 nm wavelength of 140 and 50 fs pulses obtained from Ti:sapphire laser oscillator and amplifier at 80MHz and 1kHz repetition rates, respectively. Further, we ascertained the absorption coefficients and refractive indices to establish the role of solvents on the growth of crystals. Finally, the optimized conditions for the efficient THz generation from aforesaid crystals and their comparison with the reported literature are discussed.

3.1 Nonlinear effects in Organic materials*:*

From the past two decades, usage of organic crystals as THz source has pulled the attention of scientists of the entire globe due to their moderate generation efficiency and ability to produce large bandwidths as compared to photoconductive antennas. Terahertz generation from photoconductive antennas requires incident energy of radiation of the order of bandgap of semiconductor material whereas, THz generation from nonlinear crystals has no such limitations due to availability of nonlinear frequency mixing techniques such as optical rectification (OR) and Difference Frequency Mixing(DFM). In traditional electronics, the technique of conversion of an alternating current(AC) into direct current(DC) is called rectification. Similarly, in a nonlinear crystal a varying electric field component of optical signal converted into a DC field, this phenomenon is called optical rectification [1]. To generate THz from nonlinear crystals needs to satisfy some stringent conditions such as laser pulse should be in femtosecond domain, crystal should be thin with moderate second order nonlinearity and possess good transmission in optical and THz domain.

In dielectric medium, the applied electric filed ($\vec{E}$) and induced polarisation ($\vec{p}$) are linearly related but when electric field strength is higher than atomic field (~ 10^5 to 10^8 V/m) the relation is no longer linear. The medium is transparent for small electric fields and it can be understood by linear susceptibility as the number n of the emitted photons increases with respect to the

intensity and polarization of incident photons. The higher-order nonlinear terms come into the picture and present in Taylor series expansion of the polarization as shown in Eq. 1

$$P_i = \alpha E(1 + a_1 E + a_2 E^2 + a_3 E^3 + ...) \quad (1)$$

Where α is the linear polarization and a_1,$a_{2...}$ are the nonlinear terms of higher orders in the electro-optic effect the crystal of Centro symmetry, the higher terms a_1, a_2, have to be identically equal to zero therefore, $a_1E=-a_3E$. consequently only the first term nonlinear aE we can write nonlinearity due to first term [2–4].

$$P_i = 2dE^2 \quad (2)$$

Now the equation of the polarization for the forwarding wave

$$\begin{aligned} E_1(z,t) &= E_1 \cos(\omega_1 t + k_1 z) \\ E_2(z,t) &= E_2 \cos(\omega_2 t + k_2 z) \end{aligned} \quad (3)$$

Now the polarization becomes :

$$P = 2d[E_1^{\,2} \cos^2(\omega_1 t + k_1 z) + E_2^{\,2} \cos^2(\omega_2 t + k_2 z) + 2E_1 E_2 \cos(\omega_1 t + k_1 z)\cos(\omega_2 t + k_2 z)]$$

$$\begin{aligned} P_{2\omega_1} &= dE_1^{\,2} \cos(2(\omega_1 t + k_1 z)) \\ P_{2\omega_2} &= dE_2^{\,2} \cos(2(\omega_2 t + k_2 z)) \\ P_{\omega_1+\omega_2} &= 2dE_1 E_2 \cos((\omega_1 + \omega_2)t + (k_1 + k_2)z) \\ P_{\omega_1-\omega_2} &= 2dE_1 E_2 \cos((\omega_1 - \omega_2)t + (k_1 - k_2)z) \end{aligned} \quad (4)$$

and a study term $P_{direct} = d(E_1^2 + E_2^2)$ then, the nonlinear polarization contains a steady term, a sum and difference frequency and the first overtone of both input frequency are normally called the second harmonics. The resultant frequency components of the polarization include second harmonic, sum frequency E (ω_1+ ω_2) (SFG), difference frequency E(ω_1-ω_2) (DFG) of E_1 and E_2. The optical rectification is a special case of DFG where corresponding electric field E (ω_1-ω_2) generates the DC polarizated waves whose duration lies in sub picoseconds when exited with ultrafast pulses. Essentially, the generated THz is related to derivative of second order polarization [5–7].

$$E_{THz}(t) \propto \frac{\partial^2 P^2(t)}{\partial t^2} \tag{5}$$

Hence, the generated THz is related to second order derivative of the pulse. THz frequencies can be considered as DFG with all the spectral components of the laser pulse. In order to induce a polarization oscillating at a THz frequency ω_{THz} based on DFG (difference-frequency generation), the related electric fields $E(\omega_1)$ and $E(\omega_2)$ should oscillate at narrowly separated frequencies ω_1 and ω_2, so that corresponding frequency difference $\omega_3 = \omega_{THz} = \omega_1 - \omega_2$, falls in the THz region. The phase matching conditions for wave vectors are given by:

$$\Delta\mathbf{k} = \mathbf{k_{THz}} - (\mathbf{k_1} - \mathbf{k_2}) \tag{6}$$

where k_{THz} is the wave vector of the THz-wave is defined as $k_{THz} = 2\pi n_{THz}/\lambda_{THz}$ and k_1, k_2 are the wave vectors of optical fields and defined as $k_i = \frac{2\pi n_i}{\lambda_i}$, where n_{THz} is the refractive index of material in terahertz range, while n_i (i = 1, 2) are the refractive indices of the material at the optical wavelengths λ_i(i =1, 2) of the interacting fields $E(\omega_1)$ and $E(\omega_2)$, respectively. The efficient phase matching condition is based on the coherence length (l_c). It describes the interaction length of optical and generated terahertz field rises with the thickness of the nonlinear medium up to coherence length.

$$l_c = \frac{\pi}{\Delta k} \tag{7}$$

In optical rectification process, coherent length for optical and THz wavelength can be calculated.

$$l_c = \frac{\pi c}{\omega_{THz}\left|n_{opt} - n_{THz}\right|} \tag{8}$$

Here 'c' is the light velocity, n_{opt} is optical group index given by $n_{opt} = n_{opt} - \lambda_{opt}\frac{\partial n_{opt}}{\partial \lambda}$ [8].

3.2 Terahertz Generation from NLO crystals

The NLO-based Terahertz sources work on the principle of difference frequency generation or optical rectification. In both cases they should possess extreme second-order NLO susceptibility and satisfy the phase-matching situation between the fundamental optical pump beam and the generated THz signal waves [9–20].

Nonlinear crystals used for THz generation are classified into three significant categories:

1. Inorganic crystals ($LiTaO_3$, $LiNbO_3$.etc)
2. Organic crystals (BNA, DAST, DSTMS, OH1, HMQ-TMS)
3. Semiconductor crystals ($ZnGeP_2$, GaAs, ZnTe,GaSe, CdTe, GaP)

Here we have evaluated the THz generation capability of some organic crystals like BNA, OH1 and LAP . The generated THz signal is detected using photoconductive antennas. The optical material's susceptibility is function of permittivity (ε) which depends on applied electric field E(ω). At lower frequency the permittivity is defined as a combination of acoustic phonon vibrations and optical phonon vibrations, whereas at optical (higher) frequency the electronic vibrations contribution becomes predominant. Keeping in view of fact that the origin of polarization is distinct in organic and inorganic materials, therefore, the frequency dispersion of (i = 1, 2 or 3) relationship also varies from organic NLO materials. Though many of these NLO materials possess higher nonlinear coefficients as well as minimum birefringence due to close values of refractive index in optical and terahertz frequency range. For example, the optical and terahertz refractive indices of DAST (organic) crystal are 2.1,2.3(about "***a*** "polar axis), respectively leading to minimum dispersion, there is huge variation in the refractive index values of very well-known inorganic NLO crystal $LiNbO_3$, these values are of the order of 2.2, ~5 (about "***c"*** axis), resulting in wide phase mismatch condition [21–23].

For the first time, Zhang et al. demonstrated the generation of terahertz radiation in organic DAST crystal by optical rectification (OR) in organic DAST crystal [19,21,22,24–27]. The reported THz efficiency and bandwidth results are much higher than both GaAs and LiTaO3 inorganic crystals, respectively. This work opened a new channel of THz generations from organic crystals. In present study, we have evaluated group of organic crystals (N-benzyl-2-methyl-4-nitroaniline) BNA, OH1, LAP for THz generation and the obtained results were compared with standard ZnTe under the similar experimental conditions as reported by other group [28]. Also, we ascertained the effect of precursor solvent that was used to grow on the nonlinear properties of the crystals.

3.2.1 BNA

BNA is a yellow colored non-hygroscopic promising positive biaxial organic crystal that belongs to mm2 space group and has orthorhombic structure. BNA has effectively been used for terahertz generation at pump wavelength of 800 nm. BNA (N-benzyl-2-methyl-4-nitroaniline) is a derivative of MNA(2-methyl-4-nitroaniline) developed by Hashimoto *et al.* by using vertical

Bridgman technique [29–34]. The best advantage of BNA is that it is chemically stable without a deliquescent property. Unlike DAST it is not fragile and having high laser damage threshold so it can be polished without difficulty and capable of sustaining high power amplifier lasers. The nonlinear coefficient of BNA crystal d_{333} is 234 pm/V, the highest ever reported in yellow coloured NLO crystals [35]. BNA can be grown by vertical Bridgman and solution growth techniques but the quality of the crystals grown by using Bridgman technique is poor due to lattice defects [29,36–39]. Therefore, BNA crystals grown with different solutions exhibit good surface quality. We have done a systematic study on THz generation from different types of BNA crystals grown from solutions like dimethyl sulfoxide (DMSO), Ethanol: Methanol (1:1), Acetonitrile and Ethyl acetate. The present study deals with four BNA crystals are grown using Acetonitrile, methanol, Dimethylformamide and Acetonitrile: Dimethylformamide.

3.2.1.a BNA synthesis and crystal growth

The BNA crystals were synthesized in crystal growth laboratory of Prof. S. Brahadeeswaran [40–42] by means of adding the commercially purchased reactants: 2-methyl-four-nitroaniline (MNA) (20g), hexamethylphosphorictriamide (HMPA) (100ml), sodium bicarbonate (22g), benzyl bromide (45g) and the complete mixture become refluxed for 30 hrs. at 70°C below nitrogen surroundings. Eventually, the solution turned into extracted with deionized water, diethyl ether and washed numerous instances with saturated sodium chloride solution. The natural layer become dried the usage of anhydrous sodium sulfate powder and the diethyl ether was evaporated to give yellow powder of BNA (17g, yield 19.5%). The synthesized material changed into purified in addition via re-crystallizing it several times using HPLC grade methanol as a solvent and the final compound gave a unmarried spot on silica-gel TLC (n-hexane: ethyl acetate = 7:3) [36]. The molecular structure of BNA is shown in the Figure 3.1 The solubility of BNA becomes measured gravimetrically at 30 °C the usage of the selected single and mixed solvents which include Acetonitrile, methanol, Dimethylformamide and Acetonitrile: Dimethylformamide. The BNA solutions with equilibrium concentrations have been prepared at 30 °C and have been kept in a water bath, ready with a Programmable Eurotherm temperature controller (model: 3216; accuracy ± 0.01 °C). prior to starting up the crystal growth, the bath temperature changed into raised to 5 °C above its saturation temperature and saved at this temperature for approximately 24 hrs. to dissolve any unwanted spurious nuclei present within the answer. The temperature of the solution turned into then slowly reduced to 30 °C with a cooling rate of 0.2 °C/h. After achieving the saturation temperature, the growth was achieved by isothermal solvent evaporation approach at a fixed temperature of 30 °C.

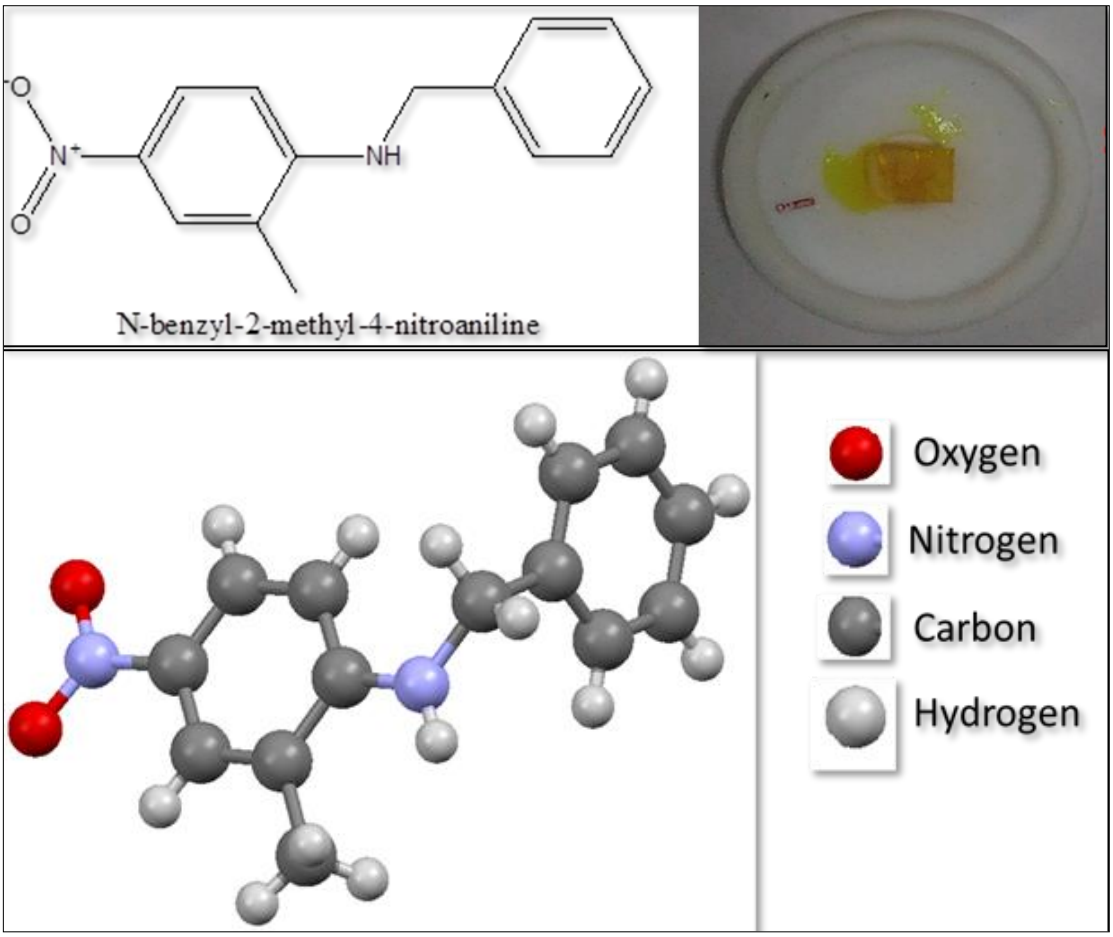

Figure 3.1. Molecular structure of BNA

3.2.1.bTHz generation and detection

Earlier reports on terahertz generation detection were done using DFG, Optical rectification and Electro optical sampling technique [37,38,43,44]. Farooqui et al. reported the intensity of THz radiation emitted by BNA crystal is higher than that of DAST under same experimental conditions [45]. Table (1) comprises of the different aspects of terahertz generation methods, such as laser parameters and growth conditions. Figure 3.2 depicts the experimental setup used for THz generation form different types of BNA crystals used in this chapter. We have employed Ti: sapphire laser (coherent made : Model Chameleon ultra-II) emitting 800 nm wavelength pulses of 140fs duration at repetition rate of 80 MHz for the generation of THz radiation between 0.1 to 2 THz range. The laser pulse obtained from the from the system was split into two parts using BS1 (90/10 beam splitter),the reflected part was treated as a pump beam and focused on BNA crystal mounted in Teflon holder as shown in Figure 3.1. A Teflon sheet was kept after crystal to filter out the uncovered residual part of pump beam. The

generated THz radiation was collimated and focused on PC antenna using gold coated parabolic mirrors (P1, P2) for detection.

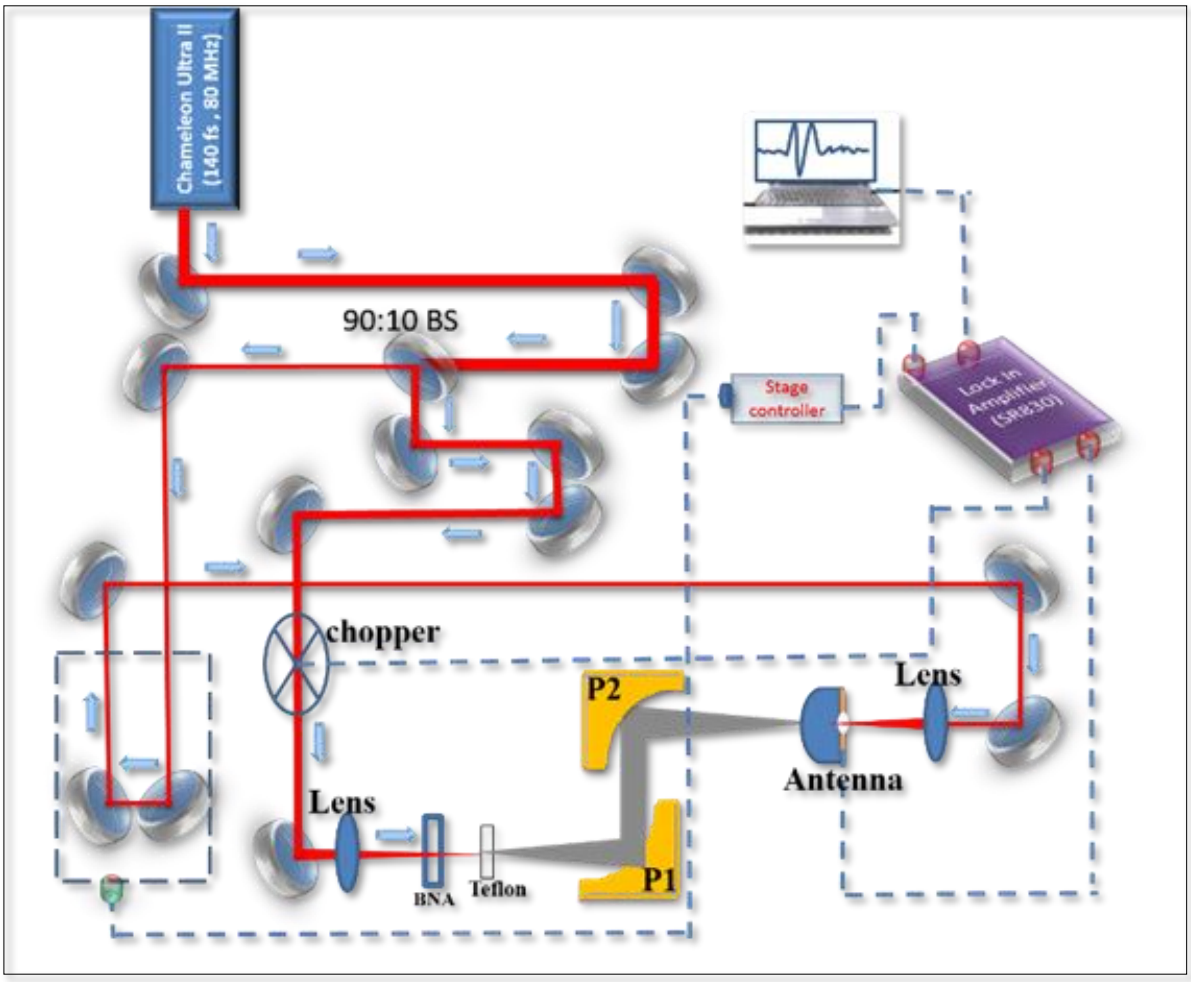

Figure 3.2. Schematic diagram of a THz generation setup

The transmitted part from beam splitter was treated as a probe beam and directed to the set of mutually tilted plane mirrors . These mirrors are fixed on linear motorized translation stage and allowed to focus the probe beam in the gap of electrodes of photoconductive antenna for the detection of generated THz radiation. A mechanical chopper rotating at 1.56 kHz was used as reference to the Lock in Amplifier (Model No. SR830). The THz radiation was recorded by varying the delay between probe beam and THz pulse generated from BNA. The entire recording process was automated using indigenously designed program in Lab-View software. THz temporal profile was recorded at different incident pump powers varies between 500 to 800mW range. Figure 3.3 depicts the terahertz temporal profiles generated from BNA crystals grown from different solvents.

It was observed that BNA crystals grown with BNA (Acetonitrile(ACN)) solvent is giving high temporal peak amplitude compared to other solvents. The generated THz peak values are of the following order:

BNA(Acetonitrile(ACN)) > BNA (Dimethylformamide (DMF) > BNA (DMF: ACN) > BNA (Methanol (MeOH)).

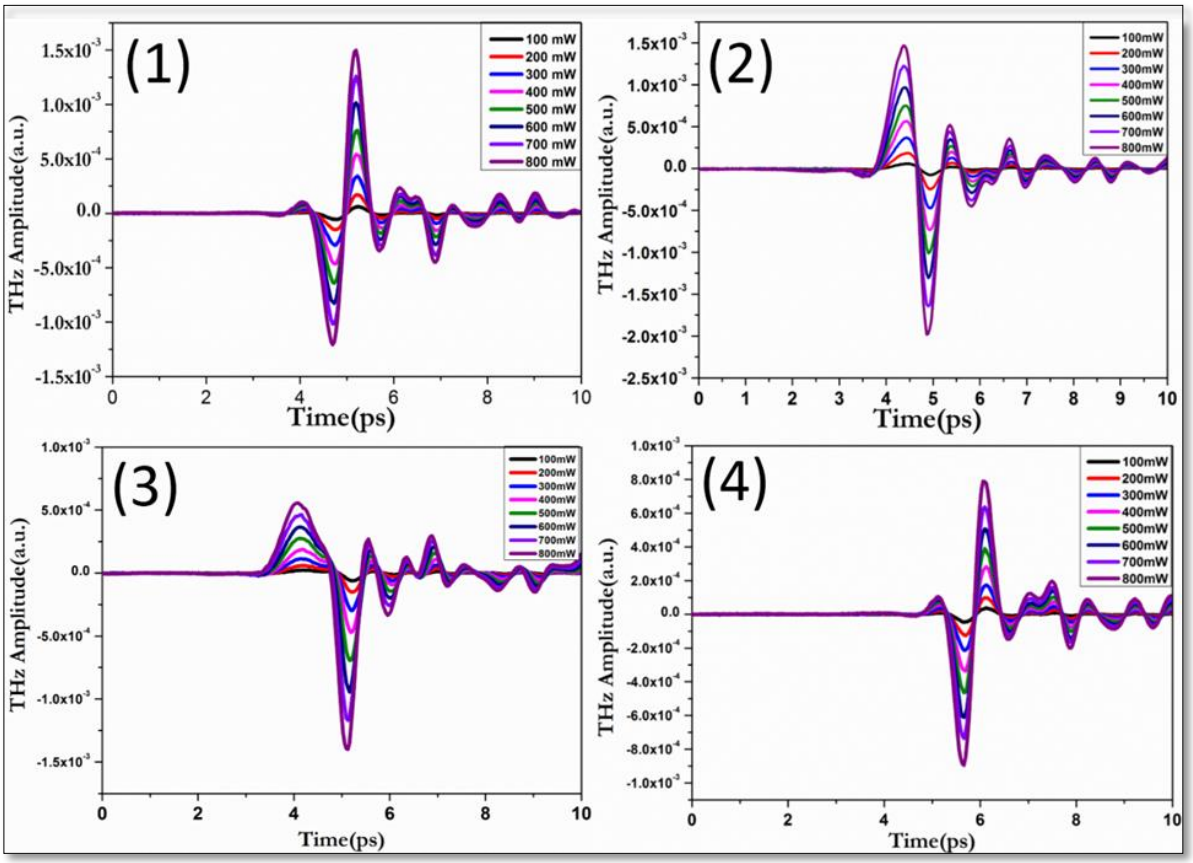

Figure 3.3. shows the time domain THz spectra generated from BNA crystals grown with different solvents. 1). BNA (Dimethylformamide (DMF)) 2). BNA (Acetonitrile(ACN)) 3). BNA (Mixed solvent DMF:ACN(1:1)) 4).BNA(Methanol(MeOH))

For the pump power of 800 mW, the obtained THz peak amplitudes for the solvents ACN, DMF, ACN: DMF, MeOH were of the order of 1.51 x 10^{-3}, 1.98 x 10^{-3}, 1.39 x 10^{-3}, 0.80 x 10^{-3}, respectively. The generated peak values were compared with ZnTe crystal under the similar experimental conditions. The reason for difference in the amplitude of generated signal will be discussed in the next section. Figure 3.4 (a)shows the comparison of terahertz peak amplitudes g using 800 mW pump power . Figure 3.4 (b)represents the corresponding Fast Fourier Transform (FFT) of the generated time domain signal. Except BNA crystal, grown with DMF: ACN (1:1) solvent, all other crystals shows bandwidth of the order of ~3 THz. In addition, proton NMR

spectroscopy was carried out to check the residual solvent content in grown crystals. All the crystals were perfectly matched with the reported stranded structure except for the crystal grown from DFM: ACN solvents. We observed two new peaks at ~1.4 and 4.3 positions which are not matching with the database of the solvent and might be due to residual elemental impurities present in the solvent or the crucible.

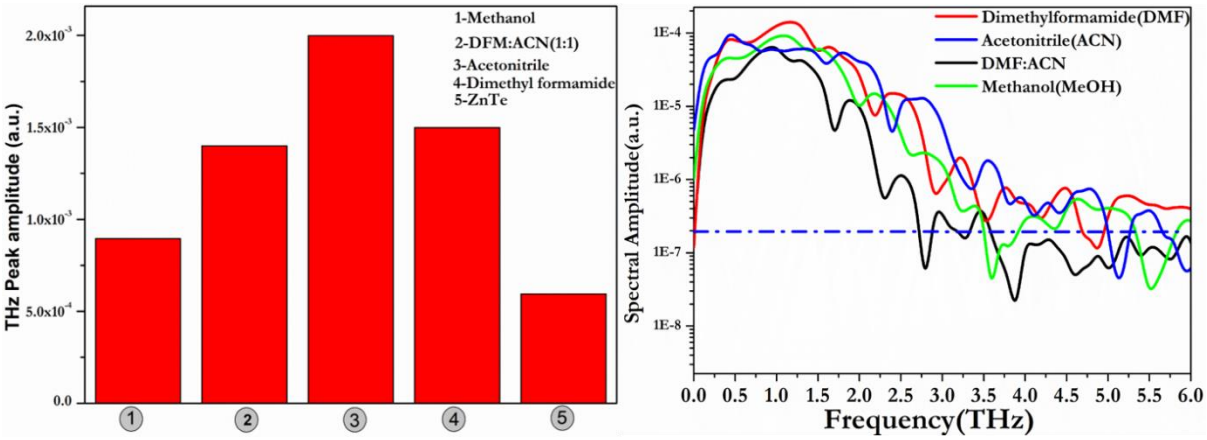

Figure 3.4. a) Terahertz peak amplitude values of different solvents. b) Frequency domain spectrum of Terahertz radiation.

3.2.1.cTerahertz power measurement with pyroelectric detector

We have evaluated the capability of the efficiency of generated THz radiation of BNA crystals using 800 nm wavelength pulses of 50 fs length at 1 kHz repetition rate obtained from Ti:Sapphire laser amplifier. The experimental setup is described in chapter 2. BNA crystal housed in the teflon holder was placed in a rotational mount. The crystal was rotated vertically using a rotator to measure the generated THz power by keeping the incident Laser power constant. The output from the BNA was mixture of generated THz and unconverted 800 nm wavelength. The unconverted pump beam was separated out by using Teflon filter and silicon plate. The power of generated THz radition was measured using a pyrodetector (Gentech Made) at room temperature. The output of the detector was fed to the lock-in-amplifier and energy of the generated energy is measured from software program. For increasing the signal to noise ratio (SNR) the laser pulses were chopped at 25 Hz range. Now, the incident power of the laser was gradually increased up to 300 mW in step by step manner to record the maximum THz generation and avoid the laser induced damage. Figure 3.5, shows the generated THz power at different rotation angles of the crystal. A maximum power of the order of 4 μW was recorded from BNA crystal grown by using ACN solvent. For crystals such as, BNA_DMF, BAN_DMF:ACN, BNA_Methanol the power values were of the order of 1.1 μW, 213 nW, 320

nW, respectively. The order of the observed power were inconsistent with temporal amplitudes discussed in the previous section.

In order to explain the variation in the generated THz powers and temporal peak amplitudes from different solvent grown crystals in the experimental were theoretically calculated based on velocity matching conditions using Eq. (9). The refractive indices (n_x, n_y, n_z) in optical domain are calculated from Sellmeier equations whereas value of n_{THz} is experimentally calculated from time domain spectroscopy data. The Sellmeier equations in optical region reported by Masazumi Fujiwara *et.al.* was further modified by Cyril Bernerd ***et al.*** were used to calculate the refractive index of BNA crystal.

$$n_x^2(\lambda) = 2.3035 + \frac{0.0297}{\lambda^2 - 0.1820} - 0.0091\lambda^2$$

$$n_y^2(\lambda) = 2.8593 + \frac{0.0655}{\lambda^2 - 0.1548} - 0.0073\lambda^2 \qquad (9)$$

$$n_z^2(\lambda) = 3.1321 + \frac{0.2199}{\lambda^2 - 0.1624} - 0.0024\lambda^2$$

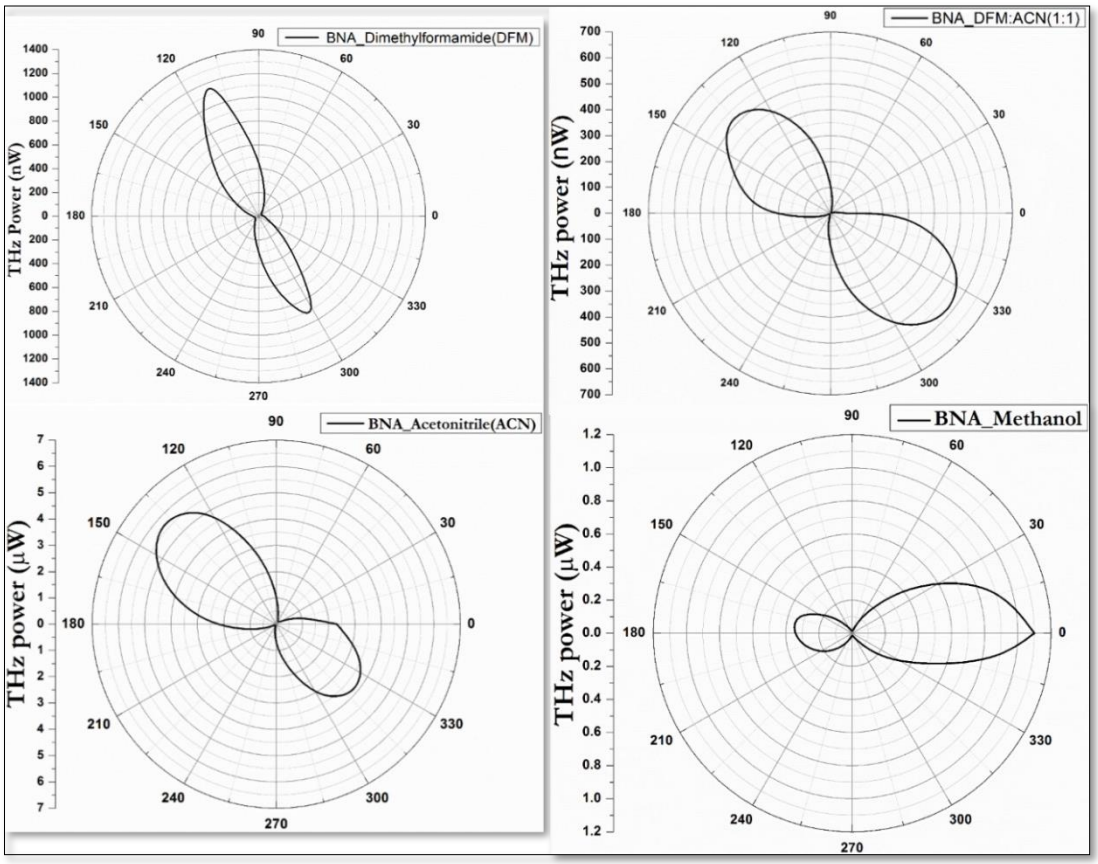

Figure 3.5. Terahertz power w.r.t angel for BNA crystals grown with different solvents.

Figure 3.6 shows the comparison of refractive indices generated by two different Sellmeier equations. There is a small deviation between the values of R.I. obtained from two Sellmeier equations. The reason for the discrepancy in the reported values is due to variation in the sellmeir coefficients given by Masazumi Fujiwara et. a*l* who have got accuracy of the order of 10^{-3}. The Terahertz refractive index in the range between 0.1 THz – 2 THz was ascertained from the transmission data obtained from time domain spectroscopy. All the four crystals were mounted on a teflon holder and subjected to THz radiation generated by photoconductive antenna as shown in the experimental setup discussed in chapter 2. Terahertz transmission data was recorded and corresponding frequency spectrum was obtained by performing FFT. The FFT data also helps to find the values of absorption coefficient and value of n_{THz}.

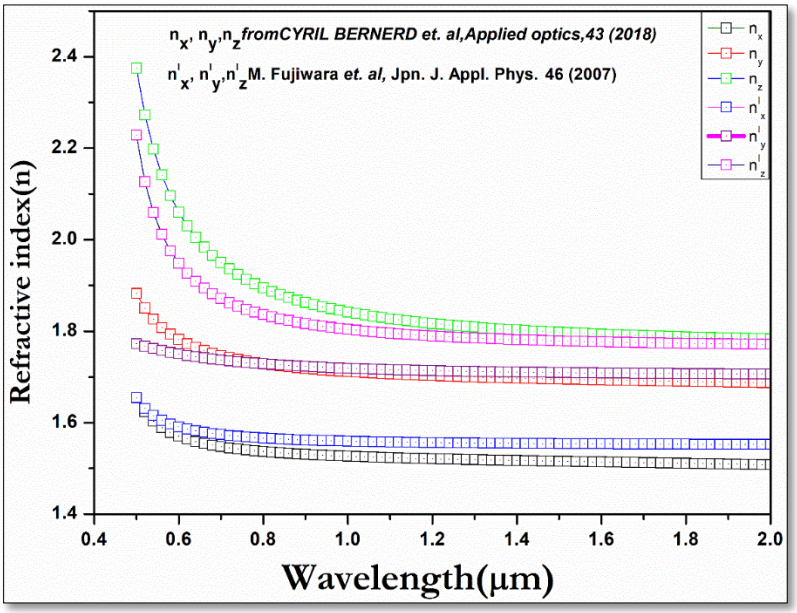

Figure 3.6. Refractive index of BNA crystal in optical range obtained from Sellmeier equations.

Figure 3.7 shows the refractive variation of indices of BNA crystals in optical and THz domain. We obtained average values of THz refractive index n_{THZ} of the order of 1.51, 1.70, 1.63, 1.72 respectively for the BNA crystals grown from ACN, DMF: ACN (1:1), DMF and Methanol, solvents. The values of THz refractive index were used to calculate the coherence length.

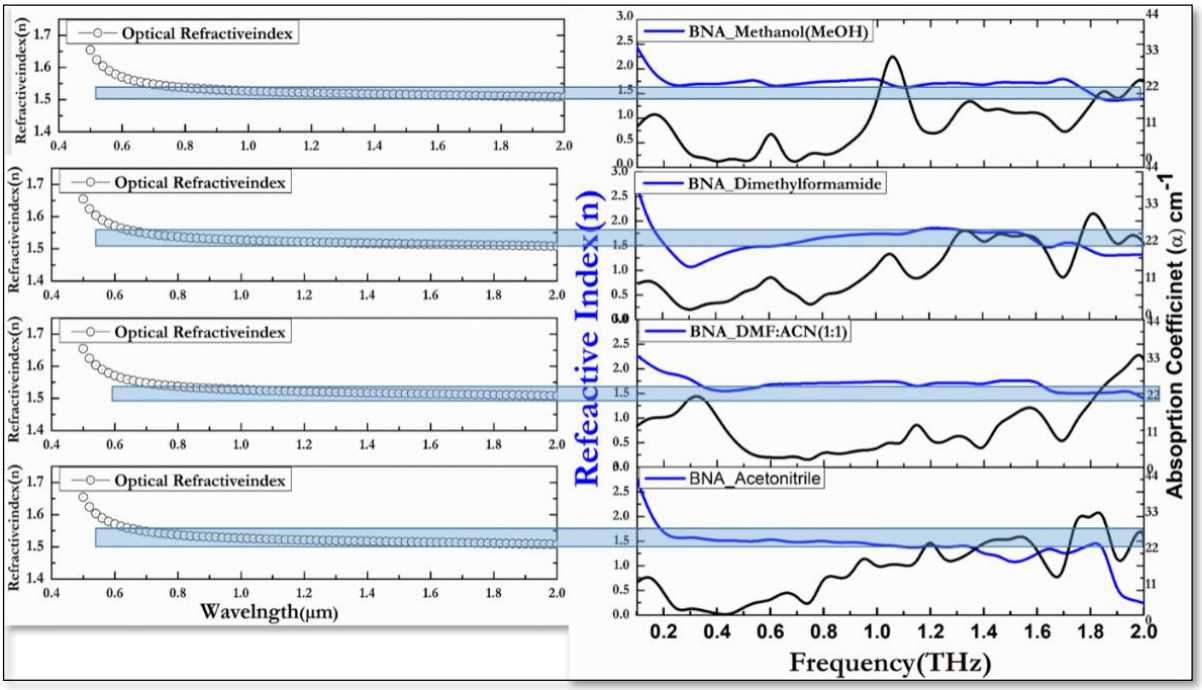

Figure 3.7. Comparison of the refractive index matching in optical and THz domain.

A comparison of the average R.I. in optical and THz range is shown in Figure 3.7. For different solvent grown crystals show different absorptions coefficients values which clearly indicates the variation in the transparency range of the crystal. A strong broad resonance absorption peaks observed at 0.7, 1.3, THz which are having an agreement with the phonon modes as reported by Kazuyoshi KUROYANAGI *et.al.* The reported calculations were done for single molecule by molecular orbital calculations Austin Model 1 (MNDO-AM1) method,21) which can explain the exiting vibrational modes of simple molecules. The phonon mode values are 0.70, 0.75, 1.40, 1.55, 2.35, and 4.55 THz in the frequency range between 0 and 5 THz. The velocity matching condition $\mathbf{n}_{THz}$, $\mathbf{n}_g$ is reasonably well matched for the ACN grown BNA crystal and is marked by the lines of the shaded region as shown the Figure 3.7 [21,26]. However, other solvent grown crystals are showing more deviation with respect to the average values of R.I. in optical domain. Another possible reason of this deviation is attributed to the effect of polarity of the solvent reported by K. Thirupugalmani et.al.. A comparative data of THz generation from different BNA crystals in terms of their method of growth, generation technique and is comprised in table 3.2. [46,47]

3.2.1.d Effect of Growth Solvent on nonlinear properties of the crystal

Generally, the organic nonlinear crystals are grown by using solution growth technique. In that case, many important factors such the solubility of the solution under saturated or supersaturated condition, interaction between solvent-solute or solute-solvent and nature of molecules in the solvent influence the quality and growth rate of the crystal [48]. Nature of the solvent and its composition plays a crucial role in the designing of the crystal. When solute species align themselves in a random manner on the surface in that case crystals grown by solution growth method is preferred. So, prior research on properties of solvent is necessary to grow the good quality crystals. In the present study we carried out THz generation from BNA crystals grown from different solvents that have different dipole moments. The dipole moment arises due to bonding of a highly electronegative atom with low electronegative atom in covalent bond. The atom with high electro-negativity pulls the shared electron pair towards their side which causes a non-uniform distribution of shared pair of electrons. The high values of polarizability and hyper polarizability are significant properties of NLO crystals. For molecules having small gap between HOMO and LUMO levels enabled the easy charge transfers mehansim. The inhibited growth in the direction of c-axis of BNA is due to dipole interaction between solvent-surface interaction. Berkovitch–Yellin showed that solute-solvent interactions influence the morphology of crystal [49]. So BNA crystal grown with pure single and mixed solvents (to understand solvent-solvent interactions) which controls the physical and optical properties of the crystal. A good quality bulk crystal can be obtained from high dipole moment solvents as compared to low dipole moment and mixed solvent crystals.

Table 3-1. dipole moments, HOMO-LUMO gap of the solvents used to grow the BNA crystals

S. No	Solvent	Dipole moment (D)	Gap=E_{HOMO}-E_{LUMO} (eV)
1	Acetonitrile	3.2	-5.303
2	Methanol	1.7	-5.978
3	DFM : ACN	3.86-3.2	
4	Dimethylformamide	3.86	-5.983

Table.3-1 shows comparisons of dipole moments, HOMO-LUMO gap of the solvents used for growing the BNA crystal. It is noted that crystal grown with high polar aprotic solvent yielded

high surface quality and generate efficient THz radiation. Though, dimethylformamide has more value of dipole moments but grown BNA crystal was small in size and gives low THz generation which could be due to its high molecular orbital bandgap values. The variation in the THz generation ability may be due to the difference in the stabilization mechanisms of the frontier orbitals of the solvents. Therefore, our studies observed that good surface quality organic BNA crystals can be grown from solvents having high dipole moments and low HOMO-LUMO gap.

Table 3-2 comparison present study with literature

Reference	Growth method	Solvent(s) used	Wavelength used for study	Terahertz generation method
Takashi Notake et.al [50]	ethanol	Solution growth method	750 – 950 nm	DFG using OPO
Katsuhiko miyamoto et.al [38]	From MNA recrystallized from hot ethanol	Vertical Bridgeman method	780- 950 nm	DFG using OPO
Masazumi Fujiwara et.al [51]	From MNA recrystallized from hot ethanol	Bridgman method	500 – 2500 nm	-----
Kazuyoshi kuroyangi et.al [43]		Vertical Bridgeman method	0.87 um	Optical rectification
Cyril Bernerd et.al [52]	Ethanol	Solution method	600 – 2000 nm	DGF using opo
K. Thriupugalmani et. al [46]	DMSO, Acetone + Ethanol + methanol, Ethonla+Methonl + DMSO+ Acetone	Solution method	800 nm	Optical rectification
Present study	ACN, DMF, MeOH	Solution method	800 nm	Optical rectification

3.2.2 OH1

2-(3-(4-hydroxystyryl)-5,5-dimethylcyclohex-2-enylidene)-malononitrile is called OH1 Crystal. it is a non-ionic, having largest figures of merit and maybe phase matched the usage of pump lasers in telecommunication variety of 1300–1560 nm [53–56]. TsonkoKolev *et al.* was the first group to invent the OH1 crystal and several other groups such as Y. Li, Z. Wu *et.al*, E. Y. Choi *et.al.*, C.

Hunziker *et.al.* have reported OH1 as a potential candidate for THz generation and detection source [57–61].

3.2.2.a Growth process

The OH1 crystal was made by Knoevenagel condensation by reacting isophorone (660mg, Sigma) and malononitrile (1.328g, Sigma) using N, N, dimethylformamide as a solvent and piperidine acetate as a catalyst at ambient conditions. The obtained 3,5,5-trimethyl(cyclohex-2-enylidene) malononitrile precipitate was re-crystallized many times using ethanol and then treated with equi-molar ratio of 4-hydroxybenzaldehyde here chloroform was used as a solvent and piperidine as catalyst. After synthesis end product appears orange-red in color was re-crystallized many times using chloroform and purified by column chromatography on silica gel. The Carbon–Hydrogen–Nitrogen (CHN) analysis was performed for the purified powder sample using Vario EL III CHN elemental analyzer by keeping Helium carrier gas. Saturated methanol solution of OH1 was prepared at 30°C and strongly covered with a single hole and kept in an unbroken water bath, equipped with a programmable temperature controller. Finally, single crystals of OH1 was harvested in about 24 days and then for further studies. OH1 crystal belongs to $Pna2_1$(*mm*2) [59]. Figure 3.8 shows the OH1 crystal used for THz generation.

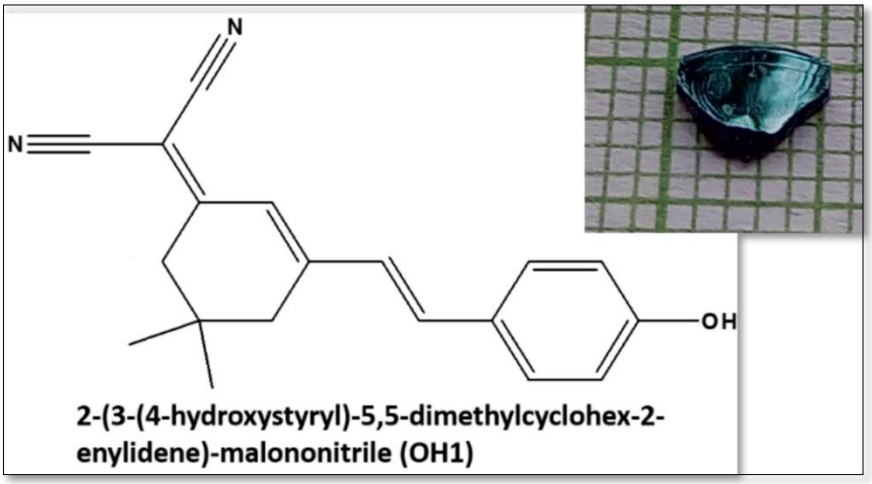

Figure 3.8. OH1 Crystal.

3.2.2.bEvaluation of OH1 crystal for THz generation

The THz generation efficiency of as grown OH1 single crystal was studied by employing the experimental set up as shown in Figure 3.2. The power of the incident laser pulses (to prevent crystal from damage) was kept below the damage threshold of the OH1 crystal. The high quality as grown OH1 single crystal of thickness 0.72 mm was placed in a Teflon holder which has been

kept in an optical rotational mount and thus used as a THz generator. The employed pump and probe beam powers were between ~ 200 mW, and ~170 mW for pump and detection of THz radiation, respectively. Teflon sheet was used to filter the unconverted pump beam from the OH1 crystal. The generated THz was detected via dipole pc antennas (gap ~5 μm, length ~20 μm) the use of photoconductive sampling method. The antenna output was fed to the preamplifier which is connected to the Lock-in Amplifier (Model no.SR830). The S/N ratio is enhanced using mechanical chopper operating at 1.569 kHz frequency. The probe beam path length was varied to measure temporal profile of THz radiation. The terahertz temporal field and the results of THz generation obtained from OH1 crystals are shown in Figure 3.9. It was found that the OH1 single crystals are capable of producing THz frequency up to 3.2 THz. The dips located in the THz spectrum between 0.1 and 3.2 THz region of the OH1 crystals are attributed to the molecular phonon and lattice phonon modes and the latter should stand up from intermolecular interactions in the crystal. Wigner representation of THz generated form OH1 crystal is shown in Figure 3.10.

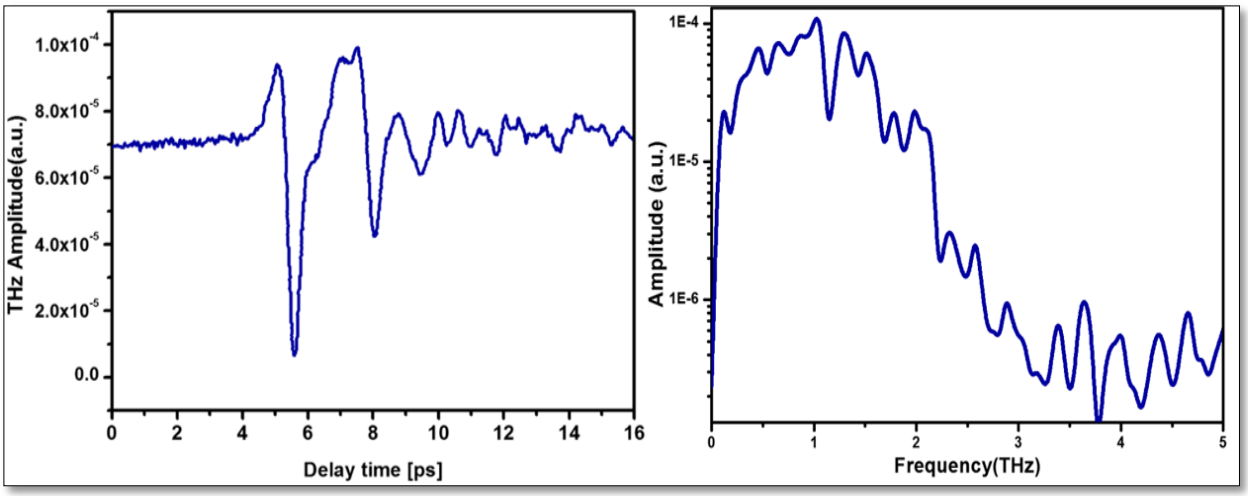

Figure 3.9. Generated THz from OH1 crystal

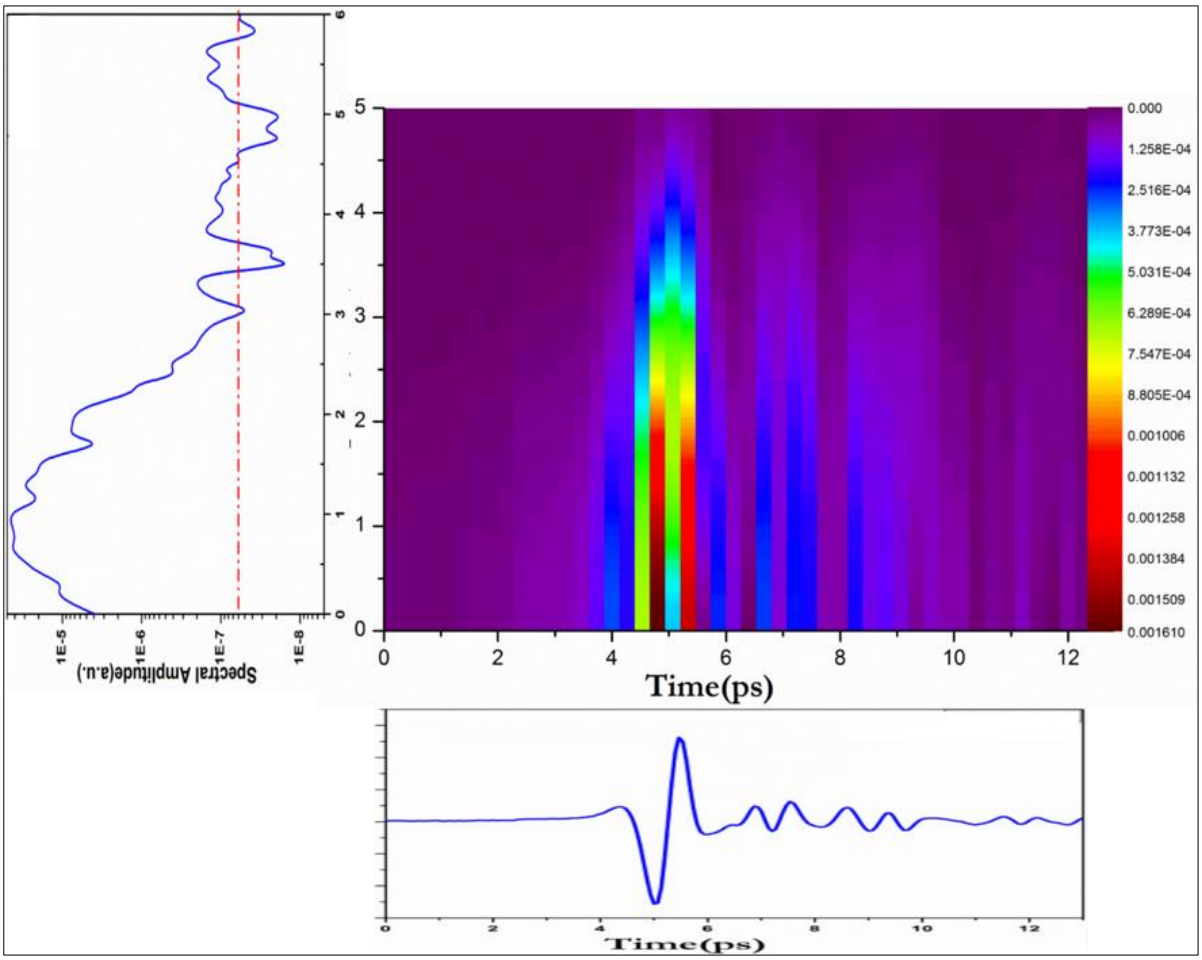

Figure 3.10. Wigner representation of a THz pulse generated from OH1 crystal. The horizontal axis corresponds to time, and the vertical axis corresponds to frequency.

3.2.3 LAP

L-arginine phosphate monohydrate, famously known as LAP is a promising nonlinear organic crystal [62]. It has higher transmission in UV region along with modest linearity and three times higher damage threshold than the aqueous solution has grown crystals, also can be treated as an ideal substitute of KDP crystal for harmonic generation in deep UV and NIR region [63]. L-Arginine phosphate was synthesized by dissolving equimolar ratio of aqueous solution of L-Arginine and Phosphoric acid and purified by repeated re-crystallization method. The colorless crystals have been grown by using gradual cooling solution growth method using water as a solvent [64–66].

Figure 3.11. LAP crystal

Lap is a monoclinic crystal and belongs to $P2_1$ space group. Lap crystal was mounted on a Teflon holder and subjected to femtosecond pulses for THz generation as described by the experimental part in Chapter 2. The THz radiation is recorded by varying delay between generated THz pulse from LAP and probe beam. Crystal was kept slightly off-focus from the lens. THz temporal profiles were recorded at different input pump powers from 500 mW to 1100mW. THz generation amplitude increases with increasing power of incident pump energy and gets saturated after 1000mW. The version in THz peak-peak amplitude with respect to incident laser strength is shown in Figure 3.12. THz peak-top amplitude is increasing with incident laser power from 300 mW to 900 mW i.e., from 86.3 to 400 a.u. The THz peak-peak amplitude is saturated at higher laser powers i.e. from 1W laser power.

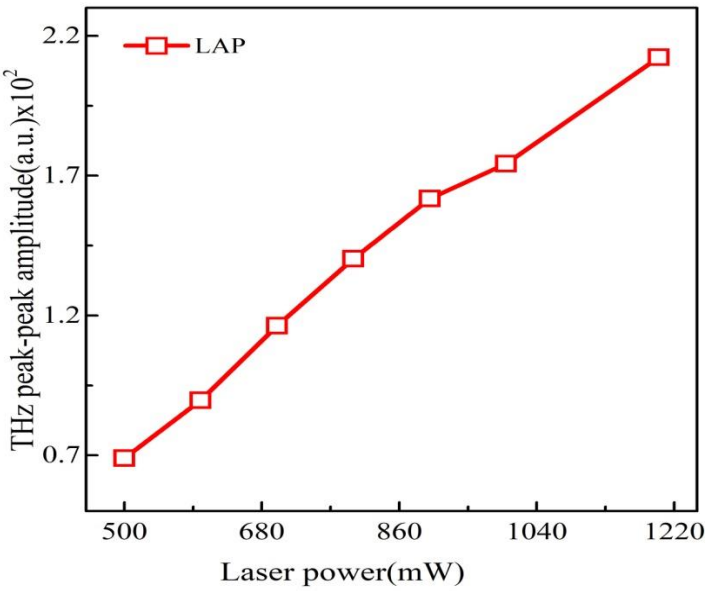

Figure 3.12. Variation of THz peak power of LAP crystal with incident energy

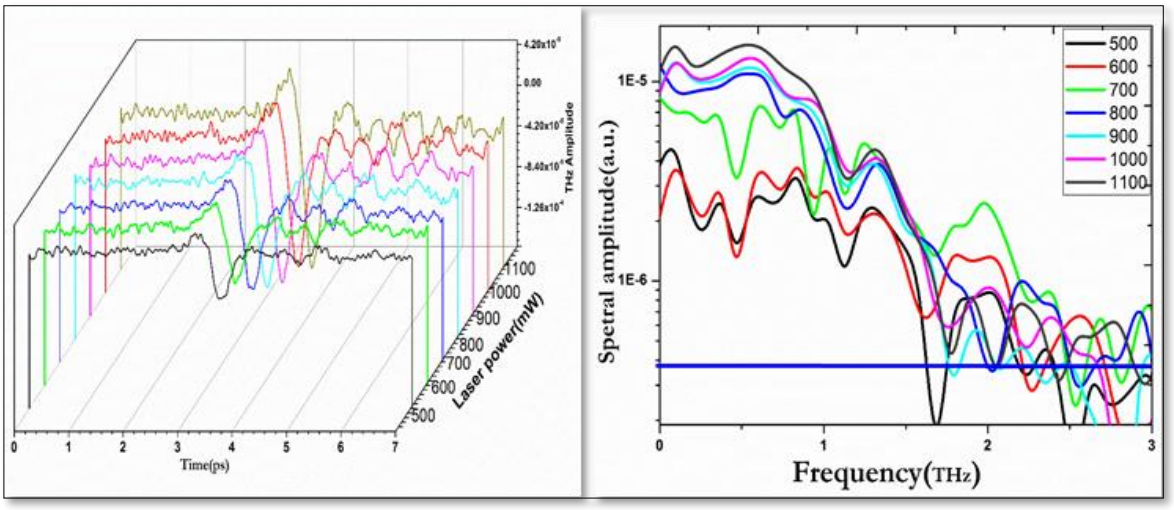

Figure 3.13. a) Temporal profiles of THz generated from LAP crystal at different powers. b) Frequency spectrum of temporal profiles.

Figure 3.13 shows the THz pulses generated from LAP crystal and the corresponding FFT spectra. A bandwidth of 2 THz was acquired by the process optical rectification from LAP crystals. After successful generation of THz, LAP crystal was subjected to THz radiation generated from pc antenna to measure the transmission spectra. The amplitude of E-M field strength of time domain spectrum before incident and after coming out the LAP crystal was measured. Transmission and absorption coefficients ($\alpha(\omega)$) were ascertained using equations discussed in chapter 2. Figure 3.12(b) indicates the frequency spectrum range up to 2 THz with sharp dips at 0.5, 1.1, 1.6 THz which are exactly correlating with absorption bands shown in

Figure 3.14. Also, the absorption values and absorption coefficients are inconsistent with the dip in generating spectra. This corresponds to phonon modes of functional groups present in the LAP crystal. For the first time we reported the frequency dependent refractive index of LAP crystal, i.e., of the order of 1.52.

3.2.3.a Refractive index

Refractive index of LAP crystal is calculated from temperature depended sellmeier equation The Sellmeier formula for a LAP crystal for each dielectric axis (x,y and z)

$$n_x(\lambda) = 2.2439 + \frac{0.0117}{\lambda^2 - 0.0179} - 0.0111\lambda^2$$

$$n_y(\lambda) = 2.4400 + \frac{0.0158}{\lambda^2 - 0.0191} - 0.0212\lambda^2 \qquad (10)$$

$$n_z(\lambda) = 2.4590 + \frac{0.0177}{\lambda^2 - 0.0226} - 0.0162\lambda^2$$

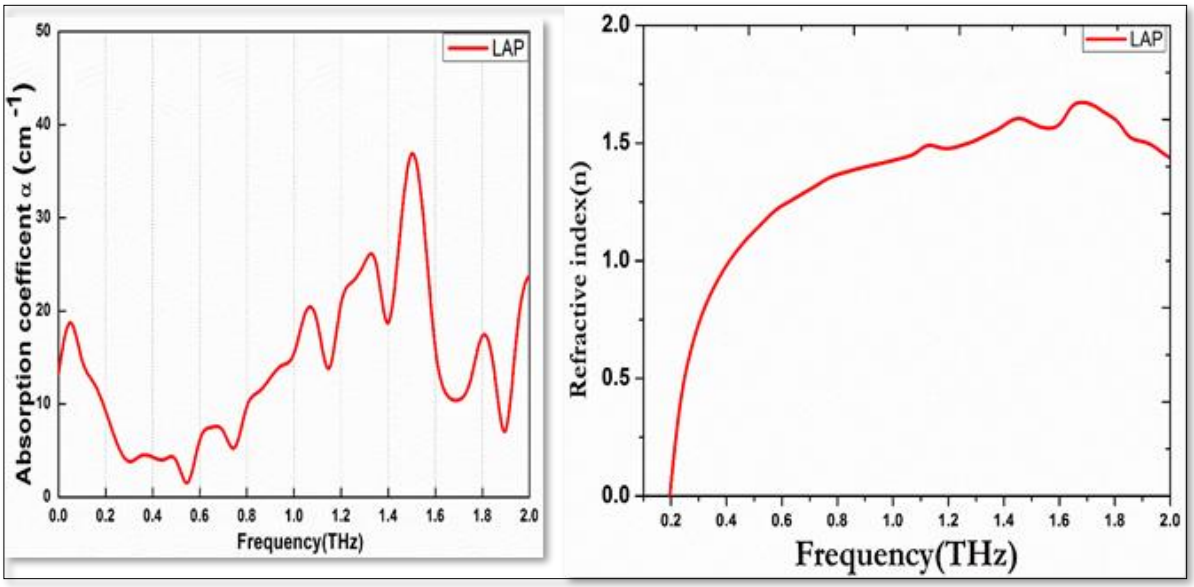

Figure 3.14. a) Absorption coefficient of LAP crystal b) Refractive index

By incorporating equation 2,3 we found temperature dependent refractive index with varying temperature w.r.t., tuning wavelength. The dn/dT value of LAP crystal is given by equation [67]

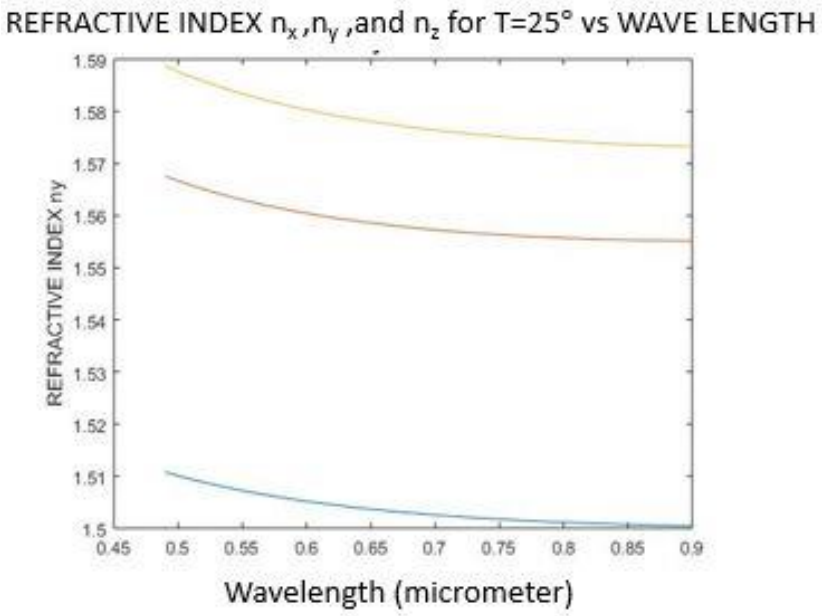

Figure 3.15. Variation of refractive index of LAP crystal with wavelength at 25 ^{0}C temperate.

$$\frac{dn}{dT} = -6.3074 \times 10^{-4} \times \frac{n\left(n^2-1\right)}{2\left(2n^2+1\right)}\, {}^{o}C^{-1} \qquad (11)$$

Here we can find near 0.8 THz refractive index of THz is matching with group refractive index. This varies crystal to crystal and also with the orientation, because n_{Thz} and n_{gr} differ with respect to crystal orientation. By analyzing the graph, we can see that $n_x<n_y<n_z$ at room temperature. Hence from equation (11) we can find the angle formed by one of the optical axes w.r.t., z-axis (v_z). By varying the values for n_x, n_y and n_z , we calculated v_z = 68.4, hence, $v+_z$> 90^{o}c and we can conclude LAP is a negative crystal.

3.3 Conclusions

The THz emission ability of three potential organic crystals BNA (with different solvents), OH1, LAP have been evaluated in terms of growth solvents, optical properties like Sellmeier equations, transmission range, and absorption coefficients. Since the transmission of all the crystals are varying in optical domain, therefore it also reflected their potential use as an efficient THz source. The effect of solvent on THz generation ability of BNA crystals has been discussed. THz generation from OH1 crystal which is well explored near communication wavelengths. However, in this thesis it has been studied at 800 nm using optical rectification technique. L-arginine phosphate monohydrate (LAP) has been studied as a THz source and its absorption and refractive index are reported in THz domain for the first time. Further study of these crystals will

be based on DFG technique or CW and DPSS lasers helping the designing of potential THz source.

S.NO	Name of the Crystal	Space group (Point Group)	2nd order nonlinear coefficient Pm/V, d_{ijk}	$n_{optcial}$ (800nm)	n_{THz}	Conversion Efficiency (η)
1.	BNA	$Pna2_1$ (*mm*2)	d_{333}= 234 d_{322}= 15.6	1.66	~1.65	26×10^{-4}
2.	DAST	P1	d_{111}=1010 d_{221} = 96	2.07	~2.2	16.1×10^{-4}
3	LAP	P21		1.51	~1.52	6.25×10^{-5}
4	OH1	$Pna2_1$ (mm2)	d_{333}= 120	2.16	~2.3	

3.4 References

1. K. L. Vodopyanov, "Optical generation of narrow-band terahertz packets in periodically-inverted electro-optic crystals: conversion efficiency and optimal laser pulse format," Opt. Express, **14**, 2263-2276 (2006).
2. C. Klingshirn, "Nonlinear optics, high density effects and stimulated emission," in *Springer Series in Materials Science, 275-306* (2010).
3. H. Reis, "Problems in the comparison of theoretical and experimental hyperpolarizabilities revisited," J. Chem. Phys, 125, 014506 (2006).
4. A. Willetts, J. E. Rice, D. M. Burland, and D. P. Shelton, "Problems in the comparison of theoretical and experimental hyperpolarizabilities," J. Chem. Phys, **97**, 7590 (1992).
5. S. Kono, M. Tani, and K. Sakai, "Generation and detection of broadband poulsed terahertz radiation," Top. Appl. Phys, **97**, 31-64 (2005).
6. X. C. Zhang and J. Xu, "Chapter 2 - Generation and detection of terahertz waves," in *Introduction to THz Wave Photonics* (2010).
7. Y. S. Lee, *Principles of Terahertz Science and Technology* (2009).
8. R. W. Boyd, *Nonlinear Optics, Third Ed.* (2008).
9. J. A. ulöp, L. Pálfalvi, G. Almási, J. Hebling, M. C. Hoffmann, H. Y. Hwang, K. Yeh, K. A. Nelson, G. Chang, C. J. Divin, C. Liu, S. L. Williamson, C. Chen, Y. Lin, Y. Huang, C. Chang, C. Pan, L. Yan, and C. Lee, "Design of high-energy terahertz sources based on optical rectification," Quantum Electron. Appl. Phys. B Am. B Appl. Phys. J.-C. Diels W. Rudolph, Ultrashort Laser Pulse Phenom, 18, 12311 (2010).
10. R. Huber, A. Brodschelm, F. Tauser, and A. Leitenstorfer, "Generation and field-resolved detection of femtosecond electromagnetic pulses tunable up to 41 THz," Appl. Phys. Lett. , **76**, 3191 (2000).
11. J. J. Carey, R. T. Bailey, D. Pugh, J. N. Sherwood, F. R. Cruickshank, and K. Wynne, "Terahertz pulse generation in an organic crystal by optical rectification and resonant excitation of molecular charge transfer," Appl. Phys. Lett, **81**, 4335 (2002).
12. K. L. Yeh, M. C. Hoffmann, J. Hebling, and K. A. Nelson, "Generation of 10 μj ultrashort terahertz pulses by optical rectification," Appl. Phys. Lett, **90**, 171121 (2007).
13. X. Xie, J. Xu, and X.-C. Zhang, "Terahertz wave generation and detection from a CdTe crystal characterized by different excitation wavelengths," Opt. Lett, **31** 7, pp. 978-980 (2006).
14. G. Chang, C. J. Divin, C.-H. Liu, S. L. Williamson, A. Galvanauskas, and T. B. Norris, "Power scalable compact THz system based on an ultrafast Yb-doped fiber amplifier," Opt. Express, **14**, 7909-7913 (2006).
15. A. Rice, Y. Jin, X. F. Ma, X. C. Zhang, D. Bliss, J. Larkin, and M. Alexander, "Terahertz optical rectification from 〈110〉 zinc-blende crystals," Appl. Phys. Lett, **64**, 1324 (1994).
16. J. D. Rowley, J. K. Pierce, A. T. Brant, L. E. Halliburton, N. C. Giles, P. G. Schunemann, and A. D. Bristow, "Broadband terahertz pulse emission from ZnGeP_2," Opt. Lett. , Vol. **37**, 788-790 (2012).
17. C. Winnewisser, P. Uhd Jepsen, M. Schall, V. Schyja, and H. Helm, "Electro-optic detection of THz radiation in LiTaO3, LiNbO3 and ZnTe," Appl. Phys. Lett, **70**, 3069 (1997).

18. A. G. Stepanov, J. Hebling, and J. Kuhl, "Efficient generation of subpicosecond terahertz radiation by phase-matched optical rectification using ultrashort laser pulses with tilted pulse fronts," Appl. Phys. Lett, **83**, 3000 (2003).

19. M. Stillhart, A. Schneider, and P. Günter, "Optical properties of 4-N,N-dimethylamino-4^'-N^'-methyl-stilbazolium 2,4,6-trimethylbenzenesulfonate crystals at terahertz frequencies," J. Opt. Soc. Am. B, **25**, 1914-1919 (2008).

20. K. Kuroyanagi, M. Fujiwara, H. Hashimoto, H. Takahashi, S. I. Aoshima, and Y. Tsuchiya, "Determination of refractive indices and absorption coefficients of highly purified N-benzyl-2-methyl-4-nitroaniline crystal in terahertz frequency regime," Japanese J. Appl. Physics, Part 2 Lett, **45**, 29–32 (2006).

21. M. Jazbinsek, L. Mutter, and P. Günter, "Photonic applications with the organic nonlinear optical crystal DAST," IEEE J. Sel. Top. Quantum Electron, **14**, 1298 - 1311 (2008).

22. F. Pan, G. Knöpfle, C. Bosshard, S. Follonier, R. Spreiter, M. S. Wong, and P. Günter, "Electro-optic properties of the organic salt 4-N,N-dimethylamino-4'-N'-methyl-stilbazolium tosylate," Appl. Phys. Lett, **69**, 13 (1996).

23. M. Jazbinšek and M. Zgonik, "Material tensor parameters of LiNbO3 relevant for electro- and elasto-optics," Appl. Phys. B Lasers Opt, **74**, 407–414 (2002).

24. U. Meier, M. Bösch, C. Bosshard, F. Pan, and P. Günter, "Parametric interactions in the organic salt 4-N,N-dimethylamino-4'-N'- methyl-stilbazolium tosylate at telecommunication wavelengths," J. Appl. Phys. **83**, 3486–3489, **83**, 3486 (1998).

25. Y. Takahashi, H. Adachi, T. Taniuchi, M. Takagi, Y. Hosokawa, S. Onzuka, S. Brahadeeswaran, M. Yoshimura, Y. Mori, H. Masuhara, T. Sasaki, and H. Nakanishi, "Organic nonlinear optical DAST crystals for electro-optic measurement and terahertz wave generation," J. Photochem. Photobiol. A Chem, **183,** 247-252 (2006).

26. S. R. Marder, J. W. Perry, and C. P. Yakymyshyn, "Organic Salts with Large Second-Order Optical Nonlinearities," Chem. Mater, **6**,1137-1147 (1994).

27. F. Pan, M. S. Wong, C. Bosshard, and P. Günter, "Crystal growth and characterization of the organic salt 4-N,N-dimethylamino-4'-N'-methyl-stilbazolium tosylate (DAST)," Adv. Mater,**8**, 592-595(1996).

28. A. Nahata, A. S. Weling, and T. F. Heinz, "A wideband coherent terahertz spectroscopy system using optical rectification and electro-optic sampling," Appl. Phys. Lett, **69**, 2321 (1996).

29. M. Fujiwara, K. Yanagi, M. Maruyama, M. Sugisaki, K. Kuroyanagi, H. Takahashi, S. I. Aoshima, Y. Tsuchiya, A. Gall, and H. Hashimoto, "Second Order nonlinear optical properties of the single crystal of N-benzyl 2-methyl-4-nitroaniline: Anomalous enhancement of the d333 component and its possible origin," Japanese J. Appl. Physics, Part 1 Regul. Pap. Short Notes Rev. Pap,**13**,23 (2006).

30. T. Asahi, T. Yabe, K. Sato, and A. Arakawa, "Growth of large diameter ZnTe single crystals by the LEK method," in *Journal of Alloys and Compounds, **371**,* 2-5 (2004).

31. K. Yoshino, M. Yoneta, K. Ohmori, H. Saito, M. Ohishi, and T. Yabe, "Annealing effects of a high-quality ZnTe substrate," J. Electron. Mater. **33**, 579–582 (2004).

32. H. J. Scheel, "Control of Epitaxial Growth Modes for High-Performance Devices," in *Crystal Growth Technology* (John Wiley & Sons, Ltd, 2004), pp. 621–644.

33. H. J. Scheel, "Historical aspects of crystal growth technology," J. Cryst. Growth, **211**, 1-12 (2000).

34. P. M. Dryburgh, "Crystal growth technology," Prog. Cryst. Growth Charact. Mater. (2003).

35. M. Fujiwara, M. Maruyama, M. Sugisaki, H. Takahashi, S. I. Aoshima, R. J. Cogdell, and H. Hashimoto, "Determination of the d-tensor components of a single crystal of N-benzyl-2-methyl-4-nitroaniline," Japanese J. Appl. Physics, Part 1 Regul. Pap. Short Notes Rev. Pap, **46,** 1528-1530 (2007).

36. H. Hashimoto, Y. Okada, H. Fujimura, M. Morioka, O. Sugihara, N. Okamoto, and R. Matsushima, "Second-harmonic generation from single crystals of N-substituted 4-nitroanilines," Japanese J. Appl. Physics, Part 1 Regul. Pap. Short Notes Rev. Pap. (1997).

37. H. Hashimoto, H. Takahashi, T. Yamada, K. Kuroyanagi, and T. Kobayashi, "Characteristics of the terahertz radiation from single crystals of N-substituted 2-methyl-4-nitroaniline," J. Phys. Condens. Matter, 13, 23 (2001).

38. K. Miyamoto, S. Ohno, M. Fujiwara, H. Minamide, H. Hashimoto, and H. Ito, "Optimized terahertz-wave generation using BNA-DFG," Opt. Express, **17**, 14832-14838 (2009).

39. T. Notake, M. Saito, M. Tang, Y. Wang, H. Minamide, and H. Ito, "Solution growth of an organic N-benzyl-2-methyl-4-nitroaniline (BNA) crystal for DFG-THz source," in *IRMMW-THz 2010 - 35th International Conference on Infrared, Millimeter, and Terahertz Waves, Conference Guide* (2010).

40. S. Karthick, D. Ganesh, K. Thirupugalmani, A. K. Chaudhary, and S. Brahadeeswaran, "Terahertz generation and optical properties of N-benzyl-2-methyl-4-nitroaniline single crystals in 0.1–2.0 THz range for photonic applications," Mater. Lett, **246,** 95-98 (2019).

41. M. Shalaby, C. Vicario, K. Thirupugalmani, S. Brahadeeswaran, and C. P. Hauri, "Intense THz source based on BNA organic crystal pumped at Ti:sapphire wavelength," Opt. Lett, **41**,1777-1780 (2016).

42. M. Shalaby, C. Vicario, and C. P. Hauri, "Intense THz source based on BNA organic crystal pumped at conventional Ti:Sapphire wavelength," in *International Conference on Infrared, Millimeter, and Terahertz Waves, IRMMW-THz* (2016).

43. K. Kuroyanagi, M. Fujiwara, H. Hashimoto, H. Takahashi, S. I. Aoshima, and Y. Tsuchiya, "All organic terahertz electromagnetic wave emission and detection using highly purified N-benzyl-2-methyl-4-nitroaniline crystals," Japanese J. Appl. Physics, Part 1 Regul. Pap. Short Notes Rev. Pap,**45**, 1 (2006).

44. T. Notake, K. Nawata, T. Matsukawa, H. Kawamata, Q. Feng, and H. Minamide, "DAST- and BNA-DFG terahertz-wave generation pumped by a dual-wavelength BBO optical parametric oscillator with independent wavelength-control," in *Optics InfoBase Conference Papers* (2012).

45. M. Farooqui, N. Dixit, A. Mishra, V. Kumar, A. N. Kaul, and A. K. Gupta, "Comparative analysis of tunable terahertz generation in DAST and BNA using difference frequency mixing," J. Opt., **43**, 137–145 (2014).

46. K. Thirupugalmani, M. Venkatesh, S. Karthick, K. K. Maurya, N. Vijayan, A. K. Chaudhary, and S. Brahadeeswaran, "Influence of polar solvents on growth of potentially NLO active organic single crystals of: N -benzyl-2-methyl-4-nitroaniline and their efficiency in terahertz generation," CrystEngComm, **19**, 2623-2631 (2017).

47. M. Venkatesh, K. Thirupugalmani, K. S. Rao, S. Brahadeeswaran, and A. K. Chaudhary, "Generation of efficient THz radiation by optical rectification in DAST crystal using tunable femtosecond laser pulses," Indian J. Phys, **91**, 319–326 (2017).

48. K. Kamada, Y. Takida, H. Minamide, Y. Shoji, S. Kurosawa, Y. Yokota, Y. Ohashi, and A. Yoshikawa, "Growth of N-benzyl-2-methyl-4-nitroaniline (BNA) single crystal fibers by

micro-pulling down method," J. Cryst. Growth **452**, 162–165 (2016).

49. F. Wireko, L. Shimon, F. Frolow, Z. Berkovitchyellin, M. Lahav, and L. Leiserowitz, "Effect of solvent on the growth of organic crystals. 1. The riddle of α-resorcinol," J. Phys. Chem. **91**, 472–481 (1987).
50. T. Notake, K. Nawata, H. Kawamata, T. Matsukawa, and H. Minamide, "Solution growth of high-quality organic N-benzyl-2-methyl-4-nitroaniline crystal for ultra-wideband tunable DFG-THz source," Opt. Mater. Express, **2**, 119-125 (2012).
51. K. Miyamoto, H. Minamide, M. Fujiwara, H. Hashimoto, and H. Ito, "Widely tunable terahertz-wave generation using an N-benzyl-2-methyl-4-nitroaniline crystal," Opt. Lett, **33**, 252-254 (2008).
52. C. Bernerd, P. Segonds, J. Debray, T. Notake, M. Koyama, H. Minamide, H. Ito, and B. Boulanger, "Quadratic nonlinear optical properties of the organic N-benzyl-2-methyl-4-nitroaniline (BNA) biaxial crystal," Opt. Lett, **43**, 818-1821 (2018).
53. F. D. J. Brunner, O.-P. Kwon, S.-J. Kwon, M. Jazbinšek, A. Schneider, and P. Günter, "A hydrogen-bonded organic nonlinear optical crystal for high-efficiency terahertz generation and detection," Opt. Express, **16**, 16496-16508 (2008).
54. C. Ruchert, C. Vicario, and C. P. Hauri, "Scaling submillimeter single-cycle transients toward megavolts per centimeter field strength via optical rectification in the organic crystal OH1," Opt. Lett, **37**, 899-901 (2012).
55. A. G. Stepanov, C. Ruchert, J. Levallois, C. Erny, and C. P. Hauri, "Generation of broadband THz pulses in organic crystal OH1 at room temperature and 10 K," Opt. Mater. Express, **4**, 870-875 (2014).
56. H. Uchida, K. Oota, K. Okimura, K. Kawase, and K. Takeya, "Single-Cycle Terahertz Pulse Generation from OH1 Crystal via Cherenkov Phase Matching," J. Infrared, Millimeter, Terahertz Waves, **9**(5), 882 (2018).
57. O. P. Kwon, S. J. Kwon, M. Jazbinsek, F. D. J. Brunner, J. I. Seo, C. Hunziker, A. Schneider, H. Yun, Y. S. Lee, and P. Günter, "Organic phenolic configurationally locked polyene single crystals for electro-optic and terahertz wave applications," Adv. Funct. Mater. , **18**, 3242–3250 (2008).
58. T. Kolev, Z. Glavcheva, D. Yancheva, M. Schürmann, D.-C. Kleb, H. Preut, and P. Bleckmann,"2-{3-[2-(4-Hydroxyphenyl)vinyl-5,5-dimethylcyclohex-2-en-1-ylidenemalononitrile," Acta Crystallogr. Sect. E **57**, o561--o562 (2001).
59. Y. Li, Z. Wu, X. Zhang, L. Wang, J. Zhang, and Y. Wu, "Crystal growth and terahertz wave generation of organic NLO crystals: OH1," J. Cryst. Growth, **402**, 53-59 (2014).
60. E. Y. Choi, M. Jazbinsek, J. H. Jeong, and O. P. Kwon, "Effect of ionic organic additives for the growth of polyene crystals synthesized by Knoevenagel condensations," CrystEngComm, **14**, 1045-1048 (2012).
61. C. Hunziker, S.-J. Kwon, H. Figi, F. Juvalta, O.-P. Kwon, M. Jazbinsek, and P. Günter, "Configurationally locked, phenolic polyene organic crystal 2-{3-(4-hydroxystyryl)-5,5-dimethylcyclohex-2-enylidene}malononitrile: linear and nonlinear optical properties," J. Opt. Soc. Am. B, 25, 1678-1683 (2008).
62. K. Aoki, K. Nagano, and Y. Iitaka, " The crystal structure of L -arginine phosphate monohydrate ," Acta Crystallogr. Sect. B Struct. Crystallogr. Cryst. Chem. (1971).
63. D. Eimerl, "Electro-Optic, Linear, and Nonlinear Optical Properties of Kdp and Its 1Somorphs," Ferroelectrics, **72**, 95-139 (1987).

64. X. Dong, J. Min-Hua, and T. Zhong-Ke, "A new phase matchable nonlinear optical crystal—L-arginine phosphate monohydrate (LAP)," Acta Chim. Sin. English Ed, **1**, 230-233 (1983).

65. A. S. Haja Hameed, G. Ravi, R. Ilangovan, A. Nixon Azariah, and P. Ramasamy, "Growth and characterization of deuterated analog of L-arginine phosphate single crystals," J. Cryst. Growth, **237**, 890-893 (2002).

66. W. J. Liu, C. Ferrari, M. Zha, L. Zanotti, and S. S. Jiang, "X-ray topographic characterization of L-arginine phosphate monohydrate crystals," Cryst. Res. Technol, **35**, 1215–1219 (2000).

67. D. Eimerl, S. Velsko, L. Davis, F. Wang, G. Loiacono, and G. Kennedy, "Deuterated l-arginine phosphate: A new efficient nonlinear crystal.," **25**, 179 - 193 (1988).

CHAPTER 4 : Terahertz Spectroscopy and Density Functional Theory based Studies of Nitro/Nitrogen-Rich Aryl-Tetrazole Derivatives

Terahertz time-domain spectroscopy (THz-TDS) probes the intermolecular interactions in the materials. The present THz-TDS study covers the 0.1- 3 THz or 5-100 cm^{-1}range of spectral region, which has low photon energy and non-ionizing portion of the electromagnetic spectrum. Spectra are recorded in a time-domain configuration where broad-band pulse of THz electromagnetic radiation passes through a sample and detected by the E-O sampling method. This procedure gives a direct measurement of the time-of-flight of THz radiation from the sample and, analysis of results infers direct means to measure interactions between the transmitting THz and the testing sample material. This chapter describes the THz-TDS study of newly synthesized aryl-tetrazoles derivatives. The effect of functional groups attached to tetrazole moiety on the energetic properties is discussed. The THz-TDS experimental results are compared with DFT studies at molecular Gaussian (using G-09) and single crystal level (using plane wave pseudopotential(PAW) method). The obtained vibrational frequencies and linear optical properties are found to have consistent with the experimental data in THz regions and UV-Visible.

Part of this chapter's work has been published as following journal article.

Time-Domain Terahertz Spectroscopy and Density Functional Theory Studies of Nitro/Nitrogen-Rich Aryl-Tetrazole Derivatives. *ACS Omega* 2020, 5, 6, 2541–2551

Damarla Ganesh, EN Rao, Mottamchetty Venkatesh, Kommu Nagarjuna Ganapathy Vaitheeswaran Akhila K. Sahoo **and Anil K. Chaudhary***

The analytical utility of THz-TDS is established through a series of transmission measurements through different types of samples composed of the High energy materials of interest embedded within a polymeric matrix. PTFE powder was mixed with explosive sample to form compressed pellets for analysis. Initial efforts have been made for quantification of the given explosive sample in the pellet using a Beer-Lambert relationship where the magnitude of selected absorption bands is related to the quantity of the sample.

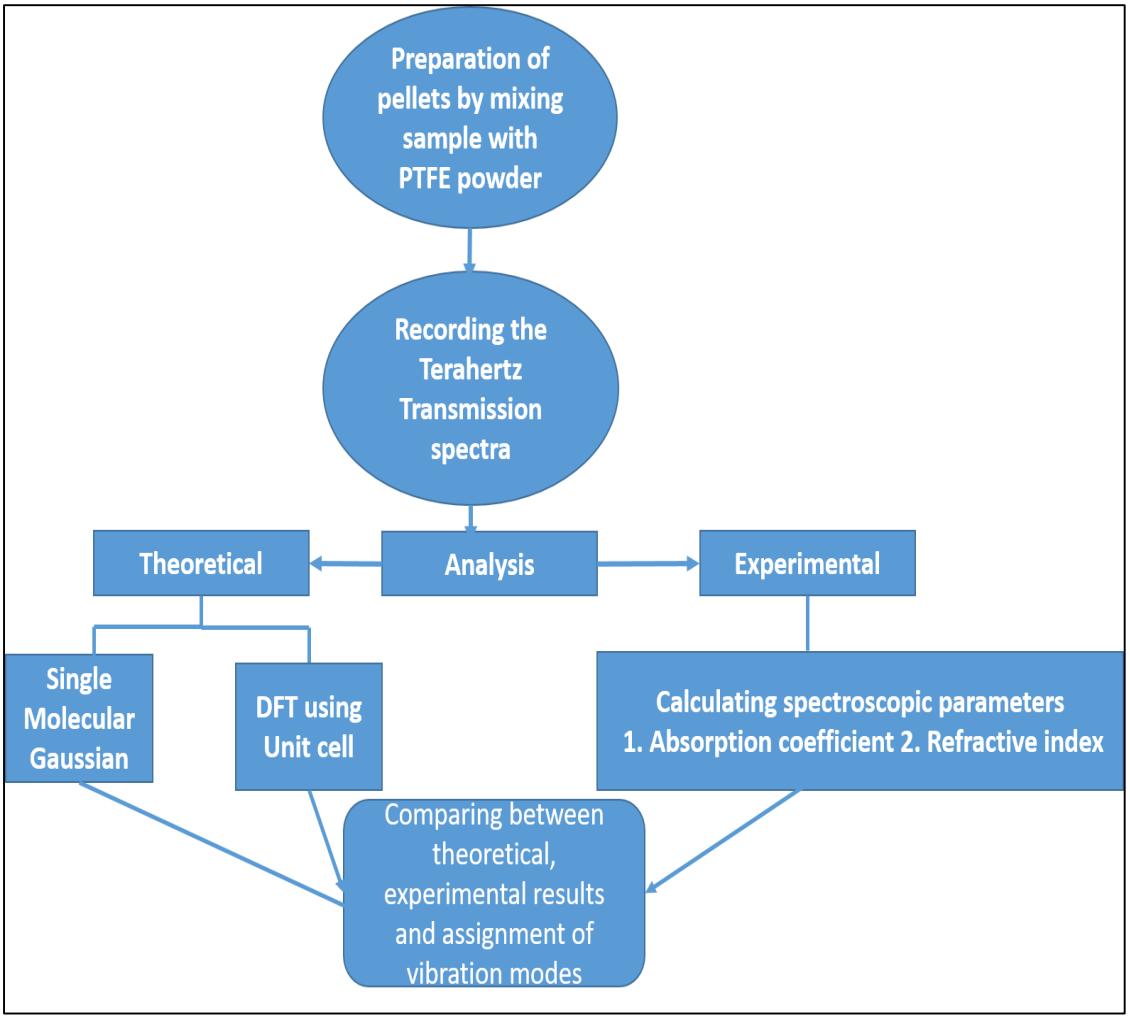

Figure 4.1. Flowchart of procedure followed in the present chapter

Also, time-domain THz spectra are used to determine the refractive index of sample pellets. This information is shown to provide dielectric spectra at THz frequencies for the components of the sample pellets.

4.1 Sample Preparation

Sample preparation is one of the important part of the time domain terahertz spectroscopy. A pellet that contains a little amount of the sample in polyethylene/polytetrafluoroethylene matrix is used for performing THz time-domain spectroscopy. The sample can also be used in form of thin films. Generally, the thin films show narrow linewidth peaks than pellets. It is due to distribution of different sized and shape particles in the host matrix and there is a possibility of undergoing structural damages due to high pressure applied during the preparation of the pellet. As a result of this strained microcrystals, spectrum undergoes inhomogeneous broadening. However, on the other hand, a thin film based waveguide technique is also used rigorously in which the sample is drop-casted on metallic plate by dissolving it in a solution then placed in a parallel plate waveguide [1]. This method results in high level of crystallinity resulting sharp features. However, we used nonchemical treatment based dry pellet method to prepare test samples. For converting solid sample in uniform shape and size the sample was dissolved in a small quantity of volatile solvent. Pellets were prepared by mixing 100 mg of the sample with 400 mg of polytetrafluoroethylene (PTFE) powder. To prepare a fine pellet, the sample powder size should be homogenously mixed with the host PTFE medium. It was achieved by mixing both the samples in ethanol solution by a spatula and follow the process of hand grinding with mortar. Then the mixture was dried and subjected to stainless steel made hydraulic press at 2.0 tons of pressure. It is recommended that pellets should have smooth surfaces and minimum surface undulations in order to minimize scattering losses of radiation. The applied pressure during pellet making is another factor that decides the quality of the pellet. The Pellets were prepared by applying two tons of pressure for the period of 5 minutes. The dimensions of pellets were 12 mm in diameter and 2 mm thickness [2].

4.1.1 Theoretical methods

The solid level theoretical calculations were done using the Cambridge Series of Total Energy(CASTEP) program [3,4]. Whereas the single molecular level calculations were performed with Gaussian-03 code. We have considered the experimental crystal structures as input and optimized the systems using Broyden-Fletcher-Goldfarb-Shanno (BFGS) algorithm with convergence thresholds for energy, force, stress and maximum displacements as $5.0x10^{-6}$(eV/atom),0.01eV/Å, 0.02 GPa and $5.0x10^{-4}$Å, respectively. The electronic Hamiltonian

with the plane-wave basis set with cut-off energy 550 eV, ultra-soft (US) pseudo-potentials (for electron-ion interactions) [5], SCF threshold $5.0x10^{-6}$(eV/atom) with 3x5x3 Monkhorst-Pack [6] k-mesh (15 irreducible k-points) in the reciprocal space was used. Generalized gradient approximation (GGA) Predew-Burke-ErnZerhof (PBE) [7] and dispersion correction Grimme (G06) [7] scheme was used to treat strong and weak electron-electron interactions. The G06 optimized structure was used for linear optical properties (absorption and refractive index spectra's) calculations. The zone centre vibrational properties (infrared(IR)-spectra) are calculated using the density functional perturbation theory (DFPT) [8,9] approach by utilizing the norm conserving (NC) pseudo-potentials [10] with 830eV cut-off energy. The valence electrons of the constituent atoms are considered as follows: H ($1\mathbf{s}^1$), N ($2\mathbf{s}^2$ $2p^3$), C ($2\mathbf{s}^2$ $2p^2$), O ($2\mathbf{s}^2$ $2\mathbf{p}^4$). The gas phase single molecule geometry optimizations and vibrational properties calculations are done using the B3LYP (Becke, 3-parameter, Lee-Yang-Par)functional [11,12] with 6-311+G(d, p) polarized basis set as implemented in Gaussian-03 [13].

4.2 Material characterization with THz spectroscopy

THz-TDS is a fascinating spectroscopic technique to characterize materials because of its coherent optical-gating detection. Time domain spectra directly helped us to extract the phase (dispersion) and amplitude (absorption) information at separate frequencies without using Kramers-Kronig relation [14,15]. Materials with non- metallic and non-polar in nature are transparent in THz range. Therefore, this special ability of penetration from organic and packing materials makes THz an important tool for qualitatively and quantitative identification of materials under concealed conditions. Grischkowsky et al. reported the use of THz-TDS spectroscopic for studying the different types of liquids, dielectrics, crystalline and gaseous materials [16–19].

4.2.1 Crystalline materials

THz is capable of stimulating inter and intra-molecular vibrational modes of many organic solids that depends on the interaction force and strength of chemical bonds. Intra molecular vibrational modes are fixed for a specific molecule, whereas molecular configuration and overall conformation decide the intermolecular vibrational modes [20]. In case of solids, number of intramolecular modes exits, but all of them are not observed in THz because of strong interaction forces. Moreover, in the THz frequency range, intermolecular modes are crystallinity dependent [17].

4.2.2 Liquids

For polar liquids, two types of molecular inter actions are covered in two different THz frequency range. The 0.1-6 THz frequency range covers the diffusive motions lead the spectrum, causing a damped absorption, at higher frequencies, resonant motions phase [23]. However, in the low-frequency regime, the polarization relaxation follows the orientation of permanent dipole moments in response to an applied electric field which is also responsible for the strong absorption [24]. The dielectric function influenced by this mechanism can be described by a simple relaxation model, e.g. (Debye model), which is characterized by relaxation time. This relaxation time is of the order of picosecond and inversion of a relaxation time provides critical frequency which falls within the THz range [23,25]. Therefore, THZ-TDS also provides significant information about the dynamics of a liquid samples.

4.2.3 Gases

Polar gases resonate at discrete frequencies when excited by the stimulated radiation falls between microwaves to FIR region. Characteristic sharp resonances are observed due to molecular rotational transitions. The heavy gas molecules have rotational resonances in higher wavelength region whereas, lighter molecules have resonances at small wavelengths. The Rotational gas spectroscopy empowers the applications in gas sensing. THz-TDS rotational gas spectroscopy was executed in the microwave regime and IR range [26,27]. THz-TDS provides the extra features of the rotational spectroscopy as compared to far-infrared regime. Time-resolved studies of THz-TDS allows identification of gaseous molecules free induction decay followed by an impulse excitation [28]. A lot of gaseous molecules have been studied by THz-TDS for their broadening effects and transition frequencies. Some of these molecules are nitrous oxide(N_2O), Methyl Chloride(CH_3Cl), Ammonia(NH_3) etc. [23,29-32].

4.2.4 Terahertz spectroscopy of tetrazole-N-(hetero)aryl derivatives

Apart from warfare blasters, high energy materials find potential applications in civil, space as detonators and rocket fuel etc. High energy materials are basically nitro rich compounds [33,34]. They consist of different moieties with five (imidazole), four (Tetrazoles), Three (Triazoles) membered nitrogen rings [35]. Tetrazoles are is a unique building block among all the nitrogen

moieties having tremendous applications in the civil sector, such as gas generating agents and pharmaceuticals [36,37].Tetrazole skeleton contains high energy than the other azole derivatives, also physical properties of these tetrazoles comparable with premium explosives like RDX and TNT [38–43]. However, tetrazoles reported so far suffer less sensitivity to friction and impact they didn't gain much attention due in the aforementioned applications. Nagarjuna Kommu, A. K. Sahoo et. al reported the preparation of nitro/nitroamino/azido substituted aryl tetrazole derivatives tetrazole-N-aryl/heteroaryl derivatives bearing $–NH_2$, $–NO_2$, $–NHNO_2$ and $–N_3$ groups [44].

They are

1. 2,6-dinitro-4-(1H-tetrazol-1-yl) aniline ($C_7H_5N_7O_4$) (**6**),
2. 2.N-(2,6-dinitro-4-(1H-tetrazo-1-yl) phenyl) nitramide ($C_7H_4N_8O_6$) (**7**),
3. 1-(3,4,5-trinitrophenyl)-1H-tetrazole ($C_7H_3N_7O_6$) (**8**),
4. 1-(4-azido-3,5-dinitrophenyl)-1H-tetrazole ($C_7H_3N_9O_4$) (**9**)

A comparison of energetic properties of these molecules is shown in table.1. All the molecules exhibit better energetic properties than TNT and equivalent to RDX. Also, they are crystalline in nature with good oxygen balance (OB%), so they can be used as an energetic plasticizer in rocket propulsion applications. The OB% of '6', '7', '8', '9' compound of the order of -79.62%, -54.02%, -54.06% and -66.38%, respectively [45]. In addition to above values, their densities ρ (in $g.cm^{-3}$), high velocities of detonation D_v (in $m.s^{-1}$), and detonation pressure D_p (in GPa) are comparable to TNT, RDX.

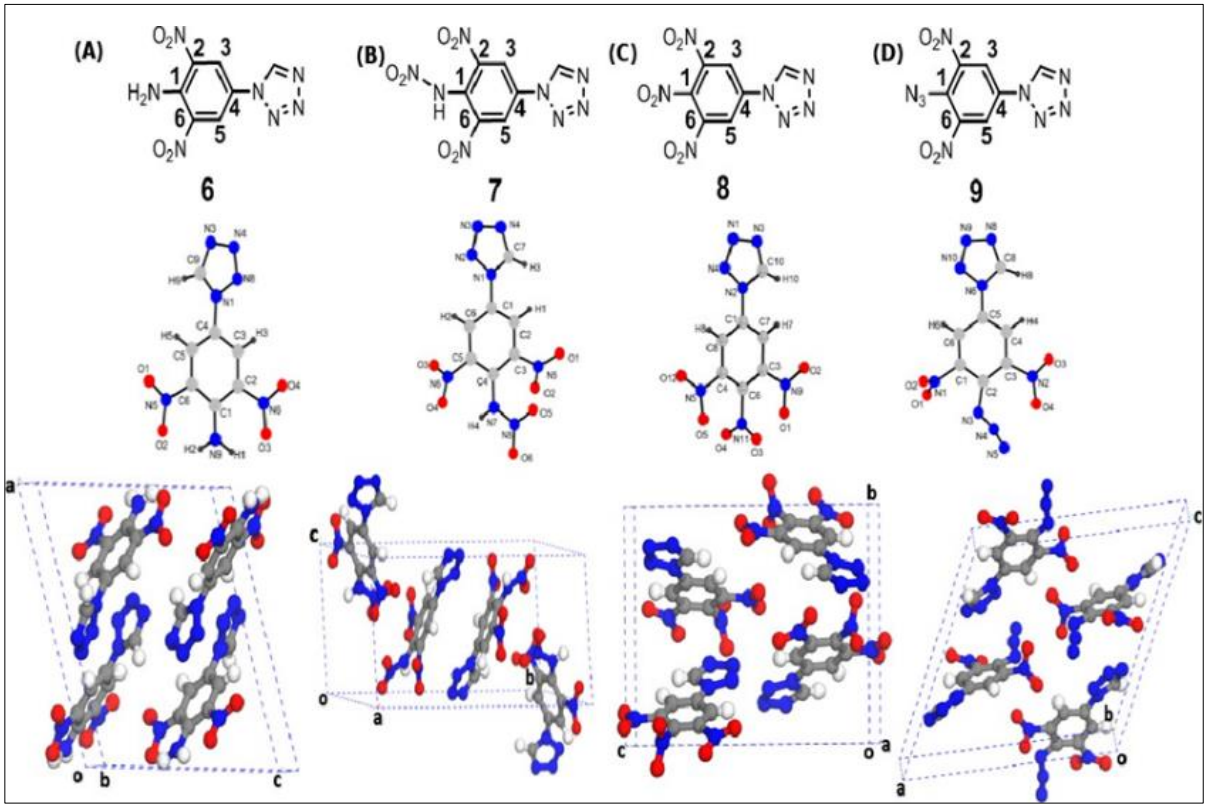

Figure 4.2. (Color online) Molecular and experimental crystal structures (from left to right) of ($C_7 H_5 N_7 O_4$) (6), ($C_7 H_4 N_8 O_6$) (7), ($C_7 H_3 N_7 O_6$) (8), ($C_7 H_3 N_9 O_4$)

As shown in Figure 4.2 substitutional functional group attached to position '1' of the molecule not only influences the energetic properties of the molecules but also responsible for the transition of crystalline to amorphous phase which is also reflected in terms of change in absorption Coefficient and refractive index. All these crystalline tetrazole derivatives are non-centrosymmetric with space groups P21/C and $P2_12_12_1$, which may possess good second harmonic generation capability.

Table 4-1. Energetic properties of 6-9 compounds. Here ϱ (in $g.cm^{-3}$), D_v (in $m.s^{-1}$), D_p (in GPa) are Crystal density, Detonation velocity and Detonation pressure [46].

Compound	(ρ)	D_v	D_p
2,6-dinitro-4-(1H-tetrazol-1-yl)aniline (6)	1.75	7899	24.1
N-(2,6-dinitro-4-(1H-tetrazol-1-yl)phenyl)nitramide(7)	1.78	8208	28.0
1-(3,4,5-trinitrophenyl)-1H-tetrazole (8)	1.79	8298	28.4
1-(4-azido-3,5-dinitrophenyl)-1H-tetrazole (9)	1.66	7734	26.2

TNT [47]	1.65	6881	19.5
RDX [47]	1.80	8795	34.9

Therefore, it is worth to study the structure-property correlations of these molecules both in experimental and theoretical aspects to explore their applications in terahertz generation, detection, and in nonlinear optical domain. Hence in the present study, we report terahertz time-domain spectroscopic response of these compounds, and the reasons behind the optical response are explored through density functional theory calculations both at single molecular and solid level. The experimental techniques and sample preparation methods used for the present study are already discussed in previous chapters.

4.2.5 Crystal Structure and Terahertz response

Except for compound ($C_7H_3N_7O_6$) (8)all the Tetrazole samples ($C_7H_5N_7O_4$) (6), ($C_7H_4N_8O_6$) (7), and ($C_7H_3N_9O_4$) (9) chosen for present study crystallize in non-centrosymmetric space groups with monoclinic symmetry whereas compound 8 is orthorhombic [44]. These materials consist of z=4 formula units/unit cell (i.e. "6"-92; "7"-100; "8"-92; "9"-92 atoms/unit cell). Moreover, all the atoms of 6,7, and 9 are located at '4e' atomic Wyckoff sites, the compound 8, atoms are occupying 4a Wyckoff site with full occupancy. Due to the change in the explosive functional groups (i.e. NH_2, NO_2, N_3, NH-NO_2) of these tetrazole derivatives, the lattice vectors (*a, b, c, d*) show increment in the following order: *a*: 8 → 7 → 6 → 9; *b*: 9 → 6 → 8 → 7; *c*:7 → 6 → 9 → 8, *d* :8 → 7 → 6 → 9.The corresponding layers of compounds 6, 7, 8, 9 are spread over xz, xy, yz, xz planes and the adjacent layers are stacked along x, y, z, x directions. This change in the chemical composition and symmetry resulted in a huge difference in their explosive nature (see Table. 4.1) and stability. Moreover, the increase in the nitrogen and oxygen percentages in the studied compounds will lead to a change in their polarization. Hence the non-centrosymmetric nature and change in the number of electrons strongly motivated us to investigate their terahertz optical responses, which are believed to be useful for their detection and nonlinear applications. The same was carried out using our time-domain terahertz spectroscopy set-up described in Chapter 2. The Terahertz absorption spectra results of the tetrazole compounds are depicted in Figure 4.3.

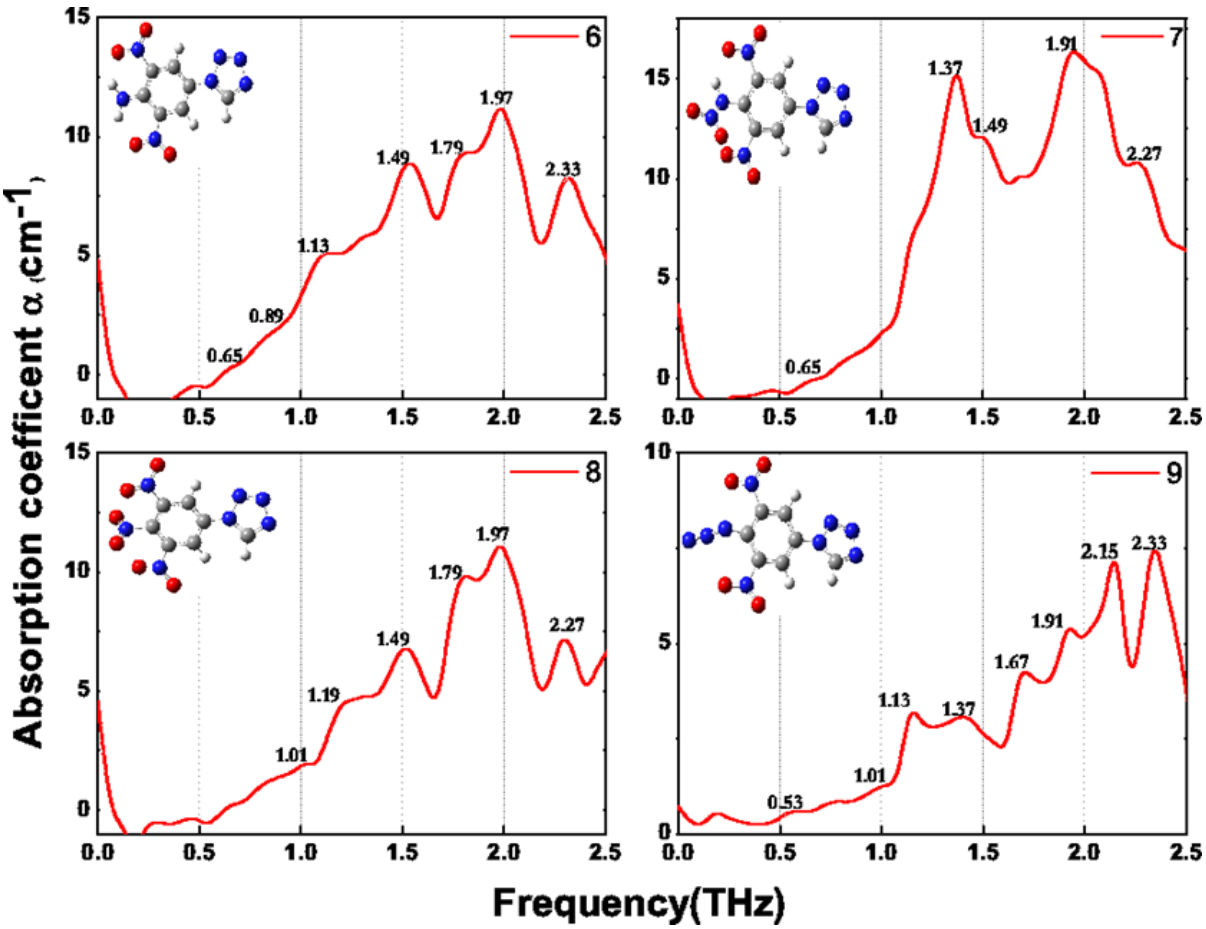

Figure 4.3. The experimental terahertz absorption spectra of 6,7,8 and 9 compounds

It is clear from the Figure 4.3 that all the compounds start absorbing radiation from 0.5 THz and seven high intensity absorption peaks are found between 1.0 and 2.5 THz range. The tetrazole molecules show absorption in 0.5 to 2.5 THz energy window as follows: for compound '6' - 0.65, 0.89, 1.13, 1.49, 1.79, 1.97, 2.33 THz; for compound '7' - 0.65, 1.49, 1.47, 1.91, 2.27 THz; for compound '8' - 1.01, 1.19, 1.49, 1.79, 1.97, 2.27 THz; for compound '9' - 0.53, 1.01, 1.13, 1.37, 1.67, 1.91, 2.15, 2.33 THz. Among these, compound '7' show highest intensity peaks hence it is more polarizable, whereas compound '9' show well defined absorption peaks and hence relatively more sensitive and easy to detect even at lower energies. Moreover, detection limit of the studied tetrazole compounds got increased from NH-NO_2 → NH_2 → NO_2 → N_3 explosive functional groups.

4.3 Theoretical study using Gaussian and DFT methods

These unique absorption spectra of studied compounds are considered to be their fingerprint spectra in the terahertz domain. In order to understand these absorption peak frequency, intensity

differences more clearly, vibrational mode analysis using density functional theory calculations both at molecular and solid level were carried out. In the first step, we performed the molecular vibrational spectra calculations by using B3LYP/6- 311+G(d, p) polarized basis set as implementing in Gaussian-03 [13]. We have considered the experimental single crystal x-ray diffraction structure as our input. The obtained frequencies do not show any imaginary part, which confirms the dynamical stability of all the studied compounds and the corresponding results plotted in Figure 4.4. The far infrared(FIR) absorption peaks of studied tetrazole molecules between 0.1 and 2.2 THz frequency windows are observed at the following frequencies: For compound, '6' - 1.13, 1.36 THz; for compound '7'-1.08,1.58, 2.09 THz; for compound '8' - 0.95, 2.02 THz; for compound '9' - 0.47, 1.15, 2.07 THz. The obtained results show considerable deviation with respect to the experimentally measured frequencies. But it is known that the vibrational spectrum in the THz range primarily depends on the molecular structure and their intra and intermolecular interaction.

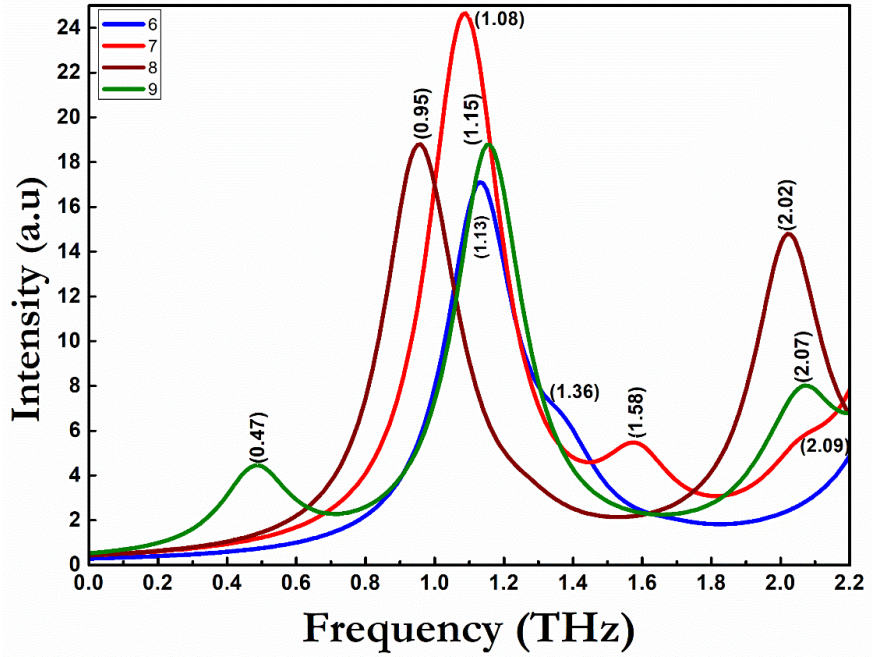

Figure 4.4. The far infrared(FIR) absorption peaks of studied tetrazole molecules between 0.1 and 2.2 THz obtained using Gaussian-03

The weak interaction of molecules and the intermolecular force results in the collective vibration mode under the THz range frequency. The vibration in the THz domain normally arises from the bending, torsion, deformation of two or more molecules. As the performed DFT calculations for single molecule level, the obtained vibrational spectrum is shown in Figure 4.4. In the spectrum 0.2-2.2 THz region can be attributed to the intra-molecule vibrations alone. The preliminary mode

analysis informs that the absorption peak of compound '6' located at 1.13 THz is attributed to torsional rotation of tetrazole moieties, and other two frequencies are due to wagging of NO_2 groups attached to the ring. The peak of compound '7' at 1.08 THz is attributed to torsional rotation of tetrazole moiety. Similarly, the reduction in the first absorption peak (red-shift) of compound '7' (1.08), '8' (0.95), '9' (0.47) when compared to compound '6' (1.13) is due to increase of additional reduced mass of nitro group of molecules. The mode at 2.02 THz of compound '8' is attributed to the rotation of twist of NO_2, and the calculated low frequency 0.95 THz mode is not clearly observed in the experimental spectrum, which could be due to the scattering losses. In case of compound '9', vibrational modes at 0.47 THz are observed due to collective rotation twists of all attached azide group to ring. Torsional rotation of tetrazole moiety was observed at 1.15 THz. A torsional rotation of all functional groups except tetrazole was observed theoretically at 2.07 THz. The difference in the intensity profiles of the studied molecules indicates the increment in the polarizability from compound '6'→ '9' → '8' → '7', which is contradicting with the experimental observations. However, the observed discrepancy between experimental and theoretical vibrational frequencies could be due to the omission of the effects from intermolecular interaction and temperature. Hence, we turned our attention to the solid state level DFT calculations of the present compounds of interest to incorporate the role of intermolecular interactions.

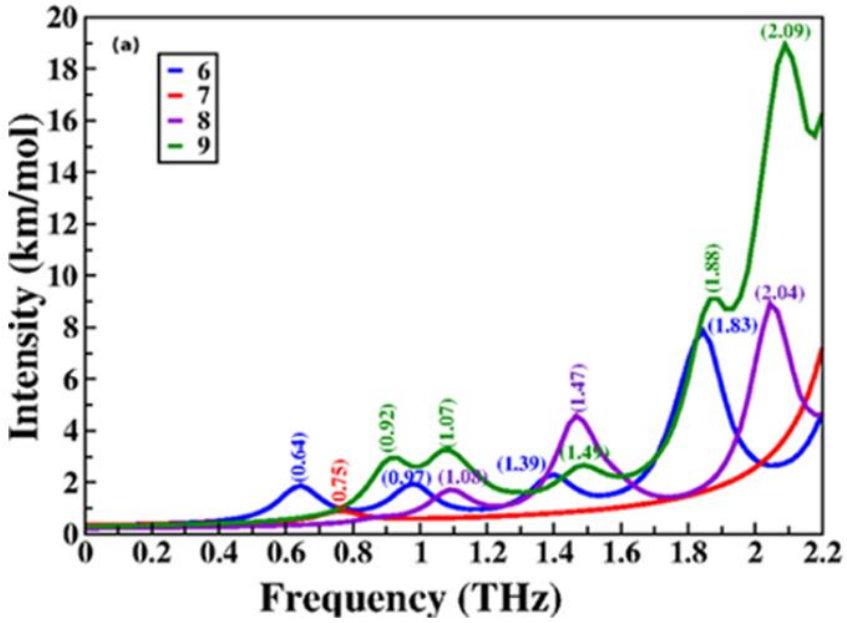

Figure 4.5. The far infrared(FIR) absorption peaks of studied tetrazole molecules between 0.1 and 2.2 THz implemented GGA-PBE exchange correlated functions as implemented in CASTEP

Initially, the experimental layered noncentrosymmetric crystal structures using GGA-PBE exchange correlated functions as implemented in CASTEP. The calculated ground state lattice vectors, angles and volumes with experimental data are tabulated in Table. 4-2. The results show considerable deviation when compared to the experimental data and are as follows:

'6' → a(14.1%) >c(7.8%) >b(2.0%); '7' → c(7.1%)>b(6.6%) >a(3.9%); '8' → a(9.0%) >b(5.2%) >c(4.1%); 9 → c(9.7%) >a(5.5%) >b(2.1%). The crystal volume and crystallographic angle are as follows:

V: for compound '8' (25.4%) > '9' 326 (23.8%) > '6' (20.6%) > '7' (16.8%)

β: for compound '6'327 (5.0%) > '7' (4.7%) > '9' (4.6%)

Table 4-2. Calculated Ground-State Lattice Vectors (a and c, in Å), Volume (V, in Å^3) of 6, 7, 8, and 9 Using PBE and Dispersion- Corrected PBE + G06 along with Experimental Data

Symmetry	Compound	Parameter	PBE	PBE+G06	Experiment
		a	14.593	12.941	12.780
$P2_1/C$	6	b	7.278	7.067	7.135
(Z=4)		c	11.910	10.754	11.043
(monoclinic)		V	1144.690	934.862	948.6
		β	115.198	108.109	109.625
		a	8.233	7.871	7.922
$P2_1/C$	7	b	19.821	18.690	18.592
(Z=4)		c	8.105	7.642	7.561
(monoclinic)		V	1286.70	1109.11	1100.77
		β	103.388	99.442	98.730
		a	8.317	7.528	7.626
$P2_12_12_1$	8	b	11.086	10.518	10.537
(Z=4)		c	14.154	13.654	13.592
(orthorhombic)		V	1305.22	1081.33	1040.25
		a	14.724	14.249	13.943
$P2_1/C$	9	b	7.104	6.872	6.957
(Z=4)		c	14.093	12.825	12.819
(monoclinic)		V	1367.89	1125.51	1104.4
		β	111.906	116.355	117.363

These results also inform that the intermolecular interactions are dominant in the studied layered compounds as follows: 6> 9 > 8> 7. This can be attributed to the difference in the arrangement of molecules in corresponding unit cells. Hence, to capture the weak interlayer non-bonded interactions, we optimized all the crystal structures with the dispersion corrected PBE functional i.e.,

PBE+G06. The obtained results show very good agreement with the experimental data and the deviations of all the obtained lattice vectors, volumes and β values are ~1%. The corresponding results are shown in Table 4-2. Hence the G06 optimization results confirm the crucial role of van der walls interactions in finding the optimized structures. We have extended the use of these (G06) structures in our further vibrational properties calculation that is very sensitive to the lattice vectors. The zone centre vibrational frequencies have been calculated for all the compounds using DFPT approach [9,48]. All of the required mode assignments from 0.1 to 2.2 THz are done, and the corresponding results are shown in Figure 4.5. The compounds 6, 7, and 9 are isostructural and crystallized at the same point group with $C_{2h}(2/m)$ symmetry with z = 4 formula units (98 atoms/unit cell) except for compound "8" which is getting crystallized in $D_2(222)$ point group symmetry with (100 atoms/unit cell). Hence, there will be 276 − 3 = 273 vibrational modes for 6, 7, and 9 and 300 − 3 = 297 modes for compound "8". The group theory representation for these acoustic (appear due to in-phase moment of atoms) and optical (appear due to out of phase moment of atoms) modes will be as follows:

$$\Gamma_{acoustic}\,(6,9) = A_u \oplus 2B_u$$

$$\Gamma_{optic}\,(6,9) = 69A_g \oplus 68A_u \oplus 69B_g \oplus 67B_u$$

$$\Gamma_{acoustic}\,(7) = A_u \oplus 2B_u$$

$$\Gamma_{optic}\,(7) = 75A_g \oplus 74A_u \oplus 75B_g \oplus 73B_u$$

$$\Gamma_{acoustic}\,(8) = B_1 \oplus B_2 \oplus B_3$$

$$\Gamma_{optic}\,(8) = 69A_1 \oplus 68B_1 \oplus 68B_2 \oplus 68B_3$$

For all the crystals, the calculated (273, 297) vibrational modes are consistent with group theory representations. Among the 273 optical modes of "6", "9" crystals, 135 ($68A_u \oplus 67B_u$) are found to be IR active and 138 modes ($68A_u \oplus 67B_u$) found to be Raman active. In case of crystal 7, out of 297 optical modes, 147 modes ($74A_u \oplus 73B_u$) are found to be IR active and 150 modes ($75A_g \oplus 75B_g$) are Raman active. Interestingly, for crystal 8, out of 273 optical modes 69A1 modes are found to be purely Raman active, 204 modes ($68B_1 \oplus 68B_2 \oplus 68B_3$) are found to be both IR+Raman active. Hence compound 8 is highly polarisable (more optically active) among the studied crystals. All the frequencies of the vibrational modes are given in Table (4-3). Since we focused on the terahertz response between 0.1 to 2.3 THz range. The snapshots of a few vibrational modes are

given in Figure 4.6. The obtained frequencies of all the crystal in the 0.1 to 2.2 THz range are mainly arising due to complete lattice translation associated with NO_2 groups and N_3 asymmetric stretching, due to which asymmetric stretching in Tetrazole ring and trinitrobenzene is also observed. Further, we compared the experimental, molecular phase and solid phase vibrational frequencies and they are shown in Table (4-3).

Table 4-3 The Calculated Zone-Center low frequency vibrational modes (in cm-1 of C7H5N7O4)(6), (C7H4N8O6) (7), (C7H3N7O6)(8), and (C7H3N7O4) (9). Here IR active modes denoted as 'I', Raman active modes as 'R.'

Compound	Experiment	Mode	Frequency	Symmetry
		M14	66.64	Bg(R)
		M13	62.05(**65.71**)	Au(I)
		M12	61.61(**59.70**)	Au(I)
		M11	59.42	Bu(I)
		M10	55.27	Ag(R)
6	65.71	M09	48.52	Bu(I)
	59.70	M08	46.47(**49.70**)	Bu(I)
	49.70	M07	41.37	Ag(R)
	37.69	M06	37.03	Bg(I)
	29.68	M05	32.60(**29.68**)	Bu(I)
	21.68	M04	21.37(**21.68**)	Au(I)
		M06	25.36(21.68)	Bg(I)
		M05	24.29	Au(I)
		M04	13.08	Ag(R)
7				
	63.71			
	49.70			
	45.69			
	21.68			
		M21	72.23	A(R)
		M20	69.94	B3(I+R)
		M19	69.29	A(R)
		M18	68.05	B1(I+R)
		M17	66.70(**65.71**)	B2(I+R)
		M16	62.07	B3(I+R)
		M15	61.68(**59.70**)	A(R)
		M14	51.90	B3(I+R)
8		M13	49.52(**49.70**)	B2(I+R)
		M12	47.28	B1(I+R)
		M11	43.05	B2(I+R)
		M10	39.06(**39.69**)	B1(I+R)
		M09	38.47	A(R)
	65.71	M08	35.90	B2(I+R)

	59.70	M07	33.98(**33.68**)	B1(I+R)
	49.70	M06	30.44	A(R)
	39.69	M05	29.73	B3(I+R)
	33.68	M04	20.90	A(R)

Compound	Experiment	Mode	Frequency	Symmetry
		M24	73.32	Bg(R)
		M23	72.90(**71.71**)	Au(I)
		M22	70.69	Bg(R)
		M21	70.15	Ag(R)
		M20	68.41	Bu(I)
		M19	67.47	Au(I)
		M18	63.90	Au(I)
		M17	63.58	Ag(I)
9		M16	56.89	Bg(R)
		M15	52.97(**55.70**)	Ag(I)
		M14	48.94(**45.69**)	Bu(I)
		M13	47.91	Ag(R)
		M12	46.24	Ag(R)
		M11	46.23	Bg(R)
	70.71	M10	41.42	Bg(R)
	63.71	M09	39.78	Au(I)
	55.70	M08	37.28	Ag(R)
	45.69	M07	36.36	Bu(I)
	37.69	M06	32.79	Ag(R)
	33.68	M05	31.65	Bg(R)
	17.67	M04	29.12	Au(I)

The results indicate that solid level calculations results are mostly matching with the experimentally observed frequencies. The observed shift between the molecular level and solid level vibrational frequencies clearly indicates the dominant role of weak intermolecular, interlayer interactions via van der walls and hydrogen bonding. The intensities of the observed frequencies are dominant in the following order: 9 > 8 > 6 > 7. Hence it can be concluded that, due to the excess number of electrons present in the azide group of compound 9, it is showing high intensity (polarizability). Similarly, in compound 8 due to the presence of extra NO_2 group electrons, it next shows higher order polarizability. In the case of compound 7 due to the presence of strong N-N bond, we were able to observe only one peak in the studied terahertz range with lowest intensity among the studied crystals. Whereas compound 6 has weak C-N and H-N bonds due to which we are getting a good number of vibrational modes in the low energy region (<2.2 THz). Overall, we can conclude that

compound "9" possesses high optical sensitivity (therefore unstable) nature, whereas compound "7" shows low optical sensitivity (highly stable) among the studied compounds.

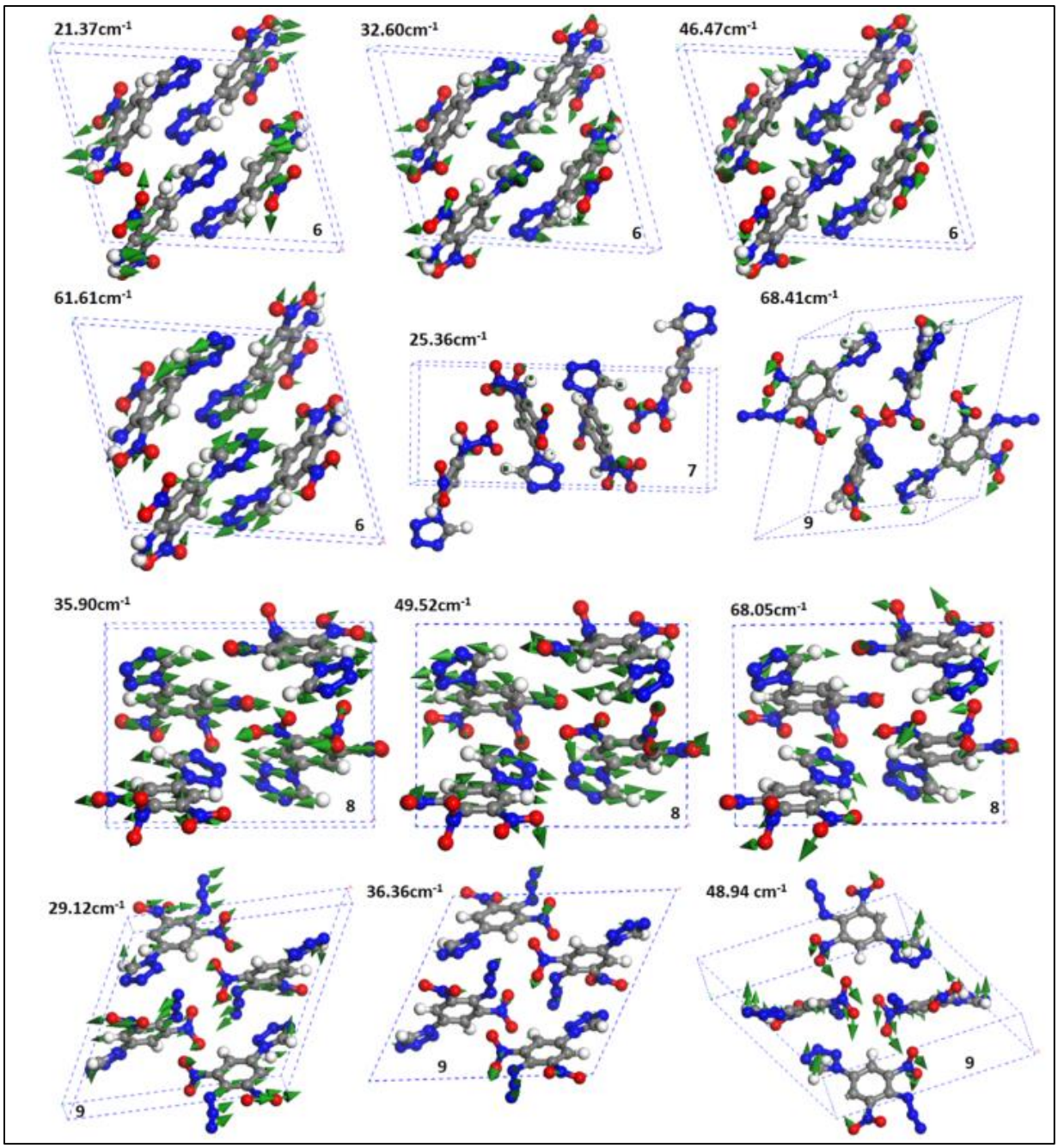

Figure 4.6. Few snapshot images of calculated vibrational frequencies (in cm^{-1}) at the solid level using PBE + G06.

Other compounds more or less show similar stability. But according to the group theory analysis and observed I+R active modes, compound 8 is optically active and stable when compared to compound "9". Hence it is easy to detect compound 8 than others and it may find possible applications in nonlinear optical domain also. The refractive index and birefringence measurement of these materials between the 0.1 to 2.2 THz range, which is very crucial parameter for any optical material applications.

4.4 Refractive index and birefringence

The nitro/nitrogen-rich aryl-tetrazoles crystallize in the noncentrosymmetric space group, and it is essential to know the role of electronic contributions in the optical properties such as absorption, band gap, refractive index, and birefringence in the given range of interest. Moreover, the THz-based study is meant for detection of explosives without ionizing the sample. Initially, we measured the absorption spectra of compounds using the UV/visible/NIR spectrometer (model: Cary 5000 with UMA attachment), and obtained results are compared with the theoretically calculated absorption spectra in [0 0 1] direction using the PBE-GO6 equilibrium structure, as shown in Figure 4.7.

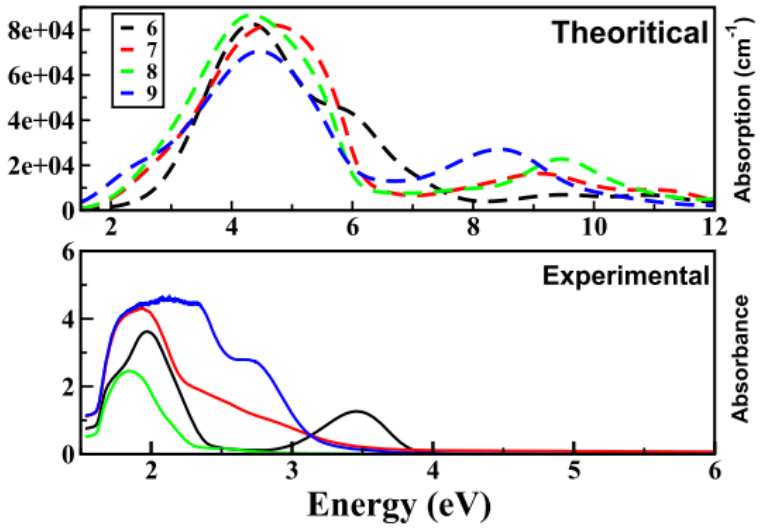

Figure 4.7. Experimental UV−visible absorption spectra of 6, 7, 8, and 9 compounds plotted along with the absorption spectra obtained at PBE+ G06 equilibrium structure

The experimental results confirm that compound "6" possesses a sharp absorption peak around 480 nm (2.58 eV), whereas absorption bands of other compounds such as "7", "8", and "9" are situated

at 450 nm (2.75 eV), 350 nm (3.54 eV), and 410 nm (3.02 eV), respectively. However, the theoretically obtained absorption spectra show that sharp absorption peaks for compounds "6", "7", "8", "9" are located at 1.3, 1.2, 1.2, and 1.0 to 2.5 eV, respectively. The broadening of the absorption peak of compound "9" is attributed to the indirect bandgap. Finally, it is clear from the experimental and theoretical results that the studied compounds possess a strong absorption band in the near-IR and THz regions. Frequency dependent complex refractive index between 0.1 and 2.2 THz was calculated using equations mentioned in chapter 2 [49,50]. Etalon effects caused due to internal reflection were ineffective since we have not taken these into account while calculating FFT [51]. The average calculated refractive index for compounds 6, 7, 8, and 9 (see Figure 4.8), and the obtained corresponding values are 1.65, 1.71, 1.72, and 1.81 respectively.

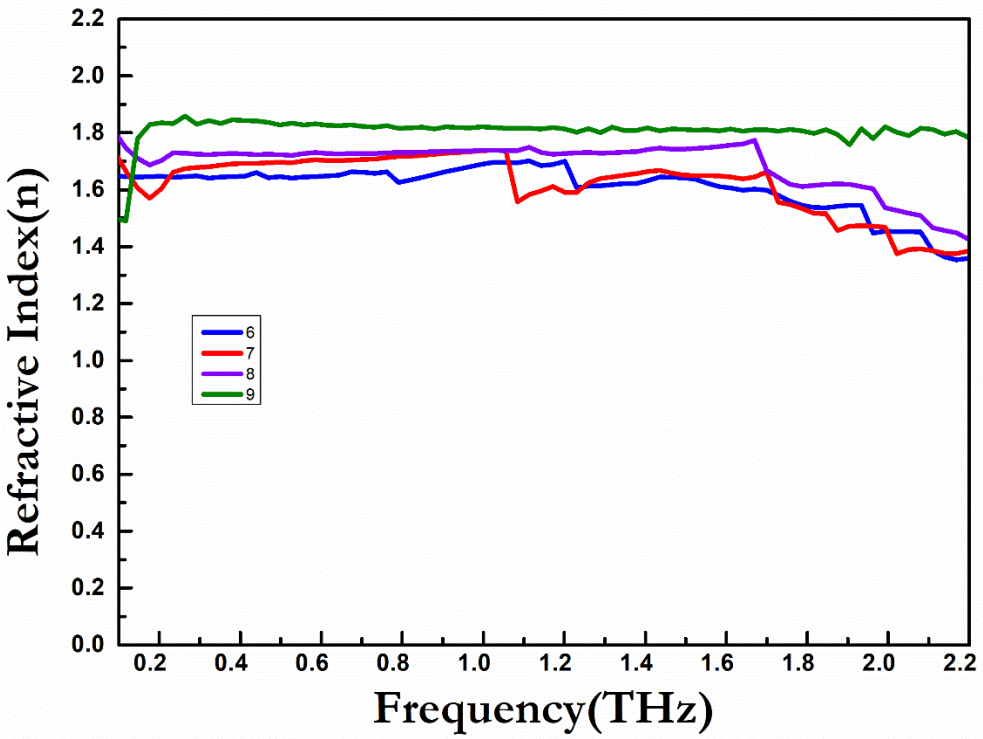

Figure 4.8. Experimental refractive index spectra comparison between 0 and 2.2 THz range of $C_7H_5N_7O_4$ (6), ($C_7H_4N_8O_6$) (7), ($C_7H_3N_7O_6$) (8), and ($C_7H_3N_9O_4$) (9)

Further verification has been done by calculations by comparing it with DFT results (see Figure 4.9). The calculations are done with great accuracy using US pseudopotentials, 380.0 eV energy cutoff, and 3 × 5 × 3 k-grid. As the chosen compounds crystallized in asymmetric space groups (monoclinic, ortho- 468 rhombic), different values of n_x, n_y, and n_z were obtained. All of the obtained results (experiment, DFT) within 0.1−2.2 THz energy window show reasonable agreement

(Table 4-4), and the same are plotted in Fig. (4-9). Moreover, the dispersion and intensity of the absorption curves are found to show considerable variations because of the change in the explosive functional group at position "1" on the tetrazole moiety. The theoretical difference in n_x, n_y, and n_z curves of studied compounds indicate that all the compounds possess large optical anisotropy. Further, the theoretically calculated (time-independent DFT) absorption spectra show considerable blue shift with respect to the experimental UV−visible spectra of the studied explosives, which is evident due to the omission of local field and exciton effects in the present DFT calculations, and these deviations can be addressed properly by including the excitonic effects through the time respectively.

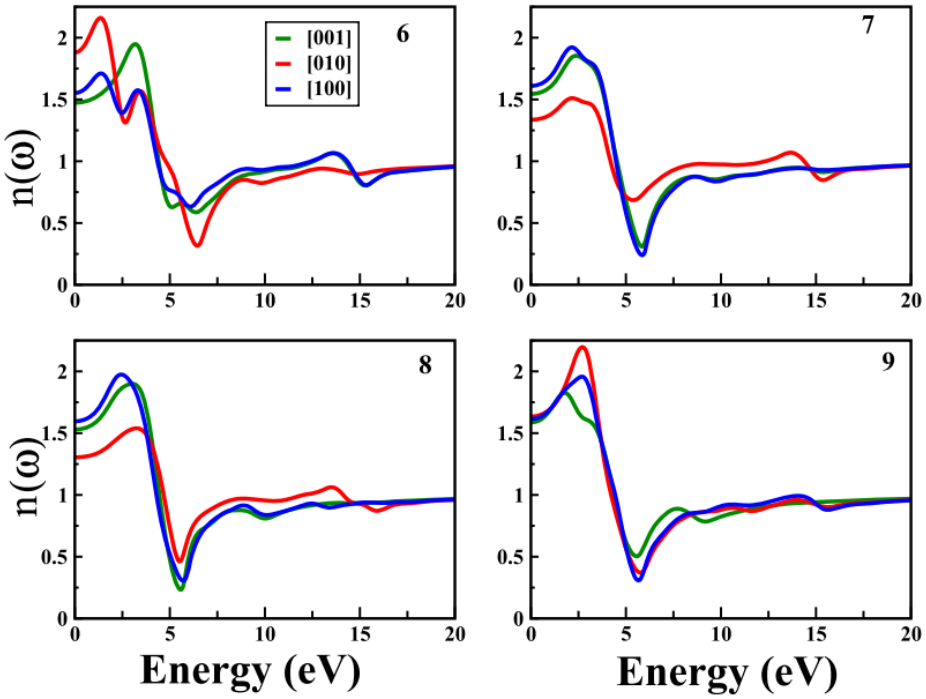

Figure 4.9. Theoretically obtained refractive index spectra (along x, y, z directions) of $C_7H_5N_7O_4$ (6), $C_7H_4N_8O_6$ (7), $C_7H_3N_7O_6$ (8), and $C_7H_3N_9O_4$

The results in Figure (5-10) and Table (4-4) also confirm that the calculated average static refractive index ($(n = n_x + n_y + n_z)/3$) values of all the compounds are relatively good in agreement with the experimentally observed values. Normally, for monoclinic NLO crystals, the refractive indices show either $n_x > n_y > n_z$ (negative biaxial) or $n_z > n_y > n_x$ (positive biaxial) trend. However, the results from shows the trend for compound "6": $n_y > n_z > n_x$, for compound "7": $n_z > n_x > n_y$, for compound "8": $n_z > n_x > n_y$, and for compound "9": $n_y > n_z > n_x$. These differences in the actual and obtained refractive indices can be attributed to the role of excitonic effects,which are not accounted for in the present study. For preliminary understanding, the birefringence (Δn) values of 6, 7, 8, and 9

compounds are calculated by taking the difference between the maximum value of refractive index to the minimum value from Table 4. The corresponding results show the following increment order: Δn (6) > Δn (8) > Δn (7) > Δn (9). Moreover, these values except for that of compound 9 are found

to be closer to the well-known nonlinear crystal DAST (0.39, 0.55, and 0.64) and higher than Recently reported carbonate fluoride crystals $ABCO_3F$ (A = K, Rb, Cs; B = Ca, Sr, Pb) (Δn around 0.1056, 0.0887, 0.0921, 0.0966) crystal birefringence values, which indicate that the studied noncentrosymmetric explosive compounds may possess good phase matching applications in visible and near-IR regions.

Table 4-4 Experimental and DFT Calculated Refractive Indices (n) along [100], [010], and [001] Crystallographic Directions and birefringence values of 6,7,8, and 9

Compound	n_x	n_y	n_z	Δn (n_{max} - n_{min})	$n_{average}$	$n_{experiment}$
6	1.474	1.886	1.555	0.412(0.331)	1.63	1.65
7	1.546	1.337	1.611	0.274(0.065)	1.49	1.71
8	1.530	1.304	1.596	0.292(0.066)	1.47	1.72
9	1.589	1.635	1.616	0.046(0.019)	1.61	1.81

Further analyses on the frequency-dependent second harmonic response of these compounds will be useful in phase transition, sensitivity correlation studies, and designing new organic nonlinear optical materials in near future.

4.5 Conclusions:

In summary, we have studied the linear and nonlinear optical properties of newly synthesized tetrazole molecules using time-domain terahertz spectroscopy, UV−visible−NIR spectroscopy, and DFT. We have also ascertained the absorption coefficients and refractive index between 0.1 and 2.2 THz range. In addition, we have performed single-molecule and single-crystal level DFT calculations. The obtained structural optimization results confirm the importance of non-bonded (vdW) interactions. The theoretically calculated zone center vibrational frequencies at the solid level

are found to be good in agreement with the experimentally observed THz absorption bands. However, the single-molecule vibrational frequency-based results can be improvised by the incorporation of intermolecular and interlayer interactions. We have also explained the optical sensitivity correlations using vibrational frequencies. The electronic absorption, refractive index, and birefringence studies reveal the feasibility of phase-matched nonlinear optical frequency mixing devices in the single-crystal form. The study also provides a good reference for growing organic nonlinear optical materials.

4.6 References

1. S. Sree Harsha and D. Grischkowsky, "Terahertz (far-infrared) characterization of tris(hydroxymethyi) aminomethane using high-resolution waveguide THz-TDS," J. Phys. Chem. A (2010).
2. G. Damarla, M. Venkatesh, and A. K. Chaudhary, "Temperature-dependent terahertz spectroscopy and refractive index measurements of aqua-soluble and plastic explosives," Appl. Opt. (2018).
3. M. C. Payne, M. P. Teter, D. C. Allan, T. A. Arias, and J. D. Joannopoulos, "Iterative minimization techniques for ab initio total-energy calculations: Molecular dynamics and conjugate gradients," Rev. Mod. Phys. (1992).
4. M. D. Segall, P. J. D. Lindan, M. J. Probert, C. J. Pickard, P. J. Hasnip, S. J. Clark, and M. C. Payne, "First-principles simulation: Ideas, illustrations and the CASTEP code," J. Phys. Condens. Matter (2002).
5. D. Vanderbilt, "Soft self-consistent pseudopotentials in a generalized eigenvalue formalism," Phys. Rev. B (1990).
6. H. J. Monkhorst and J. D. Pack, "Special points for Brillouin-zone integrations," Phys. Rev. B (1976).
7. S. Grimme, "Semiempirical GGA-type density functional constructed with a long-range dispersion correction," J. Comput. Chem. (2006).
8. S. Baroni, D. Gironcoli, D. C. S., A, and P. Giannozzi, "Phonons and related crystal properties from density functional perturbation theory," Rev. Mod. Phys. (2001).
9. V. Milman, K. Refson, S. J. Clark, C. J. Pickard, J. R. Yates, S. P. Gao, P. J. Hasnip, M. I. J. Probert, A. Perlov, and M. D. Segall, "Electron and vibrational spectroscopies using DFT, plane waves and pseudopotentials: CASTEP implementation," J. Mol. Struct. THEOCHEM (2010).
10. D. Hamann, M. Schlüter, and C. Chiang, "Norm-Conserving Pseudopotentials," Phys. Rev. Lett. (1979).
11. A. D. Becke, "A new mixing of Hartree-Fock and local density-functional theories," J. Chem. Phys. (1993).
12. J. P. Perdew, M. Ernzerhof, and K. Burke, "Rationale for mixing exact exchange with density functional approximations," J. Chem. Phys. (1996).
13. M. J. Frisch, G. W. Trucks, H. B. Schlegel, G. E. Scuseria, M. A. Robb, J. R. Cheeseman, G. Scalmani, V. Barone, B. Mennucci, G. A. Petersson, H. Nakatsuji, M. Caricato, X. Li, H. P. Hratchian, A. F. Izmaylov, J. Bloino, G. Zheng, J. L. Sonnenberg, M. Hada, M. Ehara, K. Toyota, R. Fukuda, J. Hasegawa, M. Ishida, T. Nakajima, Y. Honda, O. Kitao, H. Nakai, T. Vreven, J. A. Montgomery Jr., J. E. Peralta, F. Ogliaro, M. Bearpark, J. J. Heyd, E. Brothers, K. N. Kudin, V. N. Staroverov, R. Kobayashi, J. Normand, K. Raghavachari, A. Rendell, J. C. Burant, S. S. Iyengar, J. Tomasi, M. Cossi, N. Rega, J. M. Millam, M. Klene, J. E. Knox, J. B.

Cross, V. Bakken, C. Adamo, J. Jaramillo, R. Gomperts, R. E. Stratmann, O. Yazyev, A. J. Austin, R. Cammi, C. Pomelli, J. W. Ochterski, R. L. Martin, K. Morokuma, V. G. Zakrzewski, G. A. Voth, P. Salvador, J. J. Dannenberg, S. Dapprich, A. D. Daniels, . Farkas, J. B. Foresman, J. V Ortiz, J. Cioslowski, and D. J. Fox, "Gaussian09 Revision D.01, Gaussian Inc. Wallingford CT," Gaussian 09 Revis. C.01 Gaussian Inc., Wallingford CT (2010).

14. K. Choi, T. Hong, K. Ik Sim, T. Ha, B. Cheol Park, J. Hyuk Chung, S. Gyeong Cho, and J. Hoon Kim, "Reflection terahertz time-domain spectroscopy of RDX and HMX explosives," J. Appl. Phys. (2014).

15. M. A. Jarzembski, M. L. Norman, K. A. Fuller, V. Srivastava, and D. R. Cutten, "Complex refractive index of ammonium nitrate in the 2–20-μm spectral range," Appl. Opt. (2003).

16. M. van Exter, C. Fattinger, and D. Grischkowsky, "Terahertz time-domain spectroscopy of water vapor," Opt. Lett. **14**, 1128–1130 (1989).

17. D. Grischkowsky, S. Keiding, M. van Exter, and C. Fattinger, "Far-infrared time-domain spectroscopy with terahertz beams of dielectrics and semiconductors," J. Opt. Soc. Am. B **7**, 2006 (1990).

18. J. Liu, W. H. Fan, X. Chen, and J. Xie, "Identification of high explosive RDX using terahertz imaging and spectral fingerprints," in *Journal of Physics: Conference Series* (2016).

19. M. R. Leahy-Hoppa, M. J. Fitch, X. Zheng, L. M. Hayden, and R. Osiander, "Wideband terahertz spectroscopy of explosives," Chem. Phys. Lett. (2007).

20. P. F. Taday, I. V. Bradley, D. D. Arnone, and M. Pepper, "Using Terahertz pulse spectroscopy to study the crystalline structure of a drug: A case study of the polymorphs of ranitidine hydrochloride," J. Pharm. Sci. (2003).

21. B. M. Fischer, H. Helm, and P. U. Jepsen, "Chemical recognition with broadband THZ spectroscopy," Proc. IEEE **95**, 1592–1604 (2007).

22. B. M. Fischer, H. Helm, and P. U. Jepsen, "Chemical recognition with broadband THZ spectroscopy," in *Proceedings of the IEEE* (2007).

23. J. T. Kindt and C. A. Schmuttenmaer, "Far-infrared dielectric properties of polar liquids probed by femtosecond terahertz pulse spectroscopy," J. Phys. Chem. (1996).

24. J. E. Pedersen and S. R. Keiding, "Thz Time-Domain Spectroscopy of Nonpolar Liquids," IEEE J. Quantum Electron. (1992).

25. C. Rønne, L. Thrane, P. O. Åstrand, A. Wallqvist, K. V. Mikkelsen, and S. R. Keiding, "Investigation of the temperature dependence of dielectric relaxation in liquid water by THz reflection spectroscopy and molecular dynamics simulation," J. Chem. Phys. (1997).

26. G. Winnewisser, "Spectroscopy in the terahertz region," Vib. Spectrosc. **8**, 241–253 (1995).

27. C. H. Townes and A. L. Schawlow, *Microwave Spectroscopy*, Dover Books on Physics (Dover Publications, 1975).

28. R. A. Cheville and D. Grischkowsky, "Time domain terahertz impulse ranging studies,"

Appl. Phys. Lett. (1995).

29. H. Harde, S. Keiding, and D. Grischkowsky, "THz commensurate echoes: Periodic rephasing of molecular transitions in free-induction decay," Phys. Rev. Lett. (1991).
30. H. Harde, R. A. Cheville, and D. Grischkowsky, "Terahertz studies of collision-broadened rotational lines," J. Phys. Chem. A (1997).
31. H. Harde, N. Katzenellenbogen, and D. Grischkowsky, "Terahertz coherent transients from methyl chloride vapor," J. Opt. Soc. Am. B (1994).
32. H. Harde, J. Zhao, M. Wolff, R. A. Cheville, and D. Grischkowsky, "THz time-domain spectroscopy on ammonia," J. Phys. Chem. A (2001).
33. R. P. Singh, R. D. Verma, D. T. Meshri, and J. M. Shreeve, "Energetic nitrogen-rich salts and ionic liquids," Angew. Chemie - Int. Ed. (2006).
34. D. Srinivas, V. D. Ghule, and K. Muralidharan, "Synthesis of nitrogen-rich imidazole, 1,2,4-triazole and tetrazole-based compounds," RSC Adv. (2014).
35. J. Tian, H. Xiong, Q. Lin, G. Cheng, and H. Yang, "Energetic compounds featuring bi(1,3,4-oxadiazole): a new family of insensitive energetic materials," New J. Chem. (2017).
36. L. Yet, "Five-Membered Ring Systems: With More than One N Atom," in *Progress in Heterocyclic Chemistry* (2020).
37. L. Yet, "Five-Membered Ring Systems: With More than One N Atom," in *Progress in Heterocyclic Chemistry* (2012).
38. J. Heppekausen, T. M. Klapötke, and S. M. Sproll, "Synthesis of Functionalized Tetrazenes as Energetic Compounds," J. Org. Chem. **74**, 2460–2466 (2009).
39. N. Kommu, A. S. Kumar, J. Raveendra, V. D. Ghule, and A. K. Sahoo, "Synthesis, Characterization, and Energetic Studies of Polynitro Aryl-1,2,3-2H-Triazoles," Asian J. Org. Chem. (2016).
40. A. S. Kumar, N. Kommu, V. D. Ghule, and A. K. Sahoo, "Synthesis of trifluoromethyl-substituted N-aryl-poly-1{,}2{,}3-triazole derivatives," J. Mater. Chem. A **2**, 7917–7926 (2014).
41. A. S. Kumar, V. D. Ghule, S. Subrahmanyam, and A. K. Sahoo, "Synthesis of thermally stable energetic 1,2,3-triazole derivatives," Chem. - A Eur. J. (2013).
42. *High Energy Density Materials* (2007).
43. T. M. Klapötke and C. M. Sabaté, "Bistetrazoles: Nitrogen-rich, high-performing, insensitive energetic compounds," Chem. Mater. (2008).
44. N. Kommu, M. Balaraju, V. D. Ghule, and A. K. Sahoo, "Synthetic manifestation of nitro substituted tetrazole-N-(hetero)aryl derivatives and energetic studies," J. Mater. Chem. A **5**, 7366–7371 (2017).
45. *The Immune Response to Implanted Materials and Devices* (2017).
46. M. Sućeska, "Calculation of Detonation Parameters by EXPLO5 Computer Program,"

Mater. Sci. Forum **465**–**466**, 325–330 (2004).

47. P. Yin, J. Zhang, C. He, D. A. Parrish, and J. M. Shreeve, "Polynitro-substituted pyrazoles and triazoles as potential energetic materials and oxidizers," J. Mater. Chem. A (2014).

48. S. Baroni, S. De Gironcoli, A. Dal Corso, and P. Giannozzi, "Phonons and related crystal properties from density-functional perturbation theory," Rev. Mod. Phys. (2001).

49. Ruishu-Feng, Weiwei-Li, Qingli-Zhou, Kaijun-Mu, Liangliang-Zhang, and Cunlin-Zhang, "Terahertz spectroscopic investigations of explosives and the related compounds," Proc. SPIE - Int. Soc. Opt. Eng. **7158**, 1–9 (2009).

50. M. Hangyo, T. Nagashima, and S. Nashima, "Spectroscopy by pulsed terahertz radiation," Meas. Sci. Technol. **13**, 1727–1738 (2002).

51. Z. Tianyao, Z. Zhaohui, Z. Xiaoyan, Z. Han, Y. Fang, W. Fangming, and W. Bingfang, "Time-domain data truncation method for improving terahertz absorption spectrum reproducibility," in *IRMMW-THz 2015 - 40th International Conference on Infrared, Millimeter, and Terahertz Waves* (2015).

CHAPTER 5 : Temperature-Dependent Terahertz Spectroscopy of Explosives

This chapter reports the temperature dependent time domain terahertz spectroscopy(TDS) of the premium aqua-soluble and plastic explosives RDX, TNT, and NH_4NO_3, between 0.1 to 2.2 THz range. The temperature dependent spectroscopic study was carried out between 30°C and 200°C in a specially designed oven. The signature peaks of TNT and RDX present at 1.60 and 0.82 THz, shown significant redshift, whereas the NH_4NO_3 molecule shows a relatively small shift. The observed high-temperature-based redshift phenomenon is just the opposite to the blue shift reported at low(cryogenic) temperatures. In addition, the temperature-dependent absorption coefficient data of these molecules support the change in the concentration of the NO_2 molecule which is inconsistent with our group reported based on photoacoustic spectroscopy. The temperature dependent refractive indices of these molecules between 0.1 and 2.2 THz were calculated. Finally, to understand the sensitivity of the spectrometer signature peak of RDX with respect to the decrease in the weight concentration of RDX in the Teflon matrix was studied at 0.82 THz.

Part of this chapter's work has been published as following journal article.

Temperature-dependent terahertz spectroscopy and refractive index measurements of aqua-soluble and plastic explosives. Applied Optics, *Vol. 57, Issue 29, pp. 8743-8750 (2018*

Damarla Ganesh, Mottamchetty Venkatesh, and **Anil K. Chaudhary***

5.1 Explosives detection technique and challenges

Over the past few decades, antinational group attacks have been substantially increased in all over the world. Anthrax power hidden in the envelop, IED based mixtures, bombs, plastic, ceramic, weapons threaten people's daily life. The counter-terrorist has become an essential goal for every country. So, quick identification and detection are required. A wide variety of methods available for detection of explosives and their related compounds in a security context. These are basically classified into two categories **1.** Bulk detection systems for example: X-ray imaging, to locate high quantities of explosive materials. **2**. Trace level detection systems: particles or vapours of explosive molecules detected with corresponding signature peaks. Nevertheless, research regarding the new technologies that could identify as well as classify the explosive materials. Number of available spectroscopy techniques for explosives identification lies in mid-infrared, and optical bands [1]. But THz based sensing technology has got a lot of added advantages as compared to other existing techniques for explosive detection. THz spectroscopy technique has been developed in the field of sensing and imaging of biological, chemical, and other interdisciplinary research [2–4]. Many polar solid, liquids, gases, and explosive molecules possess signature peaks in the reflected and transmission THz spectral range [5,6]. In addition, THz spectroscopy provides information about weak vibrational modes which cannot be obtained by other means of spectroscopic technique. Terahertz radiation is non-invasive and have no health risk to the system's operator or to a suspect being scanned. Many explosives molecules such as TNT, RDX, HMX Cl20, and PETN etc. and drugs (methamphetamine) possess distinguishing spectra in the THz range that could be discernible from other substances such as packing human skin, coins and clothing [7–11].

A good numbers of study have been carried on explosive identification using the THz technology. Y. C. Shen et al. (2005) [12] reported a spectroscopic imaging method to identify explosives [13,14]. Y. Hu et al., Jian Chen et al. [15,16] reported the absorption coefficients of stranded explosives. A theoretical explanation of spectroscopic approach to RDX given by Damian G. Allis et al. [17]. A competitive study of THz spectroscopy and Raman spectroscopy was carried by A. D. Burnett et al. Joseph S [5,18]. In case of Ammonium nitrate, only few groups have reported their studies between 0.1 -3 THz. Khachatrian et al. have reported the sharp rotational vibrational features, Chen et al. reported some distinguishing weak spectral features of NH_4NO_3 between 0.1 and 3 THz at ambient temperature [15,19]. Melinger and Grischkowsky studied the low temperature vibration modes of TNT, RDX. They reported the

presence of several new peaks by lowering the temperature [20]. This study indicates the effect of temperature on absorption peaks. High temperature THz spectroscopy of n-alkanes was studied by Jonathan P [21]. The THz transmission spectrum of n-tridecane ($C_{13}H_{28}$) till 80 ^{0}C was described. However, to the best of our knowledge there is no such study carried out to understand the high temperature effect on THz transmission behaviour of Explosives and corresponding shifts in the absorption peaks, and varaition in the refractive index. High Temperature study of explosive provides the information about stability of the explosives. In case of trace level detection of explosives laboratory environmental conditions never matches with real time circumstances. The nature of the traces samples obtained after explosion is not same as unexploded as it has gone through high temperature and pressure. The effect of temperature on THz absorption signature is discussed in section 5.4.

The present chapter includes THz spectroscopy of some common explosive materials such as Ammonium Nitrate (AN), 2,4,6-trinitrotoluene (TNT) and,1,3,5-trinitroperhydro-1,3,5-triazine (RDX). AN and RDX are available in white crystalline powder form. AN is an easily available, fertilizer and a hygroscopic compound, shows an extremely high absorption in the THz frequency range. Whereas TNT is an yellow coloured amorphous compound. RDX and TNT are stable and most powerful explosives have large number of military and propellants applications. RDX molecule is a six-membered heterocyclic ring comprising of three nitrogen and three methylene groups, with a nitrite group attached to each of the nitrogen atoms in the ring. This high oxygen and nitrogen content makes RDX a powerful plastic explosive. On the other hand, TNT is a cyclic aromatic compound. However, ammonium nitrate consists of high proportion of oxygen and nitrogen for its weight. Thus it can act as an excellent oxidizer for other compounds and can itself act as an explosive. Although THz spectroscopy would be unable to quantify the ammonium nitrate chemically, its high absorption peaks could plausibly enable it to be located in a THz frequency image.

5.2 Effect of Temperature on THz spectroscopic absorption signatures

Due to variation in temperature may cause shift in frequency towards the lower or higher sides of frequency. The shift that occurs towards the high frequency side is called the “blue shift” whereas the shift towards low frequency is known as the “redshift”. The decrease in the temperate is responsible for the compression of lattice resulting the sharpening of intermolecular potential. At low temperatures due to high interaction weak factors such as van der Waals (vdW)

forces and hydrogen bonding play key role in the red shift of the peaks. It is possible that incorporation of vdW interactions lower the symmetry of the crystal and generates additional low frequency modes that are missing at ambient temperature. On the other hand, high temperature based study of THz bands attributed to various other mechanisms including intramolecular vibrations and collisional effects, etc. At higher temperature, due to thermal expiation the population of molecules are mere in higher vibrational excited states increases, as a result, there is a decreased energy spacing resulting the overall absorption envelope being shifted to lower frequency. Understanding of high temperature frequency vibrational modes and their behaviour in different environments provides a new insight in terms of adjacent binders are very important for detection of explosives. It is also important to note that participation of different intact functional groups at the time of heating. In our earlier work we carried out this proses studied in vapor form between 40 °C and 350 °C using a UV–visible wavelength based pulsed photoacoustic technique. This chapter describes the spectral features of HEMs, and the results have found good agreement with reported literature values. In addition, the study clearly confirms the release of NO_2 molecules just above 40 °C, which also supported by our previous studies on the number of explosive molecules. The study was based on the recording of strong vibronic transitions of NO_2 molecules between 30 °C and 350 °C using a pulsed photoacoustic technique [22–24]. Here the attempt is made to develop a small quantity of explosive pellets using PTFE powder at room temperature and successfully recorded their characteristic signature.

5.3 Experiment details

The experiment was carried out in two steps. In the first step the explosive pellets in the PTFE matrix were prepared, and in the second step, these pellets were subjected to the THz system for the recording of temperature-dependent time domain spectra. Sample preparation is an important factor for the recording of a characteristic signature. A pure explosive sample in powder form was mixed with PTFE powder, which has very low absorption in the THz range. An explosive sample weighing around 200 mg was mixed with 800 mg of PTFE powder using 10 ml of CH_3OH solvent. The mixture was dried for 20 min and then ground with mortar to produce a fine homogenous powder. The powder mixture was divided into two halves and transferred to the die using butter paper, and then was pressed with 2 tons of pressure to prepare a pellet. The thickness and diameter of the pellets are ~2 mm and 12 mm, respectively. The THz wavelength matches the size of the sample present in the pellets, which is responsible for the inhomogeneous broadening of the spectral peaks due to the scattering effect. Moreover,

scattering in THz spectra is caused by the refractive index mismatch between the sample crystals and the surrounding pellet medium. However, the effect of scattering due to the multiple crystalline nature of the samples can be overcome by dissolving the mixture in methanol solution. We also mixed different proportions of the RDX sample in the PTFE matrix to record the weight-percentage-based signature peak. The pure PTFE pellet was used as a reference. The THz absorption spectroscopy of explosive molecules was carried out in a specially designed small-sized oven that can accommodate the pellets inserted between two parabolic mirrors. The oven works on the Peltier heating principle and was supplied by Conversion Co. Ltd. (UK). We redesigned the hood of the oven to accommodate an explosive pellet with a 12 mm diameter. The temperature of the oven was controlled between 25 °C and 200 °C with a precision of 0.01 ^{o}C using a temperature controller supplied by the same company. The spectrometer experimental arrangement parameters are same as discussed in chapter (2).

5.4 Results and discussion

Figure 5.1 (a) and (b) show the temporal and frequency domain spectral profiles of air, PTFE, and the explosives in the THz range after passing through the pellet. It is observed that the THz pulse shows a variation in delay time after passing through different explosives. It is attributed to the change in the optical path length of radiation, which varies from sample to sample due to the change in the refractive index of the molecules. The spectral intensity clearly shows the variation in the intensity and the shift in the absorption peaks of explosive molecules. The experiment was performed in ambient room temperature. The dynamic range of the amplitude of spectral lines lies between 10^{-4} and 10^{-7}on a log scale which helps us record the weak absorption peaks of the explosive molecules.

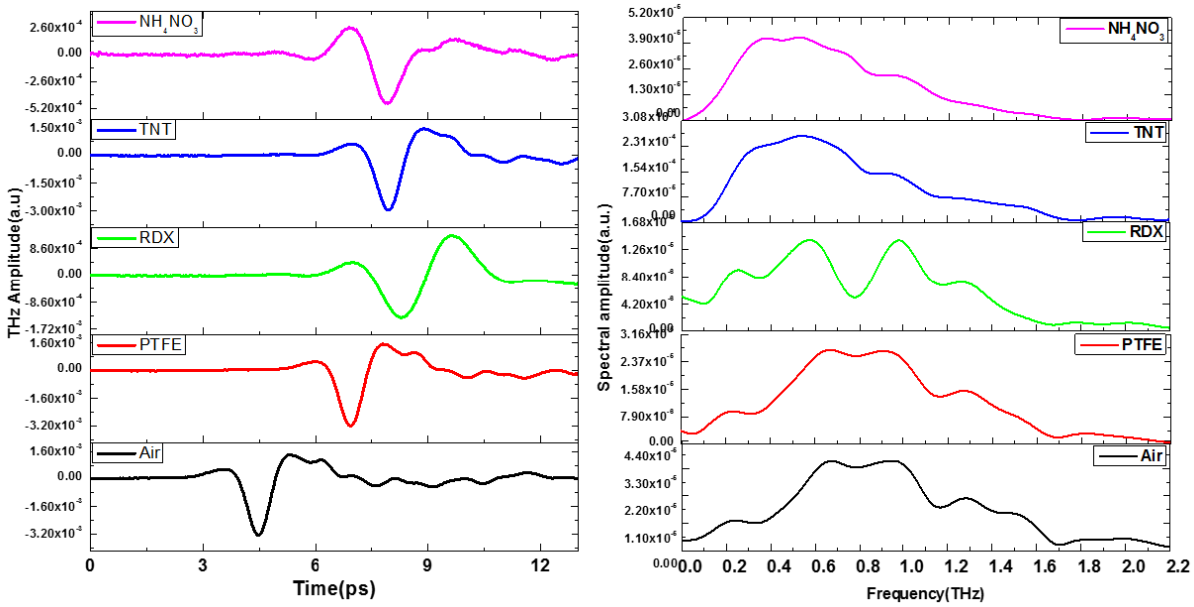

Figure 5.1. Schematic THs spectrum. (a) Temporal profile of THz pulse, (b) frequency domain spectra of different explosives

The water soluble compound NH_4NO_3 has a high absorption coefficient compared to the aqua-insoluble explosives. However, RDX has a significant characteristic absorption peak at 0.82 THz, which agrees well with the reported work. All the samples show a common feature near 1.8 THz. The absorption peak is attributed to the intermolecular vibrational modes present in the THz region. The corresponding THz absorption peaks for NH_4NO_3 present at 98.15, 108.5, and 143.7 cm^{-1} are 0.87, 1.5, and 1.81 THz, respectively. All the above mentioned studies were carried out with 100 mg of explosive sample mixed with 400 mg of PTFE matrix. We also made an attempt to study the effect of weight percentage on the signature peak of the explosive sample. Therefore, pellets with different weight concentrations of RDX such as 50, 30, and 10 mg, were prepared in the PTFE matrix. The thickness and size of the pellets were controlled by adding the same weight percentage of PTFE powder into the mixture. As a result, the total weight of the pellet matrix always remains 500 mg. The time domain spectra of different weight percentage pellets were recorded, and their corresponding absorption coefficient data were ascertained and compared with the reported values available in the literature [17]. Figure 5.2 shows the drop in the value of the absorption coefficient with a decreasing concentration of RDX in PTFE matrix at 0.81 THz. This also indicates the minimum detection limit of RDX in solid form.

5.1.1 Temperature-Dependent Absorption Spectra and Refractive Index of RDX

The recording of absorption bands in the THz region is also affected by the presence of water vapor. Consequently, many of the characteristic bands are either not visible or have low intensity. The temperature-dependent spectroscopy of molecules plays a very important role in revealing significant information about many weak vibrational modes that are not observable at room temperature. In addition, it helps excite the molecules at the ground state, which is also reflected in the coupling of oscillating modes in terms of redshift. In this section we discuss the temperature-dependent THz spectra of RDX, TNT, and NH_4NO_3 molecules in solid form. The spectra are recorded below their melting point. Shen et al., Hangyo et al., and Azad et al. reported the temperature dependent spectroscopic study at low temperature and identified the behaviour of signature peaks of RDX present at 0.82, 1.05, 1.50, and 1.96 THz.

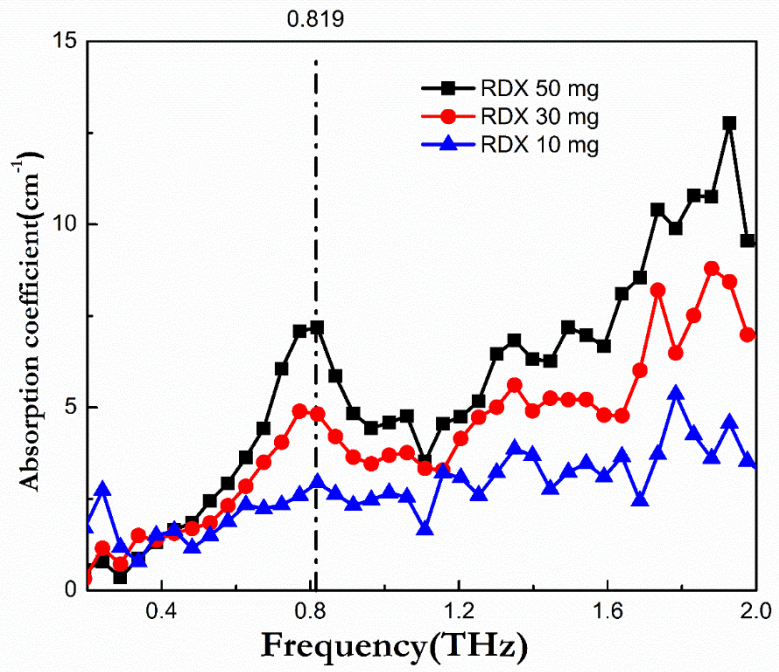

Figure 5.2. Absorption coefficients of RDX for different weight concentrations

Figure 5.3 (a) shows the temperature-dependent absorption coefficients of RDX in PTFE matrix recorded between 30 °C and 170 °C. The characteristic band present at 0.8 THz has sharp features between 30 °C and 90 °C. This can be attributed to the presence of the NO_2 group. The absorption coefficient at room temperature is 11 cm^{-1}, which decreases with increasing sample temperature. In addition, the shape of the absorption peak between 30 °C and 90 °C shows a broadening effect at 105 °C.

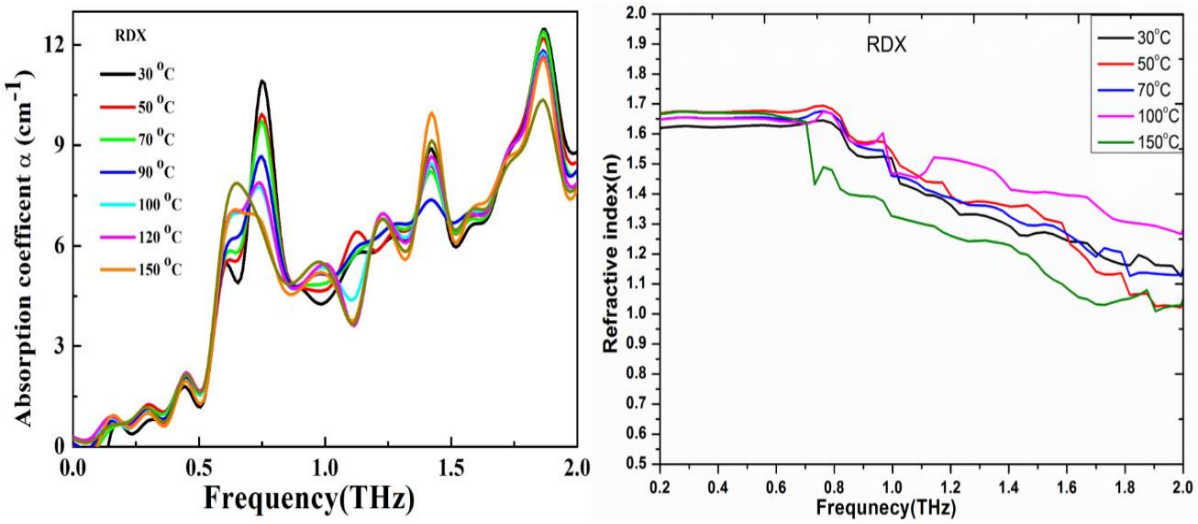

Figure 5.3. (a) Temperature-dependent absorption coefficient of RDX, (b) temperature-dependent refractive index of RDX.

This reveals the process of vaporization of water molecules and the release of NO_2 gas, which also indicates the initiation of the process of thermal decomposition of RDX. The decrease in the absorption coefficient value of the 0.8 THz peak is directly linked to the loss of NO_2 from the solid sample [25,26]. In our previous reports, we have successfully demonstrated the release of NO_2 from different explosives above 40 °C, using a pulsed photoacoustic technique. The previous study was performed in vapor using 532 and 266 nm wavelengths of a Q-switched Nd:YAG laser. The NO_2 gas release mechanism is based on a strong electronic transition and is attributed to vibronic modes of NO_2 [27]. However, the present results once again support our earlier findings in the THz domain. Further, an increase in the temperature between 120 °C and 170°C enhances the broadening of the peak width and shows some shift toward 0.62 THz, which is nothing but the redshift effect due to heating. Similarly, the peak at 1.05 THz has a small amplitude and appears in the form of a dip at room temperature. However, after crossing 105 °C, the dip is modified and converted into a hump at 120 °C. This is attributed to the hot band effect, where the weak signature peak was invisible due to water molecules. A similar type of effect is also observed at 1.4 THz. However, this peak shows the reverse trend. The absorption coefficient between 30 °C and 105 °C is lower than the absorption coefficient at 150 °C. Figure 5.3(b) shows the temperature-dependent refractive index of RDX. The refractive index was recorded between 30°C and 150°C, and it is clear that there is little variation in the refractive index up to 0.7 THz. The value of the refractive index remains constant between 1.6 and 1.65. However, after 0.7 THz there is a sharp decline in the value of the refractive index with respect to temperature, and it decreases from 1.7 to 2.0 THz. Similar types of changes are also visible in the absorption coefficient data at 0.7 THz.

5.1.2 Temperature-Dependent Absorption Spectra and Refractive Index of TNT

Figure 5.4(a) shows the temperature-dependent spectrum of TNT, which was recorded between 30 °C and 70 °C below its melting point, i.e., 80.35 °C. For TNT, characteristic absorption peaks are present at 1.6 THz and 2.17 THz [26]. One can easily see that the peak at 30 °C has a higher absorption coefficient i.e. around 7.4 cm^{-1} that decreases to 6 cm^{-1} at 50 °C and almost becomes 4.85 at 70 °C. After crossing this temperature, the peak shows an unusual reverse trend. It also indicates the process of initiation of a slow release of NO_2 from the solid sample. Similarly,

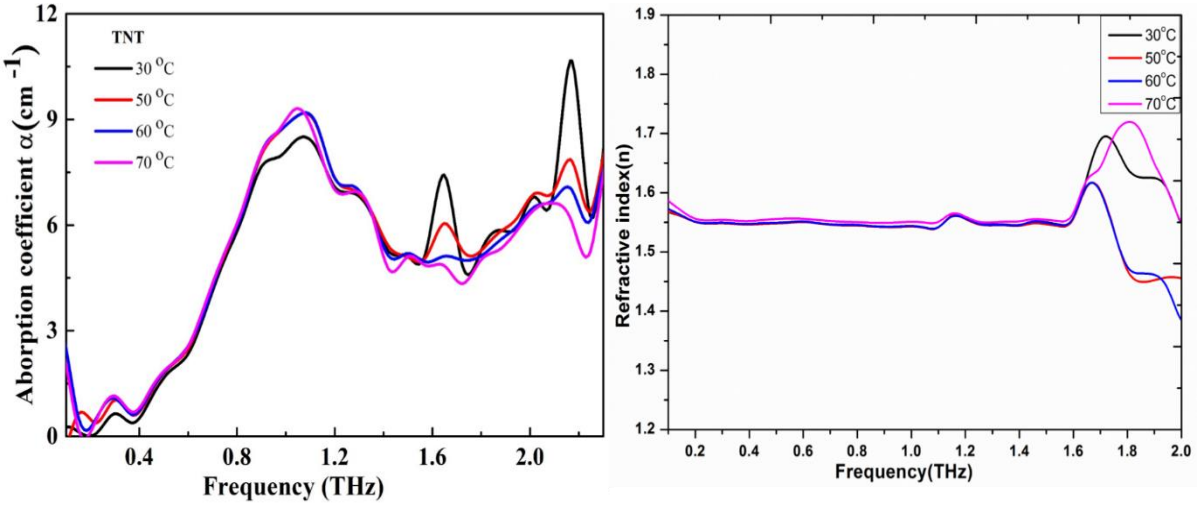

Figure 5.4. (a) Temperature-dependent absorption coefficient of TNT, (b) temperature-dependent refractive index of TNT.

the absorption coefficient of the 2.17 THz peak is 10.65 cm^{-1}, which becomes 7.8 cm^{-1} at 50°C and 6.62 cm^{-1} at 70 °C. The decreasing trend of the absorption coefficient with respect to temperature also appears in the form of a redshift toward the left side at 70 °C. This redshift effect is due to a hot band transition peak at 2.2 THz, which has a higher value at 30 °C. Therefore, the temperature-based recording of signature peaks reflects the process of thermal loss of TNT molecules at high temperatures. In addition, temperature based spectroscopy confirms the presence of some prominent signature peaks in a repeated manner, along with redshift. Two signature peaks are located at 1.77 and 2.17 THz at 30 °C that get shifted to 1.722 and 2.097 THz at 70 °C, respectively. Figure 5.4(b) shows the temperature-dependent refractive index of TNT. The refractive index was recorded between 30 °C and 70 °C, and it is clear that there is very little variation in the refractive index up to 1.6 THz. The value of the refractive index between 30 °C and 70 °C almost overlaps and remains between 1.55 and 1.60. However,

after 1.6 THz it shows great variation between 1.55 and 1.75. Similar types of changes are also visible in absorption coefficient data at 1.6 THz.

5.1.3 Temperature-Dependent Absorption Spectra and Refractive Index of NH4NO3

Figure 5.5(a) shows the temperature-dependent absorption spectra of NH_4NO_3. The frequency spectra clearly show the presence of a weak signature at room temperature. An earlier reported study of NH_4NO_3 was carried out at low temperature and demonstrated the conversion of the absorption peak into a kinkat et.al 1.7 THz [28,29]. However, when NH_4NO_3 is mixed with PTFE, it starts showing a strong signature even at room temperature. The absorption peaks at 1.2 and 1.4 THz are weaker than the peak at1.78. It also shows a maximum intensity peak at 105°C below the melting point of NH_4NO_3. Figure 5.5 (a) shows the absorption spectrum of NH_4HO_3 recorded between 30 °C and 150 °C at 0.1–2.0 THz.

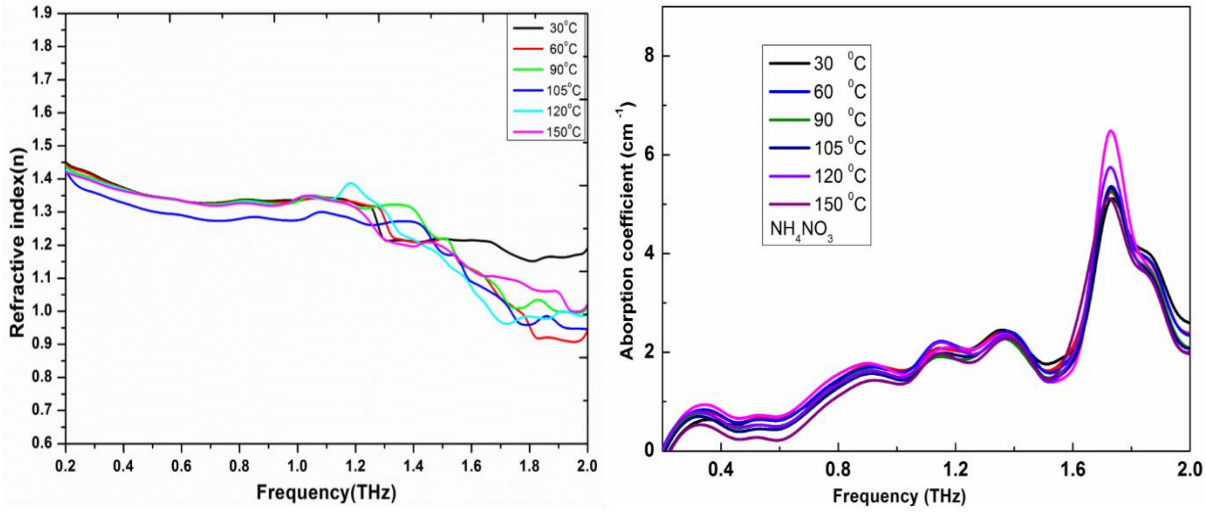

Figure 5.5. (a) Temperature-dependent absorption coefficient of NH_4NO_3, (b) temperature-dependent refractive index of NH_4NO_3.

To the best of our knowledge, it is the first demonstration of a signature peak of NH_4HO_3 at 1.73 THz. At room temperature, i.e., 30 °C, it has an absorption coefficient of the order of 5.69 cm^{-1}. Since the spectra are recorded in transmission mode, these signature peaks are visible. Further, the effect of a redshift is also visible at 1.78 THz. The value of the absorption coefficient is of the order of 5.27 cm^{-1} between 60 °C and 90 °C. It is further shifted toward 1.72 THz with a corresponding absorption coefficient of 5.05 cm^{-1} between 120 °C and 150 °C, respectively. The NH_4NO_3 is a very stable inorganic aqua molecule due to ionic bonds. Therefore, it does not show a similar type of decomposition behaviour and strong absorption

like RDX and TNT. As a result, the redshift effect is not very prominent. Figure 5.5(b) shows the temperature-dependent refractive index of NH_4NO_3. The refractive index is recorded between 30 °C and 150 °C, and it is clear that little variation exists in the refractive index up to 1.3 THz. The value of the refractive index remains between 1.42 and 1.40. However, after 1.3 THz the value of the refractive index shows a fall with respect to temperature and decreases from 1.4 to 1.0. Similar types of changes are also visible in the absorption coefficient data at 1.3 and 1.6 THz.

5.5 Sensitivity and detection limitations

We have comprised the signal sensitivity and absorption coefficients of three explosives in table 5-1.

Table 5-1 Physical and optical properties of explosive samples in THz domain

S. No	Sample name	Thickness of the pellet (mm)	THz peak value (a.u.)	Absorption coefficient (cm^{-1}) @room temperature
1	RDX	1.91	1.83×10^{-4}	11.2
2	TNT	1.97	3.4×10^{-4}	9.98
3	NH_4NO_3	2.1	1.73×10^{-5}	5.67

It is evident from the table that absorption coefficient is the material dependent property and RDX possess highest value. A 10 mg of RDX in Teflon quantity shows property 5 cm^{-1} absorption coefficient value [30]. Further improvisation is need to reduce the quantity of the sample. In present experiment the THz beam spot size was 6 mm. Therefore, by selecting suitable parabolic mirrors the spot size was reduced of the order of 2.0 mm which will also helped us to reduce the pallet diameter of the order of 2.0 mm and enhance the detection sensitivity. Similarly, temperature based study also help to understand the thermal decomposition and redshift behavior of the explosive molecules which varies from sample to sample. Finally, temperature dependent theoretical model needs to be developed to understand the vibronic and rotational transition behavior of these molecules under THz region. Because existing DFT calculations are based at 0 ^oK.

5.6 Concealed detection of explosives

As discussed in the previous sections, detection of explosives in a concealed condition is a challenging task for the homeland security. THz radiation is preferred for qualitative

identification of explosive under concealed condition because of its non-invasive nature. We have made an attempt to detect RDX in the suitcase. The RDX sample was kept inside the box as shown (red circle) in the Figure 5.6. The box was placed in between the parabolic mirrors to focus the generated THz on to the sample. Initially The reference spectrum of box without sample was recorded which was followed by scan of sample. Figure 5.7a depicts the temporal profiles of box with and without sample. However, the allowed to box transmit up to 1.6 THz only. Figure 5.7 (c, d) reagents the characteristic adoption peak of RDX at 0.8 THz and refractive index 1.5 respectively. This shows the capability of time domain THz technique to detect the explosives under concealed conditions.

Figure 5.6. Suitcase used in coneled detection (red circile indicates the sample postion)

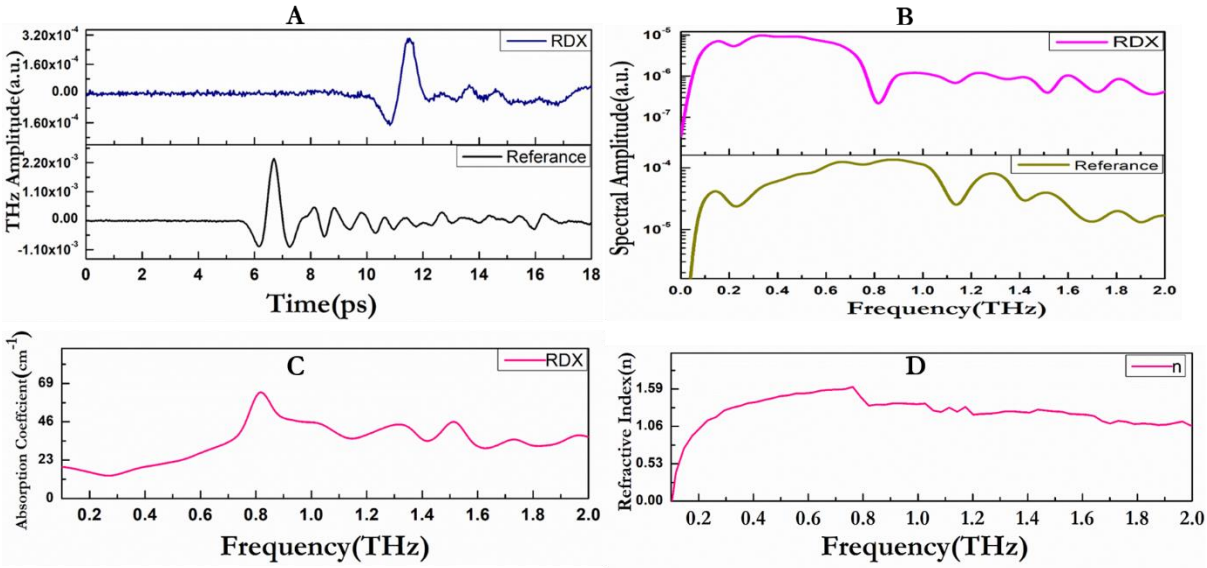

Figure 5.7. a) Temporal profiles of reference box and with RDX. b) Frequency domain spectra c) Absorption coefficient d) Refractive Index

5.7 Conclusions

We have successfully recorded the temperature dependent refractive indices and absorption coefficients of NH_4NO_3, TNT and RDX explosives below their melting points. Also, demonstrated the temperature dependent red-shift effect in these molecules. To the best of our knowledge this is the first demonstration of red shift effect and process of slow thermal decomposition mechanisms of these explosives in THz domain. It also helps to characterize the explosive molecules. In addition, the effect of change on the strength of THz signal of RDX in PTFE (Teflon) matrix is with respect to the concentration. Also a successful attempt was made to record the signature spectrum of RDX explosive sample under concealed condition.

5.8 References

1. D. L. Monts, J. P. Singh, and G. M. Boudreaux, "Laser- and Optical-Based Techniques for the Detection of Explosives," Encycl. Anal. Chem. (2006).
2. M. Tonouchi, "Cutting-edge terahertz technology," Nat. Photonics **1**, 97–105 (2007).
3. D. J. Funk, F. Calgaro, R. D. Averitt, M. L. T. Asaki, and A. J. Taylor, "THz Transmission Spectroscopy and Imaging: Application to the Energetic Materials PBX 9501 and PBX 9502," Appl. Spectrosc. **58**, 428–431 (2004).
4. J. A. Zeitler, K. Kogermann, J. Rantanen, T. Rades, P. F. Taday, M. Pepper, J. Aaltonen, and C. J. Strachan, "Drug hydrate systems and dehydration processes studied by terahertz pulsed spectroscopy," Int. J. Pharm. (2007).
5. A. G. Davies, A. D. Burnett, W. Fan, E. H. Linfield, and J. E. Cunningham, "Terahertz spectroscopy of explosives and drugs," Mater. Today **11**, 18–26 (2008).
6. P. Jepsen and B. Fischer, "Dynamic range in terahertz time-domain transmission and reflection spectroscopy," Opt. Lett. **30**, 29 (2005).
7. M. R. Leahy-Hoppa, M. J. Fitch, X. Zheng, L. M. Hayden, and R. Osiander, "Wideband terahertz spectroscopy of explosives," Chem. Phys. Lett. (2007).
8. K. Choi, T. Hong, K. Ik Sim, T. Ha, B. Cheol Park, J. Hyuk Chung, S. Gyeong Cho, and J. Hoon Kim, "Reflection terahertz time-domain spectroscopy of RDX and HMX explosives," J. Appl. Phys. (2014).
9. A. G. Davies, A. D. Burnett, W. Fan, E. H. Linfield, and J. E. Cunningham, "Terahertz spectroscopy of explosives and drugs," Mater. Today (2008).
10. Y. Sonawane, O. Joshi, and M. Wagh, "Terahertz technology: A boon to tablet analysis," Indian J. Pharm. Sci. **71**, 235 (2009).
11. Y. Shen, P. F. Taday, and M. C. Kemp, "Terahertz spectroscopy of explosive materials," in *Passive Millimetre-Wave and Terahertz Imaging and Technology* (2004).
12. Y. C. Shen, T. Lo, P. F. Taday, B. E. Cole, W. R. Tribe, and M. C. Kemp, "Detection and identification of explosives using terahertz pulsed spectroscopic imaging," Appl. Phys. Lett. **86**, 1–3 (2005).
13. J. Liu, W. H. Fan, X. Chen, and J. Xie, "Identification of high explosive RDX using terahertz imaging and spectral fingerprints," in *Journal of Physics: Conference Series* (2016).
14. Z. H. Michalopoulou, S. Mukherjee, Y. L. Hor, K. Su, Z. Liu, R. B. Barat, D. E. Gary, and J. F. Federici, "RDX detection with THz spectroscopy," J. Infrared, Millimeter, Terahertz Waves (2010).
15. J. Chen, Y. Chen, H. Zhao, G. J. Bastiaans, and X.-C. Zhang, "Absorption coefficients of selected explosives and related compounds in the range of 0.1-2.8 THz.," Opt. Express **15**, 12060–12067 (2007).
16. X. C. Zhang and J. Xu, *Introduction to THz Wave Photonics* (2010).
17. D. G. Allis, J. A. Zeitler, P. F. Taday, and T. M. Korter, "Theoretical analysis of the solid-state terahertz spectrum of the high explosive RDX," Chem. Phys. Lett. (2008).
18. M. R. Leahy-Hoppa, J. Miragliotta, R. Osiander, J. Burnett, Y. Dikmelik, C. McEnnis,

and J. B. Spicer, "Ultrafast laser-based spectroscopy and sensing: Applications in LIBS, CARS, and THz spectroscopy," Sensors (2010).

19. A. Khachatrian, S. Qadri, and J. S. Melinger, "High resolution THz spectroscopy of ammonium nitrate and potassium nitrate crystalline films," 2011 Int. Conf. Infrared, Millimeter, Terahertz Waves 1–2 (2011).
20. J. S. Melinger, N. Laman, and D. Grischkowsky, "The underlying terahertz vibrational spectrum of explosives solids," Appl. Phys. Lett. **93**, 4–6 (2008).
21. J. P. Laib and D. M. Mittleman, "Temperature-dependent terahertz spectroscopy of liquid n-alkanes," J. Infrared, Millimeter, Terahertz Waves (2010).
22. A. K. Chaudhary, K. S. Rao, and A. Sudheer Kumar, "Study of thermal decomposition mechanisms and absorption cross section of nitro-rich phenyl- and bis-series 1,2,3-triazoles," Appl. Opt. **55**, 817–824 (2016).
23. K. S. Rao and A. K. Chaudhary, "Investigation of the thermal decomposition and stability of energetic 1,2,4-triazole derivatives using a UV laser based pulsed photoacoustic technique," RSC Adv. (2016).
24. F. Yehya, A. K. Chaudhary, D. Srinivas, and K. Muralidharan, "Study of thermal decomposition mechanisms and low-level detection of explosives using pulsed photoacoustic technique," Appl. Phys. B Lasers Opt. **121**, 193–202 (2015).
25. B. M. Fischer, H. Helm, and P. U. Jepsen, "Chemical recognition with broadband THZ spectroscopy," Proc. IEEE **95**, 1592–1604 (2007).
26. J. F. Federici, B. Schulkin, F. Huang, D. Gary, R. Barat, F. Oliveira, and D. Zimdars, "THz imaging and sensing for security applications - Explosives, weapons and drugs," Semicond. Sci. Technol. (2005).
27. F. Yehya and A. K. Chaudhary, "A novel investigation of the thermal decomposition mechanism of (MTNI) and (KNO2) using time resolved pulsed photoacoustic technique," Sensors Actuators, B Chem. **178**, 324–330 (2013).
28. R. T. Hall, D. Vrabec, and J. M. Dowling, "A high-resolution, far infrared double-beam lamellar grating interferometer.," Appl. Opt. **5**, 1147–58 (1966).
29. A. Sengupta, A. Bandyopadhyay, J. F. Federici, and R. B. Barat, "Study of Morphological Effects on Terahertz Spectra Using Ammonium Nitrate," in *Optical Terahertz Science and Technology* (Optical Society of America, 2005), p. ME6.
30. R. M. Doherty and D. S. Watt, "Relationship between RDX properties and sensitivity," in *Propellants, Explosives, Pyrotechnics* (2008), Vol. 33, pp. 4–13.

CHAPTER 6 : Designing and Fabrication of Bandpass Filters in THz Region

Designing and fabrication of bandpass filter in THz domain play important role in advancement of optics in significant applications such as spectroscopy, Imaging, sensing, communication etc. In this chapter we have discussed two types of terahertz bandpass filters of free standing and metal on a dielectric substrate operating at different frequencies were designed and fabricated. The simulation has been carried out using CST Microwave Studio. Free standing bandpass filters were realized by a metallic hole array sandwiched between two polyamide layers. Metal on a dielectric substrate based bandpass filters are achieved by coating aluminum layer on silicon substrate. The filters were fabricated using UV lithography technique on a 0.05mm thick Silicon substrate over a 1 cm² area on which the unit cell in the pattern of aluminum hole array was coated by the method of physical vapor deposition technique. The obtained results show about 80% transmission. After successful characterization of these filters were used for sensing of high energy molecules. High energy molecules were drop casted on hole array and recoded the shift in the THz resonance peaks which can be used for sensing applications. This study helps to designing of low-cost bandpass THz filters, the performance of theses filters are compared with commercially available filters.

A theme of technical details in more elaborated form is published in

Ultra-thin subwavelength film sensing through the excitation of dark modes in THz metasurfaces

Sabyasachi Banerjee, C.S. Amith, Deepak Kumar, **Ganesh Damarla, Anil Kumar Chaudhary**, Sanket Goel, Bishnu P. Pal, Dibakar Roy Chowdhury, *Optics Communications 453 (2019) 124366*,

6.1 THz bandpass Filters

Terahertz bandpass filters are the surface modified periodic structure which provide the sharp plasmonics resonances at a given frequency. These resonances can be broadened, tuned and shifted by changing the parameters like periodicity, shape, thickness etc. majority of the bandpass filters designed in THz region based on patterning of subwavelength structures of metal film on different dielectric substrates. R. Mendis et.al, reported the manufacture a Universal tunable THz filters using dispersive media which can filter out from broadband THz pulses [1–4]. These filters work on the principle of traditional Extraordinary Optical Transmission(EOT). In EOT, certain frequencies pass through the filter whose wavelengths beyond the classically allowed. The corresponding frequencies depend on periodicity of hole array and other factors such as thickness of the metals, dielectric constant of metal, shape of the hole, hole diameter.

6.1.1 Extraordinary Optical Transmission

It is a well-known fact that when size of aperture is of the order of the wavelength of incident aperture diffraction occurs and this concept studied by Thomas Young, Jean Fresnel in 19th century [5,6]. In 1944 Hans Bethe found that transmission through a circular hole can be normalized to area of perforated thin metallic plate is given by

$$T \approx \frac{64}{27\pi^2}\left(\frac{r}{\lambda}\right)^4 \quad (1)$$

Where "r" is the radius of the circular hole, "λ" being the incident light wavelength. It was surprising to note that most of the theories at that time states it is proportional to square of ratio of the radius to wavelength i.e. $(r/\lambda)^2$ [7,8]. In 1988 T. W. Ebbesen opened a new channel with path breaking discovery in his publication entitled "Extraordinary Optical Transmission Through Sub-Wavelength Hole Arrays" [9,10]. He discovered that perforated metallic films with periodicity smaller than the hole exhibits great optical transmission for the frequencies where the hole size is lesser than the incident wavelength. It was understood that spectral positions of these structures are coincided with corresponding of surface plasmon polaritons (SPPs) modes. Later this relation between EOT and SPPs has been verified theoretically. It is extensively proven that the origin of EOT is due to the

excitation of those surface electromagnetic modes. When electromagnetic wave falls on metallic films it reflects off. When momentum matching condition satisfied between incident light and electrons of metals it would take couple to a Surface Plasmon Polariton (SPP) and propagates along metal dielectric interface, finally radiated out through coupling to the holes in the metal [11–13]. We know that metals consist of a "sea" of electrons which randomly move in all directions. A surface plasmon has oscillation of electrons present in the conduction band(CB) of a metal excited by the electric field of incident photons. Incident light directly cannot couple with surface modes [14,15]. The coupling can be accomplished by following ways i). Grating Coupler ii). ATR Prism coupler. iii). Subwavelength metallic hole arrays coupler [16]. EOT phenomenon has got enormous number of applications such as near-field microscopy, frequency selective surfaces, subwavelength lithography, surface enhanced Raman spectroscopy(SERS), etc.

6.1.2 Enhanced THz transmission and THz SPPs

Most EOT through subwavelength hole array has been carried out in optical region. Since in optical region material dielectric constant ($\boldsymbol{\varepsilon}$) the real part is more than that of imaginary part. But, in case of higher wavelength regime such as microwave and THz, imaginary part of $\boldsymbol{\varepsilon}$ dominates the real component i.e. $\left|\varepsilon_{real}/\varepsilon_{im}\right| << 1$ was believed to be the constraint to give EOT in this regime. However, Moreno *et. al.* reported the EOT in longer wavelength regime is often more in suitable surface modification on metallic surface. This corrugation of metallic surface leads to effective impedance which helps to couple surface Plasmon to couple with exited EM wave. Several research groups like D. Qu, H. Cao and A. Nahata, H. Cao and A. Agrawal, F. Miyamaru, and M. Hangyo reported subwavelength metallic hole arrays based enhanced transmission [17–20]. This enhancement is attributed to resonant excitation of SPP in THz region. The experimental results prove that significant dependence to hole shape on transmission magnitude [21]. In THz region dielectric properties of the metals tend to the perfect metallic properties which are also the reason for observation of certain characteristics that cannot be observed in optical region. Similarly, in THz region heavily doped semiconductors behave like a metal due to their dialectic constant $\boldsymbol{\varepsilon}_{real}$ has a negative value, so heavily doped semiconductors can be treated as metal to exhibit improved transmission in THz range. J. Gómez Rivas, C Janke and J. G. Rivas, C Janke, J. G. Rivas have demonstrated EOT through doped silicon hole array [22,23]. It was observed that enchantment in transmission is the function doping concentration and dielectric properties of the surrounding

material. Since semiconductors possess negative temperature coefficient, the change in the temperate leads to variation in the charge carrier concertation. This effect of temperature on trasmissin through hole array was studied by J. Gómez Rivas and P. Haring Bolivar, J. Gómez Rivas and C. Janke [24,25].

6.1.3 Surface Plasmon Polaritons (SPPs) and Dispersion relations

A Plasmon can be defined as quantum of the collective excitation of conduction band free electrons of a solid material. These electrons in metals are identical to molecules flowing in a liquid. In plasmonics the role of metal more significant than dielectric material [26]. The presence of the sea of electrons give a difference in both electrical properties as well as in optical properties. From Drude model the dielectric constant ε of metals is given by

$$\varepsilon_m(\omega) = 1 - \frac{\omega_p^2}{\omega(\omega + \gamma\omega)} \tag{2}$$

Where, ω_p is the bulk plasma frequency by $\omega_p = \sqrt{Ne^2/m_o}$, N is the density of electrons and γ is the rate of scattering of electrons. By ignoring the contribution from damping of the metal ($\gamma = 0$) it is evident that for $\omega > \omega_p$, the value light can transmit through the metal as the permittivity value is positive. This propagating mode, which basically originated due to coupling between bulk free electrons and photons, is known as the bulk plasmon polariton. Conversely for frequencies $\omega < \omega_p$ i.e. whose value is less than plasma frequency cannot propagate through the medium because of negative value of the dialectic constant. The propagation mode of electromagnetic radiation does not exist because of imaginary wave vector. But Ritchie theoretically proved that propagation of light is allowed on the surface in form of surface wave on the metal for the frequency between $\omega = 0$, $\omega = \omega_p/\sqrt{2}$. In general surface excitation of electromagnetic wave is the displacement and restoring of charge carriers, atoms causing the time varying polarization of magnetization. The displaced charges create electromagnetic field on the surface of metal [27,28].

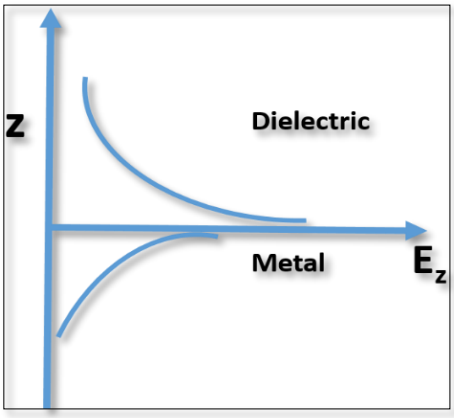

Figure 6.1. Exponentially decay field E_z as a function of z, where z>0 is dialectic medium and z>0

The collective oscillation of charges formed between metal and dielectric interfaces are formed due to combined excitation of photon and surface plasmon is called surface plasmon polariton (SPP). The decay of Electromagnetic fields associated with SPPs in metal and dialectic is shown in Figure 6.1

Dispersion relation of SPPs

From Maxwell equations in a medium we have,

$$D = \varepsilon_0 E + P$$
$$H = \frac{1}{\mu_0} B - M \quad (3)$$

where, H and E are the magnetic and electric field vectors B and D are the magnetic, electric flux density respectively. D and H are related to E and B by polarization P and magnetization M. The electromagnetic boundary conditions for D and B at boundary perpendicular to interface is given by ($B_{1\perp}$ - $B_{2\perp}$) = 0 and ($D1_\perp$ -$D_{2\perp}$) = σ_s. The tangential components of H and E given by (|E1| - |E2|) = 0 and (|H1| - |H2|) = K, where K, σ_s are the surface current density and surface charge, respectively. Consider a surface wave propagating between mediums having dielectric constants ε_1 and ε_2 propagating in z direction. Such a wave is represented by using electric field and magnetic fields given by Ex, Ez, and Hy. The conventional representation of electric field is

$$E = E_0^{\pm} e^{[i(k_x x \pm k_z z - \omega t)]} \quad (4)$$

Here "+" is for medium one(z>0), "– "is for medium two (z<0), K_x is wave vector in the direction of x and K_z is wave vector in the direction of z. The fields are given by

$$\begin{aligned} E_{xj} &= \hat{x}E_{xj}e^{\left[+i(k_{xj}x \pm k_{zj}z-\omega t)\right]} \\ E_{zj} &= \hat{z}E_{zj}e^{\left[+i(k_{xj}x \pm k_{zj}z-\omega t)\right]} \qquad j=1,2 \\ H_j &= \hat{y}H_{yj}e^{\left[+i(k_{xj}x \pm k_{zj}z-\omega t)\right]} \end{aligned} \tag{5}$$

The index j =1,2 resembles medium 1 and 2 respectively. By solving the electromagnetic equations by substituting above boundary conditions we can obtained propagation vector K_x

$$k_x = \frac{\omega}{c}\sqrt{\frac{\varepsilon_1\varepsilon_2}{\varepsilon_1+\varepsilon_2}} \tag{6}$$

k_x is the dispersion relation of surface Plasmon Polariton. In above equation ε_1, ε_2 are the dialectic constants of dielectric and metal surface respectively. The SPP has large propagation constant so it can not directly couple with incident light. This mismatch in the wave vector can be compensated using techniques such as attenuated total reflection(ATR), prism coupling or, grating coupling employing the light diffraction or waveguide coupling using an optical fiber etc. Irrespective of the coupling method the following equation using must be satisfied [29].

$$k_{spp} = k_o + k_{match} \tag{7}$$

6.1.3.a Sub-wavelength metallic hole arrays coupling

One of the ways to satisfy the above equation is to make metal films with a periodic array of perforated holes in which the k-vector associated with periodic nature of the structure compensates the required mismatch. So the equation becomes

$$k_{spp} = k_o + k_{hole\ array} \tag{8}$$

As mentioned in the previous section Ebbesan demonstrated coupling of light with optically thick subwavelength metallic hole array, the same method has been used in the present work also. The coupling of surface Plasmon with the incident light is done by grating momentum of periodic arrays.

It is the easiest technique as it does not require any additional optical components (like prism coupling or lens coupling). For light having propagation vector $k = \omega/c$ falling on a grating of with grating constant "a" incident normally($\theta=90^0$). The incident wave vector surface component of is given by

$$k_x = \frac{\omega}{c} + \sqrt{\varepsilon_1} \pm mG_x \pm mG_y = \frac{\omega}{c}\sqrt{\frac{\varepsilon_1\varepsilon_2}{\varepsilon_1+\varepsilon_2}} = k_{sp} \tag{9}$$

where G_x, G_y grating momentum, for a square lattice it value is $2\pi/a$ and m and n are integers. The incident light couples with SPPs which underpass through the subwavelength holes and reradiate in the other side.

ω is the angular frequency of the surface Plasmon given by $\omega = 2\pi c/\lambda_{sp}$. substituting this value in the above equation the wavelength of surface plasmon gives

$$\lambda_{spp}^{m,n} = \frac{L}{\sqrt{m^2+n^2}}\sqrt{\frac{\varepsilon_1\varepsilon_2}{\varepsilon_1+\varepsilon_2}} \tag{10}$$

L is the periodicity of the lattice, m, n are the integers representing the order of the scattering. In order to observe high EOT the ratio of $\varepsilon_{real}/\ \varepsilon_{real}$ should be of a high value, i.e. $\varepsilon_{real}/\ \varepsilon_{real} >> 1$. Moreno et al. demonstrated that EOT can obtain even with small value of $\varepsilon_{real}/\ \varepsilon_{real}$ by appropriate corrugation of the surface. The resonance frequency depends on the following parameters.

1. Dielectric constants surrounding dielectrics and the metals
2. Shape and size of the hole,
3. Periodicity of the hole array.

Azad et al studied the effect of SPP associated transmission on surrounding dielectric material. For the same subwavelength structure with different dielectric materials (Silicon, Air, Plastic, Quartz) the resonant mode corresponding to [±1, 0] show a considerable shift. The results show decrease in the peak amplitude with increase in the refractive index and redshift in the peak position. Some selected materials having low index values due to Wood's anomaly and resonant excitation shows high prominent maxima and minima. For high index materials Wood's anomaly effect is weaker also the resonant peaks overlap with Wood's anomaly. one of the vital things of SPPs is that they propagate along the surface of metal-dielectric interface and decay exponentially in each medium normal to the

surface. The skin depth can be defined as the length of propagation inside the metal at which the electric field value drops to 1/e times of original. Skin depth δ_m is defined as

$$\delta_m(\omega) = \sqrt{\frac{2}{\omega \mu_0 \sigma_{rm}}} \tag{11}$$

here, μ_0 is the free space permeability.

6.2 Fabrication of metallic hole array

There are two type of standard methods for planar electronic and optoelectronic devices. When the resolution of 10-20 nm is required electron beam lithography is preferred. The photo lithography is used for the resolution of the order of 100-200 nm.

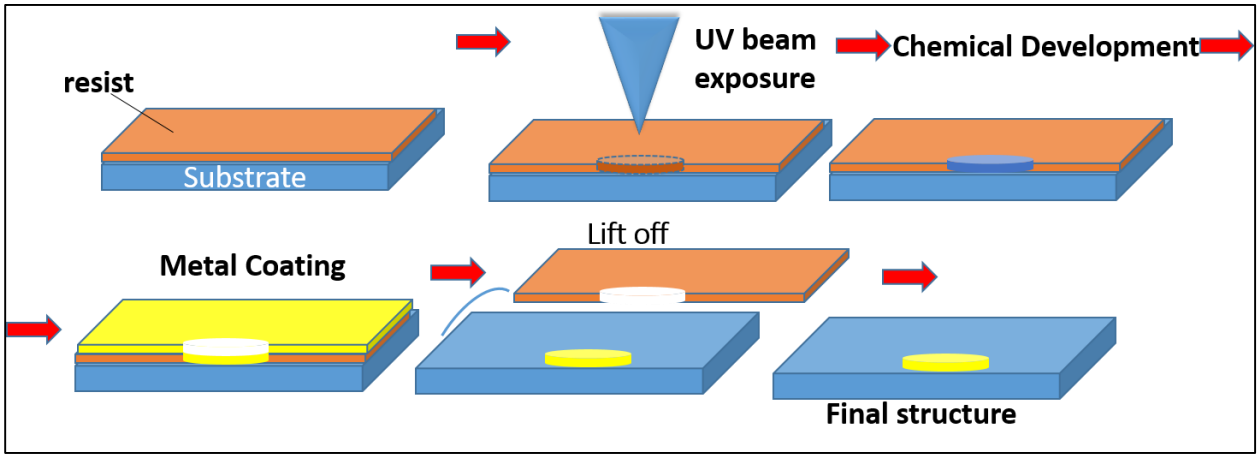

Figure 6.2. Lift off technique for the fabrication of hole arrays.

Figure 6.2 describes the fabrication process of lift off for the fabrication of desired structures. Initially the substrate wafers were cut to required dimensions. After cleaning the substrate, the photoresist was spin-coated. If the photoresist is positive type the coated substrate is exposed to UV radiation through mask, then treated for chemical development. The portion of the substrate exposed by UV is removed. In case of negative type photoresist, the exposed portion becomes resistant, the developing of this type results the removal of unexposed portion. The spin coated substrate was placed on mask aligner and illuminated with UV light. The transmitted UV light through mask will remove the photoresist. Then it will undergo metallization followed by lift off in the developer solution. In this thesis the fabrication was done as follows. The samples of circular hole arrays are

fabricated using well known conventional process of UV photolithography in clean room environment. This includes spin coating the positive photoresist (light sensitive chemical) on cleaned silicon wafer in multistep process, followed by baking with hot plate around 120° C for a period of around 150 seconds and exposure time of around 5 seconds with UV light using appropriate designed mask. The process results in patterning hole arrays on silicon wafer, which are developed using standard developer solution. After that, Al layer of thickness 150 nm is deposited by electron beam evaporation technique in ultrahigh vacuum. In the end, lift process is carried out in acetone bath to obtain the desired features of hole arrays.

6.3 Simulation and Results

We have used commercially available software, CST Microwave Studio. The working principle and workflow was discussed in chapter 2. To carry out the numerical calculations for the arrays of metallic circular holes having in plane lattice periodicities of 125 μm and 150 μm, at same cavity diameter of 100 μm. The outcomes are obtained in terms of transmission with the help of frequency domain solver by computing Maxwell's equations of electrodynamics with periodic boundary conditions. We have chosen silicon (Si) as substrate & aluminum (Al) as resonating metal with thicknesses of 25 μm & 150 nm, respectively. The wave vector of incident terahertz radiations is set normal to the surface of proposed metamaterial design.

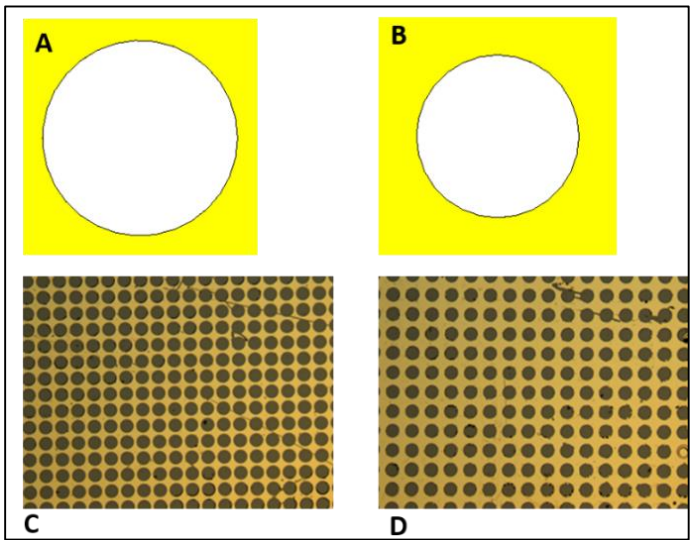

Figure 6.3. Single unit cell of design for periodicity (a) 125 μm (b) 150 μm. Fabricated images of circular hole arrays for periodicity (c) 125 μm (d) 150 μm.

The polarization independent transmission response as per symmetric nature of cavity design is calculated within frequency range of 0.2 THz – 2.0 THz. Figure 6.3 represents the geometry of unit cell of metamaterial design along with fabricated images of arrays. The fabricated samples are characterized using the state of the art terahertz time domain (THz TDS) spectroscopy to measure the transmission characteristics at room temperature in dry environment. We have used THz spectrometer by Toptica Photonics (Teraflash) having a fs laser of specifications (wavelength (1560 nm), repetition rates (100 MHz), pulse width (~ 60 fs)) towards generation of terahertz radiation having spectral resolution ~ 67 GHz. The pump pulse was divided into two beams, where one of the beams focusses on the terahertz emitter, while the other towards the detector. The source comprises of a 100 μm gap antenna and the detector antenna with 25 μm gap. A transient current is generated in emitter antenna with the help of the 60 fs pulses, which yields broadband wave packets having signatures in the terahertz frequency region. Followed by this, the terahertz pulses then pass through the samples and propagate to the receiver end. The receiver uses the concept of the "pump-probe" principle: the incident THz gets modulated during its journey through the fabricated samples, while the probe pulse measures this effect at the THz detector end. Fast Fourier transformation (FFT) is used to convert the time domain data into frequency domain. The normalization is achieved with the help of blank silicon wafer as reference.

6.3.1 Results and Discussions

Figure 6.4 represents the normalized transmission spectra of MM1 and MM2 samples contain two prominent resonance features in the frequency range 0.1 to 2 THz, these resonances can be attributed to SPP modes. It was observed that increasing periodicity of the hole array causes the shift in the plasmonic resonance. Sharp resonance peaks at 0.54 THz, o.66 THz were obtained for the hole arrays with periodicity 150 μm, 125 μm respectively. The bandwidth of the ~60 GHz and ~80 GHz with 80% of transmittance were obtained for the bandpass filters MM1 and MM2 respectively.

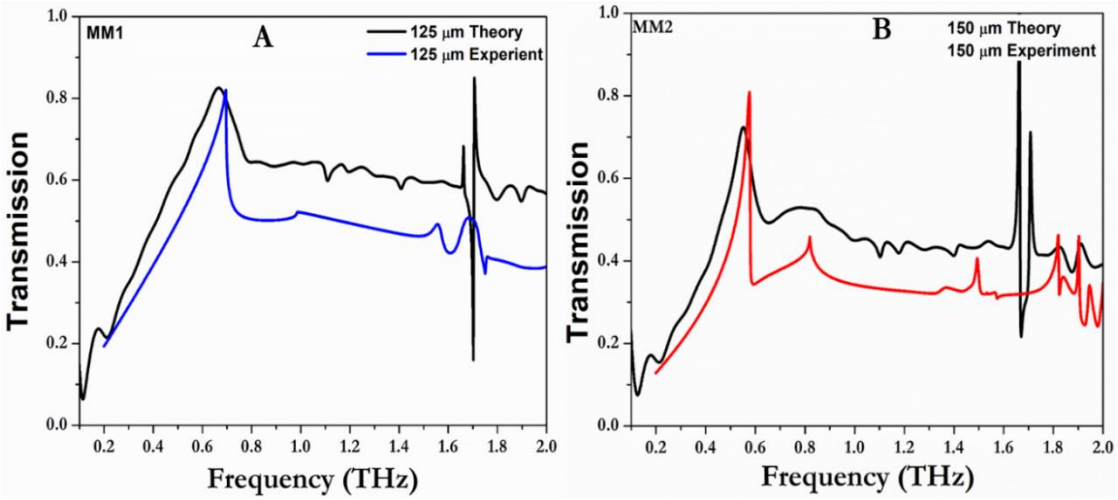

Figure 6.4. Normalized Transmission for the sample A) periodic hole array 125 μm B) periodic hole array 150 μm

There is slight shift in the theoretically simulated values to the experimentally observed resonant position. This could be due to the variation in the dielectric constant used in the simulation to the actual value of the materials used for fabrication. The resonance at 0.54 THz for the hole array (MM2) can be assigned to the [±1, 0] surface Plasmon mode at the silicon- aluminum interface. Here the value of dielectric constants of silicon $\varepsilon_{Si} = 11.70$ and aluminum $\varepsilon_{Al} = -3.3 \times 10^4 + i\, 1.5 \times 10^6$ are taken for calculations. Because of dielectric constant value of the aluminum is far higher than the value of silicon at given frequency which corresponds to appearance of another new peak at ~1.66 THz which is obtained for both filters and attributed to metal-air interface.

6.3.2 Comparison between commercial bandpass filter with proposed filters

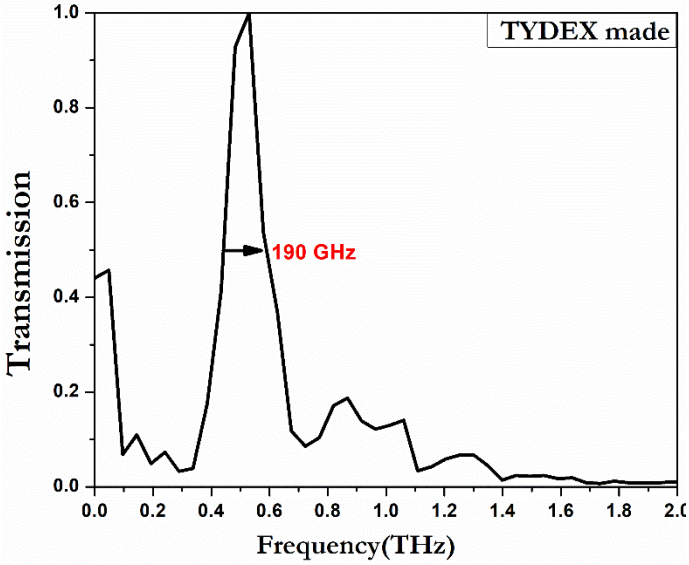

Figure 6.5. Transmission spectrum of commercial band pass filer (TYDEX company)

The performance of designed filters was compared with commercially available freestanding band pass filters manufactured by TYDEX company. The full width at half maximum (FWHM) of the transmitted spectrum for commercial filters is of the order of 190 GHz as shown the Figure 6.5, whereas for our filters its value is 50 GHz. However, commercial filters give better transmission than our filters which can further be improvised by taking care in the fabrication process. Figure 6.6 shows the electric field destitution of bandpass filters MM1 and MM2 at resonance frequency

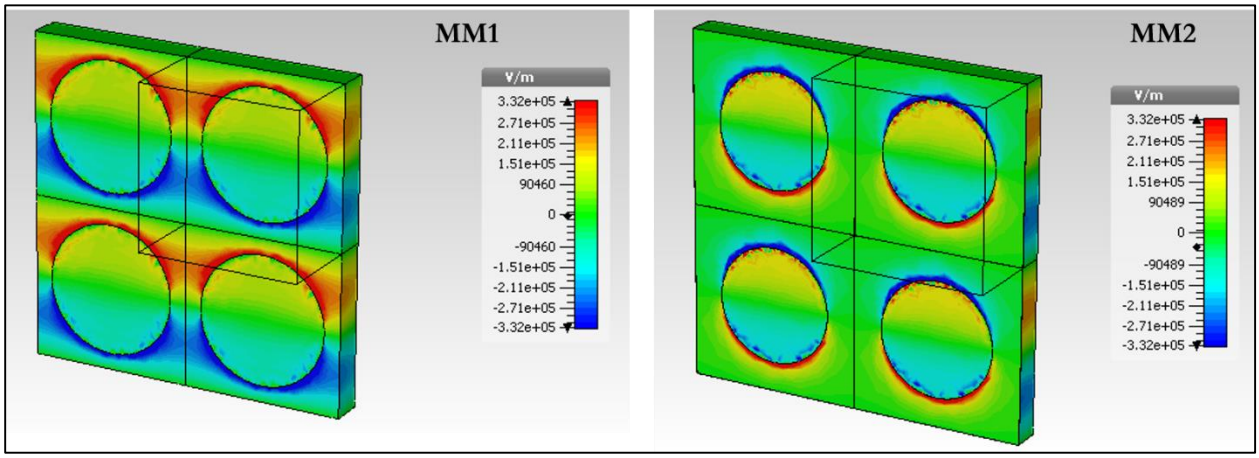

Figure 6.6. Eleatic field distributions at resonating frequency MM1(125 µm) and MM2(150µm)

6.4 Flexible THz bandpass filters

In the previous sections the bandpass filters discussed were made on silicon substrate. There are few disadvantages of using silicon as substrate. Silicon wafers are costly and sophisticated facilities are required to cut, process. We have designed a low cost, flexible bandpass filters on polyamide film. Two designs were simulated with gold hole array on polyimide and gold hole array sandwiched between two polyamide layers. The structures were optimized to following dimensions.

Table 6-1 Dimensions of simulated flexible bandpass filters

Polyimide thickness	Gold thickness	Hole radius	unit cell length
10 μm	200 nm	50 μm	75 x75

Figure 6.7 depicts the simulated transmission parameters of flexible bandpass filters. We have obtained a passband at 1.4 THz for the gold hole array over a polyimide layer. The pass band shifted to 1.2 THz when the hole array sandwiched between two polyimide layers.

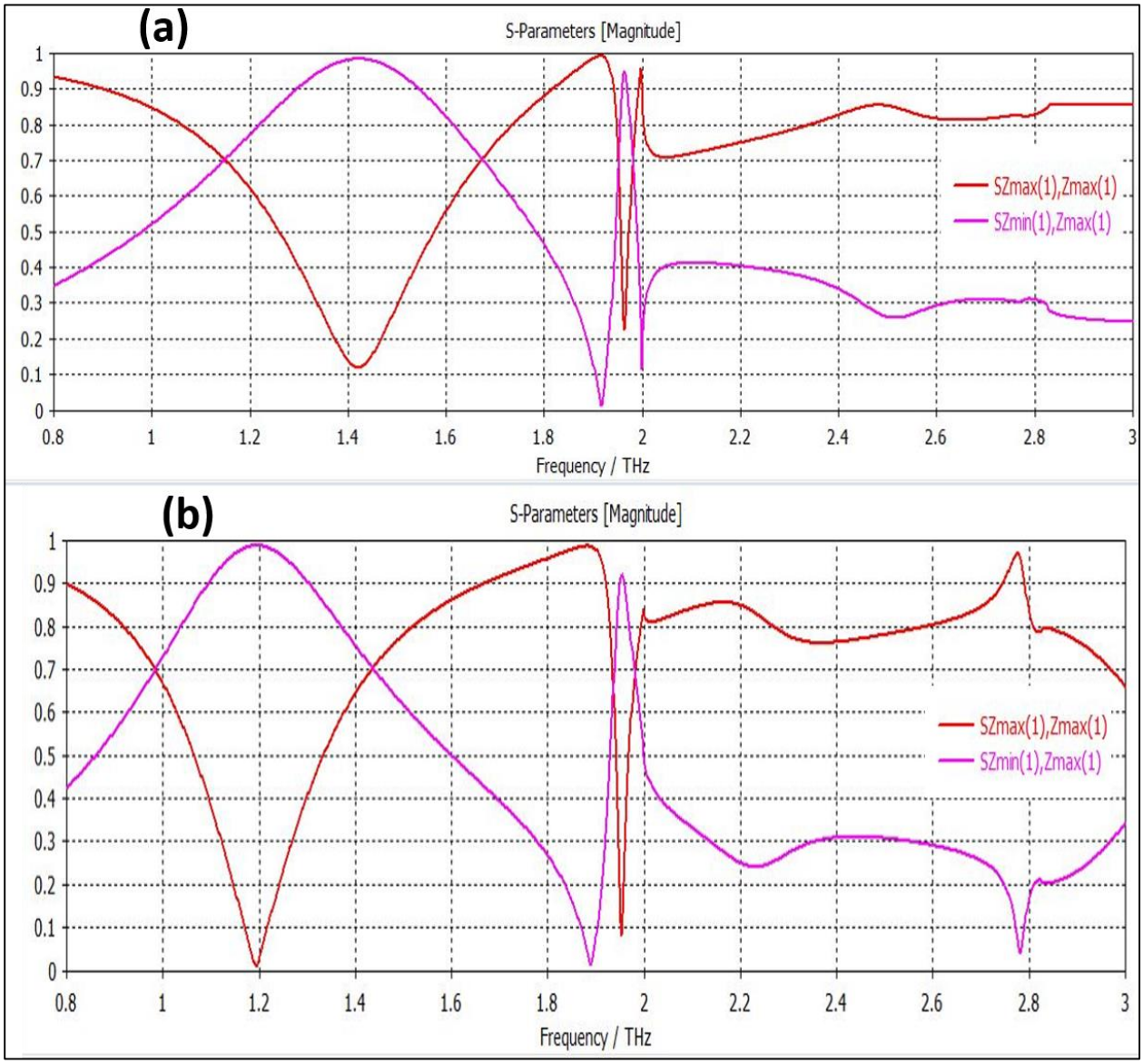

Figure 6.7. a) simulation results of polyimide on gold hole array. b) Gold hole array sandwiched between Polyimide layers

6.5 Explosive sensing using bandpass filters

The resonance peak obtained for a given bandpass filter is majorly depends on the dialectic medium present in the void Space of hole. By varying dielectic constant of medium present in the hole the plasmonics resonance peak can be shifted. The shift is unique for a given medium. This principle

can be used for sensing the material of interest. We have used the bandpass filters for sensing purposes by placing the material in the holes of periodic hole array.

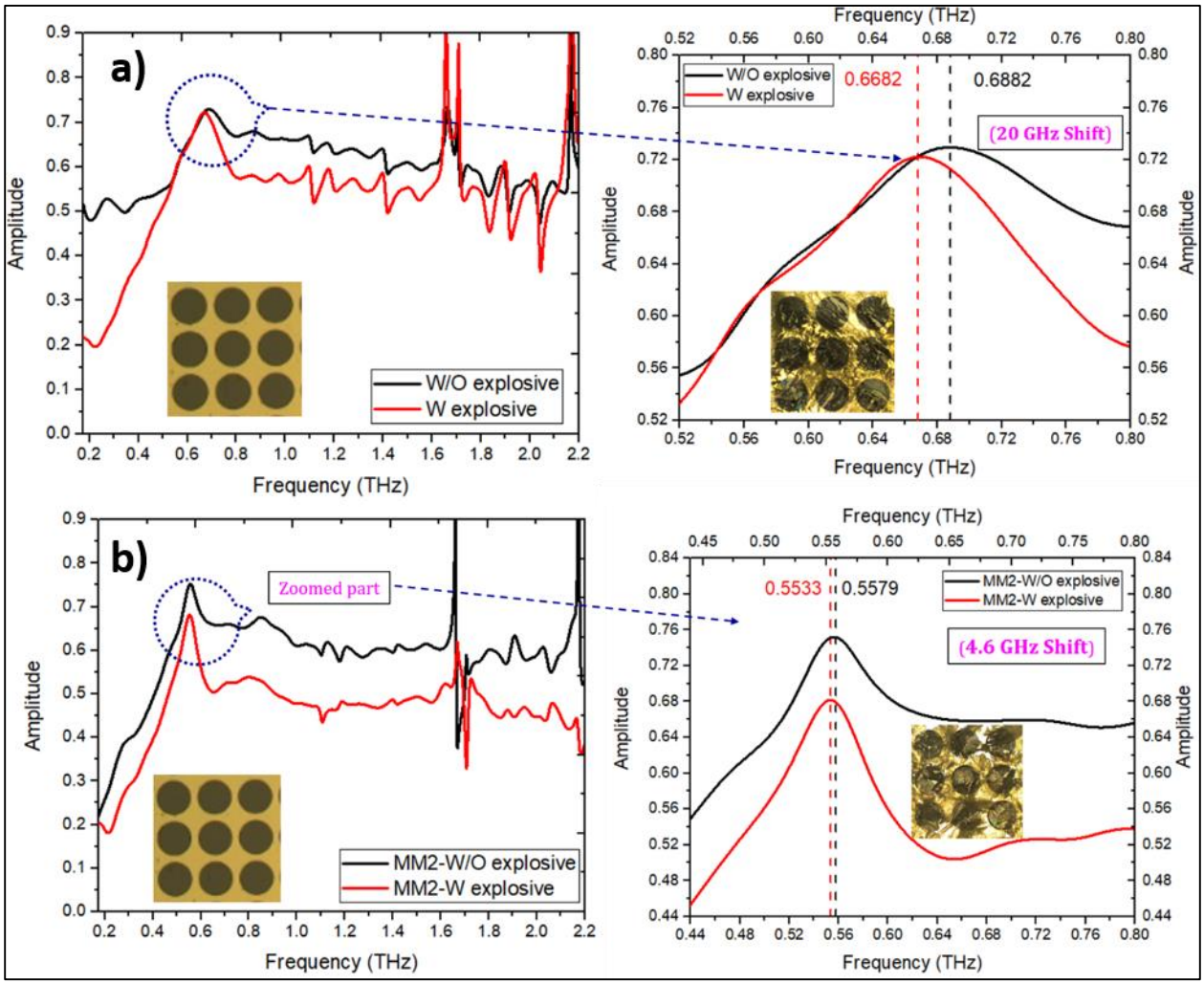

Figure 6.8. Change in the resonance peak by after drop casting of RDX a) for MM1sample b) for MM2 sample

A 10 milli molar RDX solution is prepared by mixing 20 mg of RDX in 10 ml of acetonitrile solution. This solution is drop casted on MM1(125 μm), MM2 (150 μm) hole array. Then THz transmission spectrum of theses hole array has been measured. The spectra were normalized with the reference background is shown Figure 6.8. we have obtained a shift of 20 GHz for the sample MM1 having periodicity 125 μm. The shift in resonance transmission peak reduced to 4.6 GHz for the hole array MM2 having periodicity 150 μm. This study helps to identify the appropriate periodicity of hole arrays for sensing application. This study can be improvised by designing the

bandpass filters at characteristics signature absorption peaks measuring the plasmonics shift. For trace level sensing of high-energy materials and biological samples as a substrate for SERS applications [30,31].

6.6 Conclusion:

We have successfully simulated and fabricated metal mesh hole array type bandpass filters by fabricating gold hole array on silicon substrate. Two bandpass filter having resonance with hole array periodicity 125, 150 μm having resonance frequency frequencies at 0.55, 0.66 THz, respectively. We have also theatrically designed low cost, flexible bandpass filters on polyamide substrate. The fabricated bandpass filters were used trace level sensing of high-energy molecules by measuring the plasmonics shift. This study helps developing the technology for metal mesh filters for trace levels detection applications.

6.7 References

1. L. Rao, D. Yang, L. Zhang, T. Li, and S. Xia, "Design and experimental verification of terahertz wideband filter based on double-layered metal hole arrays," in *Applied Optics*, Vol. 51, Issue 7, pp. 912-916 (2012).
2. R. Mendis, A. Nag, F. Chen, and D. M. Mittleman, "A tunable universal terahertz filter using artificial dielectrics based on parallel-plate waveguides," Appl. Phys. Lett, Lett. 97, 131106 (2010).
3. R. Mendis, A. Nag, F. Chen, and D. M. Mittleman, "A tunable universal THz filter using artificial dielectrics," in *IRMMW-THz 2010 - 35th International Conference on Infrared, Millimeter, and Terahertz Waves, Conference Guide* (2010).
4. J. Han, J. Gu, X. Lu, M. He, Q. Xing, and W. Zhang, "Broadband resonant terahertz transmission in a composite metal-dielectric structure," Opt. Express, Vol. 17, Issue 19, pp. 16527-16534 (2009).
5. D. Maystre, "Theory of wood's anomalies," Springer Ser. Opt. Sci, pp 39-83 (2012).
6. A. Hessel and A. A. Oliner, "A New Theory of Wood's Anomalies on Optical Gratings," Appl. Opt, Vol. 4, Issue 10, pp. 1275-1297(1965).
7. R. W. Wood, "On a remarkable case of uneven distribution of light in a diffraction grating spectrum," Proc. Phys. Soc. London (1901).
8. A. Degiron, H. J. Lezec, N. Yamamoto, and T. W. Ebbesen, "Optical transmission properties of a single subwavelength aperture in a real metal," Opt. Commun, Vol. 15, Issue 26, pp. 17863-17873 (2004).
9. T. W. Ebbesen, H. J. Lezec, H. F. Ghaemi, T. Thio, and P. A. Wolff, "Extraordinary optical transmission through sub-wavelenght hole arrays," Nature, Vol. 82 , pp. 49-71 (1998).
10. L. Martín-Moreno, F. J. García-Vidal, H. J. Lezec, K. M. Pellerin, T. Thio, J. B. Pendry, and T. W. Ebbesen, "Theory of extraordinary optical transmission through subwavelength hole arrays," Phys. Rev. Lett. 86, 1114 (2001).
11. H. Ghaemi, T. Thio, D. Grupp, and T. Ebbesen, "Surface plasmons enhance optical transmission through subwavelength holes," Phys. Rev. B - Condens. Matter Mater. Phys., 58, 6779(1998).
12. Y. Yang, R. Singh, and W. Zhang, "Anomalous terahertz transmission in bow-

tie plasmonic antenna apertures," Opt. Lett, Vol. 36, Issue 15, pp. 2901-2903 (2011).

13. A. M. Melo, M. A. Kornberg, P. Kaufmann, M. H. Piazzetta, E. C. Bortolucci, M. B. Zakia, O. H. Bauer, A. Poglitsch, and A. M. P. A. Da Silva, "Metal mesh resonant filters for terahertz frequencies," Appl. Opt, Vol. 47, Issue 32, pp. 6064-6069 (2008).
14. H. Raether, G. Hohler, and E. A. Niekisch, "Surface Plasmons on Smooth and Rough Surfaces and on Gratings," Springer Tracts Mod. Phys, 16, 013040 (1988).
15. J. R. Sambles, G. W. Bradbery, and F. Yang, "Optical excitation of surface plasmons: An introduction," Contemp. Phys, Volume 32, 173-183 (1991).
16. D. Sarid and W. Challener, *Modern Introduction to Surface Plasmons: Theory, Mathematica Modeling and Applications* (2010).
17. D. Qu, D. Grischkowsky, and W. Zhang, "Terahertz transmission properties of thin, subwavelength metallic hole arrays," Opt. Lett, Vol. 29, Issue 8, pp. 896-898 (2004).
18. A. K. Azad and W. Zhang, "Resonant terahertz transmission in subwavelength metallic hole arrays of sub-skin-depth thickness," Opt. Lett, Vol. 30, Issue 21, pp. 2945-2947 (2005).
19. T. Matsui, A. Agrawal, A. Nahata, R. Menon, and Z. Valy Vardeny, "Terahertz time-domain spectroscopy studies of subwavelength hole arrays in metallic films," Phys. B Condens. Matter **394**, 363–367 (2007).
20. H. Cao and A. Nahata, "Resonantly enhanced transmission of terahertz radiation through a periodic array of subwavelength apertures," Opt. Express, Vol. 12, Issue 6, pp. 1004-1010 (2004).
21. W. Zhang, "Resonant terahertz transmission in plasmonic arrays of subwavelength holes," EPJ Appl. Phys, 43, 1 - 18 (2008).
22. X. Xiao, W. Jinbo, Y. Sasagawa, F. Miyamaru, M. Zhang, M. W. Takeda, C. Qiu, W. Wen, and P. Sheng, "Resonant terahertz transmissions through metal hole array on silicon substrate," Opt. Express, 18, 18558-64 (2010).
23. C. Janke, J. Gómez Rivas, C. Schotsch, L. Beckmann, P. Haring Bolivar, and H. Kurz, "Optimization of enhanced terahertz transmission through arrays of subwavelength apertures," Phys. Rev. B - Condens. Matter Mater. Phys. (2004).

24. J. G. Rivas, C. Schotsch, P. H. Bolivar, and H. Kurz, "Enhanced transmission of THz radiation through subwavelength holes," Phys. Rev. B - Condens. Matter Mater. Phys, 19(1):8400416-8400416 (2003).

25. J. Saxler, J. Gómez Rivas, C. Janke, H. P. M. Pellemans, P. Haring Bolívar, and H. Kurz, "Time-domain measurements of surface plasmon polaritons in the terahertz frequency range," Phys. Rev. B - Condens. Matter Mater. Phys. (2004).

26. C.-P. Huang and Y.-Y. Zhu, "Plasmonics: Manipulating Light at the Subwavelength Scale," Act. Passiv. Electron. Components **2007**, 30946 (2007).

27. J. M. Pitarke, V. M. Silkin, E. V. Chulkov, and P. M. Echenique, "Theory of surface plasmons and surface-plasmon polaritons," Reports Prog. Phys. 70 1 (2007).

28. A. V. Zayats, I. I. Smolyaninov, and A. A. Maradudin, "Nano-optics of surface plasmon polaritons," Phys. Rep, 408, 131-314 (2005).

29. H. J. Lezec and T. Thio, "Diffracted evanescent wave model for enhanced and suppressed optical transmission through subwavelength hole arrays," Opt. Express, Vol. 12, pp. 3629-3651 (2004).

30. C. Y. Chan, J. B. Xu, M. Y. Waye, and H. C. Ong, "Angle resolved surface enhanced Raman scattering (SERS) on two-dimensional metallic arrays with different hole sizes," Appl. Phys. Lett, 96(3), 033104-033104 (2010).

31. S. Kim, J. H. Shin, S. Kim, S. J. Yoo, B. O. Jun, C. Moon, and J. E. Jang, "Geometric effects of nano-hole arrays for label free bio-detection," RSC Adv, 2016,6, 8935-8940 (2016).

CHAPTER 7 : Conclusions and Future scope

This chapter deals with the summary of the all the chapters and conclusion along with possible future scope of the work.

In this thesis, we focused our study on addressing the generation of intense, broadband THz radiation with nonlinear crystals of different kinds. Spectroscopic study has been done to extract the absorption coefficient and dielectric properties. Terahertz radiation has number of applications in the field of spectroscopy, biomedical, pharmaceutical industry, defense science and technology, telecommunications etc. The advancement in the electronics, data acquisition helped to fill the THz gap in the electromagnetic spectrum. One of the major challenges in THz technology is to overcome the atmospheric absorption which limits the use of THz spectroscopy and imagining from long to short distances. This problem can be solved by means of developing a high intensity THz radian sources and and sensitive detector, post processing of obtained time domain spectrum with suitable algorithm to remove the interfering absorption lines cause by the atmosphere. We have also made an attempt to design and fabricate bandpass filters in THz region for sensing applications.

7.1 Conclusions

A multipurpose THz generation and detection experimental setup has been designed where one can carry out different types of experiments such as optical pump terahertz probe, generation and detection of THz radiation using different types of materials. Since in current setup position of generator and detector components can be interchanged. Therefore, all four types of combinations like photoconductive antenna- antenna, antenna- nonlinear crystals, nonlinear crystal- antenna and nonlinear crystal- crystal as source and detector can be made. Moreover, this set-up can work in both transmission and reflection modes.

As a result, we have evaluated different types of indigenously grown organic crystals such as BNA OH1, LAP. These crystals were characterized in terms of growth solvent, optical transmission range, absorption coefficients. Since the transmission of all these crystals varying in optical domain therefore it also reflected their potential use as an efficient THz source. The solvent effect on THz generation ability of BNA crystals has been discussed. L-arginine phosphate monohydrate (LAP) has been studied as a THz source and its absorption and refractive index are reported in THz domain for the first time.

The efficiently generated THz radiation was used to identify the signature absorption peaks of high-energy materials. we have studied the linear and nonlinear optical properties of newly synthesized tetrazole molecules using time- domain terahertz spectroscopy, UV−visible−NIR spectroscopy. We have also ascertained the absorption coefficients and refractive index between 0.1 and 2.2 THz range. In addition, we have performed single-molecule and single-crystal level Density functional theory (DFT) calculations. The theoretically calculated zone center vibrational frequencies at the solid level were compared with experimentally obtained found data, they are found to be good in agreement. We have also explained the optical sensitivity correlations using vibrational frequencies. The electronic absorption, refractive index, and birefringence studies reveal the feasibility of phase-matched nonlinear optical frequency mixing devices in the single-crystal form. It is also very important to understand how these high-energy materials behave at high temperature. We have successfully recorded the temperature dependent variation in the refractive indices and absorption coefficients of NH_4NO_3, TNT and RDX explosives below their melting points. To the best of our knowledge this is the first demonstration of red shift effect and process of slow thermal decomposition mechanisms of these explosives in THz domain. It also helps to characterize the explosive molecules. In addition, the effect of change on the strength of THz signal of RDX in PTFE (Teflon) matrix is with respect to the concentration.

Also a successful attempt was made to record the signature spectrum of RDX explosive sample under concealed condition.

Finally, we have successfully simulated and fabricated metal mesh hole array type of band-pass filters by fabricating gold hole array on silicon substrate. Two bandpass pass filters having resonance with hole array periodicity of the order of 125, 150 μm having tunable resonance frequencies at 0.55, 0.66 THz, respectively. We have also theoretically designed low cost, flexible bandpass filters on polyamide substrate. The fabricated band-pass filters were used for trace level sensing of high-energy molecules by measuring the plasmonics shift. This study helps in developing the technology for metal mesh filter for trace level detection of explosives.

7.2 Future Scope

The work carried out in this thesis can be extended for following future applications:

(i)The modified experimental setup in form of time resolved terahertz spectroscopy(TRTS) can be used to study the carrier dynamics, life time of different types of semiconductors and organic materials.

(ii) By tuning the optical pump wavelength, we can study the charge transfer mechanism between some polymer such as PEDOT and explosives. It can also help to understand the phase transition under the influence of incident photons in optical domain.

(iii) We have shown temperature dependent characterization and thermal decomposition mechanism of RDX, TNT, AN in Teflon matrix. The same process can be used to detect explosive mixed in soil.

(iv) The TDTS can also be used to detect explosives under concealed condition.

(v) The same set-up can be used for 2D THz imaging of metallic and powder samples.

(vi) THz spectroscopy along with DFT calculation carried out in case of tetrazole group compounds opened a new channel of research which. help us to understand the nonlinear and dielectric behavior of new explosive molecules

(vii) THz bandpass filters can be used for high resolution spectroscopy of high energy materials, drugs and other organic molecules in trace level detection.

A part of future scope for femtosecond laser based up conversion properties is published in
Self-assembled pearl-necklace patterned up converting nanocrystals with highly efficient blue and ultraviolet emission:femtosecond laser based up conversion properties, Monami Das Modak, **Ganesh Damarla**, Somedutta Maity, **Anil K. Chaudhary** and Pradip Paik , RSC Adv., 2019, 9, 38246

Efficient Terahertz (THz) generation from some indigenously grown organic nonlinear crystals and designing of band pass filters for spectroscopy of high energy materials

ORIGINALITY REPORT

28%	4%	24%	4%
SIMILARITY INDEX	INTERNET SOURCES	PUBLICATIONS	STUDENT PAPERS

PRIMARY SOURCES

1	Damarla Ganesh, Elaprolu Narsimha Rao, Mottamchetty Venkatesh, Kommu Nagarjuna et al. "Time-Domain Terahertz Spectroscopy and Density Functional Theory Studies of Nitro/Nitrogen-Rich Aryl-Tetrazole Derivatives", ACS Omega, 2020 Publication	12%
2	Ganesh Damarla, M. Venkatesh, A. K. Chaudhary. "Temperature-dependent terahertz spectroscopy and refractive index measurements of aqua-soluble and plastic explosives", Applied Optics, 2018 Publication	9%
3	ir.uiowa.edu Internet Source	1%
4	scholarbank.nus.edu.sg Internet Source	1%
5	aoip.osa.org	

This is to certify that publication No 1 and 2 belong to / part of Student's research paper which is 28-21 = 7% i.e. less than 10%.

17.07.2020

Dr. Anil Kr. Chaudhary
Professor (Physics)
Advanced Centre of Research in High Energy Materials (ACRHEM),
UNIVERSITY OF HYDERABAD
HYDERABAD-500 046. T.S. INDIA

Research Article Vol. 57, No. 29 / 10 October 2018 / Applied Optics 8743

applied optics

Temperature-dependent terahertz spectroscopy and refractive index measurements of aqua-soluble and plastic explosives

Ganesh Damarla,[1] M. Venkatesh,[1,2] and A. K. Chaudhary[1,*]

[1]Advanced Centre of Research in High Energy Materials (ACRHEM), University of Hyderabad, Hyderabad 500046, Telangana, India
[2]The Guo China-US Photonics Laboratory, State Key Laboratory of Applied Optics, Changchun Institute of Optics, Fine Mechanics and Physics, Chinese Academy of Sciences, Changchun 130033, China
*Corresponding author: anilphys@yahoo.com

Received 9 July 2018; revised 8 September 2018; accepted 11 September 2018; posted 11 September 2018 (Doc. ID 335656); published 10 October 2018

The paper reports the temperature-dependent time domain terahertz spectroscopy of premium aqua-soluble and plastic explosives such as NH_4NO_3, TNT, and RDX between 0.1 and 2.2 THz. Tunable terahertz radiation was generated using ZnTe crystal as a source, and a photoconductive antenna was used as a detector. The temperature-dependent study was carried out between 30°C and 200°C in a specially designed oven. The signature peaks of RDX and TNT present at 0.82 and 1.60 THz, respectively, show a strong redshift, whereas the NH_4NO_3 molecule shows a comparatively small shift. The high-temperature-based redshift phenomenon is just the opposite of the blueshift recorded at low temperatures. In addition, the temperature-dependent absorption coefficient data of these molecules support the change in the concentration of the NO_2 molecule. We have also ascertained the temperature-dependent refractive indices of these molecules between 0.1 and 2.0 THz, which confirms the effect of temperature on the refractive indices. Finally, the signature peak of RDX with respect to the reduction in the weight concentration of RDX in the Teflon matrix was studied at 0.82 THz. © 2018 Optical Society of America

https://doi.org/10.1364/AO.57.008743

1. INTRODUCTION

Terahertz (THz) radiation has low energy and deep penetration ability when applied to leather, cloth, Teflon (PTFE) and packing materials [1,2]. Therefore, it is treated as a nondestructive and noninvasive tool for the analysis of explosives, drugs, and biomolecules [3]. Moreover, it covers the fingerprint region of the vibrational–rotational lines of most of the organic, inorganic and biological molecules. Recently, THz technology-clubbed materials have been used for sensing and medical diagnostic applications, such as graphene-based sensors and meta devices based on conductivity changes and refractive index in the THz regime [4–8]. NH_4NO_3, a well-known aqua-soluble fertilizer that is an inorganic molecule, is used as a principal ingredient in improvised explosive devices and presents a major challenge in detection by means of existing optical techniques. Similarly, RDX and TNT are crystalline and amorphous aromatic organic compounds. TNT is partially soluble in water, while RDX is soluble only in organic solvents. Therefore, TNT is responsible for contamination of underground water near military testing ranges. However, RDX is one of the most powerful plastic explosives. It is shock-insensitive and insoluble in water and finds potential use in industry and defense [9].

Tunable THz radiation between the 0.1 and 3 THz range can be generated using different types of optical techniques using low-temperature and semi-insulating GaAs-based photoconductive antennas and nonlinear crystals such as ZnTe, 4-N-methylstilbazolium tosylate (DAST), and N-benzyl-2-methyl-4-nitroaniline (BNA) [10–13]. The THz radiation generated is employed to record the time domain spectra of solid explosives in pellet form. The premier explosive materials have sharp spectral features above 3 THz. The detection and identification of explosives in concealed conditions in field applications are challenging and require judicious selection of the THz frequency range. The high-energy materials (HEMs) RDX and NH_4NO_3 are crystalline, whereas TNT is amorphous in nature. Khachatrian *et al.* have reported the sharp rotational–vibrational features of NH_4NO_3 at low temperatures using a metallic substrate [14]. However, NH_4NO_3 powder mixed with PTFE powder in specific proportions provides information about some distinguishing sharp vibrational modes in transmission range. Most of the solid granule samples dimensions are comparable with the wavelength of THz radiation, which enhances the scattering losses [15]. Therefore, it experiences technical difficulty in direct recording of their spectra.

Chen *et al.* reported some distinguishing weak spectral features of NH_4NO_3 between 0.1 and 3 THz at ambient temperature [16]. Hu *et al.* reported on the THz time domain spectroscopy of explosives [17]. However, most of the reported studies have not incorporated the high-temperature spectra of HEMs. These materials are used in rocket fuel, and the study of thermal decomposition mechanisms provides important information about the energy release process. In the THz domain it is also important to know the participation of different intact functional groups at the time of heating. In our earlier work we carried out this study in vapor form between 40°C and 350°C using a UV–visible wavelength based pulsed photoacoustic technique [18–21]. In the present work we have recorded the spectral signatures of HEMs, and our results have found good agreement with reported values. In addition, we have demonstrated the hot band vibration spectra of the solid explosives NH_4NO_3, RDX, and TNT. The main problem in recording THz spectra in air is related to the presence of water molecules, which have strong absorption peaks in the THz domain and also overlap some of the signature peaks of the samples [22]. But gradual heating of the sample initiates the process of vaporization. Consequently, the intensity of the water absorption band decreases with the increase in temperature. In addition, our studies clearly confirm the release of NO_2 molecules just above 40°C, which also supports our previous studies on the number of explosive molecules. The study was based on the recording of strong vibronic transitions of NO_2 molecules between 30°C and 350°C using a pulsed photoacoustic technique. Here we have also made an attempt to develop a small quantity of pellets using PTFE powder at room temperature and have successfully recorded their characteristic signature in the THz domain.

2. EXPERIMENT DETAILS

The experiment was carried out in two steps. In the first step, we prepared the explosive pellets in the PTFE matrix, and in the second step, these pellets were subjected to the THz system for the recording of temperature-dependent time domain spectra. Sample preparation is an important factor for the recording of a characteristic signature [21,23]. A pure sample in powder form was mixed with PTFE powder, which has very low absorption in the THz range. An explosive sample weighing around 200 mg was mixed with 800 mg of PTFE powder using 10 ml of CH_3OH solvent. The mixture was dried for 20 min and then ground with a mortar to produce a fine homogenous powder. The powder mixture was divided into two halves and transferred to the die using butter paper, and then was pressed with 2 tons of pressure to prepare a pellet. The thickness and diameter of the pellets are ∼2 mm and 12 mm, respectively. The THz wavelength matches the size of the sample present in the pellets, which is responsible for the inhomogeneous broadening of the spectral peaks due to the scattering effect. Moreover, scattering in THz spectra is caused by the refractive index mismatch between the sample crystals and the surrounding pellet medium (PTFE in this case). However, the effect of scattering due to the multiple crystalline nature of the samples can be overcome by dissolving the mixture in methanol solution. We also mixed different proportions of the RDX sample in the PTFE matrix to record the weight-percentage-based signature peaks.

A Ti:sapphire femtosecond oscillator (Coherent Chameleon Ultra II) was used as a laser source. It delivers *p*-polarized laser pulses of 140 fs duration at a 80 MHz repetition rate. The laser output wavelength was tuned between 780 and 850 nm for THz generation. The variable attenuator (VA; Eskpla) was employed to attenuate the output average power. The incident average power was allowed to be incident on the 110 cut ZnTe crystal of 2.0 mm thickness for THz generation. The crystal was housed in a PTFE holder and placed in an optical rotator for vertical rotation. The incident femtosecond laser pulses were loosely focused onto the crystal by means of a plano-convex lens L_1 with a focal length 30 cm. The spot diameter of the laser pulse on the ZnTe crystal was ∼234 μm. The generated THz radiation was collected using two off-axis parabolic mirrors (PM_1, PM_2). The diameter (D) and effective focal length (f_e) of the parabolic mirrors (Thorlabs MPD508762-90-M01) were ∼50 mm and ∼150 mm, respectively. The residual transmitted laser pulses from the source were separated from the THz radiation using a high-resistivity float zone silicon plate (diameter 50 mm, thickness 2 mm) and black polyethylene filter. The silicon plate has reflection coating in between 700 and 900 nm laser wavelengths. The diverging THz radiation emitted from the source was collimated and focused by mirrors PM_1 and PM_2. PM_2 focused the generated the THz radiation onto the photoconductive antenna, which was coupled with the preamplifier, and the output of the preamplifier was fed to the lock-in amplifier. The output signal from the lock-in amplifier was sent to the computer for the recording of time and frequency domain signals using an indigenously designed data acquisition program made using LabVIEW. The horizontal dynamic range of the spectrometer was limited up to 2.2 THz. The pure PTFE pellet was used as a reference. It was assumed that the explosive sample was homogeneously distributed in the PTFE matrix. Barber *et al.* reported temperature-dependent THz spectroscopy of explosives between 8 K and 300 K [24]. However, in the present report we have carried out the high-temperature study of explosive samples below their melting point to record the change in the absorption characteristics and refractive indices. The sample pellet was placed between the parabolic mirrors for the recording of the time domain spectrum, as shown in Fig. 1.

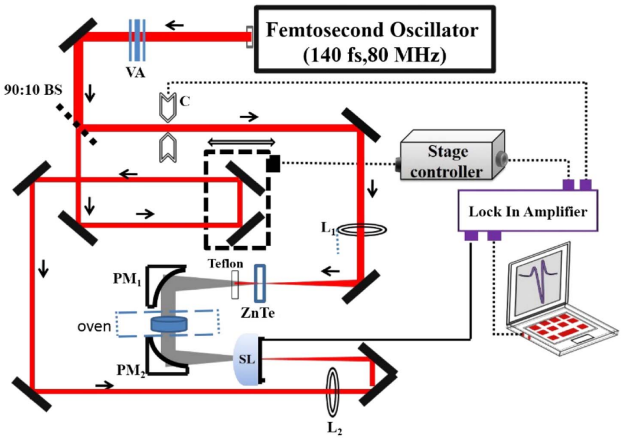

Fig. 1. Schematic layout of a THz time domain spectrometer.

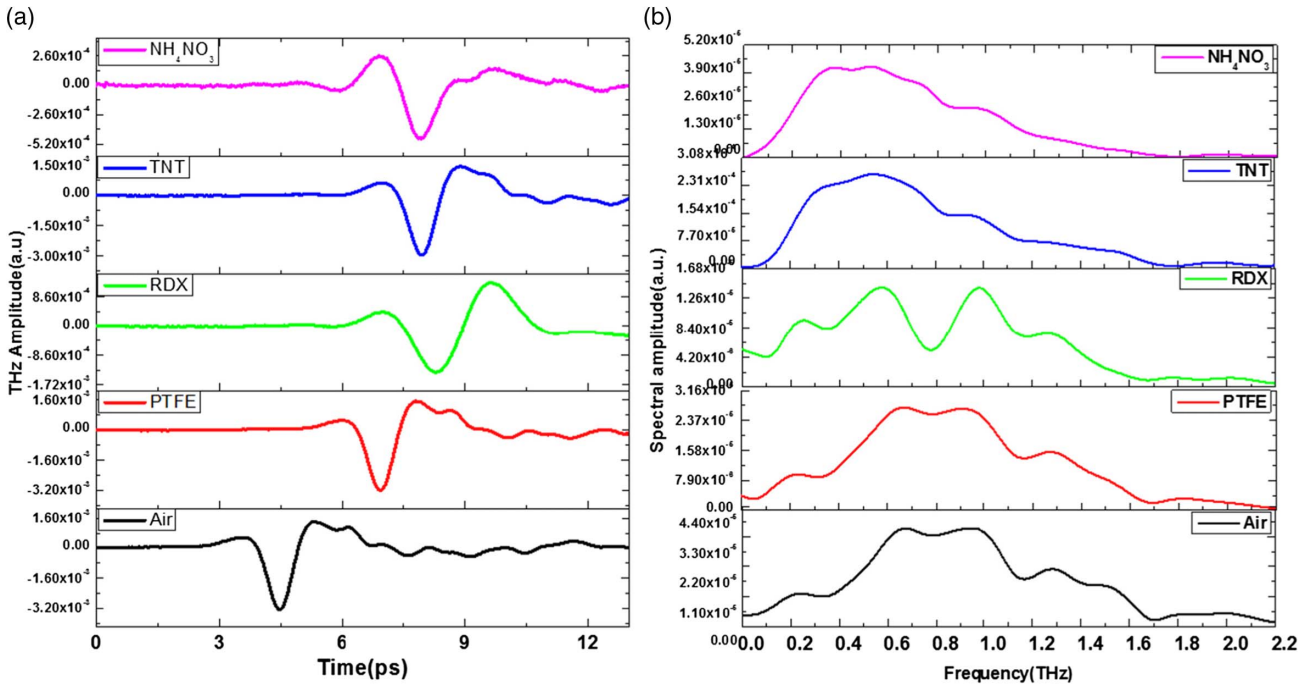

Fig. 2. Schematic THs spectrum. (a) Temporal profile of THz pulse, (b) frequency domain spectra of different explosives.

The average incident power of the THz falling on the sample pellet was of the order of 700 μW. Abid *et al.* [25] reported using optical-extinction-model-based plasmon–exciton interactions between 115 K and 295 K to generate energy of the order of 42 meV, which is equivalent to 10 THz. The authors used a Ti:sapphire laser source tunable between 750–850 nm wavelength for this purpose. However, we generated a THz radiation acceptable region at room temperature using an 800 nm wavelength. The generated broadband THz radiation spectra lies between 0.4 and 8.27 meV. The THz absorption spectroscopy of explosive molecules was carried out in a specially designed small-sized oven that can accommodate the pellets inserted between two parabolic mirrors. The oven works on the Peltier heating principle and was supplied by Conversion Co. Ltd. (UK). We redesigned the hood of the oven to accommodate an explosive pellet with a 12 mm diameter. The temperature of the oven was controlled between 25°C and 200°C with a precision of +0.01°C using a temperature controller supplied by the same company.

3. THEORY

The time domain THz signal received after passing through the samples was converted into a frequency domain spectrum using fast Fourier transform (FFT). The value of the absorption coefficient $\alpha(\omega)$ was calculated from the FFT spectrum. The transmitted field T is given by

$$T = \frac{E_{\text{sample}}}{E_{\text{Reference}}}, \tag{1}$$

where E_{sample} and $E_{\text{Reference}}$ are the amplitudes of the THz radiation after passing through the material and reference samples, respectively. We can calculate the effective thickness (l) of the sample distributed in the PTFE matrix using the formula

$$l = \frac{m}{\rho}\frac{4}{\Pi D^2}. \tag{2}$$

Here, m is the weight of the sample (100 mg), D is the diameter of the sample (12 mm), and ρ is the density of the sample. Since the pellet contains a mixture of two samples, the absorption coefficient α can be ascertained using the formula [26,27]

$$\text{Absorption coefficient}(\alpha) = -\frac{1}{l}\ln\frac{T_m}{T_R}, \tag{3}$$

where l is the effective thickness of the sample and T_m and T_R are transmitted THz amplitudes from the samples and the reference, respectively. The refractive index of the sample can be calculated by using the formula [28]

$$n = 1 + \frac{\Delta\phi \times c}{2\pi\nu \times d}, \tag{4}$$

where $\Delta\phi$ is the phase difference between the reference and the sample, ν is the frequency, d is the thickness of the pellet, and c is the velocity of light. The complex refractive index is represented using the Kramers–Kronig model,

$$n = n + i\kappa, \tag{5}$$

where n is the real part of the refractive index and κ is the extinction coefficient. κ is related to the power absorption coefficient α.

4. RESULTS AND DISCUSSION

Figures 2(a) and 2(b) show the temporal and frequency domain spectral profiles of air, PTFE, and the explosives in the THz range after passing through the pellet. It is observed that the THz pulse shows variations in delay time after passing through different explosives range. It is attributed to the change in the optical path length of the radiation, which varies from sample

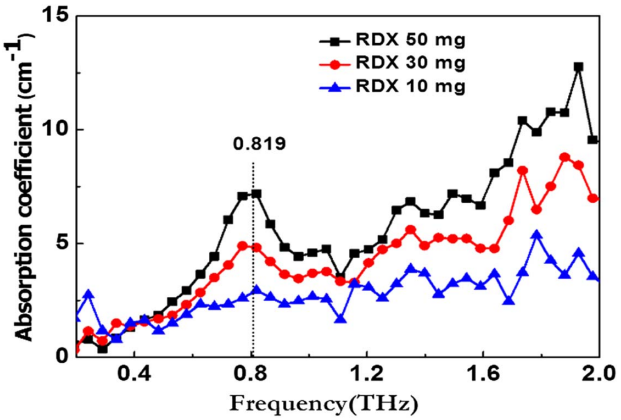

Fig. 3. Absorption coefficients of RDX for different weight concentrations.

to sample due to the change in the refractive index of the molecules. The spectral intensity clearly shows the variation in the intensity and the shift in the absorption peaks of explosive molecules. The experiment was performed in ambient room temperature.

Figure 2 depicts the temporal and frequency domain spectra of explosive samples between 0.1 and 2.0 THz. The dynamic range of the amplitude of spectral lines lies between 10^{-4} and 10^{-7} on a log scale, which helps us to record the weak absorption peaks of the explosive molecules. It is clear that the water-soluble compound NH_4NO_3 has a high absorption coefficient compared to the aqua-insoluble explosives [16]. However, RDX has a significant characteristic absorption peak at 0.82 THz, which agrees with reported work [29,30]. All the samples show a common feature near 1.8 THz. The absorption peak is attributed to the intermolecular vibrational modes present in the THz region. The corresponding THz absorption peaks for NH_4NO_3 present at 98.15, 108.5, and 143.7 cm^{-1} are 0.87, 1.5, and 1.81 THz, respectively.

All the abovementioned studies were carried out with 100 mg of explosive sample mixed with 400 mg of PTFE matrix. We also made an attempt to study the effect of weight percentage on the signature peak of the explosive sample. Therefore, pellets with different weight concentrations of RDX such as 50, 30, and 10 mg were prepared in the PTFE matrix. The thickness and size of the pellets were controlled by adding the same weight percentage of PTFE powder into the mixture. As a result, the total weight of the pellet matrix always remains 500 mg. The time domain spectra of different weight percentage pellets were recorded, and their corresponding absorption coefficient data were ascertained and compared with the reported values available in the literature [31,32].

Figure 3 shows the drop in the value of the absorption coefficient with a decreasing concentration of RDX in PTFE matrix at 0.81 THz. This also indicates the minimum detection limit of RDX in solid form.

A. Temperature-Dependent Absorption Spectra and Refractive Index of RDX

The recording of absorption bands in the THz region is also affected by the presence of water vapor. Consequently, many of the characteristic bands are either not visible or have low intensity. The temperature-dependent spectroscopy of molecules plays a very important role in revealing significant information about many weak vibrational modes that are not observable at room temperature [33,34]. In addition, it helps excite the molecules at the ground state, which is also reflected in the coupling of oscillating modes in terms of redshift. In this section we discuss the temperature-dependent THz spectra of RDX, TNT, and NH_4NO_3 molecules in solid form. The spectra are recorded below their melting point.

Shen *et al.* [34], Hangyo *et al.* [35], and Azad *et al.* [36] reported the temperature-dependent spectroscopic study at low temperature and identified the behavior of signature peaks of RDX present at 0.82, 1.05, 1.50, and 1.96 THz. Figure 4(a) shows the temperature-dependent absorption coefficients of RDX in PTFE matrix recorded between 30°C and 170°C. The characteristic band present at 0.8 THz has sharp features between 30°C and 90°C. This can be attributed to the presence of the NO_2 group [37]. The absorption coefficient at room temperature is 11 cm^{-1}, which decreases with increasing sample temperature. In addition, the shape of the absorption peak between 30°C and 90°C shows a broadening effect at 105°C. This reveals the process of vaporization of water molecules and the release of NO_2 gas, which also indicates the initiation of the process of thermal decomposition of RDX. The decrease in the

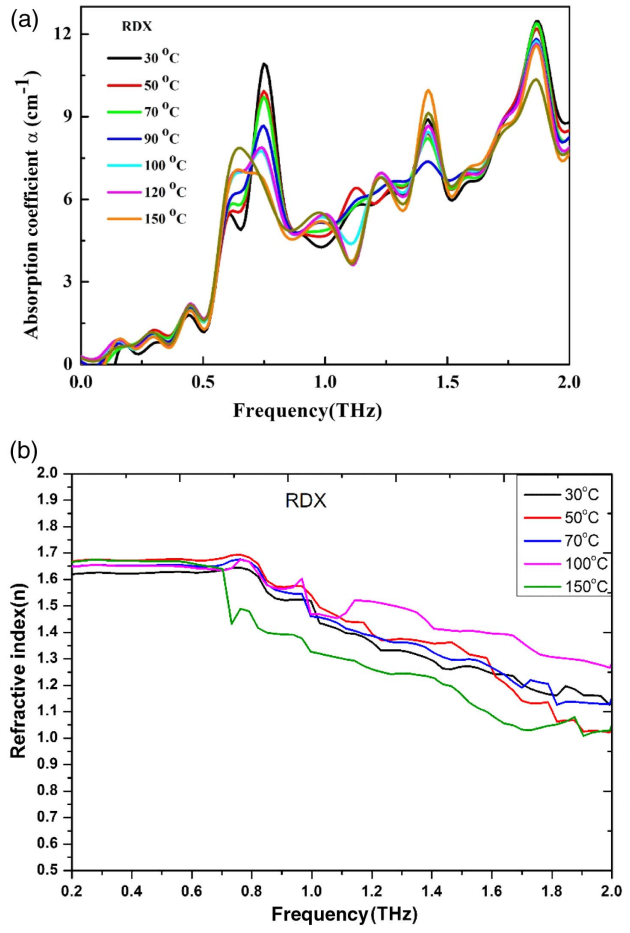

Fig. 4. (a) Temperature-dependent absorption coefficient of RDX, (b) temperature-dependent refractive index of RDX.

absorption coefficient value of the 0.8 THz peak is directly linked to the loss of NO_2 from the solid sample [38]. In our previous reports, we have successfully demonstrated the release of NO_2 from different explosives above 40°C, using a pulsed photoacoustic technique [28,39,40]. The previous study was performed in vapor using 532 and 266 nm wavelengths of a *Q*-switched Nd:YAG laser. The NO_2 gas release mechanism is based on the strong electronic transition and is attributed to vibronic modes of NO_2. However, the present results once again support our earlier findings in the THz domain. Further, an increase in the temperature between 120°C and 170°C enhances the broadening of the peak width and shows some shift toward 0.62 THz, which is nothing but the redshift effect due to heating. Similarly, the peak at 1.05 THz has a small amplitude and appears in the form of a dip at room temperature. However, after crossing 105°C, the dip is modified and converted into a hump at 120°C. This is attributed to the hot band effect, where the weak signature peak was invisible due to water molecules. A similar type of effect is also observed at 1.4 THz. However, this peak shows the reverse trend. The absorption coefficient between 30°C and 105°C is lower than the absorption coefficient at 150°C.

Figure 4(b) shows the temperature-dependent refractive index of RDX. The refractive index was recorded between 30°C and 150°C, and it is clear that there is little variation in the refractive index up to 0.7 THz. The value of the refractive index remains between 1.6 and 1.65. However, after 0.7 THz there is a large decline in the value of the refractive index with respect to temperature, and it decreases from 1.7 to 1.2 at 2.0 THz. Similar types of changes are also visible in the absorption coefficient data at 0.7 THz.

B. Temperature-Dependent Absorption Spectra and Refractive Index of TNT

Figure 5(a) shows the temperature-dependent spectrum of TNT, which was recorded between 30°C and 70°C—below its melting point, i.e., 80.35°C. For TNT, characteristic absorption peaks are present at 1.6 THz and 2.17 THz [39]. One can easily see that the peak at 30°C has a higher absorption coefficient around 7.4 cm^{-1} and decreases to 6 cm^{-1} at 50°C and almost becomes 4.85 at 70°C. After crossing this temperature, the peak shows an unusual reverse trend. It also indicates the process of initiation of a slow release of NO_2 from the solid sample. Similarly, the absorption coefficent of the 2.17 THz peak is 10.65 cm^{-1}, which becomes 7.8 cm^{-1} at 50°C and 6.62 cm^{-1} at 70°C. The decreasing trend of the absorption coefficient with respect to temperature also appears in the form of a redshift toward the left side at 70°C. This redshift effect is due to a hot band transition peak at 2.2 THz, which has a higher value at 30°C. Therefore, the temperature-based recording of signature peaks clearly reflects the process of thermal loss of TNT molecules at high temperatures. In addition, temperature-based spectroscopy confirms the presence of some prominent signature peaks in a repeated manner, along with redshift. Two signature peaks located at 1.77 and 2.17 THz at 30°C get shifted to 1.722 and 2.097 THz at 70°C, respectively.

Figure 5(b) shows the temperature-dependent refractive index of TNT. The refractive index was recorded between 30°C and 70°C, and it is clear that there is very little variation in the refractive index up to 1.6 THz. The value of the refractive index between 30°C and 70°C almost overlaps and remains between 1.55 and 1.60. However, after 1.6 THz it shows great variation between 1.55 and 1.75. Similar types of changes are also visible in absorption coefficient data at 1.6 THz.

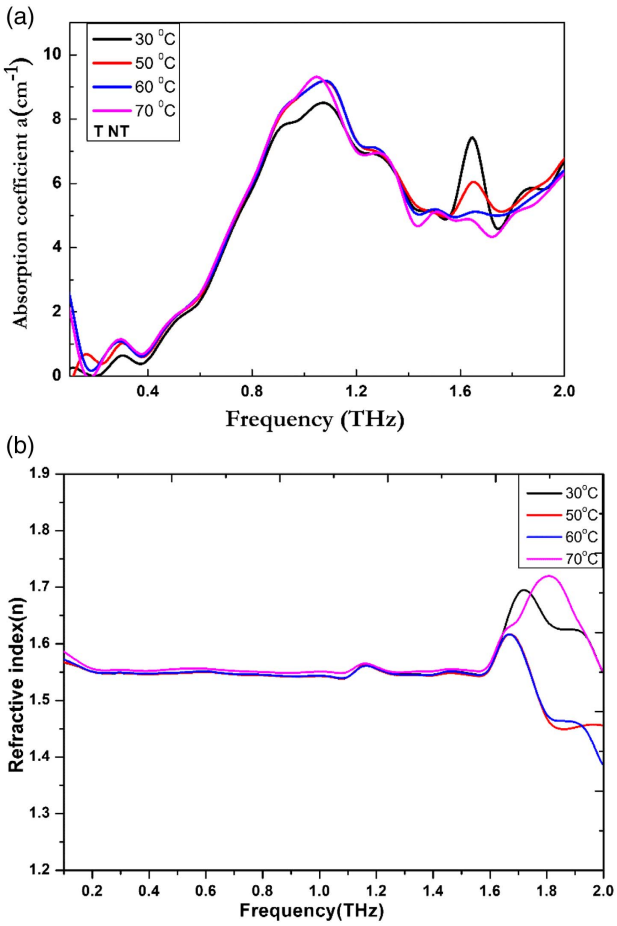

Fig. 5. (a) Temperature-dependent absorption coefficient of TNT, (b) temperature-dependent refractive index of TNT.

C. Temperature-Dependent Absorption Spectra and Refractive Index of NH_4NO_3

Figure 6(a) shows the temperature-dependent absorption spectra of NH_4NO_3. The frequency spectra clearly show the presence of a weak signature at room temperature. An earlier reported study of NH_4NO_3 was carried out at low temperature and demonstrated the conversion of the absorption peak into a kink at 1.7 THz [28,41,42]. However, when NH_4NO_3 is mixed with PTFE, it starts showing a strong signature even at room temperature. The absorption peaks at 1.2 and 1.4 THz are weaker than the peak at 1.78. It also shows a maximum intensity peak at 105°C below the melting point of NH_4NO_3.

Figure 6(a) shows the absorption spectrum of NH_4HO_3 recorded between 30°C and 150°C at 0.1–2.0 THz. To the best of our knowledge, it is the first demonstration of a signature peak of NH_4HO_3 at 1.73 THz. At room temperature, i.e., 30°C, it has an absorption coefficient of the order of 5.69 cm^{-1}. Since the spectra are recorded in transmission mode, these signature peaks are visible. Further, the effect of a redshift is also

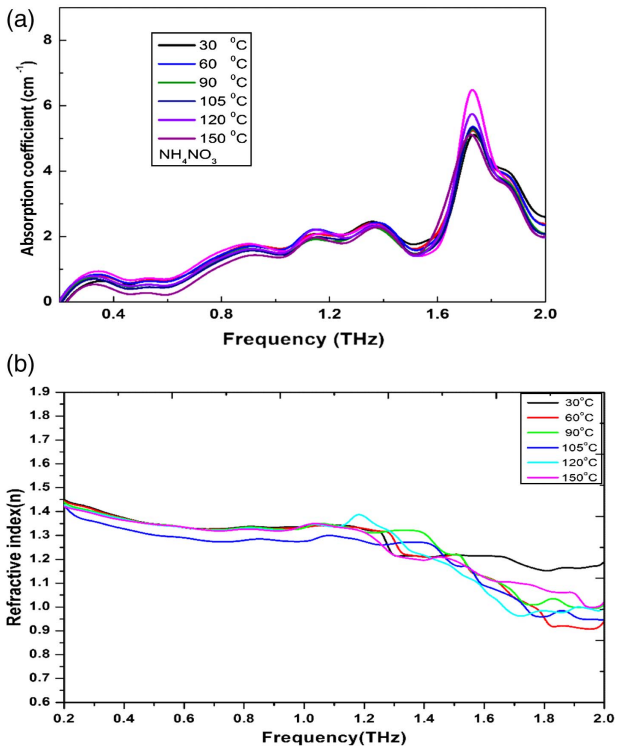

Fig. 6. (a) Temperature-dependent absorption coefficient of NH_4NO_3, (b) temperature-dependent refractive index of NH_4NO_3.

visible at 1.78 THz. The value of the absorption coefficient is of the order of 5.27 cm^{-1} between 60°C and 90°C. It is further shifted toward 1.722 THz with a corresponding absorption coefficient of 5.05 cm^{-1} between 120°C and 150°C, respectively. The NH_4NO_3 is a very stable inorganic aqua molecule due to ionic bonds. Therefore, it does not show a similar type of decomposition behavior and strong absorption like RDX and TNT [43]. As a result, the redshift effect is not very prominent.

Figure 6(b) shows the temperature-dependent refractive index of NH_4NO_3. The refractive index is recorded between 30°C and 150°C, and it is clear that little variation exists in the refractive index up to 1.3 THz. The value of the refractive index remains between 1.42 and 1.40. However, after 1.3 THz the value of the refractive index shows a fall with respect to temperature and decreases from 1.4 to 1.0. Similar types of changes are also visible in the absorption coefficient data at 1.3 and 1.6 THz.

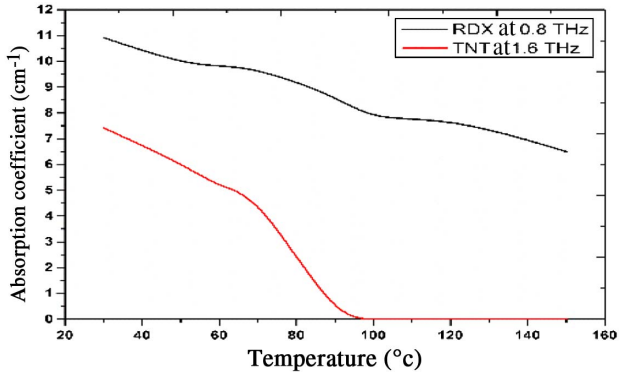

Fig. 7. Variation of absorption coefficients of RDX and TNT with temperature.

Table 1. Absorption Coefficient, Signal Sensitivity, and Sample Thickness Data for the Different Samples

Sample Pellet Name	Thickness of Pellet (mm)	THz Peak Value (a.u.)	Absorption Coefficient (cm^{-1}) at Room Temperature
RDX	1.91	1.83×10^{-4}	11.2
TNT	1.97	3.4×10^{-4}	9.98
NH_4NO_3	2.1	1.73×10^{-5}	5.67

Figure 7 shows the variation in the values of the absorption coefficients of characteristic peaks of RDX and TNT with respect to temperature. Since RDX is more stable and stronger than TNT, the loss of NO_2 takes place in multiple steps. This is also reflected in the upper curve, where the value of the absorption coefficient falls gradually from 11 to 7.7 cm^{-1}, whereas TNT shows a direct fall from 7.5 to 0 cm^{-1} after crossing the melting point.

5. SENSITIVITY AND LIMITATIONS

We have compiled the sample thickness, signal sensitivity, and absorption coefficient data of the three explosives in Table 1.

La Spada and Vegni studied a metamaterial-based wideband electromagnetic wave absorber with normal incidence and thickness dependency and reported notch action at 185 THz with normal incidence [5]. In our case it is evident from the table that the absorption coefficient is completely material dependent and more for RDX. We detected 10 mg of RDX in PTFE matrix, which shows a 5 cm^{-1} absorption coefficient value. Further improvisation is needed to reduce the quantity of the sample. In the present experiment, the THz beam spot size is 6 mm, and we require a pellet with a minimum size of 8.0 mm. Therefore, we are required to select suitable parabolic mirrors to reduce the spot size of the order of 2.0 mm, which will also help reduce the pellet diameter of the order of 2.0 mm and enhance the detection sensitivity. Similarly, the temperature-based study also helped to elucidate the redshift behavior of explosive molecules, which varies from sample to sample. Finally, a temperature-dependent theoretical model needs to be developed to explain the vibronic and rotational transition behavior of these molecules in the THz region, as existing density functional theory calculations are based at 0 K.

6. CONCLUSIONS

We have successfully recorded the temperature-dependent refractive indices and absorption coefficients of NH_4NO_3, TNT, and RDX explosives below their melting points. Also, we demonstrated the temperature-dependent redshift effect in these molecules. To the best of our knowledge, this is the first demonstration of the redshift effect and the process of slow thermal decomposition mechanisms of these explosives in the THz domain. This also helps characterize the explosive molecules. In addition, the changes in the strength of the THz signal of RDX in PTFE matrix are related to the concentration.

Funding. Defence Research and Development Organisation (DRDO), Ministry of Defence, and Govt. of India (ERIP/ER/1501138/M/01/319/D(RD)).

Acknowledgment. The authors thank the director of HEMRL, Pune, for providing pure explosive samples and the director of ACRHEM for constant support and encouragement during the experiment. Thanks are also due to Apar Industries Ltd. (Khattalwada, Umbargaon, Dist. Valsad, Gujrat-396120) for providing the high-grade PTFE (Teflon) powder used in the experiment.

REFERENCES

1. M. Tonouchi, "Cutting-edge terahertz technology," Nat. Photonics **1**, 97–105 (2007).
2. D. J. Funk, F. Calgaro, R. D. Averitt, M. L. T. Asaki, and A. J. Taylor, "THz transmission spectroscopy and imaging: application to the energetic materials PBX 9501 and PBX 9502," Appl. Spectrosc. **58**, 428–431 (2004).
3. J. A. Zeitler, K. Kogermann, J. Rantanen, T. Rades, P. F. Taday, M. Pepper, J. Aaltonen, and C. J. Strachan, "Drug hydrate systems and dehydration processes studied by terahertz pulsed spectroscopy," Int. J. Pharm. **334**, 78–84 (2007).
4. A. Vakil and N. Engheta, "Transformation optics using graphene," Science **332**, 1291–1294 (2011).
5. L. La Spada and L. Vegni, "Electromagnetic nanoparticles for sensing and medical diagnostic applications," Materials **11**, 603 (2018).
6. N. I. Zheludev and Y. S. Kivshar, "From metamaterials to metadevices," Nat. Mater. **11**, 917–924 (2012).
7. L. La Spada and L. Vegni, "Near-zero-index wires," Opt. Express **25**, 23699–23708 (2017).
8. Y. Lee, S.-J. Kim, H. Park, and B. Lee, "Metamaterials and metasurfaces for sensor applications," Sensors **17**, 1726 (2017).
9. A. G. Davies, A. D. Burnett, W. Fan, E. H. Linfield, and J. E. Cunningham, "Terahertz spectroscopy of explosives and drugs," Mater. Today **11**(3), 18–26 (2008).
10. M. Venkatesh, K. S. Rao, T. S. Abhilash, S. P. Tewari, and A. K. Chaudhary, "Optical characterization of GaAs photoconductive antennas for efficient generation and detection of terahertz radiation," Opt. Mater. **36**, 596–601 (2014).
11. K. S. Rao, A. K. Chaudhary, M. Venkatesh, K. Thirupugalmani, and S. Brahadeeswaran, "DAST crystal based terahertz generation and recording of time resolved photoacoustic spectra of N2O gas at 0.5 and 1.5 THz bands," Curr. Appl. Phys. **16**, 777–783 (2016).
12. M. Venkatesh, K. Thirupugalmani, K. S. Rao, S. Brahadeeswaran, and A. K. Chaudhary, "Generation of efficient THz radiation by optical rectification in DAST crystal using tunable femtosecond laser pulses," Indian J. Phys. **91**, 319–326 (2017).
13. P. Jepsen and B. Fischer, "Dynamic range in terahertz time-domain transmission and reflection spectroscopy," Opt. Lett. **30**, 29–31 (2005).
14. A. Khachatrian, S. Qadri, and J. S. Melinger, "High resolution THz spectroscopy of ammonium nitrate and potassium nitrate crystalline films," in *International Conference on Infrared, Millimeter, and Terahertz Waves* (2011).
15. T. Bardon, R. K. May, P. F. Taday, and M. Strlič, "Influence of particle size on optical constants from pellets measured with terahertz pulsed spectroscopy," IEEE Trans. Terahertz Sci. Technol. **6**, 408–413 (2016).
16. J. Chen, Y. Chen, H. Zhao, G. J. Bastiaans, and X.-C. Zhang, "Absorption coefficients of selected explosives and related compounds in the range of 0.1–2.8 THz," Opt. Express **15**, 12060–12067 (2007).
17. Y. Hu, P. Huang, L. Guo, X. Wang, and C. Zhang, "Terahertz spectroscopic investigations of explosives," Phys. Lett. A **359**, 728–732 (2006).
18. A. K. Chaudhary, K. S. Rao, and A. Sudheer Kumar, "Study of thermal decomposition mechanisms and absorption cross section of nitro-rich phenyl- and bis-series 1, 2, 3-triazoles," Appl. Opt. **55**, 817–824 (2016).
19. K. S. Rao and A. K. Chaudhary, "Investigation of thermal decomposition and stability of energetic 1, 2, 4-triazole derivatives using UV laser based pulsed photoacoustic technique," RSC Adv. **6**, 47646–47654 (2016).
20. F. Yehya, A. K. Chaudhary, D. Srinivas, and K. Muralidharan, "Study of thermal decomposition mechanisms and low-level detection of explosives using pulsed photoacoustic technique," Appl. Phys. B **121**, 193–202 (2015).
21. D. Grischkowsky, S. Keiding, M. van Exter, and C. Fattinger, "Far-infrared time-domain spectroscopy with terahertz beams of dielectrics and semiconductors," J. Opt. Soc. Am. B **7**, 2006–2015 (1990).
22. Y. Sonawane, O. Joshi, and M. Wagh, "Terahertz technology: a boon to tablet analysis," Indian J. Pharm. Sci. **71**, 235–241 (2009).
23. M. Walther, B. Fischer, M. Schall, H. Helm, and P. Jepsen, "Far-infrared vibrational spectra of all-trans, 9-cis and 13-cis retinal measured by THz time-domain spectroscopy," Chem. Phys. Lett. **332**, 389–395 (2000).
24. J. Barber, D. E. Hooks, D. J. Funk, R. D. Averitt, A. J. Taylor, and D. Babikov, "Temperature-dependent far-infrared spectra of single crystals of high explosives using terahertz time-domain spectroscopy," J. Phys. Chem. A **109**, 3501–3505 (2005).
25. I. Abid, W. Chen, J. Yuan, A. Bohloul, S. Najmaei, C. Avendano, R. Péchou, A. Mlayah, and J. Lou, "Temperature-dependent plasmon-exciton interactions in hybrid Au/$MoSe_2$ nanostructures," ACS Photon. **4**, 1653–1660 (2017).
26. T. Trzcinski, N. Palka, and M. Szustakowski, "THz spectroscopy of explosive-related simulants and oxidizers," Bull. Pol. Acad. Sci. Tech. Sci. **59**(4), 445–447 (2012).
27. K. Tanaka, H. Hirori, and M. Nagai, "THz nonlinear spectroscopy of solids," IEEE Trans. Terahertz Sci. Technol. **1**, 301–312 (2011).
28. M. A. Jarzembski, M. L. Norman, K. A. Fuller, V. Srivastava, and D. R. Cutten, "Complex refractive index of ammonium nitrate in the 2–20-μm spectral range," Appl. Opt. **42**, 922–930 (2003).
29. A. K. Chaudhary, A. M. Rudra, P. Kumbhakar, and G. C. Bhar, "Generation of coherent tunable deep UV radiation for detection and absorption studies of explosives RDX and TNT," J. Appl. Spectrosc. **74**, 571–577 (2007).
30. R. Feng, W. Li, Q. Zhou, K. Mu, L. Zhang, and C. Zhang, "Terahertz spectroscopic investigations of explosives and the related compounds," Proc. SPIE **7158**, 71580W (2009).
31. E. Brunol, F. Berger, M. Fromm, and R. Planade, "Detection of dimethyl methylphosphonate (DMMP) by tin dioxide-based gas sensor: response curve and understanding of the reactional mechanism," Sens. Actuators B Chem. **120**, 35–41 (2006).
32. D. G. Allis, J. A. Zeitler, P. F. Taday, and T. M. Korter, "Theoretical analysis of the solid-state terahertz spectrum of the high explosive RDX," Chem. Phys. Lett. **463**, 84–89 (2008).
33. G. Winnewisser, "Spectroscopy in the terahertz region," Vibr. Spectrosc. **8**, 241–253 (1995).
34. Y. C. Shen, P. C. Upadhya, E. H. Linfield, and A. G. Davies, "Temperature-dependent low-frequency vibrational spectra of purine and adenine," Appl. Phys. Lett. **82**, 2350–2352 (2003).
35. M. Hangyo, T. Nagashima, and S. Nashima, "Spectroscopy by pulsed terahertz radiation," Meas. Sci. Technol. **13**, 1727–1738 (2002).
36. A. K. Azad, V. H. Whitley, K. E. Brown, T. Ahmed, C. J. Sorensen, and D. S. Moore, "Temperature dependent terahertz properties of energetic materials," Proc. SPIE **9856**, 98560W (2016).
37. B. M. Fischer, H. Helm, and P. U. Jepsen, "Chemical recognition with broadband THZ spectroscopy," Proc. IEEE **95**, 1592–1604 (2007).
38. J. F. Federici, B. Schulkin, F. Huang, D. Gary, R. Barat, F. Oliveira, and D. Zimdars, "THz imaging and sensing for security applications—explosives, weapons and drugs," Semicond. Sci. Technol. **20**, S266–S280 (2005).
39. W. H. Fan, A. Burnett, P. C. Upadhya, J. Cunningham, E. H. Linfield, and A. G. Davies, "Far-infrared spectroscopic characterization of explosives for security applications using broadband terahertz time-domain spectroscopy," Appl. Spectrosc. **61**, 638–643 (2007).

40. Y. C. Shen, T. Lo, P. F. Taday, B. E. Cole, W. R. Tribe, and M. C. Kemp, "Detection and identification of explosives using terahertz pulsed spectroscopic imaging," Appl. Phys. Lett. **86**, 241116 (2005).
41. R. T. Hall, D. Vrabec, and J. M. Dowling, "A high-resolution, far infrared double-beam lamellar grating interferometer," Appl. Opt. **5**, 1147–1158 (1966).
42. A. Sengupta, A. Bandyopadhyay, J. F. Federici, and R. B. Barat, "Study of morphological effects on terahertz spectra using ammonium nitrate," in *Optical Terahertz Science and Technology* (Optical Society of America, 2005), paper ME6.
43. R. M. Doherty and D. S. Watt, "Relationship between RDX properties and sensitivity," Propell. Explos. Pyrotech. **33**, 4–13 (2008).

This is an open access article published under an ACS AuthorChoice License, which permits copying and redistribution of the article or any adaptations for non-commercial purposes.

ACS OMEGA

Article

Cite This: ACS Omega 2020, 5, 2541−2551

Time-Domain Terahertz Spectroscopy and Density Functional Theory Studies of Nitro/Nitrogen-Rich Aryl-Tetrazole Derivatives

Damarla Ganesh,[†,⊥] Elaprolu Narsimha Rao,[†,⊥] Mottamchetty Venkatesh,[†,§] Kommu Nagarjuna,[†] Ganapathy Vaitheeswaran,[†,‡] Akhila K. Sahoo,[†,∥] and Anil K. Chaudhary*[,†]

[†]Advanced Center of Research in High Energy Materials (ACRHEM), [‡]School of Physics, and [∥]School of Chemistry, University of Hyderabad, Prof. C. R. Rao Road, Gachibowli, Hyderabad 500 046, Telangana, India

[§]The Guo China-US Photonics Laboratory, State Key Laboratory of Applied Optics, Changchun Institute of Optics, Fine Mechanics and Physics, Chinese Academy of Sciences, Changchun 130033, China

ABSTRACT: The paper reports the time-domain THz spectroscopy studies of noncentrosymmetric energetic nitro/nitrogen-rich aryl-tetrazole high-energy molecules. The fingerprint spectra in the THz domain reveal the role of different functional groups attached to position "1" of the tetrazole moiety, which controls the energetic properties. These responses are deliberated through density functional theory (DFT) calculations. The synthesized aryl-tetrazoles exhibit high positive heat of formation (369−744 kJ/mol), high detonation velocities, and pressures (D_v: 7734−8298 m·s^{-1}; D_p: 24−28 GPa) in comparison to the noncentrosymmetric 2,4,6-trinitrotoluene (TNT). These compounds exhibit variation in the refractive indices and absorption between 0.1 and 2.2 THz range. The DFT studies at the molecular and single-crystal level (using plane wave pseudo potential method) endorse in detecting these bands (with ∼1% deviation). The calculated vibrational frequencies and linear optical properties are found to have good agreement with the experimental data in UV−visible and THz regions.

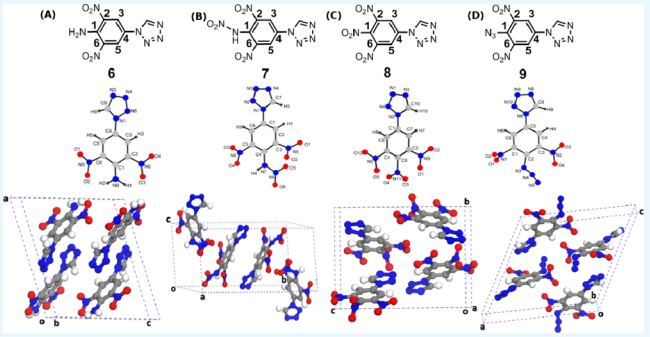

INTRODUCTION

The electromagnetic radiation between 0.1 and 3.0 THz range receives special attention in telecommunication industries because of broad band communication. In addition, it has the ability to pass through paper, leather, plastic, rubber, and different types of organic nonpolar packing materials including semiconductors, explosives, drugs, and biomolecules without ionizing the test sample. Therefore, THz-based spectroscopy and imaging are an effective means for detection of concealed objects and play a very significant role in home land security, defence, and medical fields. Because the THz spectrum lies between 100 and 5.0 cm^{-1} range which covers the weak vibrational frequency of organic molecules, the technique provides important information about the structural dynamics and intermolecular vibrations of high energy molecules (HEMs) and also helps to assign the periodicity of the materials through polymorphism and phase transition.[1−5]

In view of the importance of the time-domain THz spectroscopy technique and density functional theory (DFT)-based theoretical approach help us to study the structure−properties and correlation of HEMs.[17,18] Our group has also explored different types materials such as LT/SIGaAs-based photoconductive antenna and organic and semiconductor crystals for THz generation and its application in time-domain spectroscopy of HEMs.[19−22] Because tetrazole derivatives show superior energetic properties as compared to the other five-membered azole moieties because of high contents of nitrogen and higher value of positive heat of formation, their physical properties are comparable with premium explosives like Research department explosive (RDX) and 2,4,6-trinitrotoluene (TNT).[6−10,27,28] However, most of the reported tetrazole derivatives are very sensitive to impact and friction.[11−13] Pellizzeri et al.[35] reported the polymorphic characterization of 5(4-pyridyl)tetrazole using time-domain THz spectroscopy and solid-state DFT. A deliberation for the synthesis of nitro/nitroamino/azido-substituted aryl tetrazole derivatives, such as 2,6-dinitro-4-(1*H*-tetrazol-1-yl)aniline ($C_7H_5N_7O_4$) (6), *N*-(2,6-dinitro-4-(1*H*-tetrazol-1-yl)phenyl)nitramide ($C_7H_4N_8O_6$) (7), 1-(3,4,5-trinitrophenyl)-1*H*-tetrazole ($C_7H_3N_7O_6$) (8), and 1-(4-azido-3,5-dinitrophenyl)-1*H*-tetrazole ($C_7H_3N_9O_4$) (9) are recently reported because these compounds exhibit better energetic properties than TNT and are comparable to RDX. The important parameters are comprised in Table 1. It is interesting to see that all these reported compounds are crystalline in nature and can be used as an energetic plasticizer in rocket propulsion applications because of their good oxygen balance (OB %). For example, compounds "6", "7", "8", and "9" possess OB (%) of the order of

Received: December 3, 2018
Accepted: May 13, 2019
Published: February 7, 2020

Downloaded via UNIV OF HYDERABAD on July 24, 2020 at 08:44:23 (UTC).
See https://pubs.acs.org/sharingguidelines for options on how to legitimately share published articles.

© 2020 American Chemical Society

DOI: 10.1021/acsomega.8b03383
ACS Omega 2020, 5, 2541−2551

Table 1. Energetic Properties of 6−9 Compounds[a]

compound	(ρ)	D_v	D_p
2,6-dinitro-4-(1*H*-tetrazol-1-yl)aniline (6)	1.75	7899	24.1
N-(2,6-dinitro-4-(1*H*-tetrazol-1-yl)phenyl) nitramide (7)	1.78	8208	28.0
1-(3,4,5-trinitrophenyl)-1*H*-tetrazole (8)	1.79	8298	28.4
1-(4-azido-3,5-dinitrophenyl)-1*H*-tetrazole (9)	1.66	7734	26.2
TNT	1.65	6881	19.5
RDX	1.80	8795	34.9

[a]Here ρ (in g·cm^{-3}), D_v (in m·s^{-1}), D_p (in GPa) are crystal density, detonation velocity and detonation pressure reported from ref 16.

−79.62, −54.02, −54.06, and −66.38%, respectively. In addition, their corresponding densities ρ (in g·cm^{-3}), high detonation velocities D_v (in m·s^{-1}) and detonation pressure D_p (in GPa) are shown in Table 1. We also compared the important chemical and physical parameters with well-known energetic plasticizer, that is, bis(2-fluoro-2,2-diniroethyl)formal (it possess OB % = −74.0%, D_v = 7500 m·s^{-1}, D_p = 25 GPa).[14] However, the functional group attached to position "1" of the molecule as shown in Figure 1 not only influences the energetic properties of the molecules but also is responsible for the transition of crystalline to the amorphous phase which is also reflected in terms of change in the refractive index and absorption coefficient. Moreover, all these aryl-tetrazole derivatives are noncentrosymmetric with space groups $P2_1/C$ and $P2_12_12_1$. Therefore, we intended to study the structure−property correlations of these molecules through experiments and theory. This will help us in examining the potential of terahertz generation, detection, and nonlinear optical (NLO) response. Here, we have discussed the THz time-domain, UV−visible spectroscopic studies of the energetic polynitro-arene-tetrazole derivatives.[15] The possible reasons behind the optical response through DFT calculations both at molecular and solid levels are also provided. The experimental crystal structures are shown in Figure 1, and the corresponding energetic properties are comprised in Table 1 for reference.

EXPERIMENTAL SETUP AND SAMPLE PREPARATION

The sample pellets of 12 mm diameter of weight 500 mg were prepared by mixing 100 mg of sample with 400 mg of Teflon [polytetrafluoroethylene (PTFE)] powder. Particle sizes are comparable with far infrared (FIR) wavelength which leads to scattering losses from the surface of the pellets. This can be minimized by mixing the compound and PTFE powder with ethanol solution and subsequently grounding with mortar to make a homogeneous mixture. The mixture was dried for half an hour before subjecting to press mills. The whole mixture was loaded into a die and pressed with 2 tons of hydraulic pressure. The diameter and thickness of pellets are 12 and 2mm, respectively. A pure Teflon pellet of identical size is also prepared for reference. Figure 2 shows the experimental layout

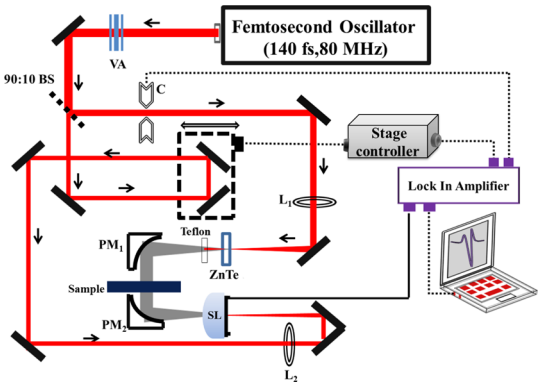

Figure 2. Schematic diagram of our terahertz time-domain spectroscopy experimental setup.

of THz generation and detection. A Ti:sapphire laser-tunable oscillator laser with pulse duration 140 fs at a repetition rate of 80 MHz (coherent chameleon ultra-II made) was used as a pumping source. Using a 90:10 beam splitter, the laser beam was split into a pump and probe. A transmitted pump beam is used for pumping the ZnTe crystal for terahertz generation. It is generated by the optical rectification process. A Teflon sheet was

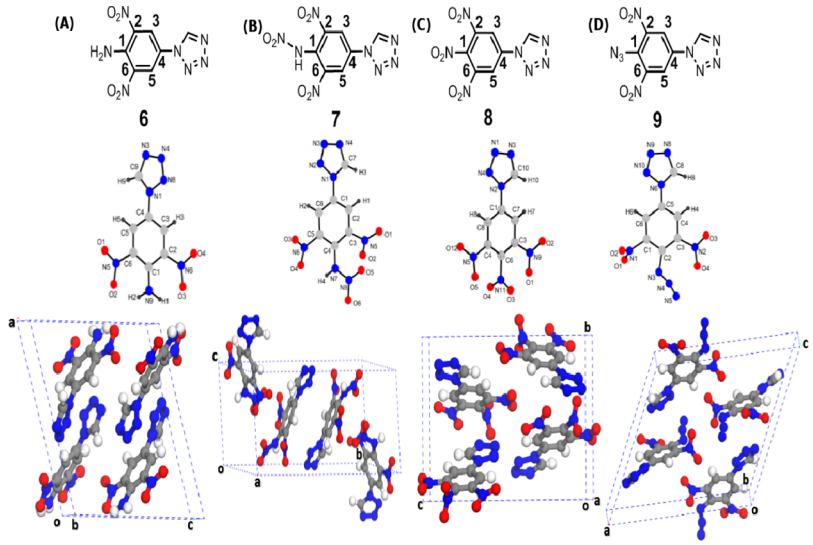

Figure 1. Molecular and experimental crystal structures[15] (from left to right) of (A) $C_7H_5N_7O_4$ (6), (B) $C_7H_4N_8O_6$ (7), (C) $C_7H_3N_7O_6$ (8), and (D) $C_7H_3N_9O_4$ (9). Here "*a*", "*b*", and "*c*" are lattice vectors.

DOI: 10.1021/acsomega.8b03383
ACS Omega 2020, 5, 2541−2551

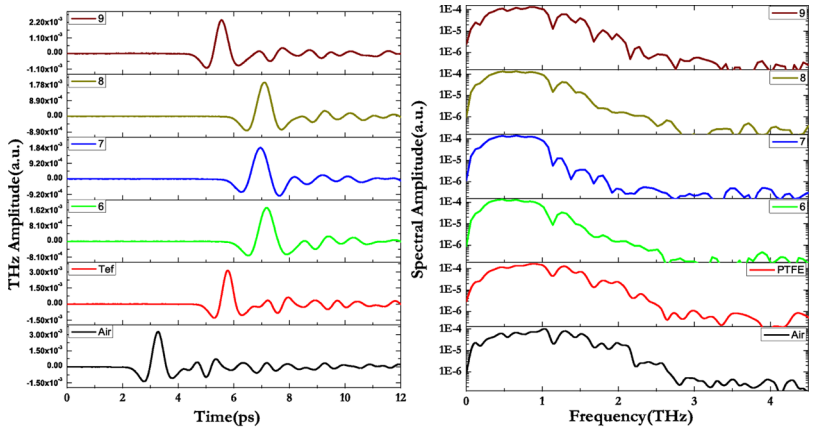

(a) a (b) b

Figure 3. (a)Time-domain THz spectra of tetrazole molecules, (b) corresponding frequency domain spectra.

used for filtering out the undesirable pump wavelength from terahertz. A half axis parabolic mirror is used to collimate and focus the generated THz radiation for detection using a photoconductive antenna (gap ≈ 5 μm, length ≈ 20 μm). In the detection arm, the reflected beam is passed through a linear translation stage and loosely focused on detecting antenna. The photoconductive antenna is connected to a low-noise current preamplifier which is fed to the lock-in amplifier (Stanford Research Systems, model no. SR830). A mechanical chopper operating at 1.5 kHz is used as a reference to the lock-in amplifier (Stanford Research Systems, model no. SR830). The data acquisition and motion control of delay stage are done by software using LabView program. All measurements were carried out at room temperature under ambient conditions. The THz temporal profile is measured by changing the delay of probe beam with respect to the THz pulse reaching to the antenna. Initially, the scan was done without any sample followed by pure Teflon pellet mounted in front of the antenna. The temporal data are converted to the frequency domain by performing fast Fourier transform (FFT). Material parameters like spectral transmittance, phase, and absorption coefficient are obtained from frequency domain data, whereas the refractive index can be obtained from both temporal and spectral data without using the Kramers–Kronig relation. Figure 3 shows terahertz temporal profile and corresponding FFT of air and Teflon pellet are shown in the inset.

Refractive index ($n(\omega)$) and absorption coefficient ($\alpha(\omega)$) were calculated from the FFT spectrum.[23] The intensity ratio of the transmitted radiation from the sample and reference provides the actual transmittance of the sample pellets and is given by eq 1

$$T = \frac{E_{\text{sample}}}{E_{\text{reference}}} \tag{1}$$

It is related to the complex refractive index $N = n + ik$, where the real part corresponds to the refractive index and the imaginary part is molar absorptivity. For measurement of the complex refractive index between 0.1 and 2.6 THz range, we have calculated the effective thickness of the sample distributed in the Teflon matrix using eq 2.

$$l = \frac{m}{\rho}\frac{4}{\pi D^2} \tag{2}$$

here, m = weight of the sample (100 mg), D = diameter of sample (12 mm), and ρ is density of the sample. Figure 2 shows the time-domain spectrum of explosive molecules. Because the pellets contain a mixture, the absorption coefficient (α) is calculated using eq 3.

$$\text{Absorption coefficient} = -\frac{1}{l}\ln\frac{T_{\text{m}}}{T_{\text{s}}} \tag{3}$$

where "l" is the effective thickness of the sample and T_{m} and T_{R} are the spectra of THz transmitted through material and reference samples, respectively. Because the particle sizes of both Teflon powder and sample are very small compared with the wavelength of radiation, one can neglect scattering losses. The refractive index is calculated using eq 4.

$$n = 1 + \frac{\delta\pi c}{2\pi\nu d} \tag{4}$$

where $\delta\pi$ is the phase difference between reference and sample, ν is frequency, d is thickness of pellet, and c is the velocity of light.

THEORETICAL METHODS

The solid-level theoretical calculations are performed with Cambridge Series of Total Energy (CASTEP) program,[29,30] whereas the molecular-level calculations are done with Gaussian-03 code. We have considered the experimental crystal structures reported by Kommu et al.[15] as input and optimized the systems using Broyden–Fletcher–Goldfarb–Shanno algorithm[31] with convergence thresholds for energy, force, stress, and maximum displacements as 5.0×10^{-6} (eV/atom), 0.01 eV/Å, 0.02 GPa, and 5.0×10^{-4} Å, respectively. The electronic Hamiltonian with the plane wave basis set with cutoff energy 550 eV, ultrasoft (US) pseudopotentials (for electron–ion interactions),[32] self-consistent field threshold 5.0×10^{-6} (eV/atom) with 3 × 5 × 3 Monkhorst–Pack[33] k-mesh (15 irreducible k-points) in the reciprocal space is used. Generalized gradient approximation (GGA), Perdew–Burke–Ernzerhof (PBE),[34] and dispersion correction Grimme (G06) scheme[36] are used to treat the strong and weak electron–electron interactions. The G06-optimized structure is used for linear optical property (absorption and refractive index spectra's) calculations. The zone centre vibrational properties (infrared (IR)-spectra) are calculated using density functional perturbation theory (DFPT)[38,39] approach by utilizing the norm conserving

DOI: 10.1021/acsomega.8b03383
ACS Omega 2020, 5, 2541−2551

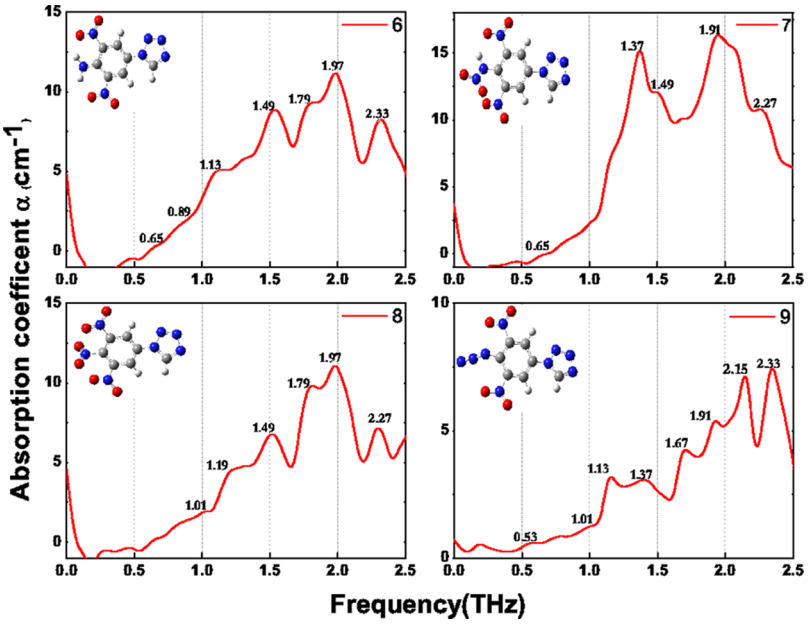

Figure 4. Experimental tera-hertz time-domain absorption spectra of 6, 7, 8, and 9. The calculated molecular level vibrational frequencies with Gaussian-03 are displayed as straight lines.

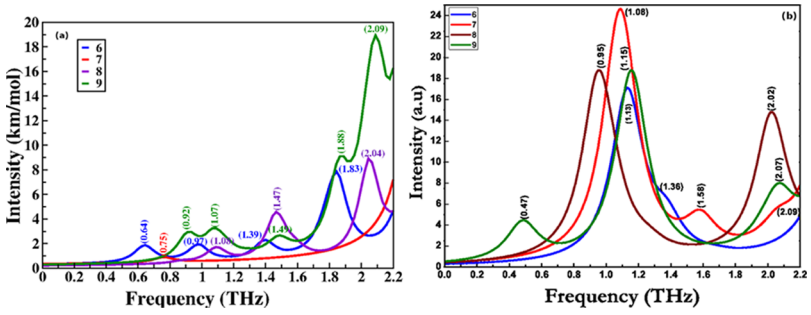

Figure 5. Calculated (a) single-molecule (b) single-crystal zone center vibrational (IR) spectra in 0.1−2.2 THz region of 6, 7, 8, and 9 using PBE + G06 dispersion-corrected method at the theoretical equilibrium structure.

pseudopotentials[40] with 830 eV cutoff energy. The valence electrons of the constituent atoms are considered as follows: H ($1s^1$), N($2s^2$ $2p^3$), C ($2s^2$ $2p^2$), O ($2s^2$ $2p^4$). The gas-phase single-molecule geometry optimizations and vibrational properties calculations are done using the B3LYP (Becke, 3-parameter, Lee−Yang−Parr) functional[41,42] with 6-311+G(d, p) polarized basis set as implemented in Gaussian-03.[24]

RESULTS AND DISCUSSION

Crystal Structure and Terahertz Time-Domain Response. All the chosen compounds ($C_7H_5N_7O_4$) (6), ($C_7H_4N_8O_6$) (7), ($C_7H_3N_7O_6$) (8), and ($C_7H_3N_9O_4$) (9) for the present study crystallize in noncentrosymmetric space groups with monoclinic symmetry except compound "8" which is orthorhombic.[15] These materials consist of z = 4 formula units/unit cell (i.e., compound "6"—92; compound "7"—100; compound "8"—92; and compound "9"—92 atoms/unit cell). Moreover, all of the atoms of compounds 6, 7, and 9 are located at "4e" atomic Wyckoff sites, whereas in compound "8", atoms are occupying "4a" Wyckoff site with full occupancy. Because of the change in the explosive functional groups (i.e. NH_2, NH−NO_2, NO_2, N_3) of these tetrazole derivatives, the lattice vectors show an increment in the following order: lattice vector "a": from compound "8" → "7" → "6" → "9"; lattice vector "b": from compound "9" → "6" → "8" → "7"; lattice vector "c": from compound "7" → "6" → "9" → "8"; and lattice angle β: from compound "8" → "7" → "6" → "9". From the experimental crystal structure, it is clear that all the studied compounds are naturally layered. The corresponding layers of compounds 6, 7, 8, and 9 are spread over xz, xy, yz, and xz planes, and the adjacent layers are stacked along x, y, z, and x directions. The change in the chemical composition and symmetry resulted in huge difference in their explosive nature (see Table 1) and stability. Moreover, the increase in the nitrogen and oxygen percentage in the studied compounds will definitely lead to change in their polarization. Hence, the noncentrosymmetric nature and change in the number of electrons strongly motivated us to investigate their terahertz optical responses, which are believed to be useful for their detection and nonlinear applications. The same was carried out using a time-domain terahertz spectroscopy setup.

The corresponding absorption spectra results of the studied compounds are shown in Figure 4. It is clear from the figure that (1) all of the compounds start absorbing radiation from 0.5 THz and high intensity absorption peaks are found between 1.0 and 2.5 THz range. (2) The studied materials show absorption in 0.5−2.5 THz energy window as follows: for compound "6"—0.65, 0.89, 1.13, 1.49, 1.79, 1.97, 2.33 THz; for compound "7"—0.65, 1.37, 1.49, 1.91, 2.27 THz; for compound "8"—1.01, 1.19,

DOI: 10.1021/acsomega.8b03383
ACS Omega 2020, 5, 2541−2551

Table 2. Calculated Ground-State Lattice Vectors (a and c, in Å), Volume (V, in Å^3) of 6, 7, 8, and 9 Using PBE and Dispersion-Corrected PBE + G06 along with Experimental Data[15]

symmetry	compound	parameter	PBE	PBE + G06	experiment
$P2_1/C$	6	a	14.593	12.941	12.780
(z = 4)		b	7.278	7.067	7.1353
(monoclinic)		c	11.910	10.754	11.0435
		V	1144.690	934.862	948.6
		β	115.198	108.109	109.625
$P2_1/C$	7	a	8.233	7.871	7.9223
(z = 4)		b	19.821	18.690	18.5920
(monoclinic)		c	8.105	7.642	7.5610
		V	1286.70	1109.11	1100.77
		β	103.388	99.442	98.730
$P2_12_12_1$	8	a	8.317	7.528	7.6268
(z = 4)		b	11.086	10.518	10.5375
(orthorhombic)		c	14.154	13.654	13.5924
		V	1305.22	1081.33	1040.25
$P2_1/C$	9	a	14.724	14.249	13.9435
(z = 4)		b	7.104	6.872	6.9570
(monoclinic)		c	14.093	12.825	12.8193
		V	1367.89	1125.51	1104.4
		β	111.906	116.355	117.363

1.49, 1.79, 1.97, 2.27 THz; and for compound "9"—0.53, 1.01, 1.13, 1.37, 1.67, 1.91, 2.15, 2.33 THz. (3) Among these, compound "7" shows highest intensity peaks and hence is more polarizable, whereas compound "9" shows well-defined absorption peaks and hence is relatively more sensitive and easy to detect even at lower energies. (4) Moreover, the detection limit of the studied tetrazole compounds got increased from NH−NO_2 → NH_2 → NO_2 → N_3 explosive functional groups. These unique absorption spectra of studied compounds are considered to be their fingerprint spectra's in the terahertz domain. To understand these absorption peak frequency and intensity differences more clearly, we extended our focus toward the vibrational mode analysis using DFT calculations both at molecular and solid levels.

In the first step, we performed the molecular vibrational spectra calculations by using B3LYP/6-311+G(d,p) polarized basis set as implemented in Gaussian-03.[24] We have considered the experimental single-crystal X-ray diffraction structure as our input. The obtained frequencies do not show any imaginary part, which confirm the dynamical stability of all the studied compounds, and the corresponding results are plotted in Figure 5. The FIR absorption peaks of studied tetrazole molecules between 0.1 and 2.2 THz frequency window are observed at the following frequencies (as shown in Figure 5): for compound "6"—1.13, 1.36 THz; for compound "7"—1.08, 1.58, 2.09 THz; for compound "8"—0.95, 2.02 THz; and for compound "9"—0.47, 1.15, 2.07 THz. The obtained results show considerable deviation with respect to the experimentally measured frequencies. However, it is known that the vibrational spectrum in the THz range depends primarily on the structure of molecules and their intra- and intermolecular interaction. The weak interaction of molecules and intermolecular force result in the collective vibration mode under the THz range frequency. The low-frequency vibration in the THz range normally comes from the deformation, torsion, and bending of two or more molecules. As we performed the DFT calculations at the single-molecule level, the obtained vibrational spectrum in the 0.2−2.2 THz region can be attributed to the intramolecule vibrations alone. The preliminary mode analysis informs that the absorption peak of compound "6" located at 1.13 THz is attributed to torsional rotation of tetrazole moieties, and other two frequencies are due to wagging of NO_2 groups attached to the ring. The peak of compound "7" at 1.08 THz is attributed to torsional rotation of the tetrazole moiety. Similarly, the reduction in the first absorption peak (red shift) of compounds "7"(1.08), "8"(0.95), "9"(0.47) when compared to compound 6(1.13) are due to increase of the additional nitro group reduced mass of the molecule. The mode at 2.02 THz of compound "8" is attributed to the rotation of twist of NO_2, and the calculated low-frequency 0.95 THz mode is not clearly observed in the experimental spectrum, which could be due to the scattering losses. In case of compound "9", mode at 0.47 THz is observed due to collective rotation twists of all attached azide groups to the ring. Torsional rotation of the tetrazole moiety was observed at 1.15 THz. A torsional rotation of all functional groups except for tetrazole was observed theoretically at 2.07 THz. The difference in the intensity profiles of the studied molecules (Figure 5b) indicates the increment in the polarizability from compounds "6" → "9" → "8" → "7", which is contradicting with the experimental observations. However, the observed discrepancy between experimental and theoretical vibrational frequencies could be due to the omission of the effects from intermolecular interaction and temperature. Hence, we turned our attention to the solid-state-level DFT calculations of the present compounds of interest to incorporate the role of intermolecular interactions.

Initially, we optimized the experimental layered non-centrosymmetric crystal structures[15] using the GGA-PBE exchange correlation functional[34] as implemented in CASTEP.[29,30] The calculated ground-state lattice vectors, angles, and volumes along with experimental data are shown in Table 2. The obtained results show considerable deviation as compared to the experimental data and are as follows: for compound "6" → a(14.1%) > c(7.8%) > b(2.0%); for compound "7" → c(7.1%) > b(6.6%) > a(3.9%); for compound "8" → a(9.0%) > b(5.2%) > c(4.1%); and for compound "9" → c(9.7%) > a(5.5%) > b(2.1%). The crystals volume and crystallographic angles deviations are as follows: V: for compound "8" (25.4%) > "9"

DOI: 10.1021/acsomega.8b03383
ACS Omega 2020, 5, 2541−2551

Table 3. Calculated Zone-Center Low-Frequency Vibrational Modes (in cm^{-1}) of $C_7H_5N_7O_4$) (6), ($C_7H_4N_8O_6$) (7), ($C_7H_3N_7O_6$) (8), and ($C_7H_3N_9O_4$) (9)[a]

compound	exp	mode	frequency	symmetry	compound	exp	mode	frequency	symmetry
6		M14	66.64	Bg(R)	7		M06	25.36(21.68)	Bg(I)
		M13	62.05(65.71)	Au(I)			M05	24.29	Au(R)
		M12	61.61(59.70)	Au(I)			M04	13.08	Ag(R)
		M11	59.42(—)	Bu(I)					
		M10	55.27	Ag(R)					
	65.71	M09	48.52	Bg(R)					
	59.70	M08	46.47(49.70)	Bu(I)					
	49.70	M07	41.37	Ag(R)		63.71			
	37.69	M06	37.03	Bg(R)		49.70			
	29.68	M05	32.60(29.68)	Bu(I)		45.69			
	21.68	M04	21.37(21.68)	Au(I)		21.68			
8					9		M24	73.32	Bg(R)
							M23	72.90(71.71)	Au(I)
							M22	70.69	Bg(R)
		M21	73.23	A(R)			M21	70.15	Ag(R)
		M20	69.94(—)	B3(I + R)			M20	68.41(—)	Bu(I)
		M19	69.29	A(R)			M19	67.47(—)	Au(I)
		M18	68.05(—)	B1(I + R)			M18	63.90(63.71)	Au(I)
		M17	66.70(65.71)	B2(I + R)			M17	63.58	Ag(R)
		M16	62.07(—)	B3(I + R)			M16	56.89	Bg(R)
		M15	61.68(59.70)	A(R)			M15	52.97(55.70)	Au(I)
		M14	51.90(—)	B3(I + R)			M14	48.94(45.69)	Bu(I)
		M13	49.52(49.70)	B2(I + R)			M13	47.91	Ag(R)
		M12	47.28(—)	B1(I + R)			M12	46.24	Ag(R)
		M11	43.05(—)	B2(I + R)			M11	46.23	Bg(R)
		M10	39.06(39.69)	B1(I + R)		71.71	M10	41.42	Bg(R)
		M09	38.47	A(R)		63.71	M09	39.78(—)	Au(I)
	65.71	M08	35.90(—)	B2(I + R)		55.70	M08	37.28	Ag(R)
	59.70	M07	33.98(33.68)	B1(I + R)		45.69	M07	36.36(—)	Bu(I)
	49.70	M06	30.44	A(R)		37.69	M06	32.79	Ag(R)
	39.69	M05	29.73(—)	B3(I + R)		33.68	M05	31.65	Bg(R)
	33.68	M04	20.90	A(R)		17.67	M04	29.12(—)	Au(I)

[a]Here, IR active modes are denoted as "I", Raman active modes are denoted as "R", and IR + Raman active modes are denoted as "I + R".

(23.8%) > "6" (20.6%) > "7" (16.8%) and β: for compound "6" (5.0%) > "7" (4.7%) > "9" (4.6%); these results also reveal that the intermolecular interactions are dominant in the studied layered compounds as follows: for compound "6" (in xz plane) > "9" (in zx plane) > "8" (in xy plane) > "7" (in zx plane). This can be attributed to the difference in the arrangement of molecules in corresponding unit cells. As the vibrational properties are very sensitive to the lattice vectors, it is important to optimize the crystal's structure to a better accuracy by including various interatomic interactions.[35,48] Hence, to capture the weak interlayer nonbonded interactions [van der Waals (vdW), hydrogen bond], we optimized all the crystal structures with the dispersion-corrected Grimme functional, that is, PBE + G06.[36] The obtained results show very good agreement with the experimental data, and the deviations of all of the obtained lattice vectors, volumes, and β values are around ∼1% (see Table 2). Hence, the G06 optimization results confirm the crucial role of weak nonbonded interactions for finding the optimized structures. We have used these (G06) structures for our further vibrational property calculations which are very sensitive to the lattice vectors.

We have calculated the zone centre vibrational frequencies of all the compounds using DFPT approach. All of the required mode assignments from 0.1 to 2.2 THz are done, and the corresponding results are shown in Table 3. The compounds 6, 7, and 9 are isostructural and crystallized in the same point group with $C_{2h}(2/m)$ symmetry with $z = 4$ formula units (98 atoms/unit cell) except for compound "8" which is getting crystallized in $D_2(222)$ point group symmetry with 100 atoms/unit cell. Hence, there will be 276 − 3 = 273 vibrational modes for 6, 7, and 9 and 300 − 3 = 297 modes for compound "8". The group theory[37] representation for these acoustic (appear due to in-phase moment of atoms) and optical (appear due to out of phase moment of atoms) modes will be as follows

$$\Gamma_{acoustic}(6, 9) = A_u \oplus 2B_u$$

$$\Gamma_{optic}(6, 9) = 69A_g \oplus 68A_u \oplus 69B_g \oplus 67B_u$$

$$\Gamma_{acoustic}(7) = A_u \oplus 2B_u$$

$$\Gamma_{optic}(7) = 75A_g \oplus 74A_u \oplus 75B_g \oplus 73B_u$$

$$\Gamma_{acoustic}(8) = B_1 \oplus B_2 \oplus B_3$$

$$\Gamma_{optic}(8) = 69A_1 \oplus 68B_1 \oplus 68B_2 \oplus 68B_3$$

The calculated optical vibrational modes (273, 297) of the compounds are in good agreement with group theory representations. Among the 273 optical modes of compounds "6" and "9", 135 ($68A_u \oplus 67B_u$) are found to be IR (I) active and 138 modes ($68A_u \oplus 67B_u$) are found to be Raman (R) active. In

DOI: 10.1021/acsomega.8b03383
ACS Omega 2020, 5, 2541−2551

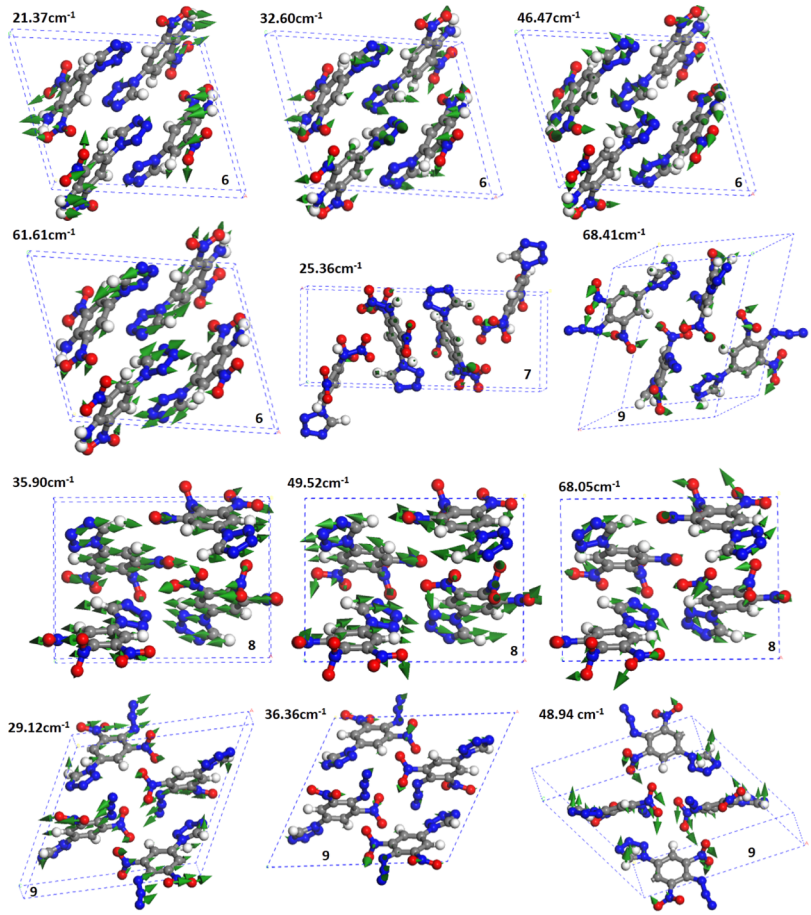

Figure 6. Few snapshot images of calculated vibrational frequencies (in cm^{-1}) at the solid level using PBE + G06.

case of compound "7", out of 297 optical modes, 147 modes ($74A_u \oplus 73B_u$) are found to be IR active and 150 modes ($75A_g \oplus 75B_g$) are Raman active. Interestingly, for compound "8", out of 273 optical modes, $69A_1$ modes are found to be purely Raman active and 204 modes ($68B_1 \oplus 68B_2 \oplus 68B_3$) are found to be both IR + Raman (I + R) active. Hence, we conclude that compound "8" is highly polarizable (more optically active) among the studied compounds. Because our current focus is on the terahertz response (0.1−2.2 THz range), mode assignments are done for these frequencies and the results are shown in Table 3. The corresponding vibrational spectra (IR) in 0.1−2.2 THz range is plotted in Figure 5. The snapshots of few vibrational modes are given in Figure 6 for future reference.

The mode assignment analysis reveals that the obtained frequencies of all the compounds between 0.1 and 2.2 THz range are mainly arising due to complete lattice translation associated with NO_2 groups and N_3 asymmetric stretching (see Figure 6), because of which asymmetric stretching in Tetrazole ring and trinitrobenzene has been observed. Few of the experimentally observed modes are well matched with the calculated symmetry-based IR frequencies (see Table 3). The main possible reasons for the observed discrepancies between theory and experimental frequencies and different broadening of the modes could be due to different scattering and temperature effects. Further, we have compared the experimental, solid-phase vibrational frequencies shown in Table 3 with the molecular phase. The results clearly indicate that most of the solid-level calculations match with the experimentally observed frequencies. The observed shift between the molecular-level and solid-level vibrational frequencies clearly indicates the dominant role of weak intermolecular, interlayer interactions via vdW and hydrogen bonding. To compare the intensity differences of the calculated frequencies, we have plotted the IR spectra in Figure 5. It is clear from the figure that intensities of the observed frequencies are dominant in the following order: compound "9" > "8" > "6" > "7". Hence, we can conclude that because of the different charge transfer mechanism of the azide group in the low-energy region, compound "9" is showing high peak intensity (polarizability) and hence is optically more sensitive. Similarly, in compound "8", because of the presence of an extra NO_2 group, electrons associated with all I + R active modes, it is showing next high polarizability. In case of compound "7", because of the presence of a strong N−N bond, we could observe only one peak in the studied terahertz range with lowest intensity among the studied compounds. However, compound "6" has weak C−N and H−N bonds because of which we are getting a good number of vibrational modes in the low energy region (<2.2 THz). Overall, we can conclude that because of the different charge transfer mechanisms, compound "9" possesses high optical sensitive (therefore unstable) nature, whereas compound "7" shows low optical sensitivity (highly stable) among the studied compounds. Other compounds show similar optical sensitivity in the studied region. In conclusion, it is easy to detect compound "8" and is optically stable than other studied noncentrosymmetric compounds. Hence, it may find possible applications in nonlinear optical domain also. Therefore, we further extended our attention to investigate the refractive index and birefringence of these compounds in the 0.1−2.2 THz range

DOI: 10.1021/acsomega.8b03383
ACS Omega 2020, 5, 2541−2551

which is a crucial parameter for obtaining proper phase matching in any nonlinear optical applications.

UV−Visible Response, Refractive Index, and Birefringence. The nitro/nitrogen-rich aryl-tetrazoles crystallize in the noncentrosymmetric space group, and it is very important to know the role of electronic contributions in the optical properties such as absorption, band gap, refractive index, and birefringence in the optical region of interest. Moreover, the THz-based study is meant for detection of explosives without ionizing the sample. Initially, we measured the absorption spectra of compounds using the UV/visible/NIR spectrometer (model: Cary 5000 with UMA attachment), and obtained results are compared with the theoretically calculated absorption spectra in [0 0 1] direction using the PBE-GO6 equilibrium structure as shown in Figure 7. The experimental results confirm

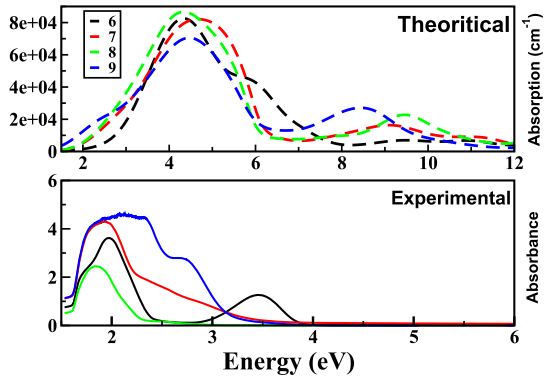

Figure 7. Experimental UV−visible absorption spectra of 6, 7, 8, and 9 compounds plotted along with the absorption spectra obtained at PBE + G06 equilibrium structure.

that compound "6" possesses a sharp absorption peak around 480 nm (2.58 eV), whereas absorption bands of other compounds such as "7", "8", and "9"are located at 450 nm (2.75 eV), 350 nm (3.54 eV), and 410 nm (3.02 eV), respectively. However, sharp absorption peaks for compounds "7", "8", and "9" are observed at 320 nm (3.87 eV), 280 nm (4.42 eV), and 475 nm (2.61 eV). This broadening may be attributed to the phonon contribution in optical transition (i.e., due to indirect band gap). However, the theoretically obtained absorption spectra show that sharp absorption peaks for compounds "6", "7", "8", "9" are located at 1.3, 1.2, 1.2, and 1.0 to 2.5 eV, respectively. The broadening of the absorption peak of compound "9" is attributed to the indirect band gap. Finally, it is clear from the experimental and theoretical results that the studied compounds possess a strong absorption band in the near-IR and THz region. Further, we have also calculated the frequency-dependent complex refractive index between 0.1 and 2.2 THz using eq 4. Etalon effects caused due to internal reflection were ineffective since we have not taken into account while calculating FFT. First, we have calculated the refractive index of Teflon by taking air as the reference.[25,26] Figure 3 shows the refractive index of Teflon between 0.1 and 2.2 THz range, and the value is 1.4 which is in good agreement with the literature values. Similarly, we calculated the average refractive index for compounds 6, 7, 8, and 9 (see Figure 8) and the obtained corresponding values are 1.65, 1.71, 1.72, and 1.81, respectively. We further verified these calculations by comparing with DFT results (see Figure 9). The calculations are done with great accuracy using US pseudopotentials, 380.0 eV energy

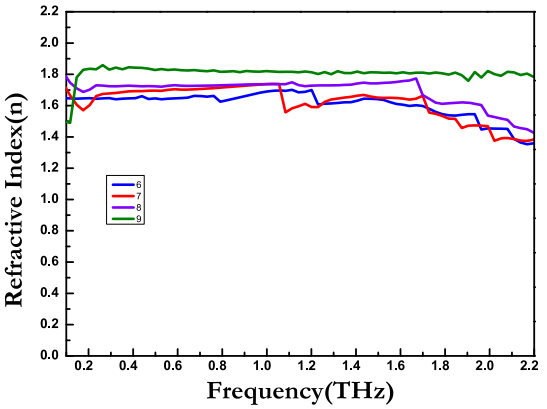

Figure 8. Experimental refractive index spectra comparison between 0 and 2.2 THz range of $C_7H_5N_7O_4$ (6), ($C_7H_4N_8O_6$) (7), ($C_7H_3N_7O_6$) (8), and ($C_7H_3N_9O_4$) (9).

cutoff, and 3 × 5 × 3 *k*-grid. As the chosen compounds crystallized in asymmetric space groups (monoclinic, orthorhombic), we could get different values of n_x, n_y, and n_z curves. All of the obtained results (experiment, DFT) within 0.1−2.2 THz energy window show reasonable agreement (Table 4), and the same are plotted in Figure 8. Moreover, the dispersion and intensity of the absorption curves are found to show considerable variation because of the change in the explosive functional group at position "1" on the tetrazole moiety. The theoretical difference in n_x, n_y, and n_z curves of studied compounds clearly indicate that all the compounds possess large optical anisotropy. Further, the theoretically calculated (time-independent DFT) absorption spectra shows considerable blue shift with respect to the experimental UV−visible spectra of the studied explosives, which is obvious due to the omission of local field effects and exciton effects in the present DFT calculations, and these deviations can be addressed properly by including the excitonic effects through time-dependent DFT calculations.[44]

The results in Figure 8 and Table 4 also confirm that the calculated average static refractive index ($(n = n_x + n_y + n_z)/3$) values of all the compounds are relatively good in agreement with the experimentally observed values. Normally, for monoclinic NLO crystals, the refractive indices show either $n_x > n_y > n_z$ (negative biaxial) or $n_z > n_y > n_x$ (positive biaxial) trend.[43] However, the results from Table 4 show the trend for compound "6": $n_y > n_z > n_x$, for compound "7": $n_z > n_x > n_y$, for compound "8": $n_z > n_x > n_y$, and for compound "9": $n_y > n_z > n_x$. These differences in the actual and obtained refractive indices can be attributed to the role of excitonic effects,[44] which are not accounted in the present study. For preliminary understanding, the birefringence (Δn) values of 6, 7, 8, and 9 compounds are calculated by taking the difference between the maximum value of refractive index to the minimum value from Table 4. The corresponding results show the following increment order: Δn (6) > Δn (8) > Δn (7) > Δn (9). Moreover, these values except for that of compound 9 are found to be closer to the well-known nonlinear crystal DAST (0.39, 0.55, and 0.64)[45] and higher than recently reported carbonate fluoride crystals $ABCO_3F$ (A = K, Rb, Cs; B = Ca, Sr, Pb) (Δn around 0.1056, 0.0887, 0.0921, 0.0966) crystal birefringence values,[46−49] which clearly indicates that the studied noncentrosymmetric explosive compounds may possess good phase matching applications in visible and near-IR regions. Further analyses on frequency-dependent second-harmonic response of these compounds will be useful in phase

DOI: 10.1021/acsomega.8b03383
ACS Omega 2020, 5, 2541−2551

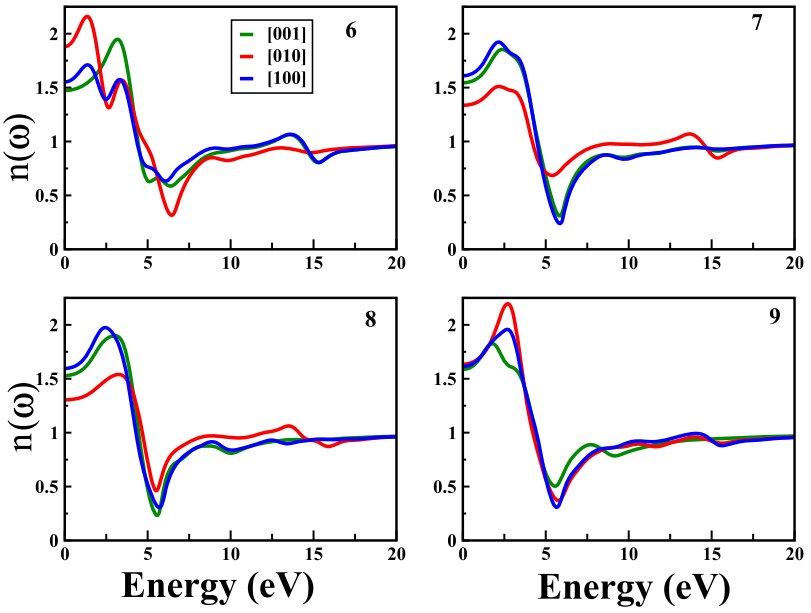

Figure 9. Theoretically obtained refractive index spectra (along *x*, *y*, *z* directions) of $C_7H_5N_7O_4$ (6), $C_7H_4N_8O_6$ (7), $C_7H_3N_7O_6$ (8), and $C_7H_3N_9O_4$ (9) at the PBE + G06 level.

Table 4. Experimental and DFT Calculated Refractive Indices (n) along [100], [010], and [001] Crystallographic Directions and Birefringence Values of 6, 7, 8, and 9

compound	n_x	n_y	n_z	Δn ($n_{max} - n_{min}$)	$n_{average}$	$n_{experiment}$
6	1.474	1.886	1.555	0.412(0.331)	1.63	1.65
7	1.546	1.337	1.611	0.274(0.065)	1.49	1.71
8	1.530	1.304	1.596	0.292(0.066)	1.47	1.72
9	1.589	1.635	1.616	0.046(0.019)	1.61	1.81

transition, sensitivity correlation studies, and designing new organic nonlinear optical materials in near future.

CONCLUSIONS

In summary, we have studied the linear and nonlinear optical properties of newly synthesized tetrazole molecules using time-domain terahertz spectroscopy, UV−visible−NIR spectroscopy, and DFT. We have also ascertained the absorption coefficients and refractive index between 0.1 and 2.2 THz range. In addition, we have performed single-molecule and single-crystal level DFT calculations. The obtained structural optimization results confirm the importance of nonbonded (vdW) interactions. The theoretically calculated zone center vibrational frequencies at the solid level are found to be good in agreement with the experimentally observed THz absorption bands. However, the single-molecule vibrational frequency-based results can be improvised by the incorporation of intermolecular, interlayer interactions. We have also explained the optical sensitivity correlations using vibrational frequencies. The electronic absorption, refractive index, and birefringence studies reveal the feasibility of phase-matched nonlinear optical frequency mixing device in the single-crystal form. The study also provides a good reference for growing organic nonlinear optical materials. We strongly believe that our present experimental and theoretical investigations on the studied explosives will open a new channel to design stable high-energy optical materials which may be used for different types of defence (detection purposes) and optical device applications.

AUTHOR INFORMATION

Corresponding Author

*E-mail: akcphys@gmail.com, anilphys@yahoo.com. Phone: 91 40 23138807.

ORCID

Ganapathy Vaitheeswaran: 0000-0002-2320-7667
Akhila K. Sahoo: 0000-0001-5570-4759
Anil K. Chaudhary: 0000-0003-1793-9930

Author Contributions

⊥Equal contribution.

Notes

The authors declare no competing financial interest.

ACKNOWLEDGMENTS

All the authors would like to thank DRDO, Ministry of Defence Govt. of India through ACRHEM under grant no. DRDO/18/1801/2016/01038:ARHEM-Phase-III for financial support. G.V. and E.N.R. would also like to acknowledge CMSD, University of Hyderabad, for providing computational facilities.

REFERENCES

(1) Tonouchi, M. Cutting-Edge Terahertz Technology. *Nat. Photonics* **2007**, *1*, 97−105.

(2) Davies, A. G.; Burnett, A. D.; Fan, W.; Linfield, E. H.; Cunningham, J. E. Terahertz Spectroscopy of Explosives and Drugs. *Mater. Today* **2008**, *11*, 18−26.

(3) Shen, Y. C.; Lo, T.; Taday, P. F.; Cole, B. E.; Tribe, W. R.; Kemp, M. C. Detection and Identification of Explosives Using Terahertz Pulsed Spectroscopic Imaging. *Appl. Phys. Lett.* **2005**, *86*, 241116.

DOI: 10.1021/acsomega.8b03383
ACS Omega 2020, 5, 2541−2551

(4) Parrott, E. P. J.; Fischer, B. M.; Gladden, L. F.; Jepsen, P. U.; Zeitler, J. A. Terahertz Spectroscopy of Crystalline and Non-Crystalline Solids. In *Terahertz Spectroscopy and Imaging*; Springer Series in Optical Sciences, 2013; Vol. *171*, pp 191−227.
(5) Brown, K. E.; Greenfield, M. T.; McGrane, S. D.; Moore, D. S. Advances in explosives analysis-part II: photon and neutron methods. *Anal. Bioanal. Chem.* **2016**, *408*, 49−65.
(6) Heppekausen, J.; Klapötke, T. M.; Sproll, S. M. Synthesis of Functionalized Tetrazenes as Energetic Compounds. *J. Org. Chem.* **2009**, *74*, 2460−2466.
(7) Kommu, N.; Ghule, V. D.; Kumar, A. S.; Sahoo, A. K. Triazole-Substituted Nitroarene Derivatives: Synthesis, Characterization, and Energetic Studies. *Chem.—Asian J.* **2014**, *9*, 166−178.
(8) Kumar, A. S.; Kommu, N.; Ghule, V. D.; Sahoo, A. K. Synthesis of trifluoromethyl-substituted N-aryl-poly-1,2,3-triazole derivatives. *J. Mater. Chem. A* **2014**, *2*, 7917−7926.
(9) Kommu, N.; Kumar, A. S.; Raveendra, J.; Ghule, V. D.; Sahoo, A. K. Synthesis, Characterization, and Energetic Studies of Polynitro Aryl-1,2,3-2 H-Triazoles. *Asian J. Org. Chem.* **2016**, *5*, 138−146.
(10) Kumar, A. S.; Ghule, V. D.; Subrahmanyam, S.; Sahoo, A. K. Synthesis of Thermally Stable Energetic 1,2,3-Triazole Derivatives. *Chem.—Eur. J.* **2013**, *19*, 509−518.
(11) Tang, Y.; Yang, H.; Wu, B.; Ju, X.; Lu, C.; Cheng, G. Synthesis and Characterization of a Stable, Catenated N11Energetic Salt. *Angew. Chem., Int. Ed.* **2013**, *52*, 4875−4877.
(12) Klapötke, T. M.; Piercey, D. G.; Stierstorfer, J. Amination of Energetic Anions: High-Performing Energetic Materials. *Dalton Trans.* **2012**, *41*, 9451−9459.
(13) Joo, Y.-H.; Shreeve, J. n. M. Nitroimino-Tetrazolates and Oxy-Nitroimino-Tetrazolates. *J. Am. Chem. Soc.* **2010**, *132*, 15081−15090.
(14) DeLuca, L. T.; Shimada, T.; Sinditskii, V. P.; Calabro, M. *Chemical Rocket Propulsion: A Comprehensive Survey of Energetic Materials*; Springer International Publishing: Switzerland, 2017; Vol. *2017*, pp 165−187.
(15) Kommu, N.; Balaraju, M.; Ghule, V. D.; Sahoo, A. K. Synthetic Manifestation of Nitro Substituted Tetrazole-N-(Hetero)Aryl Derivatives and Energetic Studies. *J. Mater. Chem. A* **2017**, *5*, 7366−7371.
(16) Sućeska, M. Calculation of Detonation Parameters by EXPLO5 Computer Program. *Mater. Sci. Forum* **2004**, *465*−*466*, 325−330.
(17) Venkataramudu, U.; Sahoo, C.; Leelashree, S.; Venkatesh, M.; Ganesh, D.; Naraharisetty, S. R. G.; Chaudhary, A. K.; Srinath, S.; Chandrasekar, R. Terahertz Radiation and Second-Harmonic Generation from a Single-Component Polar Organic Ferroelectric Crystal. *J. Mater. Chem. C* **2018**, *6*, 9330−9335.
(18) Narsimha Rao, E.; Vaitheeswaran, G. Structure-Property Correlation Studies of Potassium 4,4′-Bis(dinitromethyl)-3,3′-azofurazanate: A Noncentrosymmetric Primary Explosive. *J. Phys. Chem. C* **2019**, *123*, 10034.
(19) Venkatesh, M.; Rao, K. S.; Abhilash, T. S.; Tewari, S. P.; Chaudhary, A. K. Optical Characterization of GaAs Photoconductive Antennas for Efficient Generation and Detection of Terahertz Radiation. *Opt. Mater.* **2014**, *36*, 596−601.
(20) Mottamchetty, V.; Chaudhary, A. K. Improvised design of THz spectrophotometer using LT-GaAs photoconductive antennas, pyroelectric detector and band-pass filters. *Indian J. Phys.* **2016**, *90*, 73−78.
(21) Venkatesh, M.; Chaudhary, A. K. Generation of THz radiation from Low temperature Gallium Arsenide (LT-GaAs) photoconductive (PC) antennas using tunable femtosecond oscillator. In *12th International Conference on Fiber Optics and Photonics*, 2014, S5A.33.
(22) Damarla, G.; Venkatesh, M.; Chaudhary, A. K. Temperature-dependent terahertz spectroscopy and refractive index measurements of aqua-soluble and plastic explosives. *Appl. Opt.* **2018**, *57*, 8743−8750.
(23) Trzcinski, T.; Palka, N.; Szustakowski, M. THz Spectroscopy of Explosive-Related Simulants and Oxidizers. *Bull. Polish Acad. Sci. Tech. Sci.* **2011**, *59*, 445−447.
(24) Frisch, M. J.; Trucks, G. W.; Schlegel, H. B.; Scuseria, G. E.; Robb, M. A.; Cheeseman, J. R.; Scalmani, G.; Barone, V.; Mennucci, B.; Petersson, G. A.; et al. *Gaussian09*; Revision D.01; Gaussian Inc.: Wallingford CT, 2010.
(25) Feng, R.; Li, W.; Zhou, Q.; Mu, K.; Zhang, L.; Zhang, C. Terahertz Spectroscopic Investigations of Explosives and the Related Compounds. *Proc. SPIE—Int. Soc. Opt. Eng.*, 2009; Vol. *7158*, pp 1−9.
(26) Hangyo, M.; Nagashima, T.; Nashima, S. Spectroscopy by Pulsed Terahertz Radiation. *Meas. Sci. Technol.* **2002**, *13*, 1727−1738.
(27) (a) Singh, R. P.; Verma, R. D.; Meshri, D. T.; Shreeve, J. n. M. Energetic nitrogen-rich salts and ionic liquids. *Angew. Chem., Int. Ed.* **2006**, *45*, 3584−3601. (b) Steinhauser, G.; Klapötke, T. M. "Green" Pyrotechnics: A Chemists' Challenge. *Angew. Chem., Int. Ed.* **2008**, *47*, 3330−3347. (c) Singh, R. P.; Gao, H.; Meshri, D. T.; Shreeve, J. M. *High Energy Density Materials*; Klapotke, T. M., Ed.; Springer: Berlin, 2007; pp 35−83; (d) Klapötke, T. M. *High Energy Density Materials*; Klapotke, T. M., Ed.; Springer: Berlin, 2007; pp 85−122.
(28) (a) Klapötke, T. M.; Sabaté, C. M. Bistetrazoles: Nitrogen-Rich, High-Performing, Insensitive Energetic Compounds. *Chem. Mater.* **2008**, *20*, 3629−3637. (b) Joo, Y.-H.; Shreeve, J. n. M. High-density energetic mono- or bis(oxy)-5-nitroiminotetrazoles. *Angew. Chem., Int. Ed.* **2010**, *49*, 7320. (c) Stierstorfer, J.; Tarantik, K. R.; Klapötke, T. M. New Energetic Materials: Functionalized 1-Ethyl-5-aminotetrazoles and 1-Ethyl-5-nitriminotetrazoles. *Chem.—Eur. J.* **2009**, *15*, 5775−5792.
(29) Payne, M. C.; Teter, M. P.; Allan, D. C.; Arias, T. A.; Joannopoulos, J. D. Iterative minimization techniques forab initiototal-energy calculations: molecular dynamics and conjugate gradients. *Rev. Mod. Phys.* **1992**, *64*, 1045−1097.
(30) Segall, M. D.; Lindan, P. J. D.; Probert, M. J.; Pickard, C. J.; Hasnip, P. J.; Clark, S. J.; Payne, M. C. First-Principles Simulation: Ideas, Illustrations and the CASTEP Code. *J. Phys. Condens. Matter* **2002**, *14*, 2717−2744.
(31) Fischer, T. H.; Almlof, J. General Methods for Geometry and Wave Function Optimization. *J. Phys. Chem.* **1992**, *96*, 9768.
(32) Vanderbilt, D. Soft Self-Consistent Pseudopotentials in a Generalized Eigenvalue Formalism. *Phys. Rev. B: Condens. Matter Mater. Phys.* **1990**, *41*, 7892−7895.
(33) Monkhorst, H. J.; Pack, J. D. Special points for Brillouin-zone integrations. *Phys. Rev. B: Solid State* **1976**, *13*, 5188−5192.
(34) Perdew, J. P.; Burke, K.; Ernzerhof, M. Generalized Gradient Approximation Made Simple. *Phys. Rev. Lett.* **1996**, *77*, 3865−3868.
(35) Pellizzeri, S.; Delaney, S. P.; Korter, T. M.; Zubieta, J. Using Terahertz Spectroscopy and Solid-State Density Functional Theory to Characterize a New Polymorph of 5-(4-Pyridyl)Tetrazole. *J. Phys. Chem. A* **2014**, *118*, 417−426.
(36) Grimme, S. Semiempirical GGA-Type Density Functional Constructed with a Long-Range Dispersion Correction. *J. Comput. Chem.* **2006**, *27*, 1787.
(37) Kroumova, E.; Aroyo, M. I.; Perez-Mato, J. M.; Kirov, A.; Capillas, C.; Ivantchev, S.; Wondratschek, H. Bilbao Crystallographic Server : Useful Databases and Tools for Phase-Transition Studies. *Phase Transitions* **2003**, *76*, 155−170.
(38) Baroni, S.; de Gironcoli, S.; Giannozzi, P. Phonons and related crystal properties from density-functional perturbation theory. *Rev. Mod. Phys.* **2001**, *73*, 515−562.
(39) Milman, V.; Refson, K.; Clark, S. J.; Pickard, C. J.; Yates, J. R.; Gao, S.-P.; Hasnip, P. J.; Probert, M. I. J.; Perlov, A.; Segall, M. D. Electron and Vibrational Spectroscopies Using DFT, Plane Waves and Pseudopotentials: CASTEP Implementation. *J. Mol. Struct. THEOCHEM* **2010**, *954*, 22−35.
(40) Hamann, D. R.; Schlüter, M.; Chiang, C. Norm-Conserving Pseudopotentials. *Phys. Rev. Lett.* **1979**, *43*, 1494−1497.
(41) Becke, A. D. A new mixing of Hartree-Fock and local density-functional theories. *J. Chem. Phys.* **1993**, *98*, 1372−1377.
(42) Perdew, J. P.; Ernzerhof, M.; Burke, K. Rationale for Mixing Exact Exchange with Density Functional Approximations. *J. Chem. Phys.* **1996**, *105*, 9982−9985.
(43) Dmitriev, V. G.; Gurzadyan, G. G.; Nikogosyan, D. N. *Handbook of Nonlinear Optical Crystals*, 3rd ed.; Springer-Verlag: Berlin Heidelberg, 1999.
(44) Kronik, L.; Neaton, J. B. Excited-State Properties of Molecular Solids from First Principles. *Annu. Rev. Phys. Chem.* **2016**, *67*, 587−616.

DOI: 10.1021/acsomega.8b03383
ACS Omega 2020, 5, 2541−2551

(45) Wu, R. Z.; Fang, Z. X.; Liu, P.; Cao, Q. Z.; Qiu, M.; Li, Y.; Chen, W. K.; Huang, X.; Zhang, Y. F. Electronic Structures and Optical Properties of Organic DAST and DSTMS Crystal Materials. *Acta Phys. Chim. Sinica* **2013**, *29*, 2534.
(46) Zou, G.; Ye, N.; Huang, L.; Lin, X. Alkaline-alkaline earth fluoride carbonate crystals $ABCO_3F$ (A = K, Rb, Cs; B = Ca, Sr, Ba) as nonlinear optical materials. *J. Am. Chem. Soc* **2011**, *133*, 20001−20007.
(47) Narsimha Rao, E.; Appalakondaiah, S.; Yedukondalu, N.; Vaitheeswaran, G. Structural, Electronic and Optical Properties of Novel Carbonate Fluorides $ABCO_3F$ (A=K, Rb, Cs; B=Ca, Sr). *J. Solid State Chem.* **2014**, *212*, 171−179.
(48) Rao, E. N.; Vaitheeswaran, G.; Reshak, A. H.; Auluck, S. Effect of Lead and Caesium on the Mechanical, Vibrational and Thermodynamic Properties of Hexagonal Fluorocarbonates: A Comparative First Principles Study. *RSC Adv.* **2016**, *6*, 99885−99897.
(49) Narsimha Rao, E.; Vaitheeswaran, G.; Reshak, A. H.; Auluck, S. Role of Spin-Orbit Interaction on the Nonlinear Optical Response of $CsPbCO_3F$ Using DFT. *Phys. Chem. Chem. Phys.* **2017**, *19*, 31255−31266.

DOI: 10.1021/acsomega.8b03383
ACS Omega 2020, 5, 2541−2551

Taylor & Francis Group
an informa business

Search for keywords, authors, titles, ISBN | Search all titles

Login

Chemical Technology and Informatics in Chemistry with Applications

Edited By ***Alexander V. Vakhrushev, Omari V. Mukbaniani, Heru Susanto***

‹Back to book

Chapter Chapter 7 | 16 Pages

Thz Generation from Gallium Arsenide Semiconductor Surfaces and its Application in Spectroscopy

With ***M. Venkatesh, Ganesh Damarla, A. K. Chaudhary***

You currently do not have permission to access this title.
Please click 'Get Access' to see if you or your institution has access to this content.

GET ACCESS

This chapter reports the new approach for THz enhancement from semi-insulating (SI) and low-temperature gallium arsenide (LT-GaAs) semiconductor surfaces. The generated THz radiation is detected using photoconductive antennas (PCA). The obtained results from both types of semiconductor surfaces are compared and observed that the THz peak amplitude from semi-insulating gallium arsenide (SI-GaAs) was higher than the LT-GaAs surface. The effect of laser wavelength on generated THz peak amplitude is carried out. We have enhanced the efficiency of generated THz radiation from SI-GaAs using the combination of lens, BBO, and dual-wave plate (DWP). Further, the obtained THz radiation was used to record the transmittance of packing materials such as cardboard and plastic.

Optics Communications 453 (2019) 124366

Contents lists available at ScienceDirect

Optics Communications

journal homepage: www.elsevier.com/locate/optcom

Ultra-thin subwavelength film sensing through the excitation of dark modes in THz metasurfaces

Sabyasachi Banerjee [a,b], C.S. Amith [a], Deepak Kumar [a,c], Ganesh Damarla [d], Anil Kumar Chaudhary [d], Sanket Goel [b], Bishnu P. Pal [a], Dibakar Roy Chowdhury [a,*]

[a] Mahindra Ecole Centrale, Jeedimetla, Hyderabad, Telangana, 500043, India
[b] Department of Electrical and Electronics Engineering, BITS Pilani – Hyderabad, Jawahar Nagar, Shameerpet Mandal, Hyderabad, Telangana, 500078, India
[c] Department of Physics, Panjab University, Chandigarh, 160014, India
[d] ACRHEM, Hyderabad Central University Rd, CUC, Gachibowli, Hyderabad, Telangana 500046, India

ABSTRACT

We demonstrate ultra-subwavelength thin film sensing through experimental and numerical studies of the transmission characteristics of several symmetric and asymmetric planar split ring resonator (SRR) based terahertz metasurfaces coated with thin film of analyte layer(s). A sharp narrow-band dark mode resonance excited in the asymmetric metasurfaces is seen to be particularly very interesting to be exploited in thin film sensing, which is otherwise absent in the symmetric case. For this mode, our experiments clearly have demonstrated sensing of extreme subwavelength (close to thousandth part of the wavelength) thickness film. With the increasing thickness of the analyte layer a gradual red-shift of the resonance mode is observed. The sensitivities and figure of merit (FoM) of all the metasurfaces are derived and compared. The resonant dark modes in asymmetric metasurfaces are found to display substantially better FoM as compared to the typical dipolar modes.

1. Introduction

Metamaterials, by virtue of their unusual electromagnetic properties such as negative refractive index, cloaking [1–6] etc. have attracted considerable attention in the last two decades. Apart from these applications, metamaterials, particularly their two-dimensional variants namely, metasurfaces, form an excellent platform for thin film sensing. Despite the research boom in metasurfaces, the main impediments to the development of metasurface-based sensing devices have traditionally been Ohmic and radiative losses. However, asymmetric metamaterials can be potential candidates to resolve this problem. According to contemporary research, they seem to be more efficient in minimizing radiative losses while simultaneously displaying improved resonance quality factors over their corresponding symmetric structures [7–15].

Eigen resonance modes having noticeably weak interactions with the ambient environment have been called *Dark Modes*. These modes can exhibit high quality factors, and are dominated by magnetic dipoles and higher order multipoles. Though they are known to exist in symmetric split ring resonator (SRR) structures, but it is not straight forward to excite these modes directly with linearly polarized plane waves experimentally. These asymmetric SRRs based dark modes, can also be explained in terms of inherent Fano interferences as observed earlier [16], hence can lead to the excitation of sharp resonance dips in the frequency spectrum. Asymmetric SRR-based metasurfaces with high quality factors are extremely well suited for designing highly efficient THz sensing devices, and can result in other applications too [15,17–23].

In this work, we have designed, fabricated and characterized a symmetric and two asymmetric SRR-based metasurfaces. Thin films of polyimide have been deposited on top of the structures and the transmission characteristics of the hybrid structures have then been probed with terahertz time domain spectroscopy (THz-TDS) [24,25]. We have further extended our studies through numerical simulations with the commercially available numerical software, CST Microwave Studios. The experimental results demonstrated very good match with the simulation results and thereby motivated us to perform extensive studies on thin film sensing.

Various schemes have been proposed and demonstrated over the years for sensing in the terahertz domain, involving waveguide-based sensors [26], resonator-based terahertz sensors, etc. [17,20,27–36]. Metamaterials-based sensing through measurement of frequency shift, however, have few clear advantages over the former techniques, since their frequency response can be engineered according to requirement, and they are highly suitable for conventional THz-TDS probing owing to their arrayed homogeneous structures [37]. In this context, Xu et al. demonstrated that the introduction of high refractive index gold nanoparticles can improve the bio-sensing capabilities of THz metamaterials [38]. M. Islam et al. have reported a comprehensive study comparing the sensing efficiencies of different resonance modes excited in single split gap ring resonator-based THz metamaterials [18].

* Corresponding author.
E-mail address: dibakar.roychowdhury@mechyd.ac.in (D. Roy Chowdhury).

https://doi.org/10.1016/j.optcom.2019.124366
Received 29 May 2019; Received in revised form 23 July 2019; Accepted 9 August 2019
Available online 22 August 2019
0030-4018/' 2019 Elsevier B.V. All rights reserved.

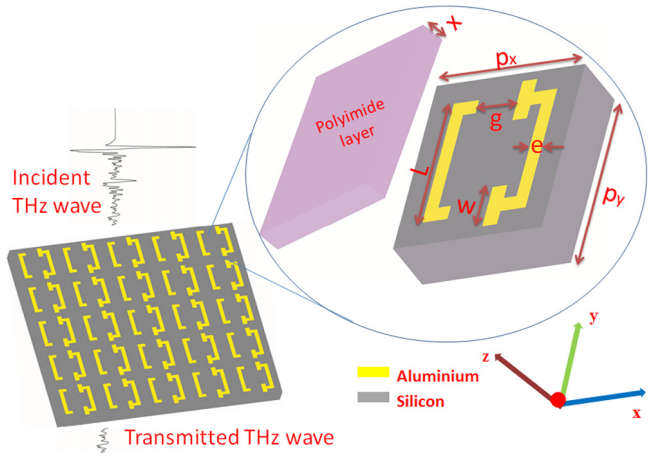

Fig. 1. Schematic of the proposed metasurface depicting incident and transmitted terahertz radiations through it. Split ring resonators are comprised of aluminum (yellow) on silicon (gray) substrate. A magnified view of a single metamolecule has been shown for clarity. The geometric parameters are w (plate length), L (resonator arm length), e (resonator arm width), g (split gap length), x (analyte thickness) and p_x, p_y (periodicity in x and y directions, respectively).. (For interpretation of the references to color in this figure legend, the reader is referred to the web version of this article.)

The refractive index of the analyte is varied for each particular deposited thickness to calculate the sensitivity, following which the Figure of Merit (FoM) of the corresponding resonance mode has also been calculated. In a quest for highly sensitive metamaterials, Gu et al. came up with a closed ring pair based free standing metamaterial structure, which displayed negative refractive index under normal incidence at a particular frequency range. In their case, the metamaterial was fabricated using double layer self-aligned photolithography [39]. A X-shaped perfect metamaterial absorber and its complementary design with four-fold rotational symmetry has been demonstrated as being better at sensing applications than their corresponding planar metasurfaces [40]. Recently, Chen et al. proposed and numerically investigated a stripe and groove corrugated comb shaped metamaterial, which employed spoof surface plasmons (SPPs) for refractive index and thickness sensing [41]. The novelty of our present proposed device lies in its simple structure (Fig. 1), the minimal complexity due to single step fabrication process, and the excitation of dark modes through exploitation of suitable geometrical asymmetry — features which have rarely been tapped into and combined for thin film sensing in previous attempts.

2. Fabrications, testing and simulations

We have fabricated three different sets of metamaterial samples (Sy, As1 and As2) on high resistivity undoped Silicon wafers. Pictures of the fabricated samples are shown in Fig. 2(a-d). The sample Sy consists of an array of symmetric split ring resonators (SRRs), with identical split gaps on opposite ends. For all our samples, unit cell periodicity (p_x, p_y, where $p_x = p_y$), the split gap (g), length of the metallic arm (L) and its width (e) were kept constant at 88 μm, 16 μm, 60 μm, and 8 μm, respectively. For the samples As1 and As2, we have intentionally introduced asymmetry into the structures by attaching plates of varying length 'w' on the terminal ends on one side of the split gap. For As1, w = 16 μm and for As2, w = 24 μm (see Fig. 2). Photolithography followed by standard development processes were implemented to create the above-mentioned sample patterns on the silicon wafers. Electron beam evaporation was employed to deposit aluminum of thickness 200 nm and subsequently, typical lift-off in acetone bath was used to realize the desired metasurfaces. Thin films of polyimide, of varying thickness x were spin coated onto the fabricated metasurfaces. The devices were hard baked using slow annealing steps from room temperature to 200 degrees Celsius to ensure uniform thickness of the analyte coating over the metasurfaces, following which they were characterized using terahertz time domain spectroscopy (THz-TDS).

The transmission characteristics of our samples were probed using THz-TDS in a dry environment at room temperature. In the current setup, a femtosecond laser (1560 nm, 100 MHz, ~60 fs) was used to generate terahertz pulses. The laser pulse is split into two parts, one part traveling to the terahertz emitter, the other part to the detector. Both the emitter and the detector are InGaAs/InP photoconductive switches, the former consisting of a 100 μm strip-line antenna while the latter has a 25 μm dipole antenna. A transient current is excited in the emitter by the ultrafast laser pulses, which in turn, produces electromagnetic wave packets with a broad spectrum in the terahertz range. The terahertz pulses thus generated, reach the receiver after transmitting through the samples. The receiver utilizes the "pump-probe" principle: the incident terahertz pulse undergoes a modulation while passing through the sample and the laser pulse probes this effect at the detector side. The frequency domain spectrum is then extracted through Fast Fourier transformation of the measured transmitted terahertz pulse. A blank silicon substrate of dimensions similar to that of the samples was also characterized and used for normalization of the measured transmitted pulse with the THz-TDS.

Computer Simulation Technology (CST) MICROWAVE STUDIO was used as a full wave numerical simulator to validate our experimental findings. CST's frequency domain solver has been employed to numerically simulate our deposited metamaterials. Tetrahedral meshing was found to be the most suitable option to configure the geometry due to the accuracy of the results and lower computational time required to generate them. Waveguide ports have been utilized to simulate the source and the detector. In our simulations, the electrical properties of the analyte (i.e. polyimide) have been defined by its electrical permittivity $\varepsilon = 3.5$, while that of the substrate (i.e. silicon) have been defined by $\varepsilon = 11.9$. Periodic boundary conditions have been adopted for the configuration.

3. Observations and discussions

3.1. Transmission properties

In this section, we examine the THz transmission properties of the designed metamaterials for both the orthogonal polarizations of the incident THz waves. In one set of experiments, the electric field polarization is kept parallel to the SRR arm, referred to henceforth as orientation 1 (O1), the results of which are shown in Fig. 3. In the other set, the electric field polarization is kept parallel to the gap, which we will refer to as orientation 2 (O2), results of which are shown in Fig. 4. Thin films of polyimide having various thicknesses are spin coated onto the metasurfaces. The resulting transmission properties are shown in Figs. 3 and 4 for three different polyimide thicknesses: 2.78 μm, 4.27 μm and 5.92 μm. For a systematic comparison, experimental data (plots a, c and e) along with the numerical simulations (plots b, d and f) are plotted in these two figures. Comparison of the two sets of plots clearly reveals that the experimental results closely match the simulations.

We observe from Figs. 3(a) and (b), that for the sample Sy in O1, the dipole mode resonance of the bare metasurface occurs at 0.748 THz frequency. Increase in thickness of the polyimide layer leads to a *red shift* in the resonant frequency. For O2 of the same sample, as shown in Fig. 4, we observe that the quadrupole mode resonance appears at 1.26 THz and a similar trend of red shift in resonance was observed for increasing polyimide thicknesses. Physically, these modes can be said to represent dipolar resonances, and in a latter section, we have described surface current distributions in support of this conjecture.

However, unlike Sy, for the samples As1 and As2, when the electric field is in O1 orientation, we observe two distinct resonances: a sharp narrow-band resonance (dark mode resonance) and a wide-band resonance (dipole resonance). This sharp resonance mode can be attributed

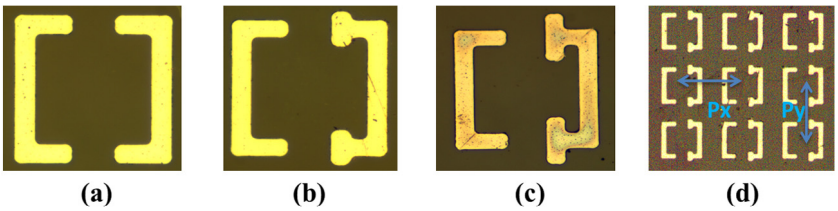

Fig. 2. Optical microscope images of the fabricated samples (a) symmetric SRR sample (Sy) (b) asymmetric SRR sample 1(As1) (c) asymmetric SRR sample 2(As2) (d) Metamaterial array of fabricated As1.

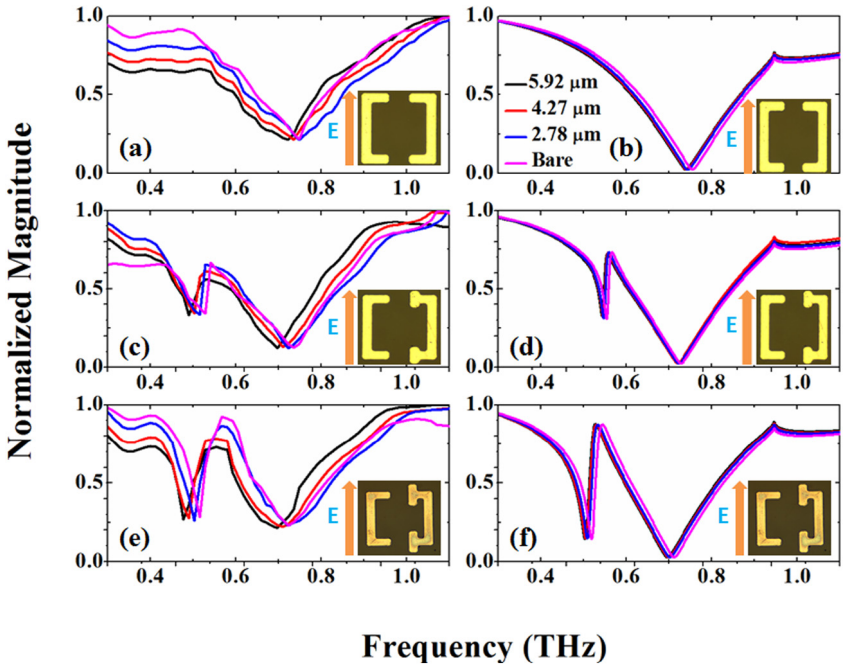

Fig. 3. Comparative plots of normalized vs. frequency when the electric field is parallel to the arm i.e. O1: (a) and (b) respectively represent experimental and simulation results, for the Sy sample. Similarly, (c) and (d) display results for As1 while (e) and (f) correspond to the same for As2.

to the excitation of dark plasmonic modes, which are non-radiative in nature resulting in strong field confinements, and are excited due to the introduction of asymmetry in symmetric SRR-based metamaterial structures [17]. The dark resonance mode is more pronounced in As2 compared to As1, due to the increased structural asymmetry in the former as compared to the latter.

In Figs. 3(c) and (d) we observe that the dark mode and dipole mode resonances for As1 occur at 0.52 THz and 0.73 THz, respectively for the bare metasurface. In case of the bare metasurface of As2, the first resonance occurs at 0.51 THz and the third occurs at 0.72 THz, as shown in Figs. 3(e) and (f). In case of O2, a resonance similar to the one excited for the Sy sample (quadrupole mode resonance), is seen to occur at 1.23 THz for As1 and at 1.20 THz for As2 as shown in Figs. 4 (c, d) and (e, f), respectively. All the higher order modes do not occur exactly at the same frequency because of the increased asymmetry in the structures.

Similar to Sy, the trend of all the resonances undergoing *red shift* with increasing polyimide thicknesses can be seen in As1 and As2 as well. This can be attributed to two factors. As the polyimide fills the capacitive gaps between the SRRs, their net capacitance is altered (effectively gets increased), resulting in a shift of the resonance frequency. Secondly, the confinement of the fringing fields at the capacitive gaps within the polyimide layer contributes to this behavior as well. However, the latter phenomenon also leads us to the sensing limitation for such a scheme as ours', since beyond a certain analyte thickness, the fringing field penetration disappears and no more appreciable shift in frequencies can be observed [42,43].

In case of As2 we have experimentally measured a difference of 1.6 μm thickness of polyimide layer using dark resonance mode (Fig. 2e). However, thinner layers of polyimide can be sensed through proper optimization of the polyimide coating process. Most importantly, it can be seen that such extremely thin film deep sub-wavelength (thousandth part of a wavelength) sensing is feasible through our design methodology for realization of thin metasurfaces for exploitation at THz frequencies.

3.2. Sensitivity

The sensitivity for thin film sensing of a metamaterial is calculated from the slope of the linear fitting function of frequency shift versus refractive index curve of the analyte [39]. Extensive simulations were conducted to observe the effects of varying the refractive index of the analyte layer above the metasurface. Resonance frequencies of the metamaterial were calculated for six different thicknesses of the polyimide layer: 2.78 μm, 4.27 μm, 5.92 μm, 10 μm, 15 μm and 20 μm and for each thickness, the refractive index of the polyimide was varied from 1 to 2. We observe distinct resonant peaks at distinct THz frequencies as we vary the refractive index of the analyte. Frequency shift here is defined as the difference between the resonance frequency at a particular analyte thickness for a particular refractive index, and the reference frequency (the resonance frequency of the metasurface in absence any analyte coating). Fig. 5 shows the frequency shift versus RI curves for the six polyimide thicknesses on As2.

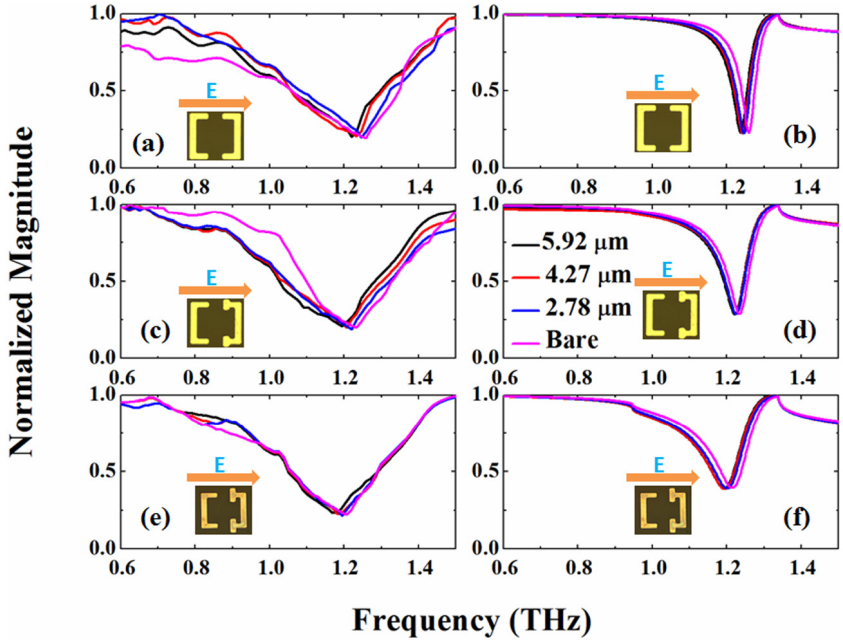

Fig. 4. Comparative plots of normalized transmission magnitude vs. frequency when the electric field is parallel to the gap i.e. O2: (a) and (b) respectively represent experimental and simulation results for Sy sample. Similarly, (c) and (d) display results for As1 while (e) and (f) correspond to the same for As2 . (For interpretation of the references to color in this figure legend, the reader is referred to the web version of this article.)

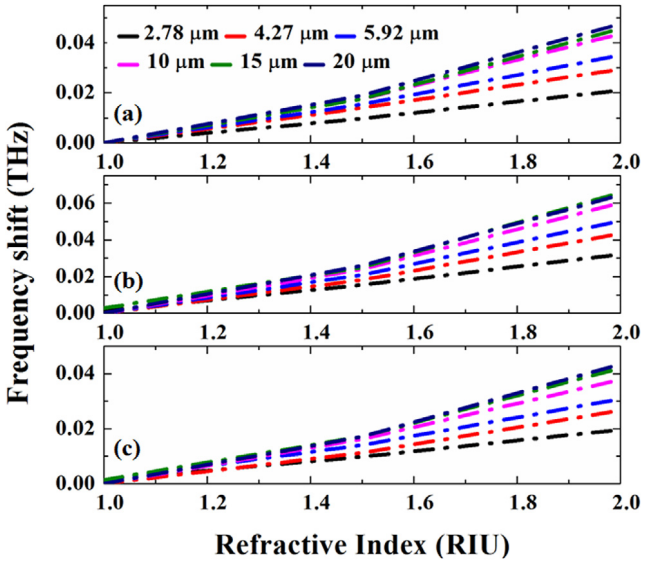

Fig. 5. Frequency shift vs Refractive Index plots for six different polyimide thicknesses: 2.78 μm, 4.27 μm, 5.92 μm, 10 μm, 15 μm and 20 μm on the sample As1 for (a) Dark mode resonance (b) Dipole mode resonance (c) Quadrupole mode resonance.

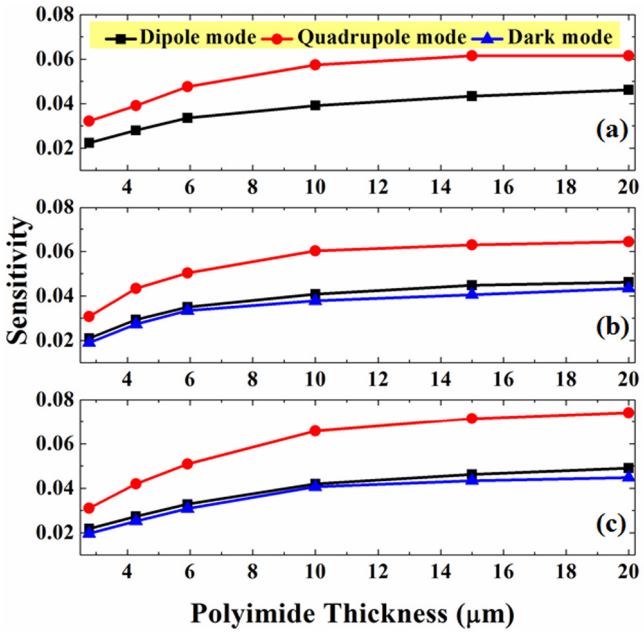

Fig. 6. Sensitivity vs Polyimide thickness plot for (a) Sy sample (b) As1 sample (c) As2 sample. Maximum sensitivity observed is 0.742 THz/RIU for the quadrupole mode resonance of As2.

Based on the above-mentioned frequency shift data, sensitivities for Sy, As1 and As2 have been calculated. Fig. 6 shows the plot between sensitivity and polyimide thickness. We observe that a maximum sensitivity of 0.742 THz/RIU occurs for the quadrupole mode resonance of As2, which is considerably higher than sensitivity values previously reported [16,42] for such simple, easily fabricated metamaterial geometries.

From Fig. 5, it can be observed that there are slight deviations from linearity in the frequency shift vs refractive index response as we approach 2 RIU, which becomes especially pronounced as the analyte thickness increases. Though this has little effect on device sensitivity, as is evident from Fig. 6, since sensitivity values already saturate at lower analyte thicknesses, it can be avoided by varying the refractive index to smaller ranges.

In Fig. 7, Q factors of Sy, As1 and As2 have been plotted as a function of polyimide thickness. In Fig. 6, we observe that sensitivity initially increases then slowly saturates with increasing analyte thickness, Q factor on the other hand initially decreases then slowly saturates. Both these phenomenon can be attributed to the saturation of resonance red-shift beyond a certain analyte thickness due to the reduction in fringing field penetrations near the capacitive gaps. In case

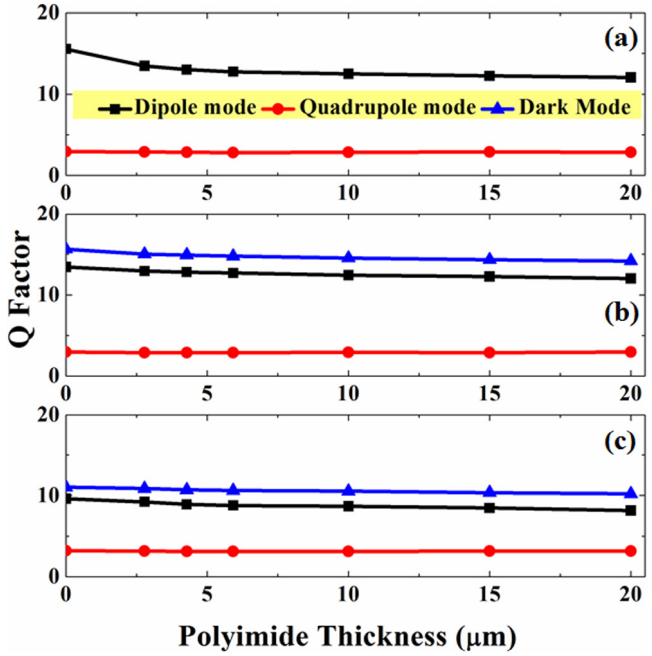

Fig. 7. Q Factor vs Polyimide thickness plot for (a) Sy sample (b) As1 sample (c) As2 sample.

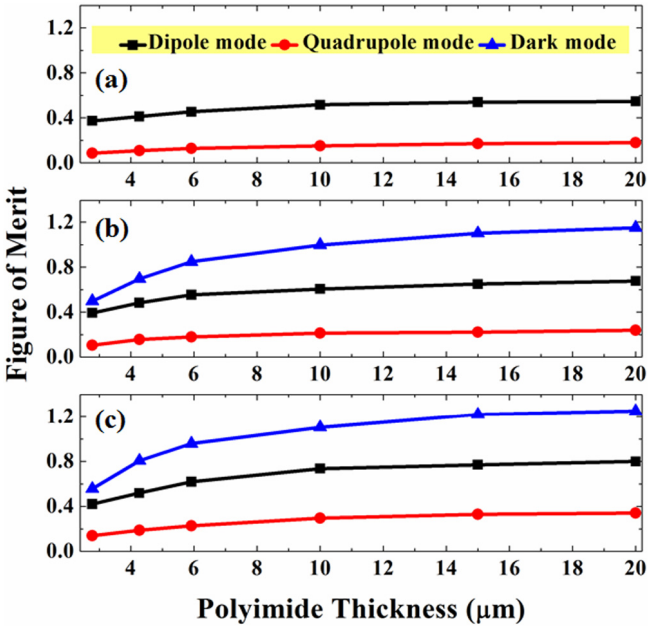

Fig. 8. FoM vs Polyimide thickness for (a) Sy sample (b) As1 sample (c) As2 sample. Maximum sensitivity observed is 1.25 for the dark mode resonance of As2.

of our sensing scheme, this saturation thickness is around 10 μm (three hundredth part of wavelength), as is evident from Figs. 6 and 7.

3.3. Figure of merit

We have further estimated the Figure of Merit (FoM) for a comprehensive description of the sensing performance of the metamaterial. FoM of a resonance mode is defined as the ratio of Sensitivity and FWHM (full-width at half maxima) of that mode. In our calculations, FoM for three different resonances in case of As1 and As2 and the two resonances in case of Sy have been examined with respect to different thicknesses of the polyimide film. The FoM values corresponding to different polyimide thicknesses on the three samples have been plotted in Fig. 8.

We have observed that the FoM increases with increasing the analyte thickness, but it tends to saturate beyond a certain thickness. This is because the electric field lines emanating out of the meta-resonators are essentially well confined near the resonators, and therefore less affected with increasing thickness of the analyte to impact the sensing capabilities. Also, we can observe that As1 and As2 serve as better sensing devices in O1, when polarization of the electric field $\boldsymbol{E}$ is parallel to the arm, as the dark mode and dipole mode order resonances have higher FoMs when compared to the quadrupole resonances, which arise when $\boldsymbol{E}$ is parallel to the gap i.e. case of O2 [22]. Dark resonance mode displays sharpest resonance because it can confine energy strongly, as can be seen from the electric field plots in Fig. 8. Therefore, in case of any variation close to the metasurface, these modes demonstrate maximum perturbation, hence resulting in higher FoMs. The maximum FoM achieved through our designs is around 1.25 for the low frequency dark mode of As2.

This argument can be further justified by observing the electric field and surface current distribution profiles of the three resonances. Fig. 8(a), (b), (c) depict the $\boldsymbol{E}$ -field profiles for the first, second and third order modes in As2, respectively while 8 (d), (e), (f) depict their corresponding surface current profiles. From the figure it is quite evident that the electric field confinement is stronger (maximum value observed was 15.67×10^6 V/m) in the first resonance mode than in any of the subsequent higher order modes. This suggests that the dark order modes are more efficient at sensing the permittivity of the coated analyte than the higher order modes owing to their non-radiative and hence, strong field confining properties.

The surface current profiles corroborate the nature of the resonant modes [44,45]. In Figs. 9e and 9f, the induced surface currents clearly indicate the higher order modes to be dipolar and quadrupolar in nature. The anti-parallel current distribution (clockwise and anti-clockwise) induced in the structure (Fig. 9d) can be attributed to the excitation of the lowest order mode i.e. the dark mode.

4. Conclusions

In this work, we have successfully designed, fabricated and measured different sets of symmetric and asymmetric SRR-based terahertz metasurfaces with the aim of sensing ultra-thin sub-wavelength dielectric film. Dark mode narrow band sharp resonances have been excited in the fabricated asymmetric metasurfaces and increasing red shifts in resonance frequencies of various orders have been observed as the metasurfaces are loaded with increasing thicknesses of thin film analyte layers. Our experiments have clearly demonstrated feasibility of our design methodology for sensing of ultra-thin films ~ almost one thousandth of the operating wavelength. We have further extended our study of the metasurfaces through numerical simulations using CST Microwave Studio and the results are in good agreement with the experimental observations. Furthermore, our study shows that the dark modes demonstrate much higher FoMs compared to the typical dipole modes excited in the same metasurfaces towards thin film sensing. Such metasurfaces should be useful in devising planar platforms for thin film sensing besides other metamaterial-based sensing applications.

Acknowledgments

Sabyasachi Banerjee, Dibakar Roy Chowdhury, and Bishnu P. Pal gratefully acknowledge support from SERB, India, Department of Science & Technology (DST), Government of India (Grant No. EMR/2015/001339); Deepak Kumar thanks DST for award of the INSPIRE doctoral research fellowship. Ganesh Damarla and Anil K Chaudhary gratefully acknowledge support from DRDO, Ministry of Defense, Government of India.

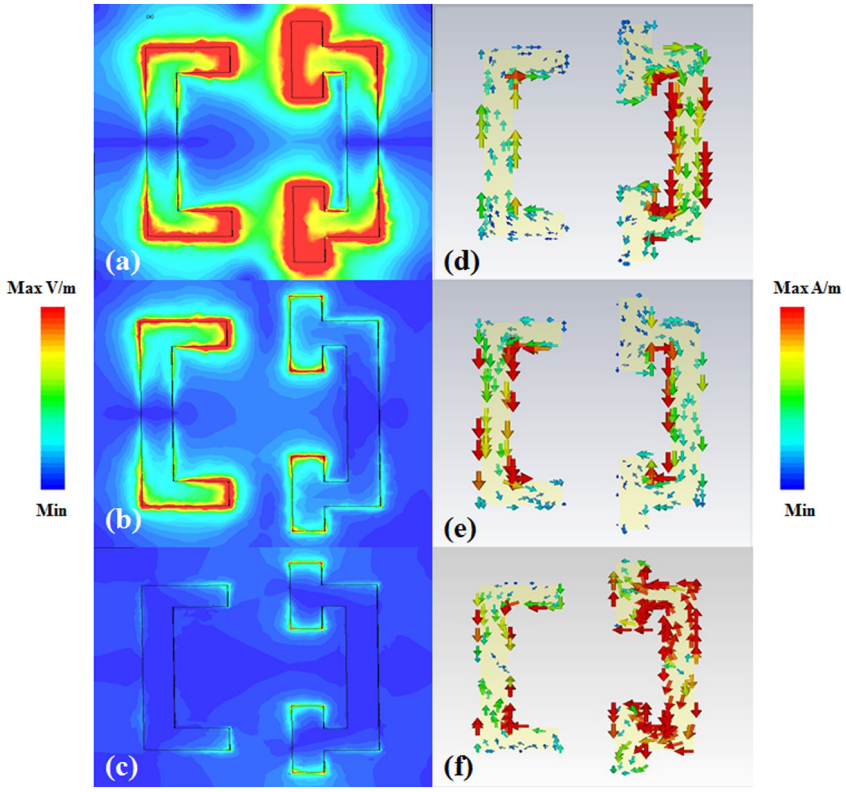

Fig. 9. (a), (b), and (c) denote the electric field profiles corresponding to the dark, dipole and quadrupole mode resonances, respectively of the sample As2. We observed maximum $\boldsymbol{E}$ field value (abs) to be 15.67×10^6 V/m for the dark mode resonance. Fig. 8(c), (d), and (e) show the corresponding surface current profiles for the three resonance modes. $\boldsymbol{E}$ field is parallel to the arm for (a, d) and (b, e) distributions, while it is parallel to the gap for distributions (c, f).

References

[1] V.G. Vaselago, The electrodynamics of substances with simultaneously negative values of epsilon and mu, Sov. Phys. Usp. 10 (1968) 509–514.

[2] J.B. Pendry, A.J. Holden, D.J. Robbins, W.J. Stewart, Magnetism from conductors and enhanced nonlinear phenomena, IEEE Trans. Microw. Theory Tech. 47 (1999) 2075–2084.

[3] S. Linden, C. Enkrich, M. Wegener, J. Zhou, T. Koschny, C.M. Soukoulis, Magnetic response of metamaterials at 100 terahertz, Science 306 (2004) 1351–1353.

[4] O. Sydoruk, E. Tarartschuk, E. Shamonina, L. Solymar, Analytical formulation for the resonant frequency of split rings, J. Appl. Phys. 105 (2009) 014903.

[5] S.J.M. Rao, D. Kumar, G. Kumar, D. Roy Chowdhury, Modulating the near field coupling through resonator displacement in planar terahertz metamaterials, J. Infrared Millim. Terahertz Waves (2017).

[6] H.T. Chen, W.J. Padilla, J.M.O. Zide, A.C. Gossard, A.J. Taylor, R.D. Averitt, Active terahertz metamaterial devices, Nature 444 (2006) 597–600.

[7] P.R. West, S. Ishii, G.V. Naik, N.K. Emani, V.M. Shalaev, A. Boltasseva, Searching for better plasmonic materials, Laser Photonics Rev. 4 (2010) 795–808.

[8] V.A. Fedotov, M. Rose, S.L. Prosvirnin, N. Papasimakis, N.I. Zheludev, Sharp trapped-mode resonances in planar metamaterials with a broken structural symmetry, Phys. Rev. Lett. 99 (2007) 147401.

[9] E. Plum, V.A. Fedotov, N.I. Zheludev, Planar metamaterial with transmission and reflection that depend on the direction of incidence, Appl. Phys. Lett. 94 (2009) 131901.

[10] I. Al-Naib, R. Singh, C. Rockstuhl, F. Lederer, S. Delprat, D. Rocheleau, M. Chaker, T. Ozaki, R. Morandotti, Excitation of a high q sub-radiant resonance mode in mirrored single-gap asymmetric split ring resonator terahertz metamaterials, Appl. Phys. Lett. 101 (2012) 071108.

[11] W. Cao, R. Singh, I.A.I. Al-Naib, M. He, A.J. Taylor, W. Zhang, Low-loss ultra-high-Q dark mode plasmonic Fano metamaterials, Opt. Lett. 37 (2012) 3366–3368.

[12] Qin Xie, Guang-Xi Dong, High – Q Fano resonance in terahertz frequency based on asymmetric metamaterial resonator, Nanoscale Res. Lett. 13 (2018) 294.

[13] Chunfeng Ding, Lian Wu, Dengang Xu, Jianquan Yao, Xianhong Sun, Triple band high q factor Fano resonances in bi-layer THz metamaterials, Opt. Commun. 370 (2016) 116–121.

[14] R. Singh, I. Al-Naib, W. Cao, C. Rockstuhl, M. Koch, W.L. Zhang, The Fano resonance in symmetry broken terahertz metamaterials, IEEE Trans Terahertz Sc. Tech. 3 (2013) 820–826.

[15] L.H. Du, J. Li, Q. Liu, J.H. Zhao, L.G. Zhu, High-Q Fano-like resonance based on asymmetric dimer structure and its terahertz sensing application, Opt. Mat. Exp. 7 (2017) 1335–1342.

[16] Yogesh Kumar Srivastava, Longqing Cong, Ranjan Singh, Dual-surface flexible THz Fano metasensor, Appl. Phys. Lett. 111 (2017) 201101.

[17] D. Roy Chowdhury, Xiaofang Su, Y. Zeng, C. Xiaoshuang, A.J. Taylor, A. Azad, Excitation of dark plasmonic modes in symmetry broken terahertz metamaterials, Opt. Express (2017) 19401.

[18] C. Wu, A.B. Khanikaev, R. Adato, N. Arju, A.A. Yanik, H. Altug, G. Shvets, Fano-resonant asymmetric metamaterials for ultrasensitive spectroscopy and identification of molecular monolayers, Nat. Mat. 11 (2012) 69–75.

[19] M. Islam, S. Jagan Mohan Rao, Gagan Kumar, B.P. Pal, D. Roy Chowdhury, Role of resonance modes on terahertz metamaterials based thin film sensors, Sci. Rep. 7 (2017) 7355, http://dx.doi.org/10.1038/s41598-017-07720-9.

[20] I. Al-Naib, Thin-film sensing via Fano resonance excitation in symmetric terahertz metamaterials, Int. J. Infrared Millim. Terahertz Waves 39 (2018) 1.

[21] S.J. Park, S.A.N. Yoon, Y.H. Ahn, Dielectric constant measurements of thin films and liquids using terahertz metamaterials, RSC Adv. (73) (2016).

[22] R. Tahiaoui, A.C. Strikwerda, P.U. Jespen, Terahertz plasmonic structure with enhanced sensing capabilities, IEEE Sens. J. 16 (2016) 2484–2488.

[23] W. Xu, Lijuan Xie, Y. Ying, Mechanisms and applications of terahertz metamaterial sensing: a review, Nanoscale 9 (2017) 13864–13878, http://dx.doi.org/10.1039/C7NR03824K.

[24] D. Grischkowsky, Søren Keiding, Martin van Exter, Ch. Fattinger, Fattinger far-infrared time-domain spectroscopy with terahertz beams of dielectrics and semiconductors, J. Opt. Soc. Amer. B Opt. Phys. 7 (1990) 2006–2015.

[25] R.D. Averitt, A.J. Taylor, Ultrafast optical and far-infrared quasiparticle dynamics in correlated electron materials, J. Phys.: Condens. Matter. 14 (2002) R1357.

[26] Maidul Islam, Dibakar Roy Chowdhury, Amir Ahmad, Gagan Kumar, Terahertz plasmonic waveguide based thin film sensor, J. Lightwave Technol. 35 (23) (2017).

[27] C. Debus, P.H. Bolivar, Frequency selective surfaces for high sensitivity terahertz sensing, Appl. Phys. Lett. 91 (2007) 184102.

[28] S.Y. Chiam, R. Singh, W. Zhang, A.A. Bettiol, Controlling metamaterial resonances via dielectric and aspect ratio effects, Appl. Phys. Lett. 97 (2010) 191906.

[29] E. Cubukcu, S. Zhang, Y.S. Park, G. Bartal, X. Zhang, Split ring resonator sensors for infrared detection of single molecular monolayers, Appl. Phys. Lett. 95 (2009) 043113.

[30] N. Liu, T. Weiss, M. Mesch, L. Langguth, U. Eigenthaler, M. Hirscher, C. Sonnichsen, H. Giessen, Planar metamaterial analogue of electromagnetically induced transparency for plasmonic sensing, Nano Lett. 10 (2009) 1103.
[31] C. Wu, A.B. Khanikaev, R. Adato, N. Arju, A.A. Yanik, H. Altug, G. Shvets, Fano-resonant asymmetric metamaterials for ultrasensitive spectroscopy and identification of molecular monolayers, Nature Mater. 11 (2012) 69–75.
[32] I. Al-Naib, C. Jansen, M. Koch, High Q-factor metasurfaces based on miniaturized asymmetric single split resonators, Appl. Phys. Lett. 93 (2008) 083507.
[33] R. Singh, W. Cao, I. Al-Naib, L. Cong, W. Withayachumnankul, W. Zhang, Ultrasensitive terahertz sensing with high-Q Fano resonances in metasurfaces, Appl. Phys. Lett. 105 (2014) 171101.
[34] L.Q. Cong, M. Manjappa, N.N. Xu, I. Al-Naib, W.L. Zhang, R. Singh, Fano Resonances in terahertz metasurfaces: a figure of merit optimization, Adv. Opt. Mat. 3 (2015) 1537–1543.
[35] M.B. Ketchen, D. Grischkowsky, T.C. Chen, C.-C. Chi, I.N. Duling, N.J. Halas, J.-M. Halbout, J.A. Kash, G.P. Li, Generation of sub-picosecond electrical pulses on coplanar transmission lines, Appl. Phys. Lett. 48 (12) (1986) 751–753.
[36] M. Nagel, H. Kurz, Corrugated waveguide based genomic biochip for marker-free THz read-out, Int. J. Infrared Millim. Terahertz Waves 27 (4) (2006) 517–529.
[37] J.F. O'Hara, W. Withayachumnankul, I. Al-Naib, A review on thin-film sensing with terahertz waves, Int. J. Infrared Millim. Terahertz Waves 33 (2012) 245–291, http://dx.doi.org/10.1007/s10762-012-9878-x.
[38] Wendao Xu, Lijuan Xie, Jianfei Zhu, Xia Xu, Zunzhong Ye, Chen Wang, Yungui Ma, Yibin Ying, Gold nanoparticle-based terahertz metamaterial sensors: mechanisms and applications, ACS Photon. (2016).
[39] G. Jianqiang, H. Jiaguang, L. Xinchao, R. Singh, Z. Tian, Q. Xing, W. Zhang, A close-ring pair terahertz metamaterial resonating at normal incidence 17 (22) (2009) 20307.
[40] L. Cong, S. Tan, R. Yahiaoui, F. Yan, W. Zhang, R. Singh, Experimental demonstration of ultrasensitive sensing with terahertz metamaterial absorbers: A comparison with the metasurfaces, Appl. Phys. Lett. 106 (2015) 031107, http://dx.doi.org/10.1063/1.49061.09.
[41] Xu Chen, Wenhui Fan, Ultrasensitive terahertz metamaterial sensor based on spoof surface plasmon, Sci. Rep. 7 (2017) 2092, http://dx.doi.org/10.1038/s41598-017-01781-6.
[42] Manoj Gupta, Yogesh Kumar Srivastava, Manukumara Manjappa, Ranjan Singh, Sensing with toroidal metamaterial, Appl. Phys. Lett. 110 (2017) 121108, http://dx.doi.org/10.1063/1.4978672.
[43] John F. O'Hara, Ranjan Singh, Igal Brener, Evgenya Smirnova, Jiaguang Han, Antoinette J. Taylor, Weili Zhang, Thin-film sensing with planar terahertz metamaterials: sensitivity and limitations, Opt. Express 16 (3) (2008) 1786.
[44] Dibakar Roy Chowdhury, Ranjan Singh, John F. O'Hara, Hou-Tong Chen, Antoinette J. Taylor, Abul K. Azad, Dynamically reconfigurable terahertz metamaterials through photo doped semiconductor, Appl. Phys. Lett. 99 (2011) 231101.
[45] Dibakar Roy Chowdhury, Ranjan Singh, Antoinette J. Taylor, Hou-Tong Chen, Abul K. Azad, Ultrafast manipulation of near field coupling between bright and dark modes in terahertz metamaterials, Appl. Phys. Lett. 102 (2013) 011122.

Study of water Loss in the Rose petals using Terahertz Spectroscopy

Ganesh Damarla[1], A.K. Chaudhary[1#] and M. Venkatesh[1, 2]

*1. Advanced Centre of Research in High Energy Materials **(ACRHEM),***
University of Hyderabad, Hyderabad 500046, Telangana, India
2. Center for THz-Driven Biomedical Systems, Dept. of Physics and Astronomy,
Seoul National University, Seoul, South Korea.

Corresponding author e-mail: akcphys@gmail.com, anilphys@yahoo.com

Abstract— **We report the water loss study in rose petals using time domain spectroscopy between 0.1 and 2.5 THz range. It was carried out between 30 - 110 ^{0}C under control temperature condition. The result is cross verified using FTIR spectra.**

Keywords: **THz, FTIR , Absorption, Rose, Petal**

I. INTRODUCTION

THz spectroscopy is a non-destructive and non-invasive tool to study the change in the leaf water and other organic and bio molecules[1]. Since THz band is highly absorbed by water, therefore, biological samples shows characteristic absorption in THz domain. The present study is aimed to understand the role of water and process of dehydration in rose petal with respect to temperature. The botanical name of Rose flower is Rosa damascene, whci has lot of medical applications[2][3]. The climatic change is also responsible for the change in the chemical composition of rose petals. We have designed a THz spectrometer using ZnTe crystal as source and LTGaAs PC antenna as a detector. Further, we have cross verified our experimental findings with the Fourier transfer infrared spectrometer (FTIR) . The FTIR spectra of rose petals at room temperature confirms the concentration of water in rose. In addition, it also provides significant information about the process of chemical changes which occurs due rise in the temperature.

II. EXPERIMENTAL SECTION

The Ti: Sapphire femto oscillator (Coherent Chameleon Ultra II) was used as a Laser source. It delivers P-polarized laser pulses of 140 fs pulse duration with a repetition rate of 80 MHz. The laser output wavelength was tuned between 780 and 850 nm for THz generation. The variable attenuator (from Eskpla Company) was employed to attenuate the output average power. The average power, was allowed to incident on the ZnTe crystal, which is used as a THz source[4]. The 2 mm, 110 cut ZnTe crystal was housed in a Teflon holder, which was kept in an optical rotator for vertical rotation. The laser pulses were loosely focused onto the crystal by means of a plano convex lens of focal length (f) 10 cm. The spot diameter of laser pulse on ZnTe crystal was ~234 microns. The generated THz pulses were collected using two half axis parabolic mirrors. The diameter (D) and an effective focal length (f_e) of parabolic mirrors (MPD508762-90-M01) were ~50 mm and ~150 mm, respectively. The residual transmitted laser pulses from the source were separated from THz radiation using a high resistivity float zone (HRFZ) silicon plate (diameter 50 mm, thickness 2 mm) and black polyethylene filter. The silicon plate has reflection coating in between 700 and 900 nm laser wavelengths. The diverging THz radiation emitted from the source was collimated and focused by PM_1 and PM_2 mirrors. The PM_2 mirror is used to focus the generated THz radiation on the PC antenna which was coupled with preamplifier. The output of the preamplifier was fed to the Lock in Amplifier. The output signal from Lock-in-amplifier is sent to the computer for the recording of time and frequency domain spectra using an indigenously designed data acquisition program developed using Labview software.

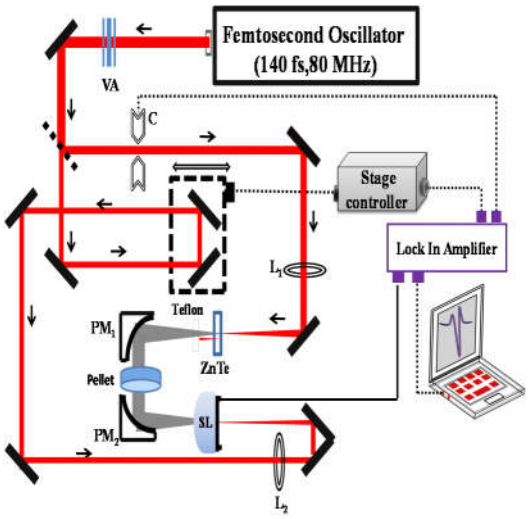

Figure 1. Schematic diagram of a THz time-domain spectrometer setup.

III. THEORY

Authorized licensed use limited to: University of Hyderabad IG Memorial Library. Downloaded on July 24,2020 at 08:40:25 UTC from IEEE Xplore. Restrictions apply.

The amplitude of E-M field strength of time domain of before and after passing through the rose petal was measured . FFT of time domain signal provides the Frequency domain spectra of the sample. Transmission and Absorption coefficient (α(ω)) were ascertained using following equations (1and 2). [5]

$$T = \frac{E_{sample}}{E_{\text{Re}\,ference}} \text{ ---------- (1)}$$

$$Absorption = -\frac{1}{l}\ln\frac{T_m}{T_s} \text{ ---------- (2)}$$

Where l is the effective thickness of the petal is around 200 microns where T_m, T_R are THz transmittance in rose petal and reference (air), respectively

IV. RESULTS AND DISCUSSION

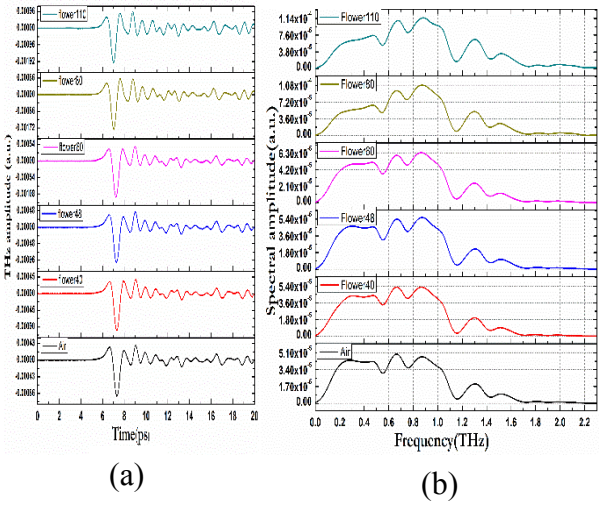

(a) (b)

Figure 2. (a) Temporal shape of a THz-pulse. (b) corresponding frequency spectrum.

Fig 2.shows the temporal and spectral profiles of rose petal subjected to terahertz radiation between 30-110 ºC temperature range. The change in the strength of spectral intensity along with considerable shift in the time delay clearly shows the effect of water loss . It is also attributed to the change of optical path length and chemical changes occurs in rose petals. Fig.3 shows the FTIR spectrum of rose petal between 30- 110 ºC. The absorption dip located at 3300 cm^{-1} is attributed to –OH stretching mode and represent the water concentration which is decreasing with respect to increase in the temperature. This is also reflected in water absorption peak present at 1.66 THz of Fig. 4. In addition FTIR spectra also shows the two absorption peaks located at 2846 and 2916 cm^{-1} , respectively. These absorption peaks correspond to C-H stretch present in carbonyl /carboxy group which has its signature peak at 1734 cm^{-1}. THz spectroscopy is a unic technique to identify the vibrational features of molecular functional groups. Fig 4. shows some interesting behaviour of absorption peak located at 1.7 THz which shows considerable change in the intensity with respect to rise in the temperature. It is attributed to increase in the concentration of carbonyl group.

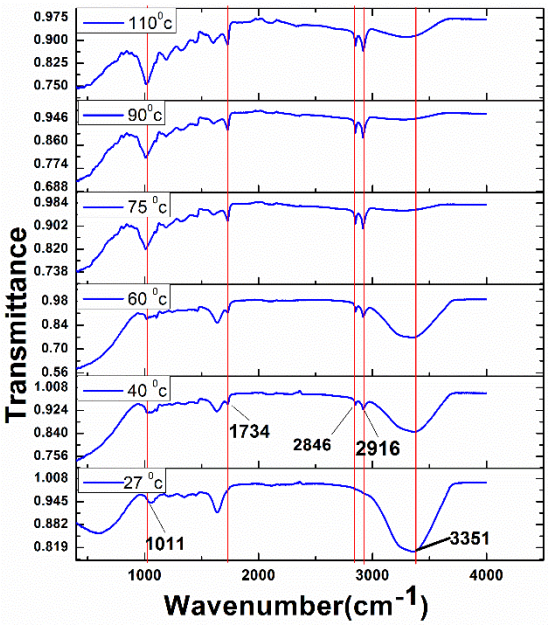

Figure 3. FTIR spectra of rose petals at different temperatures.

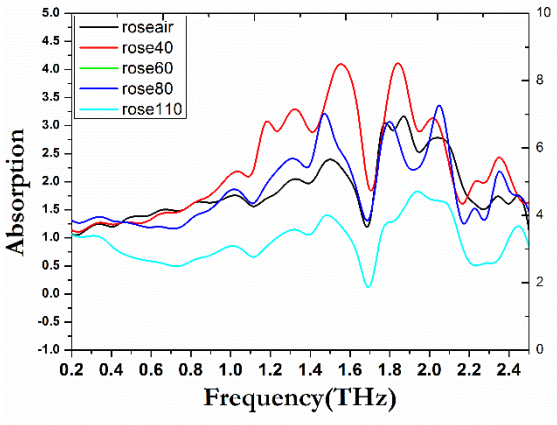

Figure 4. Terahertz absorption spectra of Rose petals.

The complex Refractive index in THz range also help to ascertain the chemical change and water loss occurs with respect to increasing temperature[6] . The Refractive index of the sample can be calculated by using equation No.3.

$$n = 1 + \frac{\Delta\phi \times c}{2\pi\nu \times d} \quad \text{\_\_\_\_\_(3)}$$

Where $\Delta\phi$ =the phase difference between reference and sample, ν is frequency, **d** is thickness of rose petal and **c** the velocity of light. Fig.5 shows the temperature dependent R.I. of rose petal. Which is showing drastic change in the value of R.I. between room temperature to110 ºC range.

Authorized licensed use limited to: University of Hyderabad IG Memorial Library. Downloaded on July 24,2020 at 08:40:25 UTC from IEEE Xplore. Restrictions apply.

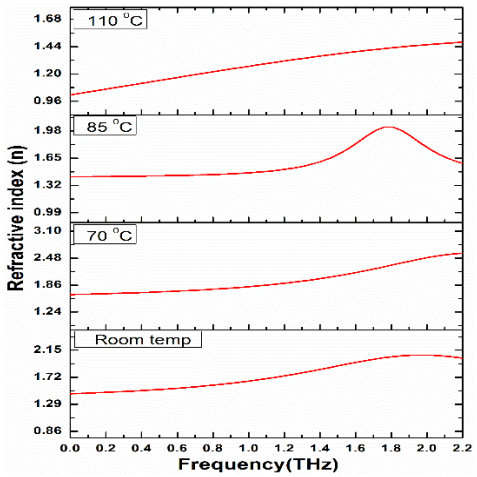

Figure 5.Temp. dependent Refractive Index of Rose petals.

V. CONCLUSIONS

We have successfully investigated the role of water concentration in the rose petal in THz frequency range. The process of water loss along with chemical changes with respect to dehydration is also confirmed by FTIR spectra. In addition, the dehydration process are also verified in terms of refractive index measurement in THz domain.

V. ACKNOWLEDGEMENTS

We gratefully acknowledge the financial support from the DRDO, Ministry of Defense, Govt. of India, India under Phase –III

VI. REFERENCES

[1] M. Tonouchi, "Cutting-edge terahertz technology," *Nat. Photonics*, vol. 1, no. 2, pp. 97–105, 2007.

[2] M. H. Boskabady, M. N. Shafei, Z. Saberi, and S. Amini, "Pharmacological effects of Rosa damascena," *Iran. J. Basic Med. Sci.*, vol. 14, no. 4, pp. 295–307, 2011.

[3] K. Rusanov, N. Kovacheva, B. Vosman, L. Zhang, S. Rajapakse, A. Atanassov, and I. Atanassov, "Microsatellite analysis of Rosa damascena Mill. accessions reveals genetic similarity between genotypes used for rose oil production and old Damask rose varieties," *Theor. Appl. Genet.*, vol. 111, no. 4, pp. 804–809, 2005.

[4] M. Venkatesh, K. Thirupugalmani, K. S. Rao, S. Brahadeeswaran, and A. K. Chaudhary, "Generation of efficient THz radiation by optical rectification in DAST crystal using tunable femtosecond laser pulses," *Indian J. Phys.*, vol. 91, no. 3, pp. 319–326, 2017.

[5] T. Trzcinski, N. Palka, and M. Szustakowski, "THz spectroscopy of explosive-related simulants and oxidizers," *Bull. Polish Acad. Sci. Tech. Sci.*, vol. 59, no. 4, pp. 445–447, 2012.

[6] M. a Jarzembski, M. L. Norman, K. a Fuller, V. Srivastava, and D. R. Cutten, "Complex refractive index of ammonium nitrate in the 2-20-microm spectral range.," *Appl. Opt.*, vol. 42, no. 6, pp. 922–30, 2003.

Authorized licensed use limited to: University of Hyderabad IG Memorial Library. Downloaded on July 24,2020 at 08:40:25 UTC from IEEE Xplore. Restrictions apply.

Contents lists available at ScienceDirect

Materials Letters

journal homepage: www.elsevier.com

Terahertz generation and optical properties of N-benzyl-2-methyl-4-nitroaniline single crystals in 0.1–2.0 THz range for photonic applications

S. Karthick [a, b], D. Ganesh [c], K. Thirupugalmani [d], A.K. Chaudhary [c], S. Brahadeeswaran [a]

[a] Crystal Research Laboratory, Department of Physics, Bharathidasan Institute of Technology, Anna University, Tiruchirappalli 620024, India
[b] Graduate Institute of Photonics, National Changhua University of Education, Changhua, Taiwan
[c] Advanced Center of Research in High Energy Materials (ACRHEM), University of Hyderabad, Hyderabad 500046, India
[d] Department of Physics, ERK Arts and Science College, Dharmapuri 636905, India

ARTICLE INFO

Keywords:
Organic materials
Crystal growth
Optical materials and properties
Terahertz generation

ABSTRACT

We report on the THz generation and optical characterizations such as index of refraction, absorption coefficients of indigenously grown, potentially NLO active N-benzyl-2-methyl-4-nitroaniline (BNA) single crystals grown from four different solvents such as N, N dimethylformamide (DMF), Methanol (MeOH), Acetonitrile (ACN) and ACN: DMF (1:1) in an intentionally selected frequency range of 0.1–2.0 THz at room temperature (RT). The DMF was identified to be a promising candidate as it facilitated reduction in the inclusions. The powder Second Harmonic Generation (SHG) measurements performed on BNA polycrystalline samples revealed that their efficiencies were about 8.4 and 2.3 times higher than KDP and Urea samples respectively. The absorption coefficients and refractive indices made in this technologically important THz range using the BNA crystals grown from selected solvents exhibited, interestingly, solvent dependency.

1. Introduction

In past few decades, extensive search has been carried out for identifying suitable sources and detectors of terahertz (THz) waves as they exhibit wide variety of applications in science and technology, in particular, spectroscopy, non-destructive evaluation, imaging of biological samples, materials characterization, detecting defects in tablet coating, quality control of food and agricultural products and homeland security etc. [1–3].Organic single crystals such as 4-N,N-dimethylamino-4′-N′-methylstilbazoliumtosylate (DAST),2-(3-(4-hydroxystyryl)-5,5-dimethylcyclohex-2-enylidene)-malononitrile (OH1), N-benzyl-2-methyl-4-nitroaniline (BNA) have attracted attention as effective THz generator compared to benchmark inorganic counterparts such as zinc telluride (ZnTe), gallium phosphide (GaP) etc [4]. However, solution grown organic THz crystals are often affected by defects such as primary inclusions (foreign particles and/or solvent inclusions) [5,6]. Among the materials mentioned above, the BNA, is a promising and potentially NLO active organic single crystal in generating efficient THz waves [4,7] and we have recently shown that high crystals-safe conversion efficiency could be achieved through optical rectification process [8]. The present manuscript succinctly explains our attempts on growing optical quality BNA single crystals in select group of solvents and exploring their optical properties such as refractive indices and absorption coefficients in the technologically important region between 0.1 and 2.0 THz. The latter aspect assumes significance due to the fact that many biomolecules such as proteins, DNA and oligonucleotides have their collective vibrational modes at this low frequency range [9] and explosives such as TNT (2,4,6-trinitrotoluene), PETN (pentaerythritol tetranitrate), HMX (tetramethylenetetranitramine), RDX (hexahydro-1,3,5-trinitro-1,3,5-triazine) and DNT (dinitrotoluene) exhibit their characteristic fingerprints in this region [10,11]. Whereas dynamics of free carriers in doped semiconductors (less explored, in general) could well be observed below 2 THz due to their strongest absorption [12], many visibly opaque materials are found to be transparent in this frequency range [13]. Hence the results presented in this manuscript are of crucial importance as the potentially NLO active BNA crystals which are grown in selected solvents have been employed for the generation of intense THz waves and they exhibited, interestingly, varying refractive indices and absorption coefficients depending upon the solvents employed in the measured region. Although a detailed report on refractive indices and absorption coefficients on BNA crystal is available [14] the focus was mainly on their directional dependencies and associated resonances in the 0–5 THz range.

2. Experimental procedure

2.1. Synthesis, solubility, crystal growth and THz measurements on BNA

The title compound was prepared as reported in the literature [7]. The solubilities of BNA in all the four solvents were measured gravimetrically between 25 and 40 °C (shown in Fig. 1). Using the solubility

https://doi.org/10.1016/j.matlet.2019.03.039
Received 22 February 2019; Received in revised form 8 March 2019; Accepted 9 March 2019
Available online xxx
0167-577/ © 2019.

UNCORRECTED PROOF

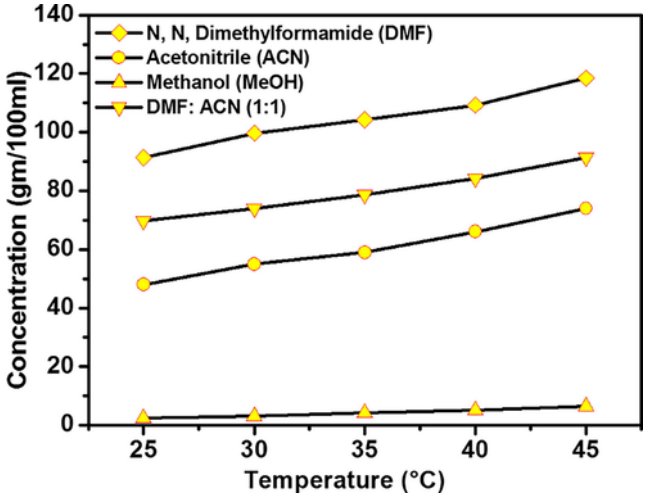

Fig. 1. Solubility plot of BNA.

data of BNA in all the four solvents, saturated solutions were prepared at 30 °C and kept in a growth chamber (Model: Eurotherm3216) and solutions were cooled with a cooling rate of 1 °C per day and single crystals were grown. From the growth results it was observed that DMF yielded nearly inclusion free bulk single crystals of BNA. The Coherent Chameleon Ultra II Ti: Sapphire femto-oscillator which provides laser pulses of 140 fs and 80 MHz was used. The output average power was attenuated by employing Eskpla variable attenuator. The output average power was made to fall on the 2 mm thick, 110 cut ZnTe crystal and the generated THz waves was used for measuring the optical properties. The output signal from lock-in-amplifier was sent to the computer for recording of time and frequency domain spectra using an indigenously designed data acquisition program developed using Labview software.

3. Results and discussion

The SHG efficiency of KDP, urea and BNA powder samples of average particle size of about 250 μm were measured using Nd:YAG laser and the results are shown in Fig. 2a. From the plot, it could be observed that, the second harmonic intensity of KDP, urea and BNA were 466.5, 1694 and 3948 counts per second respectively. The BNA crystals grown in aforementioned solvents were studied for their ability to generate THz frequencies using 40 fs pulses obtained from femtosecond laser amplifier at 1 kHz repetition rate. The generated power was measured using sensitive pyroelectric detector. The schematic diagram of the THz spectrometer used for these measurements is shown in Fig. 2b. The comparative conversion efficiency of all the four BNA crystals are provided in the Table 1. The results of THz generation from all the four solvents grown BNA crystals are shown in Fig. 3b. From the results, we could see that, BNA single crystals are capable of generating THz waves up to 2 THz (in the lower range) and the spectra thus recorded for the corresponding solvents gave similar patterns in this range of 0.1–2 THz. The dips observed in this region were due to the intermolecular interactions and, molecular and lattice phonon modes inside the medium. THz frequency in this obtained range of 0.1–2 THz can able to pass through the materials such as paper, cardboard, plastics, wood, leather and ceramics etc [15]. Fast Fourier Transform (FFT) of time domain signal provides the frequency domain spectra of the sample. THz transmission spectra of BNA crystals are shown in Fig. 3a. Transmission temporal profile and the absorption coefficient (α(ω)) of all the four BNA single crystals in THz region were ascertained using the following Eqs. (1) and (2)

$$T = \frac{E_{Sample}}{R_{Reference}} \tag{1}$$

$$\alpha(\omega) = -\frac{1}{l} ln \frac{T_m}{T_s} \tag{2}$$

where l is the thickness of the BNA crystals, T_m and T_R are the THz transmittance of the crystals and reference (air), respectively. The difference in the temporal profile is due to change in the refractive index and thickness of crystals. However, it was noticed that all the crystals studied exhibited reasonable transmission in the given THz range. The Fig. 3c and d show absorption coefficients and refractive indices of BNA single crystals grown from the abovementioned solvents respectively. The amplitude of E-M field strength before and after passing through the BNA crystal was measured by using THz-TDS. From the figure it could be observed that the solvents influence the quality of the grown crystals as the solvated solute molecules get differently absorbed at the solution-crystal interface [5]. It was also noticed that the absorption peaks observed at 0.6 and 1.05 THz for both DMF and MeOH grown BNA single crystals were absent for the ACN: DMF (1:1) and ACN grown crystals. However, there has been relatively strong absorption at 1.15 and 1.2 THz in ACN: DMF (1:1) and ACN solvent grown single crystals respectively with slight shift as compared to the absorption peaks observed for DMF and MeOH grown BNA crystals. The considerable variations in the absorption could be attributed to differently incorporated solvent molecules at the solution-crystal interface [4]. The corresponding frequency dependent refractive index of all the BNA crystals were measured in the range 0.1–2 THz using the equation

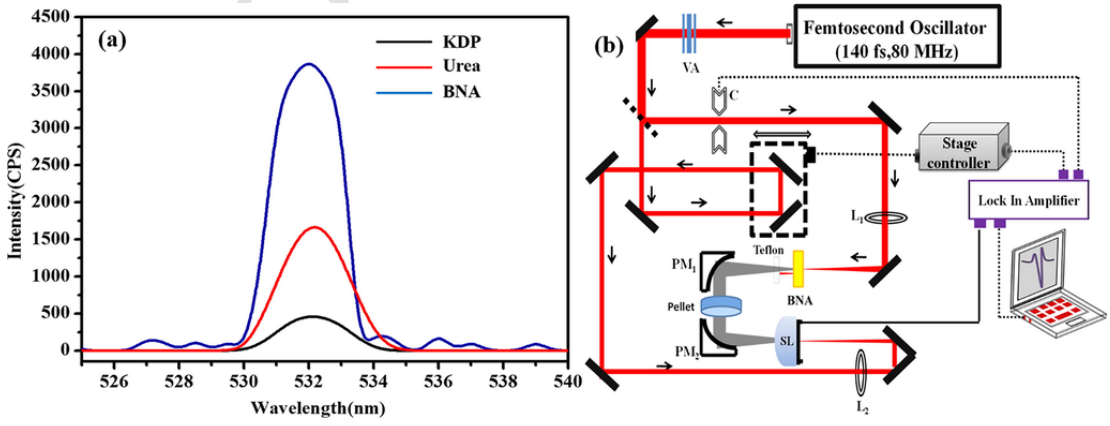

Fig. 2. (a) Comparison of SHG and (b) Schematic diagram of THz setup.

Table 1
Comparison of THz conversion efficiency of all the solvent grown crystals.

Name of the solvent used	Thickness (mm)	Incident Power (mW)	Generated THz Power (μW)	Conversion Efficiency $\dot{E}$ (%)
DMF	0.361	350	9.10	26.00×10^{-4}
MeOH	0.224	350	0.21	00.60×10^{-4}
ACN: DMF	0.321	350	1.00	02.85×10^{-4}
ACN	0.310	350	1.10	03.14×10^{-4}

$$n = 1 + \frac{\acute{\emptyset} \times c}{2\pi\upsilon \times d} \tag{3}$$

where Φ is the phase difference, d is the thickness of the crystal and c is the velocity of light. The average refractive index of all samples is ~1.56 and does not vary significantly with frequency. Thus, considering the above factors, BNA single crystals grown from DMF solvent has relatively higher conversion efficiency compared to other solvents explored.

4. Conclusions

In conclusion, it was reported that high optical quality BNA single crystals could be grown from selected solvents and it was observed that DMF could yield relatively better-quality BNA crystals. The grown crystal when studied for their ability to generate THz waves in the technologically important range between 0.1 and 2.0 THz exhibited solvent dependent conversion efficiencies and both absorption coefficients and refractive indices also exhibited noticeable variations in the measured range. Such variations in the optical properties could be attributed to primary inclusions at the solution-crystal interface. These observations reveal that sufficient care is necessitated while selecting solvents suitable for the crystals under consideration which otherwise could hinder the utilization of such highly efficient THz material for practical applications.

Conflict of interest

None declared.

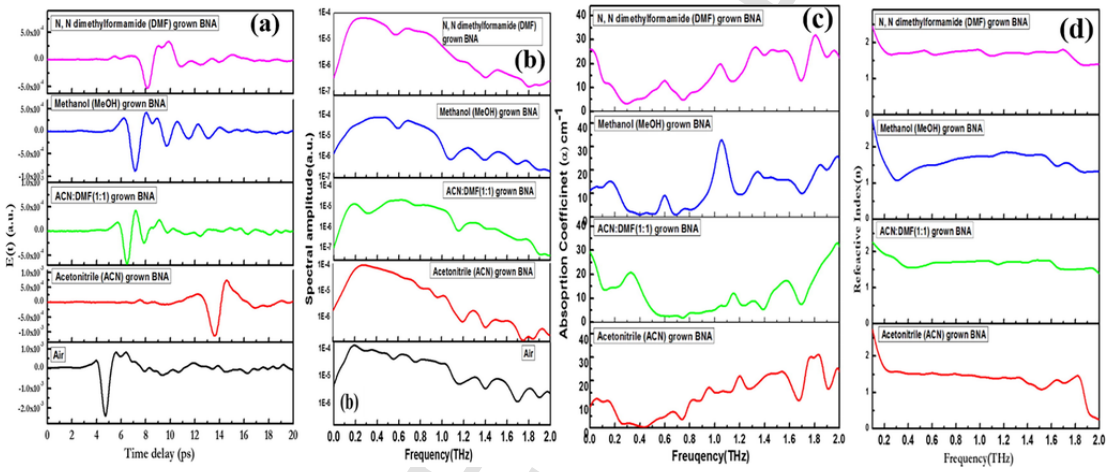

.Fig. 3 (a) Temporal electric field and (b) Amplitude spectrum of generated THz pulse (c) Absorption co-efficient and (d) the corresponding index of refraction for all the solvent grown crystals in the THz region

UNCORRECTED PROOF

References

[1] M. Tonouchi, Cutting-edge terahertz technology, Nat. Photon. 1 (2007) 97–105.

[2] K. Kawase, Y. Ogawa, Y. Watanabe, H. Inoue, Non-destructive terahertz imaging of illicit drugs using spectral fingerprints, Opt. Express 11 (2003) 2549–2554.

[3] A.H. Reshak, D. Stys, S. Auluck, I.V. Kityk, Dispersion of linear and nonlinear optical susceptibilities and the hyperpolarizability of 3-methyl-4-phenyl-5-(2-pyridyl)-1,2,4-triazole, Phys. Chem. Chem. Phys. 13 (2011) 2945–2952.

[4] K. Thirupugalmani, M. Venkatesh, S. Karthick, K.K. Maurya, N. Vijayan, A.K. Chaudhary, S. Brahadeeswaran, Influence of polar solvents on growth of potentially NLO active organic single crystals of N-benzyl-2-methyl-4-nitroaniline and their efficiency in terahertz generation, CrystEngComm. 19 (2017) 2623–2631.

[5] K. Kamada, Y. Takida, H. Minamide, Y. Shoji, S. Kurosawa, Y. Yokota, Y. Ohashi, A. Yoshikawa, Growth of N-benzyl-2-methyl-4-nitroaniline (BNA) single crystal fibers by micro -pulling down method, J. Cryst. Growth 452 (2016) 162–165.

[6] S. Brahadeeswaran, S. Onduka, M. Takagi, Y. Takahashi, H. Adachi, M. Yoshimura, Y. Mori, T. Sasaki, Growth of high-quality DAST crystals for THz applications, J. Cryst. Growth 292 (2006) 441–444.

[7] H. Hashimoto, Y. Okada, H. Fujimura, M. Morioka, O. Sugihara, N. Okamoto, R. Matsushima, Second-harmonic generation from single crystals of N-substituted 4-nitroanilinnes, Jpn. J. Appl. Phys. 36 (1997) 6754–6760.

[8] M. Shalaby, C. Vicario, K. Thirupugalmani, S. Brahadeeswaran, C.P. Hauri, Intense THz source based on BNA organic crystal pumped at Ti:sapphire wavelength, Opt. Lett. 41 (2016) 1777–1780.

[9] A.G. Markelz, A. Roitberg, E.J. Heilweil, Pulsed terahertz spectroscopy of DNA, bovine serumalbumin and collagen between 0.1 and 2.0 THz, Chem. Phys. Lett. 320 (2000) 42–48.

[10] C.B. Reid, E. MacPherson, J.G. Laufer, A.P. Gibson, J.C. Hebden, V.P. Wallace, Accuracy and resolution of THz reflection spectroscopy for medical imaging, Phys. Med. Biol. 55 (2010) 4825–4838.

[11] J. Chen, Y. Chen, H. Zhao, G.J. Bastiaans, X.C. Zhang, Absorption coefficients of selected explosives and related compounds in the range of 0.1-2.8 THz, Opt. Express 15 (2007) 12060–12067.

[12] M.V. Exter, D. Grischkowsky, Optical and electronic properties of doped silicon from 0.1 to 2 THz, Appl. Phys. Lett. 56 (1990) 1694–1696.

[13] R.I. Stantchev, D.B. Phillips, P. Hobson, S.M. Hornett, M.J. Padgett, E. Hendry, Compressed sensing with near-field THz radiation, Optica 4 (2017) 989–992.

[14] K. Kuroyanagi, M. Fujiwara, H. Hashimoto, H. Takahashi, S. Aoshima, Y. Tsuchiya, Jpn. J. Appl. Phys. 45 (2006) 761–764.

[15] R. Kalaivanan, K. Srinivasan, Synthesis, growth and characterization of organic nonlinear optical material: N-benzyl-2-methyl-4-nitroaniline (BNA), Opt. Laser Technol. 90 (2017) 27–32.

UNCORRECTED PROOF

RSC Advances

PAPER

View Article Online
View Journal | View Issue

Check for updates

Cite this: *RSC Adv.*, 2019, **9**, 38246

Self-assembled pearl-necklace patterned upconverting nanocrystals with highly efficient blue and ultraviolet emission: femtosecond laser based upconversion properties†

Monami Das Modak,[b] Ganesh Damarla,[c] Somedutta Maity,[b] Anil K. Chaudhary[c] and Pradip Paik *[ab]

This work reports new findings on the formation of a pearl-necklace pattern in self-assembled upconverting nanocrystals (UCN-PNs) which exhibit strong upconversion emission under an NIR excitation source of a femtosecond laser (Fs-laser). Each nano-necklace consists of several upconversion nanoparticles (UCNPs) having a size *ca.* 10 ± 1 nm. UCN-PNs are arranged in a self-organized manner to form necklace type chains with an average length of 140 nm of a single row of nanoparticles. Furthermore, UCN-PNs are comprised of UCNPs with an average interparticle separation of *ca.* 4 nm in each of the nanonecklace chains. Interestingly, these UCN-PNs exhibit high energy upconversion especially in the UV region on interaction with a 140 Fs-laser pulse duration at 80 MHz repetition rate and intense blue emission at 450 nm on interaction with a 900 nm excitation source is obtained. The preparation of self-assembled UCNPs is easy and they are very stable for a longer period of time. The emission (fluorescence/luminescence) intensity is very high which can make them unique in innumerable industrial and bio-applications such as for disease diagnosis and therapeutic applications by targeting the infected cells with enhanced efficiency.

Received 15th August 2019
Accepted 15th November 2019

DOI: 10.1039/c9ra06389g

rsc.li/rsc-advances

Open Access Article. Published on 22 November 2019. Downloaded on 7/24/2020 9:31:16 AM.
This article is licensed under a Creative Commons Attribution-NonCommercial 3.0 Unported Licence.

1. Introduction

Upconverting nanocrystals are attractive due to several unique properties and for their applications in materials, materials science, industrial applications for designing solar cells, sensors *etc.* and for biomedical medical applications.[1,2] Rare-earth upconverting materials have been demanded as they are the best energy upconverting (NIR-to-visible) materials ever known, therefore currently researchers are focusing on their design, synthesis and spectroscopic properties. Furthermore, upconverting materials possess potential uses in biological labeling and bio-assays and their extent of uses has increased remarkably with time.[3–7] All these unique features drive us to synthesize self-assembled UCNPs having strong upconversion emission. To the best of our knowledge, self-assembled pearl-necklace type upconverting nanoparticles (UCN-PNs) are never known. A report was found where UCNPs were impregnated in porphyrin dendrimers.[8] In this work we are enabled to prepare self-assembled UCNPs in *in situ* condition without incorporating any external polymeric components. The as-prepared UCN-PNs have been formed by consuming all precursors into solid crystal nuclei as white precipitates at lower reaction temperature and then with increasing the reaction temperature crystal growth occurred followed by the formation of UCN-PNs. The as-prepared UCN-PNs have excellent dispersibility in non-polar solvent (*e.g.*, cyclohexane) and are stable for more than a year. As UCN-PNs exhibit excellent upconversion emission under 980 nm NIR excitation source and 140 femtosecond pulse duration at 80 MHz repetition rate, there is a vast ambit for using them in complex biolabeling by tuning their spectral properties. Further, for present available systems there are several draw backs in achieving good efficiency for the DNA detection,[9] bio-imaging,[10] sensors and fluorophores,[11–13] analytes and several other important biomedical applications such as for the treatment of cancers[14–17] which can be improved by using UCN-PNs.

Self-assembled materials can be obtained from nature to the laboratory. Self-assembly in living system is biologically controlled whereas; self-assembly formation in laboratory is controlled artificially. The assembly of nanomaterials is purely represented by non-covalent bonding and controlled both by kinetic and thermodynamically. Inside laboratory self-

[a]*School of Biomedical Engineering, Indian Institute of Technology, BHU, Varanasi 221 005, UP, India. E-mail: paik.bme@iitbhu.ac.in; pradip.paik@gmail.com*

[b]*School of Engineering Sciences and Technology, University of Hyderabad, Hyderabad 500 046, Telangana, India*

[c]*Advanced Center of Research in High Energy Materials, University of Hyderabad, Hyderabad, Telangana, 500 046, India*

† Electronic supplementary information (ESI) available. See DOI: 10.1039/c9ra06389g

This journal is © The Royal Society of Chemistry 2019

Open Access Article. Published on 22 November 2019. Downloaded on 7/24/2020 9:31:16 AM.
This article is licensed under a Creative Commons Attribution-NonCommercial 3.0 Unported Licence.

assembly processes are used for designing the artificial nanostructures, such as for assembling proteins, peptides, nucleotides, supramolecular biopolymers *etc.* and they have myriad applications in biomedicals for developing artificial membranes and for various biofunctions.[18–20] Self-assembly of various inorganic (metals/hybrids) nanoparticles is well known.[21–23] The formation of self-assembled necklace type nanostructures is very much interesting in the area of modern nanotechnology. Necklace nanostructures of UCNPs can exhibit unique properties with their associated building blocks (nanoparticles below 10 nm). The self-assembled architectures of nano sized UCNPs can offer a potential platform for future applications, especially in nonlinear optical property based nanotechnology. Self-assembled nanobuildings have become the most exciting nanometre-sized branched architectures, which are formed by repeating nanoscopic building blocks. Hence, the effort of forming such self-assembled UCN-PNs can be considered as spontaneous assembly of branched building blocks of nanoparticles. Usually, the interactions between the molecules associated with such net-work structures can be referred to the supramolecular chemistry,[24] where non-covalent interactions play major roles between molecules. UCNPs can also be used for the photodynamic therapy (PDT) by which cancer can be treated. On excitation of UCN, in presence of oxygen, photosensitized molecules can be activated with an appropriate excitation wavelength for producing singlet oxygen species ($^1O_2$) and reactive oxygen species (ROS) which can kill the nearby cancer cells. In PDT, UV- vis light can excite the photosensitizers. For such strategy, UCNPs have shown excellent promising candidate as after exposing them to NIR radiation, emission of UV and or visible light can occur.[25–27] Further, to treat the cancer, recently a sacrificial template strategy has been developed by Huang *et al.*[28] to fabricate yolk–shell nanoparticles combination with UCNPs and CuS nanoparticles which demonstrated very efficient energy transfer between the UCNPs and CuS. The as prepared UCNPs@CuS nanoparticles showed higher ability for productions of OH radicals, ROS and $^1O_2$ and exhibits an enhanced photothermal effect while exposing to NIR light kill the cancer cell. Uniform ultrasmall-sized UCNPs ($NaGdF_4$ nanocrystals) below 10 nm was also been prepared by Liu *et al.*,[29] using PEG-PAA-di-block copolymer (byg ligand exchange approach) and used for the imaging.

In the above line, present work is focused on the synthesis of self-assembled UCN-PNs and their upconversion behavior. The upconversion luminescences of self-assembled UCN-PNs are interesting which have been studied here. In a set of experiments, the upconversion behaviors of UCN-PNs have been studied with femtosecond (Fs) laser (140 femtosecond pulse duration at 80 MHz repetition rate) along with CW-980 nm NIR. Further, visible-to visible photoluminescence has also been studied. The NIR to UV/vis upconversion properties is also observed for UCN-PNs which is represented here in detail. At the end, probable mechanisms for the visible–visible/CW-980 NIR/Fs-laser based upconversions with energy band diagrams for different emissions have been elucidated.

2. Experimental section

2.1. Materials

Aqueous solutions of three lanthanide precursors such as, $Cl_3Y\cdot 6H_2O$, $Cl_3Yb\cdot 6H_2O$, $Cl_3Er\cdot 6H_2O$ (99%), octadecene (90%), methanol (98%) (Sigma Aldrich) and oleic acid ($C_{18}H_{34}O_2$, 65%), ammonium fluoride (NH_4F; 95%), sodium hydroxide (NaOH, 97%), from Qualigens, Kemphasol and SDFCL, respectively were received and used in those forms without further purifications.

2.2. Synthesis method

UCN-PNs were synthesized by solvothermal decomposition process of lanthanide precursors and technical grade chemicals. Three different precursors were prepared in presence of de-ionized H_2O. These three precursors were then dried at 110–115 °C. Further, in decomposed compound organic solvents (oleic acid and octadecene) were added and stirred at 140 °C. Then it was cooled down to room temperature. Then, a solution of CH_3OH, NH_4F and NaOH was added at room temperature and stirred to remove excess oxygen and water, and heated further to 340 °C (rate of 20 °C min^{-1}). Entire synthesis was performed under argon gas atmosphere and a vacuum condition was maintained at 100 °C. Next day, the synthesized sample was collected with acetone *via* centrifugation with 9000 rpm for 15–20 min. The precipitated product was collected by dispersing with cyclohexane (40 ml). Finally it was washed with ethanol and D.W. (1 : 1) for 3–4 times. The resulted solution was preserved in a container as its colloidal form. The self-assembled UCN-PNs are stable for more than a year. Surprisingly, no agglomeration or settling was found, however after a couple of weeks the white particles seemed to be settled clearly at the bottom of container and it can be readily dispersed at room temperature and subsequent characterization revealed that necklace net-work structures are persist for more than a year. The detail of synthesis method was filled for an Indian Patent (ref: TEMP/E-1/21065/2017CHE, dated: 14/06/2017).

2.3. Characterizations

Transmission Electron Microscopy (TEM) and High Resolution Transmission Electron Microscopy (HRTEM) (model FEI TecnaiG2-TWIN 200 KV) were used to study the morphology and sizes of the as-synthesized UCN-PNs. Energy Dispersive X-ray Analysis (EDXA) were performed for the elemental analysis. Crystal structure was revealed using X-ray diffraction pattern (XRD with Co Kα-radiation). The solid state structure present in UCN-PNs was analysed with Raman Spectroscopy (Wi-Tec, alpha 300), upconversion fluorescence study was performed through fluorescence spectrophotometer (Hitachi, F-4600) attached with a NIR laser source (λ = 980 nm) externally. Further, photoluminescence was performed with 450 nm excitation source using PL mode of Multimode Reader (Synergy H4 Hybrid Reader). A Ti-Sapphire tunable oscillator was used with femtosecond (Fs) laser-pulses and the experimental set-up of Fs-laser has provided in ESI File.†

Open Access Article. Published on 22 November 2019. Downloaded on 7/24/2020 9:31:16 AM.
This article is licensed under a Creative Commons Attribution-NonCommercial 3.0 Unported Licence.

3. Results and discussion

The self-assembly of nanonecklace network formations and sizes of the as-prepared UCNPs have been shown in Fig. 1(a)–(d) with different magnification TEM images. TEM was performed using the colloidal solution of UCN-PNs on copper grid (200 mesh, carbon coated). Fig. 1(a)–(c) confirm the self-assembled pearl necklace-type net-work formations of synthesized UCN particles. TEM images (Fig. 1(a)–(c)) show the caterpillar-like/pearl chain type necklace formations at different magnification. Inset of Fig. 1(b) clearly shows the density of the particles for different chains. In Fig. 1(c), lengths of the chains have been shown clearly, where the dotted lines with different colour have been drawn for different chain lengths. Further, it can be noted that the chains are formed with a single row of nanoparticles without overlapping and the distance between two adjacent particles are nearly constant. Most of the regions throughout the sample are able to contain a uniform size of the particles. Overlapping between the particles is almost negligible due to the possible electrostatic interactions. The high crystallinity is confirmed by high resolution TEM images. Fig. 1(d) and (e) show a clear lattice fringes with inter-fringes *d* of 0.31 nm. The crystalline nature of the UCN-PNs further has been confirmed through the XRD analysis (shown in subsequent section). Fig. 1(f) shows the SAED pattern with clearly visible ring type diffraction pattern. Fig. 1(f) has further confirmed five diffraction planes such as (101), (220), (311), (400) and (331) which correspond to the formations of α- and major β-$NaYF_4$ UCNPs. Fig. 1(g) represents the average particle diameter and its distribution is found to be average *ca.*, 10 nm ± 1 nm. Further, the length of nanonecklaces, number of particles per necklace and interparticle separation has also been calculated from TEM results. From Fig. 1(h)–(j), it can be confirmed that the average nanonecklace length of 140 nm which consists of 7–13 numbers of particles per necklace and interparticle distance observed to be *ca.* 4 nm. X-ray diffraction study was performed to confirm the solid state crystalline structure and is shown in Fig. S1.† The peak positions that appeared are corresponding to the diffraction planes (101), (220), (311), (400) and (331), respectively. The *d*-spacing values have also been calculated and found to be 2.9 Å, 2.0 Å, 1.63 Å, 1.43 Å and 1.26 Å, respectively, which are matching for the α-/β-$NaYF_4$ crystalline phases for UCNPs.[30–32] The elemental analysis was performed through the Energy Dispersive X-ray Analysis (EDXA) (Fig. S2†) and confirms for the presence of the elemental Na, Y, F, Er and Yb (see Table S1†).

The upconversion fluorescence spectrum for UCN-PNs under 980 nm NIR CW laser-excitation source is shown in Fig. 2. During experiment the power density was maintained to 1000 mW cm^{-2}. From Fig. 2, it can be observed that UCN-PNs exhibited a very strong upconversion emission. Intense emission bands with their maximum positions are appeared at λ = 526 nm, 545 nm and 659 nm for the green emission (G), which are much higher in intensity (4.3 times) than that of the red emission band (R). Green emissions band appeared at 526 nm between 509 nm and 531 nm and at 545 nm between 532 nm and 570 nm are attributed to the transitions in the energy levels-$2H_{11/2}$, $4S_{3/2}$ (excited energy levels) and -$4I_{15/2}$ (ground state energy level of Er^{3+} ion), respectively, through direct energy transferring modes from sensitizer ion (Yb^{3+}) to activator ion (Er^{3+}). A less intense (compared to the green emission) red emission bands at 659 nm (between 632–691 nm) has appeared with $4F_{9/2}$ to $4I_{15/2}$ energy transfer which follows a less population in $4F_{9/2}$ energy level through the energy transfer path $4I_{13/2}$ → $4F_{9/2}$. Herein, $4I_{13/2}$ level is populated with non-radiative relaxations between $4I_{11/2}$ and $4I_{13/2}$ energy levels. Further, very weak emission bands are observed at λ = 382 nm, 411 nm and 497 nm corresponding to the energy transition modes, $4G_{11/2}/2H_{9/2}$ → $4I_{15/2}$ and $4F_{5/2}$ → $4I_{15/2}$, respectively. These weak emission bands are observed owing to the continuous of input source which excites the Er^{3+} ions sequentially to

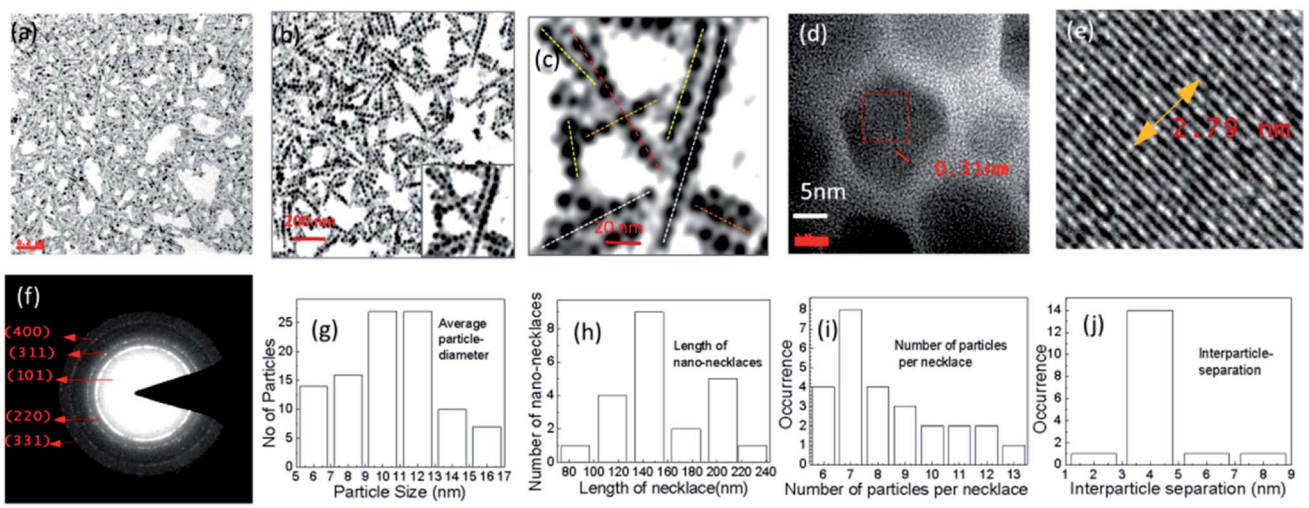

Fig. 1 TEM images of the synthesized colloidal-UCNPs (UCN-PNs at different magnifications). Panels: (a and b) = 200 nm, inset in panel (b) shows the clear formation of pearl nanonecklaces (c) = 20 nm, (d) and (e) = high resolution micrograph showing lattice fringes, (f) = SAED ring pattern, histogram of (g) = particle diameter, (h) nano-necklace length, (i) total number of particles per necklace, (j) interparticle-separation.

This journal is © The Royal Society of Chemistry 2019

Open Access Article. Published on 22 November 2019. Downloaded on 7/24/2020 9:31:16 AM.
This article is licensed under a Creative Commons Attribution-NonCommercial 3.0 Unported Licence.

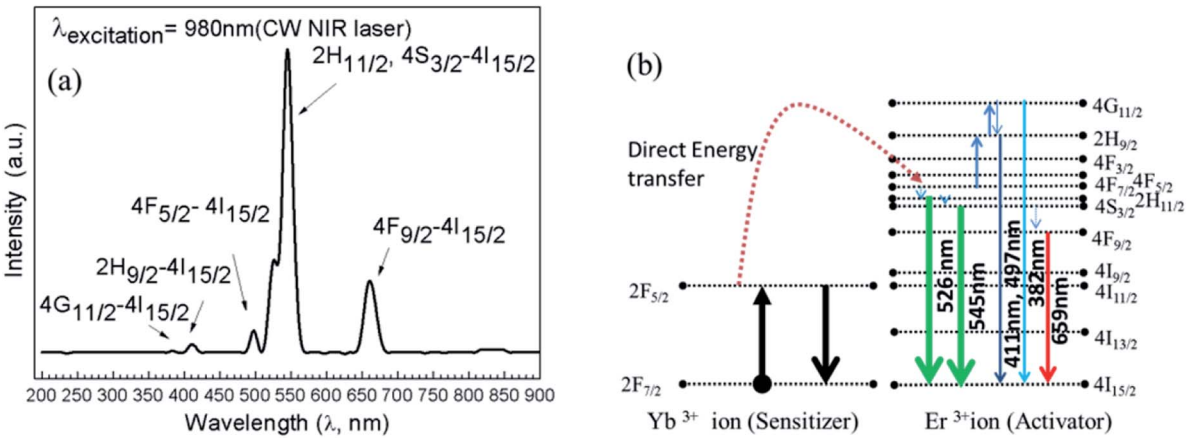

Fig. 2 (a) Upconversion emission spectrum examined with UCN-PNs colloidal solution (b) corresponding energy diagram, under 980 nm NIR-laser excitation source.

the next higher energy levels following the path $4I_{15/2} \rightarrow 4I_{11/2} \rightarrow 4F_{7/2} \rightarrow 4G_{11/2}$. It can be noted that, indirect energy transfers and cross relaxations resulted in very weak emission bands.[30,33] It also can be noted that, for UCN particles ($NaYF_4$,Yb^{3+};Tm^{3+}), Tm^{3+} ion is responsible for blue emission (440–500 nm)[30] following the energy transition paths, $1D_2 \rightarrow 3F_4$ and $1G_4 \rightarrow 3H_6$. However, for our UCN-PNs, without introducing Tm^{3+} precursors we are able to achieve high intense blue emission which could be helpful as blue emitting nanophosphors and can be effective for designing biomedical devices and applications.[34] In can be noted that, for the monodispersed UCNPs, highest intensity was obtained at 546 nm is 1853 a.u., whereas for self-assembled UCNP (UCN-PNs), highest intensity obtained at 546 nm is 3789 a.u. Hence, the enhancement of intensity (considering visible emissions at 546 nm) is about ~2 times higher in UCN-PNs compared to the monodispersed UCNPs (see for experimental observations see Fig. S7†), where same amount (weight basis) of UCNPs were dispersed in a fixed volume of solvent.

It is very interesting to mention that 980 nm NIR excitation resulted weak blue emissive band (Fig. 2) and when we examined the sample with a couple of lower excitation wavelength sources as example, $\lambda = 800$–900 nm, then a high intense blue emissions occurred at 450 nm corresponds to the energy transition path, $2H_{9/2} \rightarrow 4I_{15/2}$. Fig. 3(a) represents the emission spectra with their corresponding energy transitions under 900 nm excitation source and Fig. 3(b) represents the respective energy level diagram supported by direct energy transfers from Yb^{3+} to Er^{3+} ion.

The insets in Fig. 3(a) shows the visible blue emissions of UCN-PNs from the UCN-PNs sample kept in glass bottle and quartz cuvette, with direct irradiation of 200 nm wavelength source. Fig. 4(a) and (b) show the UCN-PNs solution (during synthesis) in stirring condition within reaction chamber and glass bottle and 4c shows blue emissions for the UCN-PNs just after washing, respectively. These UCN-PNs are stable at least for one year owing to their high surface zeta potential value (ξ) of about −55.49 mV (Fig. S3†).

Fig. 5 shows the Raman spectrum for UCN-PNs, where the bands appeared at 260 cm^{-1}, 303 cm^{-1}, 364 cm^{-1} and 395 cm^{-1} (below 700 cm^{-1}) confirm the formation of hexagonal-phases.[35,36] Beyond 700 cm^{-1}, the appearance of strong bands at 725 cm^{-1}, 2887 cm^{-1} and 3512 cm^{-1} are evidences for the presence of cubic-phases conjugated with oleic acid (capping agent). Thus both the results obtained from XRD and Raman confirmed the formation of UCN-PNs with major β-phase along with a less extent of α-phase.

As reported earlier, the appearance of bands due to the presence of vibrational modes above 700 cm^{-1} are found very weak for the minute quantity of hexagonal crystalline phase in UCNPs. With the formation of α-$NaYF_4$ phase, the Raman-spectra broadened within 1384–1416 cm^{-1} and 1041–932 cm^{-1} along with two additional bands appeared in between 703–687 cm^{-1} and 279–260 cm^{-1}.[37,38] Relatively, weaker bands appeared between 700–1700 cm^{-1} and between 2820–2980 cm^{-1} due to the presence of capping agent (oleic acid).[39] Weakly intense Raman bands appeared between 1073 cm^{-1} and 1445 cm^{-1} confirm the presence of asymmetry C–O–C and CH_3 stretching, respectively, whereas presence of C–CH_3/C–H/O–H bonds are confirmed by the medium intense bands appeared near 2885 cm^{-1} and 3620 cm^{-1}. It is also noticed that the, bands appeared between 3300–3500 cm^{-1} are ascribed to the (–N–H) vibration band which contributes for the formations of self-assembled nano necklace net-work structures between UCNPs (full range Raman spectrum has provided in ESI Fig. S4†). Further, the FTIR spectrum of UCN-PNs is shown in Fig. S5† which confirms the presence of various functional groups including N–H bending vibration at 1558 cm^{-1} and other oleic acid-capped groups at 2921 cm^{-1}, 2850 cm^{-1} appearing with highest intensity attached with the UCN-PNs.[40,41]

However, the present analysis gives us a clear indication of α- and β-phase formation within UCN-PNs crystals and is further supported by the TEM and XRD results (Fig. 1(f) and S1†). The presence of two phases effectively influences for the inhancement of upconversion efficiency which has been discussed in the subsequent sections.

Open Access Article. Published on 22 November 2019. Downloaded on 7/24/2020 9:31:16 AM.
This article is licensed under a Creative Commons Attribution-NonCommercial 3.0 Unported Licence.

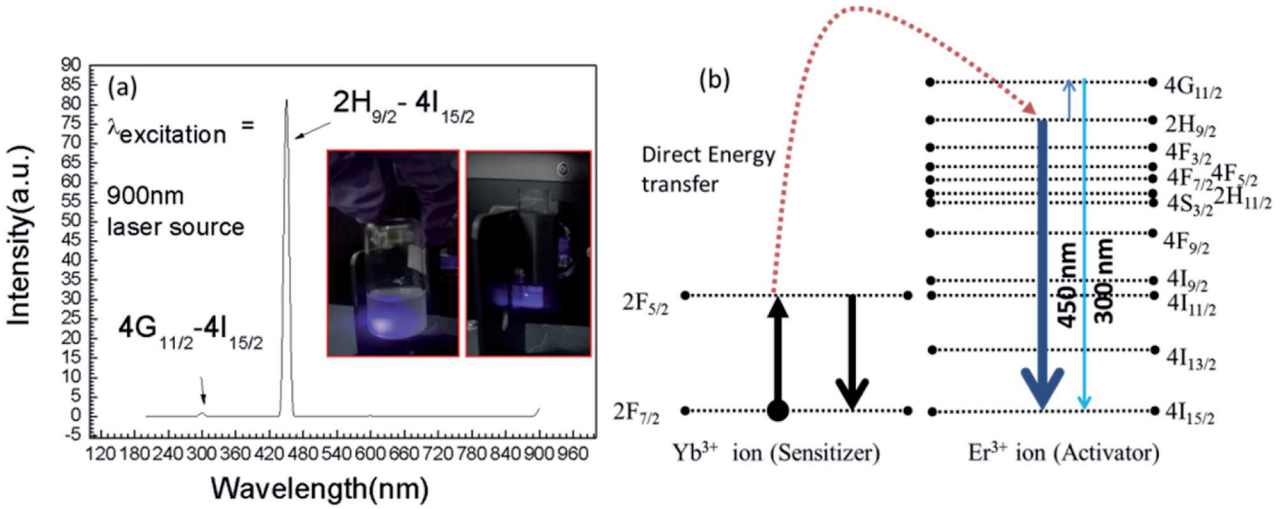

Fig. 3 (a) Upconversion emission spectrum obtained with $\lambda_{excitation}$ of 900 nm CW laser source. Inset of (a) is showing the blue emission from UCN-PNs and (b) is the corresponding energy band diagram.

PL of the UCN-PNs has also been studied. From PL study (Fig. 6), a visible–visible wavelength conversion emission bands are observed. The excitation wavelength source was used with $\lambda = 450$ nm and the observed emissions obtained here are in between 400–650 nm. This is an interesting observation which has never been reported even for any type of UCNPs. It can be noted that for all rare earth materials and for UCNPs only NIR to visible upconversion was reported.[42,43] In another study, NIR–NIR upconversion was also reported previously in literature.[34,44–47] However, visible to visible wavelength conversion is a unique phenomenon observed for UCN-PNs, and to the best of our knowledge it has never been reported. For UCN-PNs, the observed emission bands with their highest band positions appeared at 422 nm, 462 nm, 520 nm/546 nm, 572 nm and 638 nm, correspond to the energy transfers as, $2H_{9/2} \rightarrow 4I_{15/2}$ and $2H_{11/2}/4S_{3/2} \rightarrow 4I_{15/2}$ and $4F_{9/2} \rightarrow 4I_{15/2}$, respectively. The energy level diagram correspond to the PL spectra (Fig. 6(a)) is shown in Fig. 6(b). The band energy diagram includes two incidences of direct energy transfers between two rare earth ions (Yb^{3+} and Er^{3+}) and passes through several cross relaxations and, radiative and non-radiative decays that resulted in a number of emission bands. They are as follows:

Energy transfer-I occurred for $2F_{5/2} \rightarrow 2H_{9/2}$ transition, energy transfer-II occurs from $2F_{5/2} \rightarrow 4F_{9/2}$ resulting efficient blue and red emissions with $2H_{9/2} \rightarrow 4I_{15/2}$ and $4F_{9/2} \rightarrow 4I_{15/2}$ transitions, respectively. Whereas, the green emissions occurred with four non-radiative relaxations such as, $2H_{9/2} \rightarrow 4F_{3/2}$, $4F_{3/2} \rightarrow 4F_{5/2}$, $4F_{5/2} \rightarrow 4F_{7/2}$, $4F_{7/2} \rightarrow 2H_{11/2}$ or $4S_{3/2}$ from $2H_{9/2}$ level with $2H_{11/2}/4S_{3/2} \rightarrow 4I_{15/2}$ transitions (see Fig. 6(b)).

3.1. Study the upconversion luminescence with femtosecond (Fs)-laser source with different excitation wavelengths

Interaction of UCN-PNs with femtosecond-laser (Fs) results in high energy upconversion emissions under five different excitation wavelengths, such as $\lambda = 940$ nm, 950 nm, 960 nm,

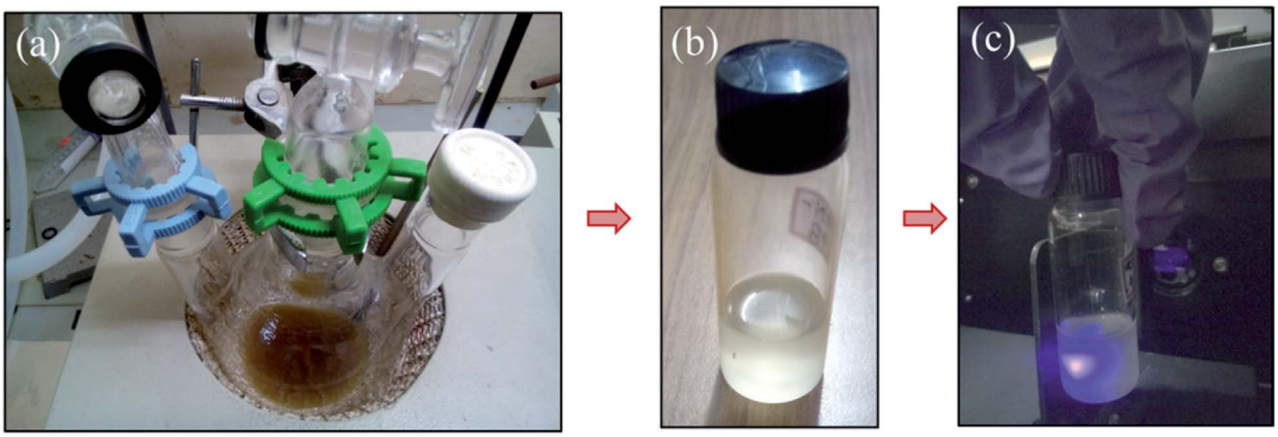

Fig. 4 (a) Image is captured during synthesis (stirring condition) of UCN-PNs at high reaction temperature (~330–340 °C) with 1 h 53 min reaction time (b) UCN-PNs colloidal sample and (c) intense blue emission in sample glass bottle, after washing done completely.

This journal is © The Royal Society of Chemistry 2019

Open Access Article. Published on 22 November 2019. Downloaded on 7/24/2020 9:31:16 AM.
This article is licensed under a Creative Commons Attribution-NonCommercial 3.0 Unported Licence.

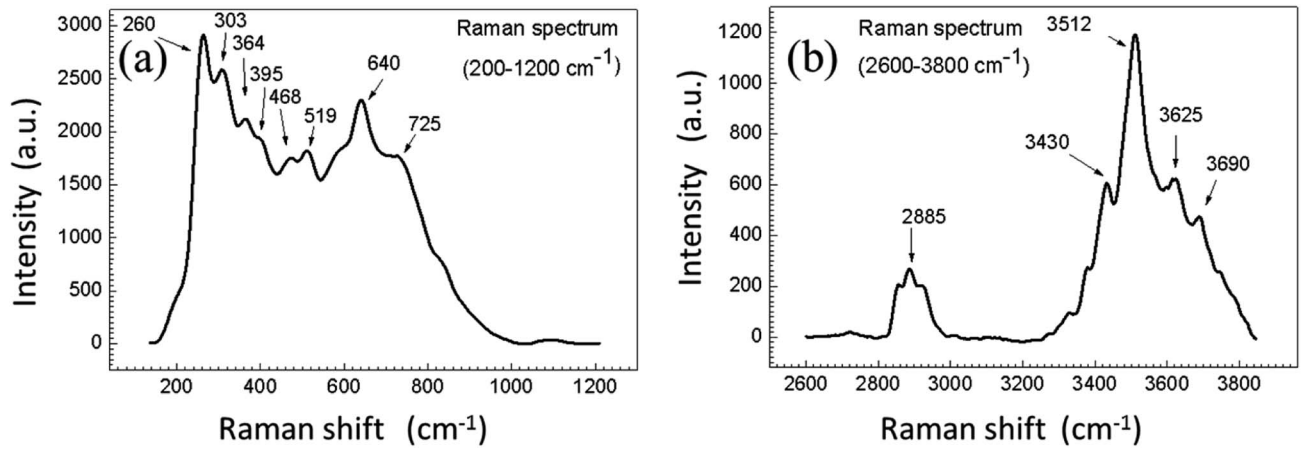

Fig. 5 (a) Raman spectrum between 200–1200 nm, (b) Raman spectrum between 2600–3800 nm, confirm the presence of both cubic (α) and beta (β) phases in sample. The measurement was recorded at room temperature. The entire spectrum is shown in ESI (see Fig. S4†).

970 nm and 980 nm. Each of the incident pump wavelength has yielded distinct emissions in both UV and visible regions. The emission spectra along with their corresponding energy level diagrams are shown in Fig. 7 and 8. In energy diagrams, width of each emission band is adjusted according to the intensity of the band received from the emission spectra.

3.1.1. Fs-laser-940 nm incident pump wavelength. Emissive bands are observed between 239–397 nm in UV/violet region; 474 nm (blue emission); 544 nm (green emission); 604 nm, 670 nm and 718 nm (red emission bands) in visible region (Fig. 7(a)-i). The energy level diagram with respect to the observed emission wavelengths has been drawn and shown in Fig. 7(a)-ii which states three direct energy transfers from sensitizer ($2F_{5/2}$) to activator ion ($4F_{7/2}$ and $4F_{9/2}$) and thereafter it passes through the different transitions within electronic states of Er^{3+} ion. Three major energy transfer occurred and can be represented as, (i) $2F_{5/2}(Yb^{3+}) \rightarrow 4F_{7/2}(Er^{3+})$; (ii) $2F_{5/2}(Yb^{3+}) \rightarrow 4F_{9/2}(Er^{3+})$ and (iii) $2F_{5/2}(Yb^{3+}) \rightarrow 4G_{11/2}(Er^{3+})$, with a total of three non-radiative relaxations such as, $4G_{11/2}(Er^{3+}) \rightarrow 2H_{9/2}(Er^{3+})$, $4F_{7/2}(Er^{3+}) \rightarrow 2H_{11/2}(Er^{3+})$, $2H_{11/2}(Er^{3+}) \rightarrow 4S_{3/2}(Er^{3+})$, respectively.

3.1.2. Fs-laser 950 nm incident pump wavelength. During the interaction of UCN-PNs and Fs-laser 950 nm excitation source, emissive bands are obtained in between 265–432 nm of UV/violet regions; 455 nm (blue emission); 493 nm (intermediate region); 540 nm (green emission); 602 nm, 669 nm and 722 nm (red emissions) in visible regions (Fig. 7(b)-i). Intensities of bands in lower wavelengths (265–493 nm) appeared to be weak compared to the green and red emissions but definitely with few numbers. The energy level diagram is shown in Fig. 7(b)-ii three direct energy transfers and following energy transitions, (i) $2F_{5/2}(Yb^{3+}) \rightarrow 4F_{7/2}(Er^{3+})$; (ii) $2F_{5/2}(Yb^{3+}) \rightarrow 4F_{9/2}(Er^{3+})$ and (iii) $2F_{5/2}(Yb^{3+}) \rightarrow 2H_{9/2}(Er^{3+})$, with a total of five non-radiative relaxations, $4G_{11/2}(Er^{3+}) \rightarrow 2H_{9/2}(Er^{3+})$, $2H_{9/2}(Er^{3+}) \rightarrow 4F_{3/2}(Er^{3+})$, $4F_{3/2}(Er^{3+}) \rightarrow 4F_{5/2}(Er^{3+})$, $4F_{7/2}(Er^{3+}) \rightarrow 2H_{11/2}(Er^{3+})$, $2H_{11/2}(Er^{3+}) \rightarrow 4S_{3/2}(Er^{3+})$.

3.1.3. Fs-laser 960 nm incident pump wavelength. Once UCN-PNs was interacted with Fs-laser (960 nm), emissive bands

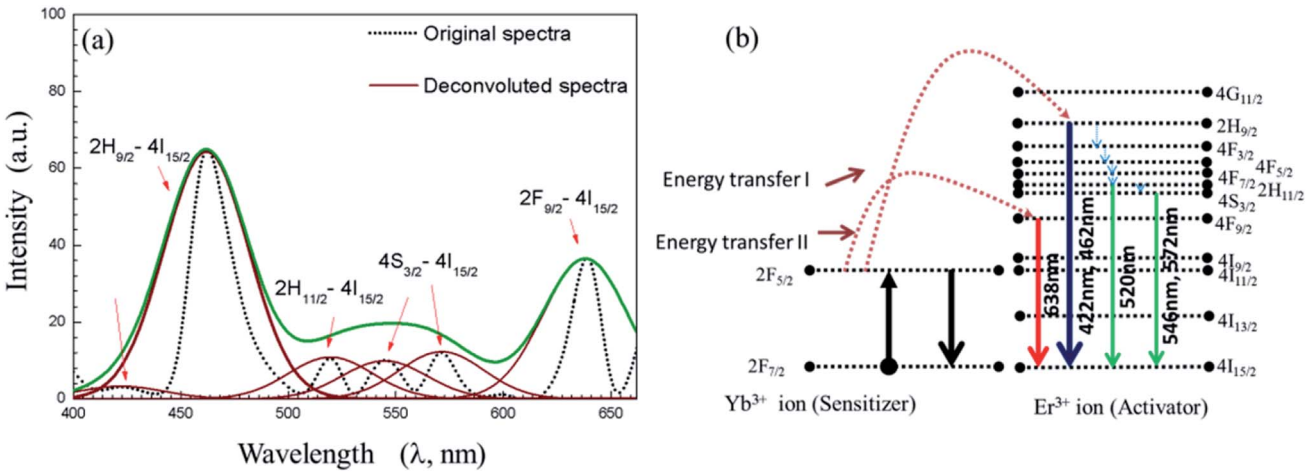

Fig. 6 (a) Photoluminescence (PL) spectra of colloidal UCN-PNs sample obtained with 450 nm excitation wavelength (b) energy diagram drawn from PL emission spectra in (a).

Open Access Article. Published on 22 November 2019. Downloaded on 7/24/2020 9:31:16 AM.
This article is licensed under a Creative Commons Attribution-NonCommercial 3.0 Unported Licence.

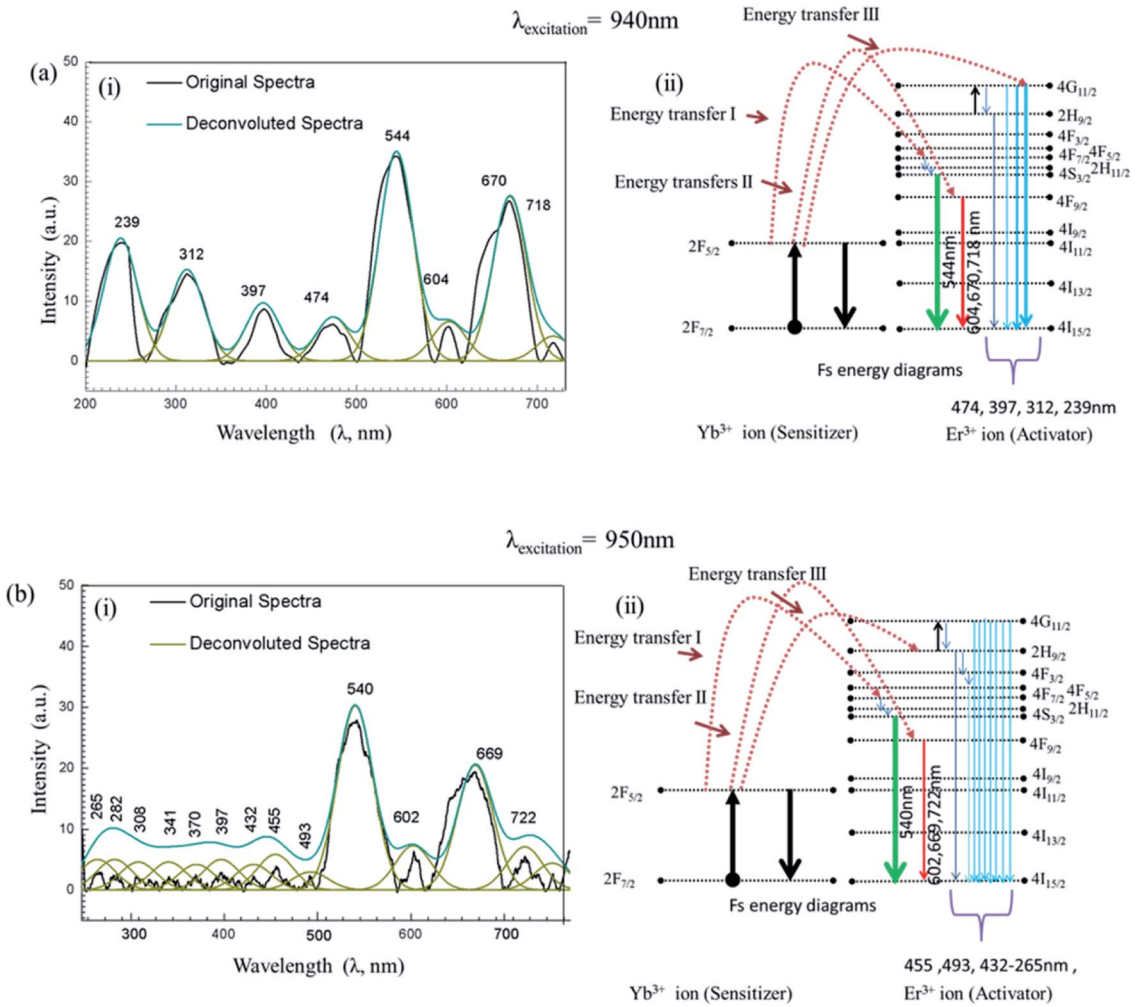

Fig. 7 Upconversion luminescence spectra and their corresponding energy diagram with femtosecond (Fs) arrangement. (a) Spectra (i) and energy level diagram (ii) under 940 nm; (b) spectra (i) and energy level diagram (ii) under 950 nm; excitation wavelengths.

obtained between 282–400 nm in UV/violet region; 465 nm (blue emission); 545 nm (green emission); 604 nm, 669 nm and 721 nm (red emissions) in visible regions (Fig. 8(a)-i). Intensities of bands in lower wavelengths (282–465 nm) are appeared to be weak compared to the green and red emissions. Green and red emissions obtained in the same intensity. The corresponding energy level diagram is shown in Fig. 8(a)-ii with three direct energy transfers, such as (i) $2F_{5/2}(Yb^{3+}) \rightarrow 4F_{7/2}(Er^{3+})$; (ii) $2F_{5/2}(Yb^{3+}) \rightarrow 4F_{9/2}(Er^{3+})$ and (iii) $2F_{5/2}(Yb^{3+}) \rightarrow 2H_{9/2}(Er^{3+})$, similar to 950 nm, differing only with number of non-radiative relaxations following the energy transfer path, $4G_{11/2}(Er^{3+}) \rightarrow 2H_{9/2}(Er^{3+})$, $4F_{7/2}(Er^{3+}) \rightarrow 2H_{11/2}(Er^{3+})$, and $2H_{11/2}(Er^{3+}) \rightarrow 4S_{3/2}(Er^{3+})$.

3.1.4 Fs-laser 970 nm incident pump wavelength. UCN-PNs were also interacted with Fs-laser with 970 nm irradiation and emissive bands obtained in between 241–447 nm in UV/violet regions; 463 nm (blue emission); 490 nm (intermediate region); 540 nm (green emission); 602 nm, 655 nm and 721 nm (red emissions) in visible regions (Fig. 8(b)-i). Emission bands appeared in lower wavelengths (241–490 nm) are quite strong in intensity; even one high intensity band is appeared with 241 nm peak position in UV region. These emission bands can be explained with separate energy band diagram in Fig. 8(b)-ii. Emission occurred due to three direct energy transfers between the different energy levels, such as (i) $2F_{5/2}(Yb^{3+}) \rightarrow 4F_{7/2}(Er^{3+})$; (ii) $2F_{5/2}(Yb^{3+}) \rightarrow 4F_{9/2}(Er^{3+})$ and (iii) $2F_{5/2}(Yb^{3+}) \rightarrow 4G_{11/2}(Er^{3+})$, including five non-radiative relaxations, $4G_{11/2}(Er^{3+}) \rightarrow 2H_{9/2}(Er^{3+})$, $2H_{9/2}(Er^{3+}) \rightarrow 4F_{3/2}(Er^{3+})$,$4F_{3/2}(Er^{3+}) \rightarrow 4F_{5/2}(Er^{3+})$, $4F_{7/2}(Er^{3+}) \rightarrow 2H_{11/2}(Er^{3+})$ and $2H_{11/2}(Er^{3+}) \rightarrow 4S_{3/2}(Er^{3+})$.

3.1.5 Fs-laser 980 nm incident pump wavelength. Finally, to compare the upconversion of UCN-PNs obtained after interaction with CW-980 nm NIR, the same sample interacted with the Fs-laser with $\lambda = 980$ nm. Once interacted with Fs-laser the upconversion emissive bands are observed between 243–402 nm (in UV/violet regions); 473 nm (blue emission); 541 nm (green emission); 603 nm, 660 nm and 719 nm (red emissions) in visible regions (Fig. 8(c)-i). A very high intensity band is observed in UV region compared to others. The energy level diagram is shown in Fig. 8(c)-ii with three direct energy transfers such as, (i) $2F_{5/2}(Yb^{3+}) \rightarrow 4F_{7/2}(Er^{3+})$; (ii) $2F_{5/2}(Yb^{3+}) \rightarrow 4F_{9/2}(Er^{3+})$ and (iii) $2F_{5/2}(Yb^{3+}) \rightarrow 4G_{11/2}(Er^{3+})$, with three non-radiative relaxations, (i) $4G_{11/2}(Er^{3+}) \rightarrow 2H_{9/}$

This journal is © The Royal Society of Chemistry 2019

Open Access Article. Published on 22 November 2019. Downloaded on 7/24/2020 9:31:16 AM.
This article is licensed under a Creative Commons Attribution-NonCommercial 3.0 Unported Licence.

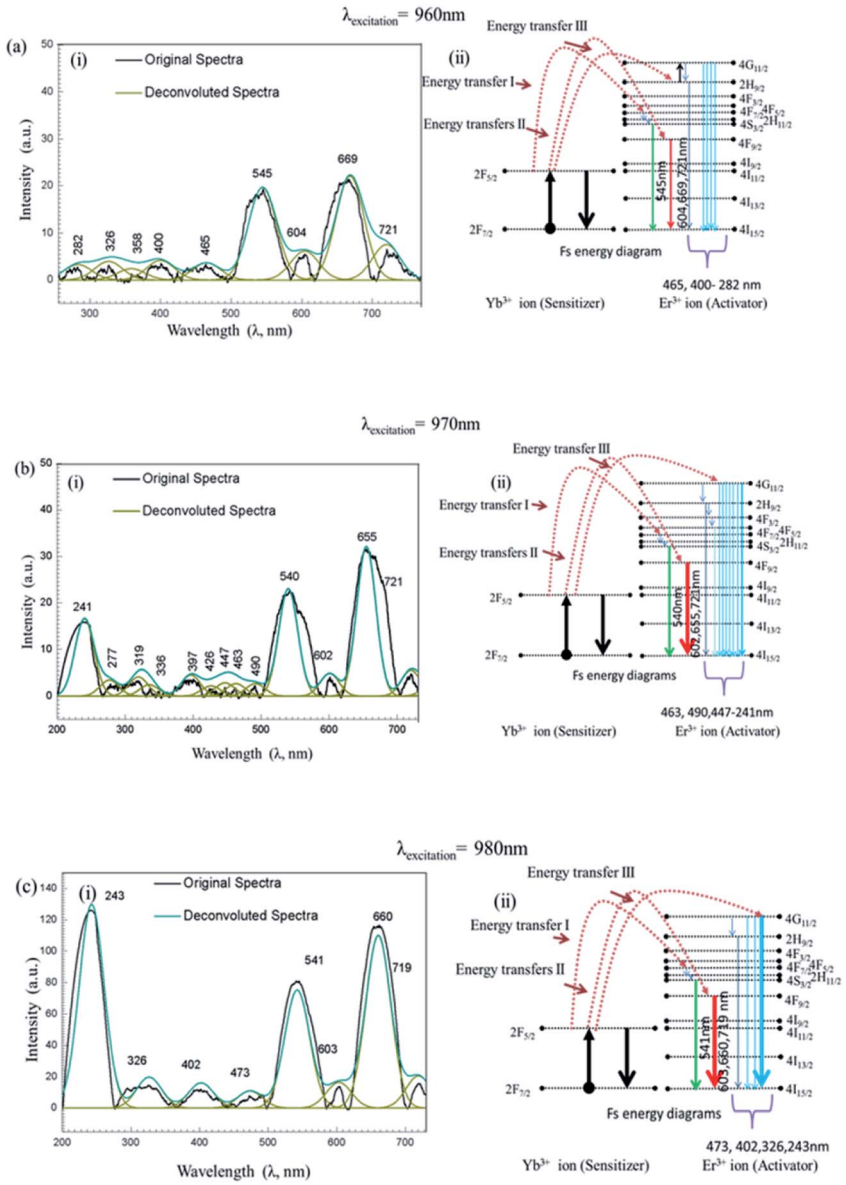

Fig. 8 Upconversion luminescence spectra and their corresponding energy diagram with femtosecond (Fs) arrangement. (a) Spectra (i) and energy band diagram (ii) under 960 nm; (b) spectra (i) and energy level diagram (ii) under 970 nm; (c) spectra (i) and diagram (ii) under 980 nm excitation wavelengths.

$_2(Er^{3+})$, (ii) $4F_{7/2}(Er^{3+}) \rightarrow 2H_{11/2}(Er^{3+})$ and (iii) $2H_{11/2}(Er^{3+}) \rightarrow 4S_{3/2}(Er^{3+})$. Thus, five emission spectra in Fig. 7 and 8 revealed the high energy emissions under different excitation wavelengths, which never been observed for CW-NIR laser (980 nm). Among five of them, the highest UV emission (UV_{full}) was found under 980 nm excitation wavelength. Apart from that, the other emissions green (G)/red (R) are also significant and appear with highest intensity in case of 980 nm excitation wavelength. Blue emissions are also observed in each of the cases.

Furthermore, intensity ratios between UV, R and G under Fs-laser treatment were calculated for five different excitation wavelengths and are shown in Fig. 9. Intensity changes for different emissions (UV, G and R) under different excitation wavelengths (940 nm, 950 nm, 960 nm, 970 nm and 980 nm) resulted in different relative ratio plots UV_{full}/G; UV_{full}/R_{full}; G/R1, G/R2, G/R3; and G/R_{full} shown in Fig. 9(a)–(d), respectively. Different in efficient population of photons in different energy levels under 940–980 nm excitation sources could be the possible reasons for the occurrence of different intensity.

3.2. Discussion

It can be mentioned that the α and β $NaYF_{4c}$ nanocrystals produce with a delayed nucleation during synthesis. Hence, reaction time and temperature play an important role in obtaining different $NaYF_4$ nanopolyhedra. The UCN crystal growth follows by four sequential stages such as (i) delayed nucleation, (ii) particle-growth, (iii) shrinkage and (iv) aggregation.[48,49] In stage I: in this stage, with prolonging reaction

Open Access Article. Published on 22 November 2019. Downloaded on 7/24/2020 9:31:16 AM.
This article is licensed under a Creative Commons Attribution-NonCommercial 3.0 Unported Licence.

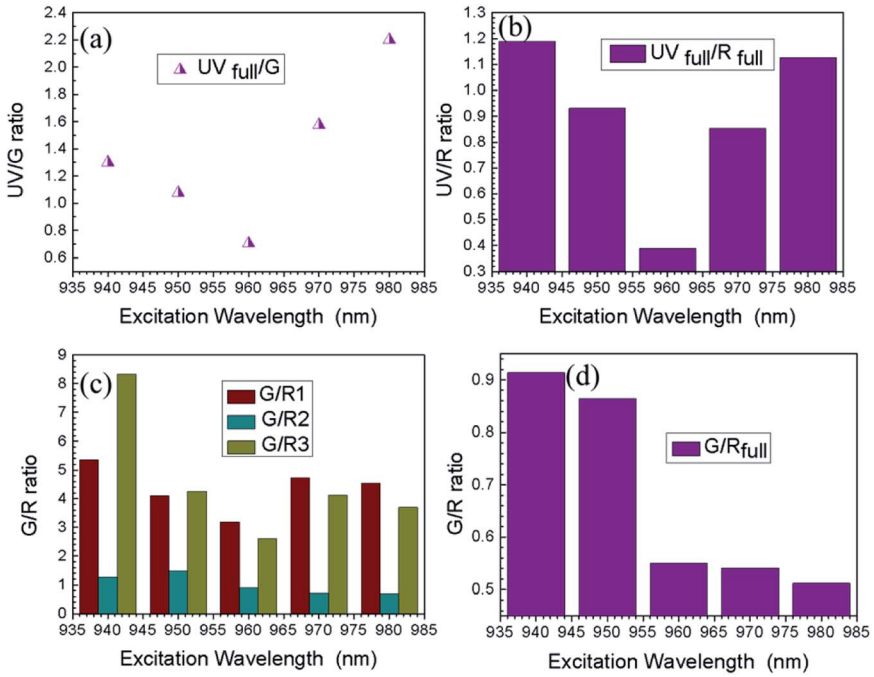

Fig. 9 Shows the ratio plots for the intensity of different emission: (a) UV_{full}/G, (b) UV_{full}/R_{full}; (c) G/R1, G/R2, G/R3; (d) G/R_{full} *vs.* excitation wavelengths.

time, α-phases start to appear and up to a certain period (~70 min) nanocrystal size increases. Hence co-precipitating reaction between sodium fluoride and lanthanide precursors helps to form the α-phases and after that the monomer concentration increases. In stage: II: at initial period, the monomer concentration becomes high and after certain interval the monomers become exhausted and their sizes do not increase further and finally α-$NaYF_4$ dissolves. Stage: III: during third stage, the nanocrystals redispersed by strong coordination between nanocrystal surface and ligands of organic compounds (OA, 1-ODE). Under this condition, small truncated cubes formed. Stage IV: in this stage a non-uniform aggregates are formed from small nanocubes due to higher surface energy and attractive forces from surface-ligands. Now, continuing the reaction the phases-transition between α- to β-phase takes place through the Ostwald-ripening enhanced process in presence of selective lanthanide elements; Y and elements in between (Dy–Lu):Yb,Er.[48,49]

However, binding of N–H groups (as their existence were assured by both Raman and FTIR spectra) to nanocrystal surface, presence of van der Waals forces interaction between nanocrystals surface and oleic-acid ligand, strong co-ordination interaction between nanocrystal surface and several capping-groups could be the possible reasons of pearl-necklace patterned – morphological evolution.

It can be noted that upconversion luminescence properties with Fs-laser irradiation for different rare earth elements along with their applications were reported elsewhere.[50–58] Such as YVO4 single crystal upconversion luminescence was observed under infrared (IR) Fs-irradiation which resulted in broad characteristic emission in visible region (350–600 nm).[50] For, Ce^{3+} doped YAP crystal, upconversion luminescence appeared in both ultraviolet and visible region under a focused 800 nm Fs-laser irradiation.[51] Visible emission bands were also found with $NaYF_4$–glass ceramic doped with Er^{3+} ions under 800 nm CW laser treatment.[52] Intracellular imaging of cancer cells (such as HeLa cells, cervical cancer cells, collected on 8 Feb, 1951 from Henrietta Lacks), by using the Fs-pulse laser (100 Fs, 920 nm) was performed with very high resolution using non-functionalized $NaYF_4$:Er^{3+},Yb^{3+}.[53] Further, red and green upconversion luminescence was reported with 5% Er^{3+} doped $NaYF_4$ nanocrystals with using two Fs-laser (excitation wavelengths 800 nm, 1490 nm) simultaneously.[55] Tunable enhanced ultraviolet luminescence can be developed by using UCNPs for recording highly effective and rapid *in situ*-real time biocompatible photoactivation.[54] Optogenetic proteins have huge applications in neurology and brain science along with cell biology. However, it was found that the narrow excitation wavelength limits the applications of optogenetics which has recently manipulated and improved using tunable Fs-laser system.[59] Moreover, for ultra-deep *in vivo* bio-imaging non-linear optical effects using Fs-laser excitation in AIEgen nanocrystals was found effective.[60] By a group of researchers, it is reported that Ti:Sapphire Fs-laser, with pulse duration of about 160 fs, is very useful for generation of high harmonic as example fifth harmonic generation from photonic crystal and is useful in designing opto-electronic devices with effectively high efficiency.[58] Further, it can be noted that for the rare-earth doped luminescent nanomaterials, colour tuning is having important significance for several applications such as designing of display device, bio-labeling, optoelectronic device *etc.* The tuned luminescence properties can be developed from Er^{3+}

 This journal is © The Royal Society of Chemistry 2019

Open Access Article. Published on 22 November 2019. Downloaded on 7/24/2020 9:31:16 AM.
This article is licensed under a Creative Commons Attribution-NonCommercial 3.0 Unported Licence.

doped glass ceramic using 800 nm Fs-laser excitation sources.[61] Thus, the present findings *i.e.*, the development of UCN-PNs and their improved luminescence properties in UV and visible ranges are very interesting and can be used in device making for industrial (optoelectronics) to biomedical such as for disease diagnosis and therapeutic applications by targeting the infected cells with enhanced efficiency.

4. Summary and conclusions

In this work, $NaYF_4$ nanonecklaces (UCN-PNs) with lanthanides (Yb^{3+}, Er^{3+}) have been synthesized for the first time with one pot chemical synthesis approach, by controlling the reaction temperature in *in situ* condition, without adding any external polymeric components during synthesis process. UCN-PNs contain both of the α- and β-phase within its solid structure and are very stable. Presence of these two phases in UCN-NPs could be the cause of high energy upconversion and make them very seminal and are with caterpillar/necklace type of structure.

This self-assembled pearl-necklaces type structural -network may be allowed for designing 2D nanostructures with defining clear geometry.

Apart from that, the bright blue emission make them very attractive with lower excitation wavelength source with visible to visible upconversion.[10,62] With higher wavelength source with Fs-laser, UV emission becomes prominent making them a suitable candidate for industrial and biomedical applications.[63–65] The different emissions (green/red/blue/cyan/UV) could be useful in colour tuning and magnetic sorting[66,67] by changing their excitation wavelengths.

Conflicts of interest

There are no conflicts to declare.

Acknowledgements

Authors acknowledge the financial support awarded to P. Paik by DST-Nanomission, India (ref: SR/NM/NS-1005/2015), Science and Engineering Research Board, India (ref: EEQ/2016/000040). M. D. Modak acknowledges the DST INSPIRE fellowship (IVR No. 201400000480, No. DST/INSPIRE Fellowship/2015/IF150215), Department of Science and Technology, Ministry of Science and Technology for pursuing PhD. Authors also want to acknowledge Defence Research and Development Organizations (DRDO) , Ministry of Defence , and Government of India (ERIP/ER/1501138/M/01/319/D(RD)) for providing Femtosecond – laser facility.

Notes and references

1 D. Astruc, E. Boisselier and C. Ornelas, *Chem. Rev.*, 2010, **110**, 1857–1959.
2 C. C. Lee, J. A. MacKay, J. M. J. Fréchet and F. C. Szoka, *Nat. Biotechnol.*, 2005, **23**, 1517–1526.
3 L. Wang, R. Yan, Z. Huo, L. Wang, J. Zeng, J. Bao, X. Wang, Q. Peng and Y. Li, *Angew. Chem., Int. Ed.*, 2005, **44**, 6054–6057.
4 C. ZHANG, L. SUN, Y. ZHANG and C. YAN, *J. Rare Earths*, 2010, **28**, 807–819.
5 M. Wang, G. Abbineni, A. Clevenger, C. Mao and S. Xu, *Nanomedicine*, 2011, **7**, 710–729.
6 G. Yi, H. Lu, S. Zhao, Y. Ge, W. Yang, D. Chen and L.-H. Guo, *Nano Lett.*, 2004, **4**, 2191–2196.
7 G. Chen, H. Qiu, P. N. Prasad and X. Chen, *Chem. Rev.*, 2014, **114**, 5161–5214.
8 T. V. Esipova, X. Ye, J. E. Collins, S. Sakadžić, E. T. Mandeville, C. B. Murray and S. A. Vinogradov, *Proc. Natl. Acad. Sci. U. S. A.*, 2012, **109**, 20826–20831.
9 L. Wang and Y. Li, *Chem. Commun.*, 2006, 2557–2559.
10 Q. Liu, T. Yang, W. Feng and F. Li, *J. Am. Chem. Soc.*, 2012, **134**, 5390–5397.
11 Z. Li, Y. Zhang and S. Jiang, *Adv. Mater.*, 2008, **20**, 4765–4769.
12 F. Wang and X. Liu, *J. Am. Chem. Soc.*, 2008, **130**, 5642–5643.
13 V. Muhr, C. Würth, M. Kraft, M. Buchner, A. J. Baeumner, U. Resch-Genger and T. Hirsch, *Anal. Chem.*, 2017, **89**, 4868–4874.
14 C. Hazra, V. N. K. B. Adusumalli and V. Mahalingam, *ACS Appl. Mater. Interfaces*, 2014, **6**, 7833–7839.
15 Y. Ma, S. Huang, M. Deng and L. Wang, *ACS Appl. Mater. Interfaces*, 2014, **6**, 7790–7796.
16 D. K. Chatterjee, M. K. Gnanasammandhan and Y. Zhang, *Small*, 2010, **6**, 2781–2795.
17 L. Y. Ang, M. E. Lim, L. C. Ong and Y. Zhang, *Nanomedicine*, 2011, **6**, 1273–1288.
18 L.-L. Li, H.-W. An, B. Peng, R. Zheng and H. Wang, *Mater. Horiz.*, 2019, **6**, 1794–1811.
19 G. Pandit, K. Roy, U. Agarwal and S. Chatterjee, *ACS Omega*, 2018, **3**, 3143–3155.
20 S. Whitelam and R. L. Jack, *Annu. Rev. Phys. Chem.*, 2015, **66**, 143–163.
21 A. Saini, R. Kaur, N. Singh, A. Kuwar and N. Kaur, *ACS Appl. Bio Mater.*, 2019, **2**, 135–143.
22 M. Dolci, D. Toulemon, Z. Chaffar, J.-L. Bubendorff, F. Tielens, M. Calatayud, S. Zafeiratos, S. Begin-Colin and B. P. Pichon, *ACS Appl. Nano Mater.*, 2019, **2**, 554–565.
23 D. Perahia, R. Traiphol and U. H. F. Bunz, *Macromolecules*, 2001, **34**, 151–155.
24 M.-C. Daniel and D. Astruc, *Chem. Rev.*, 2004, **104**, 293–346.
25 C. Wang, L. Cheng and Z. Liu, *Theranostics*, 2013, **3**, 317–330.
26 C. Wang, H. Tao, L. Cheng and Z. Liu, *Biomaterials*, 2011, **32**, 6145–6154.
27 Q. Chen, C. Wang, L. Cheng, W. He, Z. Cheng and Z. Liu, *Biomaterials*, 2014, **35**, 2915–2923.
28 C.-X. Huang, H.-J. Chen, F. Li, W.-N. Wang, D.-D. Li, X.-Z. Yang, Z.-H. Miao, Z.-B. Zha, Y. Lu and H.-S. Qian, *J. Mater. Chem. B*, 2017, **5**, 9487–9496.
29 K. Liu, L. Dong, Y. Xu, X. Yan, F. Li, Y. Lu, W. Tao, H. Peng, Y. Wu, Y. Su, D. Ling, T. He, H. Qian and S.-H. Yu, *Biomaterials*, 2018, **158**, 74–85.
30 J.-C. Boyer, L. A. Cuccia and J. Capobianco, *Nano Lett.*, 2007, **7**, 847–852.

Open Access Article. Published on 22 November 2019. Downloaded on 7/24/2020 9:31:16 AM. This article is licensed under a Creative Commons Attribution-NonCommercial 3.0 Unported Licence.

31 S. Heer, K. Kömpe, H. U. Güdel and M. Haase, *Adv. Mater.*, 2004, **16**, 2102–2105.
32 K. N. Reddy, M. A. H. Shareef and N. Pandaraiah, *J. Mater. Sci. Lett.*, 1983, **2**, 83–84.
33 H. Song, B. Sun, T. Wang, S. Lu, L. Yang, B. Chen, X. Wang and X. Kong, *Solid State Commun.*, 2004, **132**, 409–413.
34 M. Lee, Y. H. Park, E. B. Kang, A. Chae, Y. Choi, S. Jo, Y. J. Kim, S.-J. Park, B. Min, T. K. An, J. Lee, S.-I. In, S. Y. Kim, S. Y. Park and I. In, *ACS Omega*, 2017, **2**, 7096–7105.
35 D. T. Klier and M. U. Kumke, *J. Mater. Chem. C*, 2015, **3**, 11228–11238.
36 X. Luo and K. Akimoto, *Appl. Surf. Sci.*, 2013, **273**, 257–260.
37 C. Renero-Lecuna, R. Martín-Rodríguez, R. Valiente, J. González, F. Rodríguez, K. W. Krämer and H. U. Güdel, *Chem. Mater.*, 2011, **23**, 3442–3448.
38 H. Assaaoudi, G.-B. Shan, N. Dyck and G. P. Demopoulos, *CrystEngComm*, 2013, **15**, 4739–4746.
39 S. Wilhelm, T. Hirsch, W. M. Patterson, E. Scheucher, T. Mayr and O. S. Wolfbeis, *Theranostics*, 2013, **3**, 239–248.
40 Z. Li, H. Miao, Y. Fu, Y. Liu, R. Zhang and B. Tang, *Nanoscale Res. Lett.*, 2016, **11**, 441.
41 M. He, P. Huang, C. Zhang, F. Chen, C. Wang, J. Ma, R. He and D. Cui, *Chem. Commun.*, 2011, **47**, 9510–9512.
42 J. A. Capobianco, F. Vetrone, J. C. Boyer, A. Speghini and M. Bettinelli, *Opt. Mater.*, 2002, **19**, 259–268.
43 H. Guo, N. Dong, M. Yin, W. Zhang, L. Lou and S. Xia, *J. Phys. Chem. B*, 2004, **108**, 19205–19209.
44 M. Nyk, R. Kumar, T. Y. Ohulchanskyy, E. J. Bergey and P. N. Prasad, *Nano Lett.*, 2008, **8**, 3834–3838.
45 G. Chen, T. Y. Ohulchanskyy, R. Kumar, H. Ågren and P. N. Prasad, *ACS Nano*, 2010, **4**, 3163–3168.
46 T.-Y. Hsieh, W.-C. Huang, Y.-D. Kang, C.-Y. Chu, W.-L. Liao, Y.-Y. Chen and S.-Y. Chen, *Adv. Healthcare Mater.*, 2016, **5**, 3016–3026.
47 A. Xia, Y. Gao, J. Zhou, C. Li, T. Yang, D. Wu, L. Wu and F. Li, *Biomaterials*, 2011, **32**, 7200–7208.
48 N. T. K. Thanh, N. Maclean and S. Mahiddine, *Chem. Rev.*, 2014, **114**, 7610–7630.
49 H.-X. Mai, Y.-W. Zhang, L.-D. Sun and C.-H. Yan, *J. Phys. Chem. C*, 2007, **111**, 13730–13739.
50 L. Yang, C. Wang, Y. Dong, N. Da, X. Hu, D. Chen and J. Qiu, *Opt. Express*, 2005, **13**, 10157–10162.
51 L. Yang, Y. Dong, D. Chen, C. Wang, X. Hu, N. Da, G. Zhao, J. Xu, X. Jiang, C. Zhu and J. Qiu, *Opt. Express*, 2006, **14**, 243–247.
52 X. Shang, P. Chen, T. Jia, D. Feng, S. Zhang, Z. Sun and J. Qiu, *Phys. Chem. Chem. Phys.*, 2015, **17**, 11481–11489.
53 F. Vetrone, R. Naccache, A. de la Fuente, F. Sanz-Rodríguez, A. Blazquez-Castro, E. M. Rodriguez, D. Jaque, J. G. Solé and J. A. Capobianco, *Nanoscale*, 2010, **2**, 495–498.
54 J. Shen, G. Chen, T. Y. Ohulchanskyy, S. J. Kesseli, S. Buchholz, Z. Li, P. N. Prasad and G. Han, *Small*, 2013, **9**, 3213–3217.
55 X. Shang, P. Chen, W. Cheng, K. Zhou, J. Ma, D. Feng, S. Zhang, Z. Sun, J. Qiu and T. Jia, *J. Appl. Phys.*, 2014, **116**, 063101.
56 Y. Dong, J. Xu, G. Zhou, G. Zhao, M. Jie, L. Y. Yang, L. Su, J. Qiu, W. Feng and L. lin, *Opt. Express*, 2006, **14**, 1899–1904.
57 M. H. Yuan, H. H. Fan, Q. F. Dai, S. Lan, X. Wan and S. L. Tie, *Opt. Express*, 2015, **23**, 21909–21918.
58 P. Tzankov, O. Steinkellner, J. Zheng, M. Mero, W. Freyer, A. Husakou, I. Babushkin, J. Herrmann and F. Noack, *Opt. Express*, 2007, **15**, 6389–6395.
59 W. Ji, S. Wang, J. Zhao, Y. Tian, H. Pan, B. Zheng, M. Yang, H. Tian, M. Hu, H. Wang and J. Chang, *J. Appl. Phys.*, 2019, **125**, 163105.
60 Z. Zheng, D. Li, Z. liu, H.-Q. Peng, H. H.-Y. Sung, R. T. K. Kwok, I. D. Williams, J. W. Y. Lam, J. Qian and B. Z. Tang, *Adv. Mater.*, 2019, **31**, 1904799.
61 L.-Z. Deng, Y.-H. Yao, L. Deng, H.-Y. Jia, Y. Zheng, C. Xu, J.-P. Li, T.-Q. Jia, J.-R. Qiu, Z.-R. Sun and S.-A. Zhang, *Front. Phys.*, 2018, **14**, 13602.
62 O. S. Kwon, H. S. Song, J. Conde, H. Il Kim, N. Artzi and J. H. Kim, *ACS Nano*, 2016, **10**, 1512–1521.
63 B. Del Rosal and D. Jaque, *Methods Appl. Fluoresc.*, 2019, **7**, 022001.
64 Y. Liu, X. Meng and W. Bu, *Coord. Chem. Rev.*, 2019, **379**, 82–98.
65 G. Yi, H. Lu, S. Zhao, Y. Ge, W. Yang, D. Chen and L. H. Guo, *Nano Lett.*, 2004, **4**, 2191–2196.
66 J. H. Kim, F. Deng, F. N. Castellano and J. H. Kim, *ACS Photonics*, 2014, **1**, 382–388.
67 X. Zhang, Z. Zhang, Z. Liu, C. Zhang, B. Zhang, X. Mi and H. Zheng, *J. Lumin.*, 2019, **205**, 374–379.

This journal is © The Royal Society of Chemistry 2019

Optics and Laser Technology 103 (2018) 126–134

Contents lists available at ScienceDirect

Optics and Laser Technology

journal homepage: www.elsevier.com/locate/optlastec

Full length article

Generation of terahertz from $ZnGeP_2$ crystal and its application to record the time-resolved photoacoustic spectra of nitromethane

K.S. Rao, D. Ganesh, A.K. Chaudhary *

Advanced Centre of Research in High Energy Materials (ACRHEM), University of Hyderabad, Hyderabad 500046, India

ARTICLE INFO

Article history:
Received 16 August 2017
Received in revised form 13 November 2017
Accepted 4 January 2018

Keywords:
Pulsed THz
UV
PA spectra
Nitromethane
Methanol

ABSTRACT

This paper reports the generation of THz radiation through the optical rectification process from type-I cut Zinc germanium phosphate ($ZnGeP_2$or ZGP) crystal using optical parametric amplifier pulses (tunable between 1.15–1.6 μm range, at 60 fs pulse duration and 1 kHz repetition rate) as pump wavelengths at an average power of 50 mW. Also, we have ascertained the conversion efficiency of the generated THz signal, which is of the order of 0.62% at 1.5 THz. Further, the generated radiation is employed for the recording of absorption bands (in terms of PA spectra) of nitromethane and methanol vapor at room temperature using bandpass filters having central frequencies of 0.5 and 1.5 THz. In addition, we have employed the UV-266 nm as an excitation wavelength to record the time domain photoacoustic (PA) spectra of nitromethane (CH_3NO_2). In case of UV and THz radiations, the excitation mechanisms follow strong electronic ($\pi^* \leftarrow n$) and weak vibrational–rotational due to ultrafast transition, respectively. In case of UV-266 nm the characteristic PA spectra has been also presented as a function of vapor pressure and data acquisition time with two different PA cells. The current study reveals the effect of the nanoseconds and the ultrafast pulses on some of the common excited acoustic modes (due to similar functional group), which follow two different types of excitation mechanism.

© 2018 Elsevier Ltd. All rights reserved.

1. Introduction

Terahertz (THz) part of the electromagnetic spectrum lying between the millimeter wave and infrared (100 GHz–10 THz) region [1]. The THz band has various unique features when compared to other bands of electromagnetic spectrum. It can interact strongly with polar materials, thereby penetrating through non-polar and non-metallic materials. It has a high reflection on metallic surfaces due to the high electrical conductivity of metals. Especially, for the generation and detection of THz radiation opened a new channel of applications of THz waves in spectroscopy and imaging [2,3]. In THz based spectroscopy, these frequencies are access to the vibrational-rotational translations lines of gas/liquid/solids materials. Therefore, the recorded time-resolved absorption spectra of materials in the THz domain can be treated as a characteristic spectrum of corresponding molecules.

In the first part of the report, we have demonstrated the generation terahertz radiation from ZGP crystal. It is one of the promising crystal due to the availability of few best sellmeir dispersion equations in the optical and THz domain [4]. It has symmetry, positive uniaxial ($n_e > n_o$) crystal belongs to chalcopyrite group, has transparency range $\lambda = 0.74–12$ μm and non-hygroscopic in nature. Also, as compared to another chalcopyrite middle infrared nonlinear optical crystals, $ZnGeP_2$ crystal exhibits high nonlinear optical coefficient, d_{36} reaching 75 pm/V; wide transparency range (0.67–13 μm). It possesses adequate birefringence for phase matching; high thermal conductivity (0.35 W/cm K); high laser damage threshold; stable physicochemical property; high performance of the mechanical character. Due to the low photon energy of THz radiation (which can easily penetrate through non-metals) as well as high damage threshold of ZGP crystal. Its crystallite property does not show any change before and after exposed to the optical and THz radiations. Also, the crystal has good sustainability after exposing to the THz radiation. Therefore, we can treat this one of the promising crystal for the generation of THz radiation using near-infrared wavelengths. It is one of the preferred crystal used for difference frequency generation (DFG) for generating the efficient monochromatic IR and THz radiation [5–9]. In case of DFG based THz generation, two closer laser wavelengths, i.e., signal and pump beams (in near IR range or IR region) are mixed in type-I cut ZGP crystal. Whereas, in case of OR only single beam of near IR wavelength obtained from the femtosecond laser is sufficient to generate the broadband THz radiation. Many research

* Corresponding author.
E-mail addresses: anilphys@yahoo.com, akcphys@gmail.com (A.K. Chaudhary).

https://doi.org/10.1016/j.optlastec.2018.01.009
0030-3992/© 2018 Elsevier Ltd. All rights reserved.

groups reported the generation of narrowband and broadband THz pulses from ZGP crystal using different types of nonlinear optical process [1,5,10–12]. It is well known that OR is second-order nonlinearity based optical process; it generates a transient D.C. polarization, which creates THz radiation for ultrashort excitation pulses. Advances in THz pulse generation technology using OR process made significant enhancement in the energy of the generated signal. For its applications in communications, imaging and spectroscopy, coherent control, and chemical recognition [13–16]. THz spectroscopy is developed using the pump-probe technique, where the sample is subjected to THz pump beam and weak optical beam used as a probe (coherent detection technique). The generated power of THz radiation can be measured using pyroelectric detector (incoherent technique). The probable frequency range of THz generated from $ZnGeP_2$ crystal lies between 0.1–10 THz [10–12]. However, obtained frequency range also depends on the type of detection arrangements. For example, generated range of THz radiation from ZnTe crystal (Electro-Optic sampling technique) cover 0.1–10 THz. Whereas Si-GaAs based photoconductive antennas, the technique is limited up to 2.2 THz. The present report restricted for measuring the power of full-emitted radiation along with the 0.5 and 1.5 THz radiation external bands pass filters. The power of THz radiation was measured using pyroelectric detector.

However, in the second step, the demonstration has been made to show the potential use of THz radiation for recording the photoacoustic (PA) spectra of nitromethane and methanol. The photoacoustic spectroscopy is a well-established technique for the detection of gas molecules using different laser sources [17–22]. Nitromethane (NM) is a volatile organic compound, having chemical formula CH_3NO_2 and vapor pressure of 30 Torr at room temperature, can easily be evaporated into the atmosphere [23,24]. It consists of a nitro-group creating a heavy frame for its methyl group which acts as a light internal rotator [25]. It is widely used as a laboratory solvent, synthetic reagent, fuel, and also possess explosive properties [26,27]. It also exhibits a rotational spectrum in the far-infrared, terahertz (THz) region due to its strong dipole moment of the order of 3.46 D [28,29]. However, methanol (available at 97 Torr at room temperature) is the first member of alcohol group and consists of an -OH group, which is attached to a hydrocarbon chain to form CH_3OH. Since the -OH group of methanol is electronegative while the CH- group is positive. The charge separation makes methanol a polar liquid. Consequently, it shows significant absorption in IR and THz regions [30]. Also, it is an important biomarker gas present in the human breath [31].

Nitromethane and methanol liquids are easily available in the laboratory. At room temperature, they possess sufficient vapor pressures of 30 and 97 Torr pressure range, respectively. Moreover, these molecules have several vibrational and rotational lines in the THz domain [12,28,29]. Nitromethane is an explosive compound, however, in futuristic applications, the released byproducts of high energy materials during the process of thermal decomposition can be identified using the THz based PA spectroscopy. Therefore, in the present study, we have selected nitromethane and methanol vapor to understand the ultrafast PA response in the THz domain. An attempt has been made to record the photoacoustic spectra of nitromethane and methanol using full THz radiation, 0.5 and 1.5 THz bands (from the emitted THz radiation) by incorporation of external bandpass filters for the first time. Previously, Angelo Sampaolo et al. developed quartz-enhanced photoacoustic (QEPAS) gas sensor for the detection of methanol vapor in the CW-terahertz (THz) spectral range. They employed quartz tuning fork and quantum cascade laser as an excitation source for THz radiation [32]. In addition, several other researchers reported the radiative transitions of nitromethane and methanol molecules regarding their rotational-vibrational modes using far-infrared and CW-THz spectrometer [28,29,33–38]. The CO_2 laser also was used to pump CH_3-OH vapor for making the THz source of different frequency range [39–43]. It also confirms that methanol has strong absorption in the THz frequency range. Whereas, previously reported work discussed the THz (generated from DAST crystal) based PA spectra of pure N_2O molecules deals with weak transitions from rotational lines J = 19, 58, respectively [44]. Nitromethane has only strong electronic transitions in UV wavelength region. Therefore, in the third step, we have recorded the UV 266 nm based PA spectra along with THz frequencies. The motivation for the recording of characteristic PA spectra of nitromethane using UV radiation is correlated to the strong electric transitions which are responsible for the excitation of vibration modes. These modes are recorded in two different types of PA cells as a function of vapor pressure, and data acquisition time. However, nitromethane follows photodissociation process which is responsible for the cleavage of C-NO_2 bond to produce free NO, NO_2 and other byproducts due to $\pi^* \leftarrow$ n transition when excited by 266 nm wavelength [45].

2. Experimental details

The experiment was carried out in three parts, (I) THz radiation was generated from the $ZnGeP_2$ crystal of $5 \times 5 \times 5$ mm^3 using optical parametric amplifier (Light Conversion Inc. TOPAS-C) pulses tunable between 1.15–1.6 μm range, at 60 fs pulse duration and 1 kHz repetition rate. (II) The generated THz radiation was employed to record the PA spectra of CH_3NO_2 and CH_3OH at room temperature, using a cylindrical PA cell of internal radius (R) of 7 mm and length (L) of 6.5 cm made of stainless steel. Two Teflon sheets (each 25 mm diameter, 1 mm thickness) were used as windows of PA cell. (III) The fourth harmonic wavelength (i.e. 266 nm) of Nd: YAG laser (Model Spit, Germany) of pulse duration 7 ns and 10 Hz repetition rate was employed to study the comparative photoacoustic spectra of nitromethane at room temperature by varying the pressure of air. The PA spectra were recorded using two different PA cells (Cell-1: R = 7 mm, L = 6.5 cm, Cell-2: R = 7.5 mm, L = 7.5 cm). Here, quartz plates of 25 mm diameter were used as windows for PA cell.

Fig. 1(a) shows the schematic layout of generation of THz and its application in PA spectroscopy. The emitted power of the pump wavelengths (tunable between 1.15–1.6 μm) obtained from the optical parametric amplifier is different. However, the beam diameter of pulses adjusted to 3 mm and their power was fixed at 50 mW using the external neutral density filters. A gold-coated parabolic mirror (PM) was used to focus the THz beam at the center of the PA cell, which was placed 5 cm away from the crystal. Pyroelectric detector (Gentec THZ1.5B-MT-USB) measured the average pulse power of THz radiation; its noise equivalent power was 2 nW at room temperature. It can be operated when the incident pulse has modulation frequencies between 25.1–26.1 Hz range. Therefore, in the present case, the pump pulses modulated at the rate of 25.4 Hz using the digital optical chopper (Model No. SDC-500) and allowed to an incident on the ZGP crystal. A Teflon sheet of 1 mm thickness (kept after the ZGP crystal) and Silicon plate 50 mm diameter and 2.0 mm thickness (kept after the parabolic mirror (PM)) were used to block the unconverted pump pulses. The generated THz signal was allowed to the incident at the center of the pyroelectric detector. The head of the sensor was connected to a T-Rad system, which has inbuilt lock-in-amplifier. Finally, the output of the T-Rad was fed to the personal computer (PC) for signal processing and monitoring the power of the generated THz signal.

The nitromethane (methanol) liquid was kept in a Borosil flask. A rotary pump was used to evacuate the PA cell up to 650 Torr, after that released vapor of nitromethane (methanol) in the air inside the Borosil flask was allowed into the PA cell. The pressure of the vapor lies between 80–650 Torr, range. Gas inlet valve

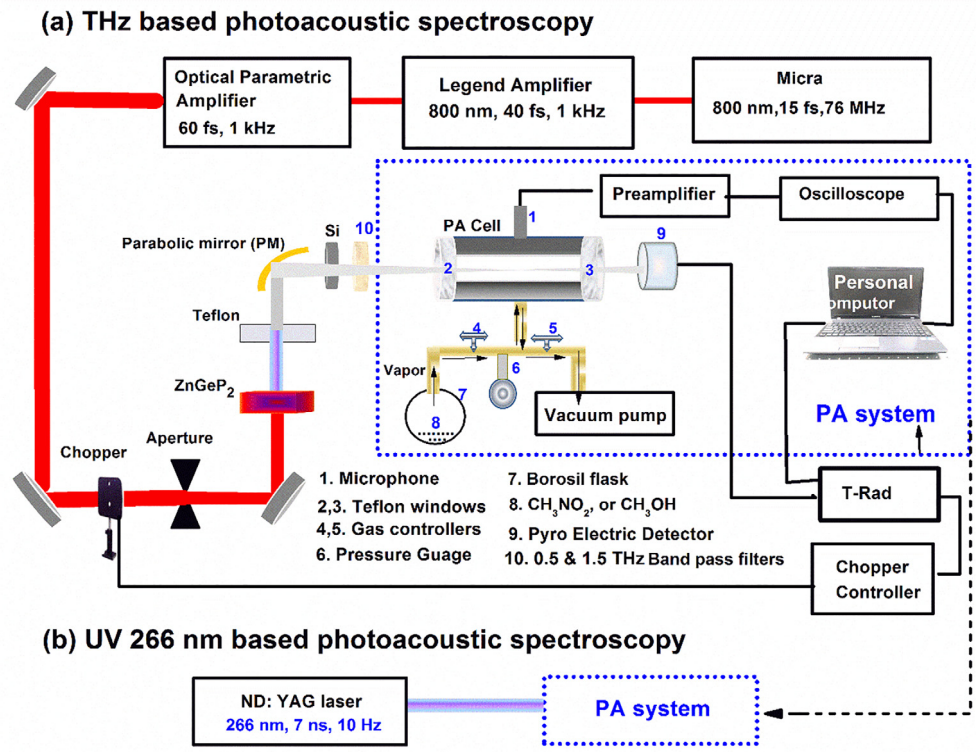

Fig. 1. Experimental setup for (a) THz (b) UV 266 nm based PA spectroscopy.

controlled the rate of flow. Two band-pass filters (BPF) at central frequencies 0.5 THz and 1.5 THz (TYDEX made, BPF 0.5–47, BPF 1.5–47), which are equivalent to 600 and 200 μm wavelength, respectively were placed before the PA cell for the selection of excitation wavelength in terahertz domain. A pre-polarized microphone (BSWA, China) of responsivity 50 mV/Pa was used to detect the generated acoustic signal, which was housed in the center of PA cavity. The output signal of the microphone was fed to the preamplifier, which was coupled to 200 MHz oscilloscopes (Tektronix, USA). The analysis was carried out using data acquisition program, which was developed using LabView software through personal computer. The resultant time domain signal was considered after averaging the 100-time domain signals. The time domain signals (PA signals) converted into frequency domain (PA spectra) using fast Fourier transform. In the second part of the experiment, the PA system was subjected to the UV 266 nm radiation for recording the pressure based PA spectra of nitromethane [45], at incident laser energy (E_{in}) = 35 μJ and data acquisition time (t) = 0.5 ms. The input/output energies of UV 266 nm laser pulses measured with a power meter (EPM2000, Coherent).

3. Results and discussion

The results and discussion are comprised of three subsections, Section 3.1 deals with the coherence length and theoretical conversion efficiency of ZGP crystal, whereas Section 3.2 presented the measurements of generated power of THz radiation from ZGP crystal. Finally, Section 3.3 deals with the THz and UV based PA spectroscopy. The Section 3.3.1 deals with the use of generated THz radiation to record the PA spectra of nitromethane and methanol vapors, while Section 3.3.2 discusses the study of UV based PA spectra of nitromethane recorded at different vapor pressures and data acquisition time using two different PA cells to ascertain the suitable PA cavity for recording of THz based PA spectra as well as to identify the characteristic signatures of nitromethane.

3.1. Theoretical conversion efficiency of ZGP crystal

In case of optical rectification process, the coherence length of crystal (l_c) between the optical and THz wavelengths can be calculated using well-known equation [46]

$$l_c = \frac{\pi c}{\omega_{THz}|n_{g,opt} - n_{THz}|} \quad (1)$$

where 'c' is the velocity of light, $n_{g,opt} = n_{opt} - \lambda_{opt}\frac{\partial n_{opt}}{\partial \lambda}\Big|_{\lambda_{opt}}$ is the optical group refractive index, and n_{THz} is the refractive index of THz radiation.

Fig. 2 exhibits the calculated coherence length of crystal (l_c) at optical pump wavelength 1.3 μm and the THz frequency tunable

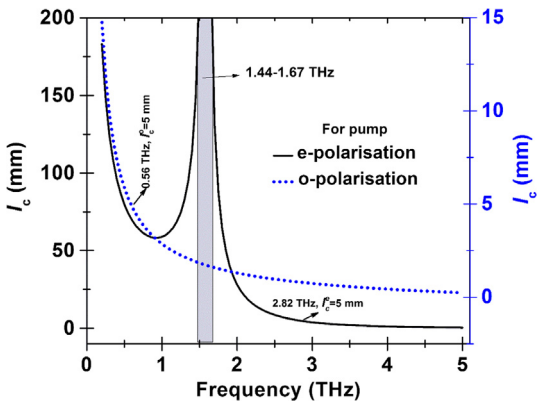

Fig. 2. The coherence length of crystal between 0.2 and 5 THz range at the ordinary and extraordinary optical pump wavelength 1.3 μm.

between 0.2 and 5 THz using Eq. (1). It shows that the crystal possess different coherence lengths for two different types of polarizations. The coherence length for an e-polarized pump wavelength of the crystal showing continuous growth with decreasing bandwidth of pulses between the 1.44–1.67 THz range. Whereas, in case of ordinary pump wavelength the coherence length of the crystal is restricted between 0.24–14.74 mm in the range of 5 THz. The corresponding coherence length of the crystal is at 0.56 and 2.82 THz in 5 mm. Since the reported ZGP crystal thickness is 5 mm, and the pump has e-polarization. Therefore, the crystal is generating the strong THz radiation (which is also reflected in Fig. 3(a)). It is attributed to the coherence length of the crystal (l_c) which is greater than the length/thickness of the crystal (l) and leads to generate the powerful THz radiation [44]. However, THz generation is also possible when the coherence length is less than the thickness of the crystal. It is inferred that the optical rectification process is initiated on the surface of the ZGP crystal and generate the THz radiation which is transmitted through the entire length of the crystal due to good transmission in the THz domain. Consequently, the thickness of the crystal does not show much influence on the power of THz radiation.

The conversion efficiency (η) of generated THz signal is ascertained using following equation

$$\eta = \frac{n^e_{opt}\omega_{THz}}{n^o_{THz}\omega_o} \tag{2}$$

Since the optical refractive index $n^e_{opt} \equiv n(\omega_1) = n(\omega_2)$. In this case, the momentum mismatch is proportional to the index mismatch, $\Delta n = n^e_{opt} - n^o_{THz}$, between the optical and THz waves:

$$\Delta k = \Delta n \frac{\omega_{THz}}{c} \tag{3}$$

The Manley-Rowe relations determine the ultimate upper limit of the optical-to-THz conversion efficiency. Finally, the optical-to-THz conversion efficiency obeys the inequality relation,

$$\frac{I_{THz}(L)}{I_o(0)} \leqslant \frac{n^e_{opt}\omega_{THz}}{n^o_{THz}\omega_{opt}} \sim 10^{-3} - 10^{-2} \tag{4}$$

where n^e_{opt}, n^o_{THz}, and ω_o, ω_{THz} are the refractive indices and angular frequencies of the optical pump, THz wavelengths, respectively [1]. The calculated conversion efficiencies at 0.5 and 1.5 THz bands at optical pump wavelength 1.3 μm is given in Table 1.

Since ZGP is a positive uniaxial crystal ($n_e > n_o$), therefore the polarization for pump wavelength and THz radiations are extraordinary and ordinary, respectively. Table 1 shows that the highest conversion efficiency, i.e. η = 0.62% is achieved at for extraordinary pump at 1.5 THz. This is also supported by data shown in Fig. 3 (c) and (d). The output power measured at 1.5 THz is more rather than 0.5 THz.

3.2. Measurement of THz power from ZGP crystal

Fig. 3(a) exhibits the measured power of THz radiation without inserting the PA cell in the propagation direction at input power P_{in} = 50 mW of pump wavelengths. The power was measured at the focal point of the parabolic mirror (f = 10 cm). Fig. 3(b)–(d) shows the measured power after passing through evacuated PA cell with bandpass filters at central frequencies 0.5 and 1.5 THz, respectively. The maximum power of THz radiation is recorded between the pump wavelength range of 1.275–1.350 μm. Rowley et al. generated the intense undistorted THz pulses using 1 mm thick (012) type $ZnGeP_2$ pumped by 1.28 μm wavelength of the intensity of ~15 GW/cm^2 [11]. In addition, they have also demonstrated the THz generation of 1.1–2.4 μm range in the 3.0 mm long crystal. In the present case, type-I cut (ϕ = 45°, θ = 8°) of thickness 5.0 mm $ZnGeP_2$ (110) crystal was employed to achieve the maximum THz power between 1.28–1.32 μm range. The same cut crystal is suitable for generation of FIR wavelengths (THz radiation) using difference frequency mixing process. However, the present case demonstrates the use of same crystal in optical rectification process.

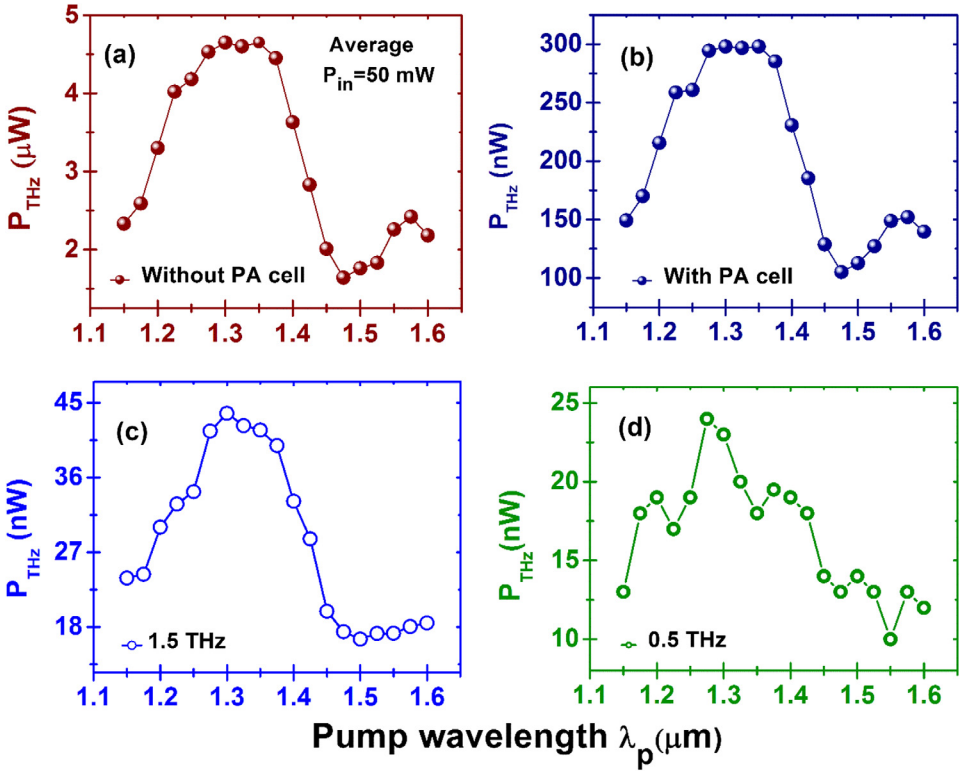

Fig. 3. Power of THz radiation (a) without PA cell (b) with PA cell and along with filters (c) 1.5THz (d) 0.5 THz.

Table 1
Conversion efficiency η (%).

At	η (%); for pump wavelength	
	e-polarization	o-polarization
0.5 THz	0.21%	0.20%
1.5 THz	0.62%	0.61%

Fig. 3(c) shows that the maximum THz power passing through the 1.5 THz bandpass filter which is achieved at 1.3 μm incident wavelength. Therefore, the coherence length of the crystal was ascertained at the same pump wavelength. Also, the comparative results show that generated THz power is of the order of 4.65 μW at 1.3 μm pump wavelength. Since the THz radiation is a weak thermal signal in FIR region, it is dissipating heat to the wall of the cell and also due to thermal convection and conduction process. The cell also does not support as a suitable waveguide for the propagation THz signal. In addition, the presence of bandpass filters, Teflon windows, and surrounding atmosphere are also contributing towards reducing the power of incident THz radiation. Therefore, the output power of THz after passing through the PA cell due to reasons mentioned above becomes 298.0 nW only, which is 15.5 times less than the actual incident power.

The 1.5 THz BPF transmits higher power than the 0.5 THz and follows the similar trend of transmission in the entire range. Therefore, it confirms that wide range of THz spectra dominated by 1.5 THz rather the 0.5 THz. The output power of 0.5 THz BPF is half of the 1.5 THz and shows random variation as a function tunability range of pump wavelength as shown in Fig. 3(d). The measurement also confirms that freely generated THz power (without any bandpass filters) is almost six times higher than the 1.5 THz and 15 times higher than the 0.5 THz range.

As mentioned above, the present report is only restricted to measure the power of full-emitted THz radiation. The probable frequency range of THz generated from $ZnGeP_2$ crystal lies between 0.1–10 THz [10–12]. Moreover, nitromethane and methanol molecules have strong vibrational and rotational lines in the 0.5 and 1.5 THz bands. Therefore, we have selected the 0.5 and 1.5 THz bands (using external bandpass filters) from the emitted radiation for the recording of PA spectra.

3.3. THz and UV based PA spectroscopy

3.3.1. THz based PA spectra of nitromethane and methanol

Fig. 4(a)–(c) and (e)–(g) shows that the PA spectra of nitromethane and methanol recorded using two bandpass filters having central frequencies at 0.5, 1.5 THz, and full THz radiation generated from the ZGP crystal, respectively. THz radiation generated using the pump wavelength at 1.3 μm with the average incident power of 50 mW. The time domain signal corresponds to full THz radiation and the bandpass filters having central frequencies are not shown in the insets of Fig. 4 like UV 266 nm which is shown in Fig. 6. Because the signal to noise ratio is very low in case of THz radiation, therefore, we have concentrated on fast Fourier transform spectra only.

Fig. 4(d) and (h) shows the noise spectra of air at 650 Torr using the full THz radiation. The measured power of THz radiation after passing through the evacuated PA cell and along with bandpass filters having central frequencies of 1.5 and 0.5 THz are 298.0, 43.7 and 24 nW, respectively. The corresponding powers are used to excite the nitromethane and methanol vapors. The exited acoustic modes of nitromethane and methanol with THz radiation are comprised in Table 2. The strength of PA spectra of nitromethane and methanol with THz radiation is higher than the noise level. The major noise peak is present at 43.7 kHz and has the intensity of the order of 0.24 mV. The PA spectra resolution of these molecules is higher than 0.24 mV. Which clearly indicates that the generated PA signal from the molecules vapor is due to the absorption of THz radiation.

Nitromethane has major predominant acoustic modes at full THz radiation as compared to the bandpass filters of central frequencies 0.5 and 1.5 THz. Slingerlands et al. reported the high-resolution spectra of nitromethane; it has a higher value of absorption coefficient (~0.6 1/m) at 17 cm^{-1} (0.5 THz) as compared to the value at 50 cm^{-1} (1.5 THz) [28]. Fig. 4(a) shows the significance of absorption at 0.5 THz. It exhibits the presence of two strong peaks

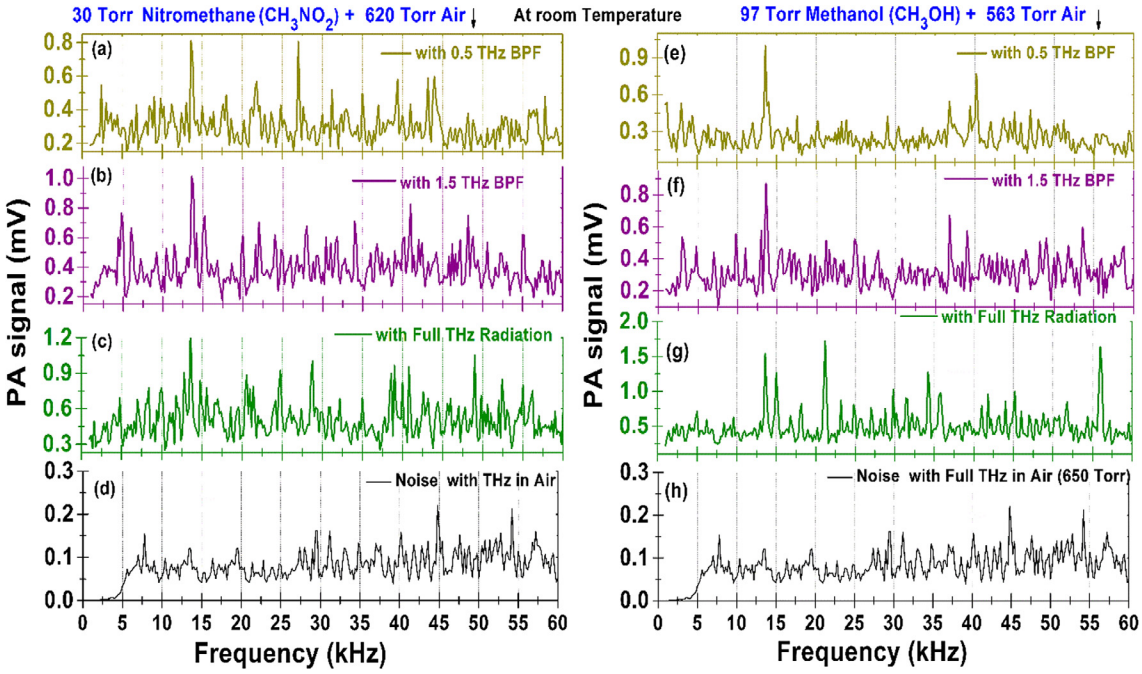

Fig. 4. THz based PA spectra of methanol (CH_3OH) and nitromethane (CH_3NO_2).

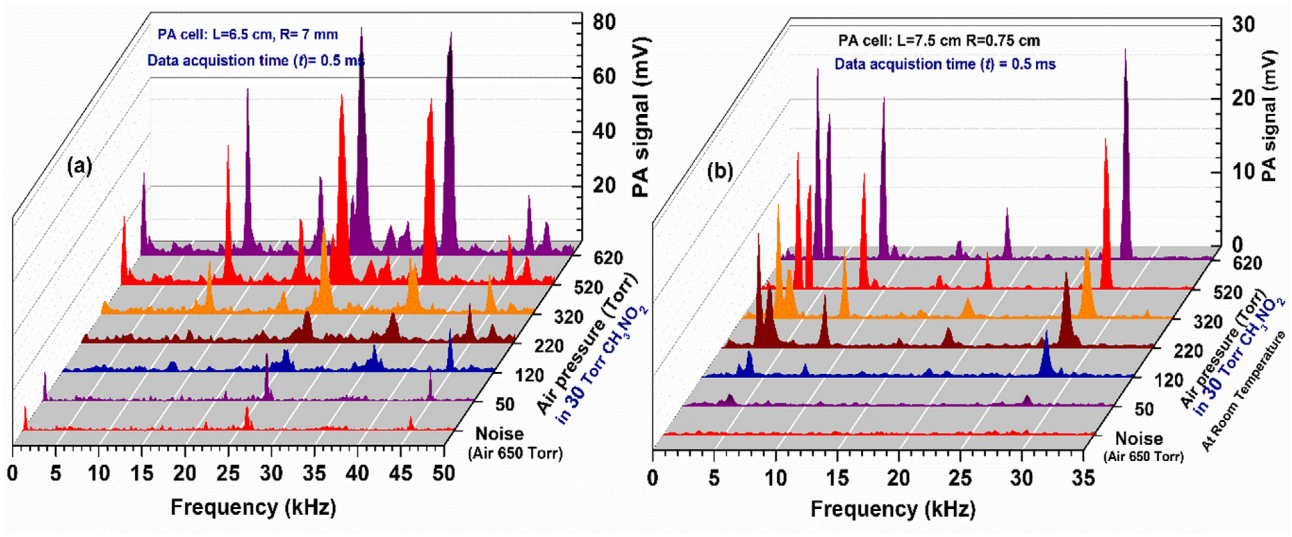

Fig. 5. 266 nm based PA spectra of nitromethane (30 Torr) for PA cells of (a) L = 6.5 cm, R = 0.7 cm, (b) L = 7.5 cm, R = 0.75 cm with increase in the air pressure at room temperature.

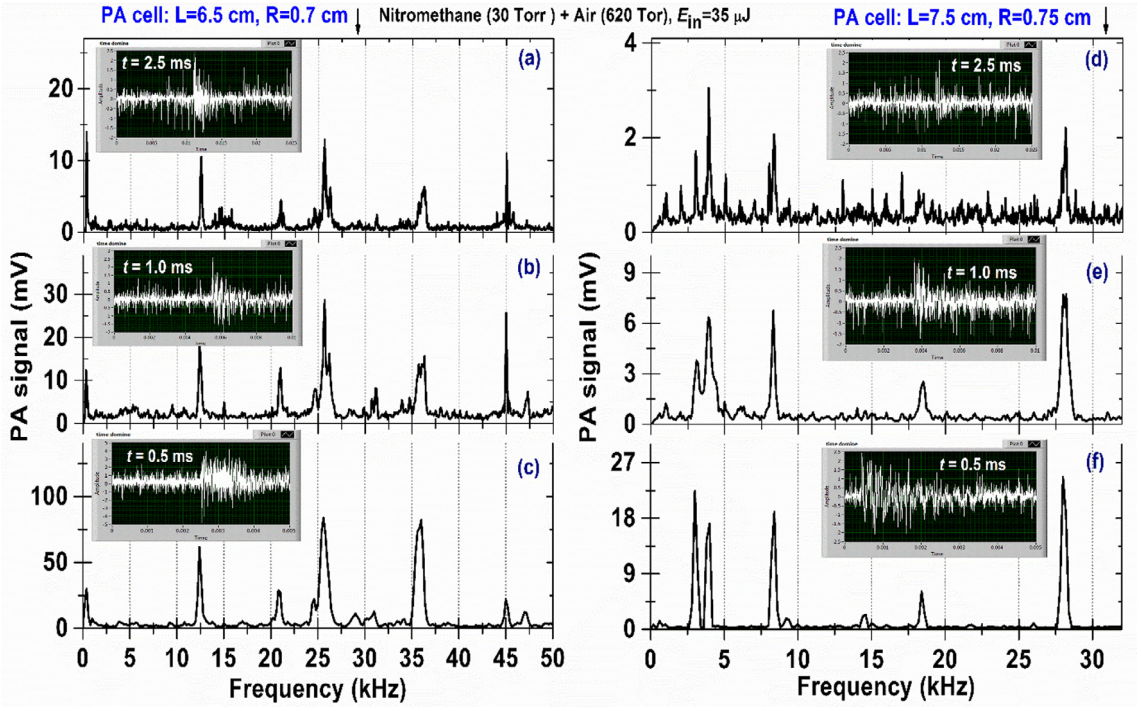

Fig. 6. PA spectra of NM (30 Torr) in air (620 Torr) with respect to data acquisition times 0.5, 1.0, 2.5 ms, respectively, at incident laser energy (E_{in}) = 35 μJ.

Table 2
Excited acoustic modes of PA cavity (L = 6.5 cm, R = 0.7 cm), with THz radiation.

THz	Nitromethane: excited acoustic modes *f* (kHz)												
Full THz	10.0	13.6	14.8	20.6	21.8	24.8	28.8	35.0	39.0	49.0	52.4	56.2	
at 1.5 THz	4.8	6.0	13.6	15.2	22.0	24.0	28.0	34.0	41.0	48.2	50.6	55.0	
at 0.5 THz	2.4	13.6	21.8	27.0	31.2	35.0	39.4	43.2	44.0	57.8			
	Methanol: Excited acoustic modes *f* (kHz)												
Full THz	13.6	15.0	18.2	21.2	23.2	24.8	29.8	34.2	35.8	41.8	45.2	51.8	56.0
at 1.5 THz	3.0	9.8	13.6	24.8	27.8	29.0	30.8	36.8	39.0	48.4	53.6		
at 0.5 THz	3.0	13.6	17.6	20.2	23.8	29.0	30.4	36.8	40.2	47.0	53.6		

at 13.6 and 39.0 kHz as compared to 1.5 THz modes, even though the input power of 0.5 THz bandpass filter is low. The rotational lines correspond to 0.5 and 1.5 THz frequencies are different for nitromethane, but in the present case, the exact rotational lines for nitromethane are not able to identify like previously reported N_2O gas [44]. However, as mentioned above, nitromethane has absorption at THz region and the absorption coefficient of 0.5 THz is higher than 1.5 THz [28].

Fig. 4(g) shows the PA spectrum of methanol vapor, which has some predominant acoustic modes present at 13.6, 15.0, 21.2, 34.2, and 56.0 kHz, respectively at full THz radiation. Fig. 4 (e) and (f) shows that it has major acoustic modes for 0.5 and 1.5 THz BPF are present at 13.6, 36.8, 39.0, 53.6 kHz and 13.6, 29.0, 36.8 and 40.2 kHz respectively. Matsushima et al. showed that at 1.489 THz and 1.525 THz frequencies were attributed to $(n', k'; j') \leftarrow (n\prime\prime, k''; j'')symm$ which are given by $R(0,5;6) \leftarrow (0,4;5)A$ and $R(0,-5;16) \leftarrow (0,-4;15)E$ respectively [33]. It indicates that the transitions near to 1.5 THz region are attributed to R branch of rotational quantum numbers of methanol. The number of predominant excited acoustic modes is higher for full THz radiation than the 1.5 and 0.5 THz bands. However, in the full THz domain methanol has several new rotational lines, each one corresponding to particular frequencies. As a result, the strength of PA signal is higher. Kalmykov et al. demonstrated that methanol has strong absorption between 0.1–2.75 THz range. The presence of OH group in methanol molecule significantly influence the absorption of the broad mode of THz frequency lies between 0.5–2.0 THz range [47]. This is also reflected in PA spectra of methanol (CH_3OH) because some of the excited modes are stronger than the modes of the nitromethane (CH_3NO_2). It is also observed that at full THz radiation, the intensity of PA signal for methanol (97 Torr) is higher than the nitromethane (30 Torr). This clearly indicates that the methanol vapor has strong absorption at THz wavelengths or due to the high quantity of methanol than the nitromethane. However, 13.6 kHz is the common strongest mode in the PA spectra of nitromethane and methanol. The PA cavity has several resonance frequencies (acoustic modes), in this case, the mode present at 13.6 kHz is the strongest one. It appears to be contributed by CH_3 group, which is common in nitromethane (CH_3NO_2) and methanol (CH_3-OH). As we have already discussed in our previous report that the excitation mechanism of given gas/vapor depends on the incident radiation which leads to exciting the different acoustic modes (cavity modes) [44]. Therefore, the predominant order of acoustic modes exclusively depends on the absorption properties of gas/vapor molecules along with the intensity of incident laser pulses. Here, 600 μm and 200 μm wavelengths are selected as excitation wavelengths and use to excite the nitromethane and methanol molecules. Due to full THz radiation, many of the cavity modes are excited at the same time, but they can also abandon each other due to the interference of generated PA signal produced by THz pulses. Also, the propagation velocity of generated PA signal varies as a function of wavelength. Therefore, the excited acoustic modes of nitromethane and methanol with THz radiation comprised in Table 2 are different.

In Section 3.3.2, we have presented the UV-266 nm based PA spectra of nitromethane to ascertain its signature PA spectra with two different PA cells. Also, compared the strength of PA signal generated using THz, UV radiations and their mechanisms.

3.3.2. UV 266 nm based comparative study of PA spectra of nitromethane

It is well known that the quality factor is high for low volume PA cells, which leads to generating the strong of PA signal. The THz radiation leads to vibration of weak rotational lines of molecules; as a result, there is a possibility of generation of lower PA signal. Therefore, the PA cell of L = 6.5 cm, R = 7 mm (to achieve higher PA signal) was used to record the THz based PA spectra nitromethane and methanol. However, before recording the THz based PA signal of nitromethane, the experiment has been performed using UV 266 nm wavelength with two different PA cavities. Nitromethane has strong absorption at 266 nm wavelength (absorption between 190–355 nm ranges) [48]. The central frequencies of excited predominant acoustic modes for time-resolved PA spectra do not vary with respect to increase in pressure, data acquisition time, and incident laser energy for a given PA cell [45,49,50]. However, the time-resolved PA spectra vary significantly with cell design and excitation wavelength. Also, to achieve strong PA signal for low volume PA cell, in this section, we have incorporated the comparative time-resolved PA spectra of nitromethane at 266 nm wavelength with respect to data acquisition time (t) in two different types of PA cells. Fig. 5(a) and (b) shows the recorded PA spectra of nitromethane using the PA cell dimensions of L = 6.5 cm, R = 0.7 cm, and L = 7.5 cm, R = 0.75 cm, respectively. The vapor pressure of nitromethane at room temperature is 30 Torr and the remaining pressure shown in Fig. 5 (a) and (b) is nothing but air. The PA cell dimension of L = 6.5 cm and R = 0.7 cm is shown in Fig. 5(a). This Fig. 6(a) shows the higher strength PA signal as compared to PA cell of L = 7.5 cm, R = 0.75 cm (Fig. 5(b)), which confirms once again the low volume PA cell possess highest PA signal than higher volume PA cell. It is also to be noted that the pressure lies 80 and 650 Torr range, nitromethane has only 30 Torr in all quantities of total pressure, however, by increasing the air pressure, the strength of PA signal is enhancing due to the change in the density of the medium. Moreover, the recorded noise of PA signal in the presence of air at 650 Torr, which is low in case of both the cells as shown in Fig. 5(a) and (b). Therefore, it confirms that acoustic signal is generated due to the contribution of nitromethane only, but the enhancement of the PA signal depends on the mixed density of the medium inside PA cavity.

It is well-known fact that the frequency of excited acoustic modes is varying with respect to dimension (design) of PA cavity. The differences in the frequency of acoustic modes are clearly shown in Figs. 5 and 6, respectively for two different cells. For same PA cell, there is not much change in the central frequencies of predominant acoustic modes with variation in the pressure and data acquisition times. Fig. 6(a)–(c) and (d)–(f) shows the comparative PA spectra of NM (30 Torr) in the air (620 Torr) with respect to data acquisition times 0.5, 1.0, 2.5 ms, respectively, at incident laser energy (E_{in}) = 35 μJ. The predominant excited acoustic modes for two cavities with respect to data acquisition times are comprised in Table 3. The step size (ΔHz) between the two data points in PA spectra for data acquisition times 0.5, 1.0 and 2.5 ms are ΔHz = 200, 100, and 40 Hz, respectively. It is also clear from the data in Table 3, the central frequencies of excited modes almost identical for different data acquisition times for a given PA cell. In case of lower volume PA cell i.e. (L = 6.5 cm, R = 0.7 cm) higher order acoustic modes are present, and these frequencies are occupied entire response range of microphone i.e. 0–60 kHz. Therefore, the PA cell i.e. (L = 6.5 cm, R = 0.7 cm) was chosen to record the THz based PA spectra of nitromethane and methanol.

In case of UV region, the intensity of PA signal as well as signal to noise ratio is higher due to the higher photon energy of UV radiation and low repetition rate [51]. Therefore, time-resolved PA spectra are very sharp and well resolved. In addition, the higher photon energy leads to initiate the process of photodissociation of molecules due to electronic transitions [45,52–55]. The radiative and nonradiative transitions can complete within the same relaxation lifetime of molecules. The radiative lifetimes of UV–visible and THz wavelengths are 10^{-8} sec and 10^{-2} sec, respectively. It shows that recording of non-radiative transitions in UV–Vis region is of the order of few milliseconds, which coincides with the data

Table 3
Excited acoustic modes of two PA cells.

t (ms)	f (kHz) for L = 6.5 cm, R = 0.7 cm				
0.5	12.4	20.8	25.6	36.0	45.0
1.0	12.4	21.0	25.7	36.3	45.0
2.5	12.52	21.0	25.6	36.24	45.0
t (ms)	f(kHz) for and L = 7.5 cm, R = 0.75 cm				
0.5	3.0	4.0	8.4	18.4	28.0
1.0	3.1	3.9	8.3	18.5	28.0
2.5	3.0	3.88	8.32	18.16	28.12

acquisition time (t) for recording the PA signal. As a result, the detected acoustic signal has high intensity for nanosecond laser system. However, most of the gas/vapor molecules do not have absorption in UV 266 nm range, but the molecules possess several rotational lines in THz range. Therefore, the reported work shows the potential use of THz radiation without pump-probe arrangement to record the photoacoustic spectra of nitromethane and methanol using bandpass filters having central frequencies 0.5 and 1.5 THz. In case of FIR or THz frequency, the photon energy is very low which only contributes towards inner ultrafast transitions of weak rotational lines. As a result, it produces less thermal fluctuations leads to the generation of PA signal with low intensity. Therefore, in this case, the signal to noise ratio is very low. However, the present experiment shows the feasibility to record the THz based PA spectrum of molecules due to efficient generation of THz radiation from ZGP crystal.

4. Conclusions

The efficient THz radiation has been generated successfully from the type-I cut (DFG) $ZnGeP_2$ crystal through optical rectification process. The comparative results show that generated THz power is of the order of 4.65 μW at 1.3 μm pump wavelength. The measured power of THz at 1.5 THz band is higher than the 0.5 THz. The estimated conversion efficiency of the generated THz signal is of the order of 0.62% at 1.5 THz band. Further, the generated THz radiation is used to record the time domain PA spectra of nitromethane and is compared with methanol. The results reveal that these molecules have strong absorption at the THz range, including the specific bands at 0.5 THz and 1.5 THz. In addition, UV 266 nm is used as an excitation wavelength to record the characteristic PA spectra of nitromethane with two different cells as a function of vapor pressure and data acquisition time. And the comparative study has been done with THz and UV wavelengths for two different excitation mechanisms.

Acknowledgements

The authors gratefully acknowledge the D.R.D.O., Ministry of Defence, Govt. of India, India, for financial support. Thanks to be also due to the Director of ACRHEM, University of Hyderabad for the encouragement.

References

[1] Y.S. Lee, Principles of Terahertz Science and Technology, 2009, 10.1007/978-0-387-09540-0.
[2] D. Grischkowsky, S. Keiding, M. van Exter, C. Fattinger, Far-infrared time-domain spectroscopy with terahertz beams of dielectrics and semiconductors, J. Opt. Soc. Am. B 7 (1990) 2006–2015, https://doi.org/10.1364/JOSAB.7.002006.
[3] B.B. Hu, M.C. Nuss, Imaging with terahertz waves, Opt. Lett. 20 (1995) 1716, https://doi.org/10.1364/OL.20.001716.
[4] P. Kumbhakar, T. Kobayashi, G.C. Bhar, Sellmeier dispersion for phase-matched terahertz generation in ZnGeP2, Appl. Opt. 43 (2004) 3324–3328, https://doi.org/10.1364/AO.43.003324.
[5] W. Shi, Y.J. Ding, P.G. Schunemann, Coherent terahertz waves based on difference-frequency generation in an annealed zinc–germanium phosphide crystal: improvements on tuning ranges and peak powers, Opt. Commun. 233 (2004) 183–189, https://doi.org/10.1016/j.optcom.2004.01.016.
[6] W. Shi, Y.J. Ding, N. Fernelius, K. Vodopyanov, Efficient, tunable, and coherent 0.18-5.27-THz source based on GaSe crystal, Opt. Lett. 27 (2002) 1454–1456, https://doi.org/10.1364/OL.28.000136.
[7] Y. Sasaki, A. Yuri, K. Kawase, H. Ito, Terahertz-wave surface-emitted difference frequency generation in slant-stripe-type periodically poled LiNbO[sub 3] crystal, Appl. Phys. Lett. 81 (2002) 3323, https://doi.org/10.1063/1.1518779.
[8] C. Staus, T. Kuech, L. McCaughan, Continuously phase-matched terahertz difference frequency generation in an embedded-waveguide structure supporting only fundamental modes, Opt. Express. 16 (2008) 13296, https://doi.org/10.1364/OE.16.013296.
[9] N.E. Yu, K.S. Lee, D.-K. Ko, C. Kang, S. Takekawa, K. Kitamura, Temperature dependent narrow-band terahertz pulse generation in periodically poled crystals via difference frequency generation, Opt. Commun. 284 (2011) 1395–1400, https://doi.org/10.1016/j.optcom.2010.10.092.
[10] J.D. Rowley, J.K. Wahlstrand, K.T. Zawilski, P.G. Schunemann, N.C. Giles, a.D. Bristow, Terahertz generation by optical rectification in uniaxial birefringent crystals, Opt. Express. 20 (2012) 16968, https://doi.org/10.1364/OE.20.016968.
[11] J.D. Rowley, D.A. Bas, K.T. Zawilski, P.G. Schunemann, A.D. Bristow, Terahertz emission from $ZnGeP_2$: phase-matching, intensity, and length scalability, J. Opt. Soc. Am. B 30 (2013) 2882, https://doi.org/10.1364/JOSAB.30.002882.
[12] J.D. Rowley, J.K. Pierce, A.T. Brant, L.E. Halliburton, N.C. Giles, P.G. Schunemann, A.D. Bristow, Broadband terahertz pulse emission from ZnGeP2, Opt. Lett. 37 (2012) 788–790, https://doi.org/10.1364/OL.37.000788.
[13] J. Federici, L. Moeller, Review of terahertz and subterahertz wireless communications, J. Appl. Phys. 107 (2010), https://doi.org/10.1063/1.3386413.
[14] P.U. Jepsen, D.G. Cooke, M. Koch, Terahertz spectroscopy and imaging – modern techniques and applications, Laser Photon. Rev. 5 (2011) 124–166, https://doi.org/10.1002/lpor.201000011.
[15] K. Yamaguchi, M. Nakajima, T. Suemoto, Coherent control of spin precession motion with impulsive magnetic fields of half-cycle terahertz radiation, Phys. Rev. Lett. 105 (2010) 3–6, https://doi.org/10.1103/PhysRevLett. 105.237201.
[16] B. Fischer, M. Hoffmann, H. Helm, G. Modjesch, P.U. Jepsen, Chemical recognition in terahertz time-domain spectroscopy and imaging, Semicond. Sci. Technol. 20 (2005) S246–S253, https://doi.org/10.1088/0268-1242/20/7/015.
[17] F. Yehya, A.K. Chaudhary, Study of damping, saturation and surface losses on low level detection of NO_2 using time resolved pulsed photo acoustic technique, Opt. Commun. 312 (2014) 16–22, https://doi.org/10.1016/j.optcom.2013.08.052.
[18] A. Miklós, a. Lörincz, Windowless resonant acoustic chamber for laser-photoacoustic applications, Appl. Phys. B Photophys. Laser Chem. 48 (1989) 213–218, https://doi.org/10.1007/BF00694347.
[19] R. Kästle, M.W. Sigrist, Temperature-dependent photoacoustic spectroscopy with a Helmholtz resonator, Appl. Phys. B Lasers Opt. 63 (1996) 389–397, https://doi.org/10.1007/s003400050101.
[20] F. Yehya, A.K. Chaudhary, D. Srinivas, K. Muralidharan, Study of thermal decomposition mechanisms and low-level detection of explosives using pulsed photoacoustic technique, Appl. Phys. B 121 (2015) 193–202, https://doi.org/10.1007/s00340-015-6218-6.
[21] D.M. Mittleman, R.H. Jacobsen, R. Neelamani, R.G. Baraniuk, M.C. Nuss, Gas sensing using terahertz time-domain spectroscopy, Appl. Phys. B – Lasers Opt. 67 (1998) 379–390, https://doi.org/10.1007/s003400050520.
[22] R. Bartlome, M. Kaučikas, M.W. Sigrist, Modulated resonant versus pulsed resonant photoacoustics in trace gas detection, Appl. Phys. B Lasers Opt. 96 (2009) 561–566, https://doi.org/10.1007/s00340-009-3572-2.
[23] D. Cavagnat, L. Lespade, Internal dynamics contributions to the CH stretching overtone spectra of gaseous nitromethane NO_2CH_3, J. Chem. Phys. 106 (1997) 7946–7957, https://doi.org/10.1063/1.473807.
[24] J.M. Seminario, M.C. Concha, P. Politzer, A density functional/molecular dynamics study of the structure of liquid nitromethane, J. Chem. Phys. 102 (1995) 8281, https://doi.org/10.1063/1.468960.
[25] D.C. McKean, R.A. Watt, Vibrational spectra of nitromethanes and the effects of internal rotation, J. Mol. Spectrosc. 61 (1976) 184–202, https://doi.org/10.1016/0022-2852(76)90241-1.
[26] Y. Ren, M. Li, J. Yang, J. Peng, Y. Gu, An alternative to nitromethane as solvent: the promoting influence of nitro-functionalized imidazolium salts for synthesis and catalysis, Adv. Synth. Catal. 353 (2011) 3473–3484, https://doi.org/10.1002/adsc.201100530.
[27] A.E. Tutton, The explosive nature of the sodium and potassium derivatives of nitromethane, Nature. 51 (1895) 328. http://www.scopus.com/inward/record.url?eid=2-s2.0-51149163429&partnerID=40&md5=ad8fc07c76e19cb8d327b05695948695.
[28] E.J. Slingerland, E.G.E. Jahngen, T.M. Goyette, R.H. Giles, W.E. Nixon, Terahertz absorption spectra of nitromethane, J. Quant. Spectrosc. Radiat. Transf. 112 (2011) 2323–2329, https://doi.org/10.1016/j.jqsrt.2011.06.006.
[29] D. Cavagnat, L. Lespade, Vibrational overtone spectroscopy and internal dynamics in gaseous nitromethane NO[sub 2]CH[sub 2]D, J. Chem. Phys. 108 (1998) 9275, https://doi.org/10.1063/1.476382.
[30] C. Reid, S Pectroscopic Methods for Medical Diagnosis At Terahertz Wavelengths, 2009.

[31] C. Wang, P. Sahay, Breath analysis using laser spectroscopic techniques: breath biomarkers, spectral fingerprints, and detection limits, Sensors 9 (2009) 8230–8262, https://doi.org/10.3390/s91008230.
[32] A. Sampaolo, P. Patimisco, M. Giglio, M.S. Vitiello, H.E. Beere, D.A. Ritchie, G. Scamarcio, F.K. Tittel, V. Spagnolo, Improved tuning fork for terahertz quartz-enhanced photoacoustic spectroscopy, Sensors (Switzerland) 16 (2016), https://doi.org/10.3390/s16040439.
[33] F. Matsushima, K.M. Evenson, L.R. Zink, Absolute frequency measurements of methanol from 1.5 to 6.5 THz, J. Mol. Spectrosc. 164 (1994) 517–530, https://doi.org/10.1006/jmsp.1994.1094.
[34] E.J. Slingerland, T.M. Goyette, R.H. Giles, W.E. Nixon, New experimental methods in Terahertz spectroscopy, in: Proc. SPIE, 2011, pp. 1–9. 10.1117/12.873290.
[35] S. Ioppolo, B.A. McGuire, M.A. Allodi, G.A. Blake, THz and Mid-IR spectroscopy of interstellar ice analogs: methyl and carboxylic acid groups, Faraday Discuss. 168 (2014) 461, https://doi.org/10.1039/c3fd00154g.
[36] J.C. Pearson, B.J. Drouin, S. Yu, H. Gupta, Microwave spectroscopy of methanol between 2.48 and 2.77 THz, J. Opt. Soc. Am. B 28 (2011) 2549–2577, https://doi.org/10.1364/JOSAB.28.002549.
[37] L.H. Xu, H. Shi, J. Fisher, R.M. Lees, J.C. Pearson, B.J. Drouin, New terahertz methanol spectroscopy for HIFI on the Herschel mission, IRMMW-THz 2006 – 31st Int. Conf. Infrared Millim. Waves 14th Int. Conf. Terahertz Electron. 93113, 2006, pp. 228. 10.1109/ICIMW.2006.368436.
[38] R.F. Curl, F.K. Tittel, Tunable infrared laser spectroscopy, Annu. Reports Prog. Chem. Sect. C 98 (2002) 219–272, https://doi.org/10.1039/b111194a.
[39] E. Telles, H. Odashima, L. Zink, K. Evenson, Optically pumped FIR laser lines from CH_3OH: new laser lines, frequency measurements, and assignments, J. Mol. Spectrosc. 195 (1999) 360–366, https://doi.org/10.1006/jmsp.1999.7834.
[40] J. Zhi-Xian, Z. Du-Luo, M. Liang, C. Zu-Hai, Pulsed CH_3OH terahertz laser radiation pumped by 9P(36) CO_2 lasers, J. Phys. Conf. Ser. 276 (2011) 12212, https://doi.org/10.1088/1742-6596/276/1/012212.
[41] J. Zhi-Xian, Z. Du-Luo, M. Liang, Q. Chun-Chao, C. Zu-Hai, An efficient pulsed CH_3OH terahertz laser pumped by a TEA CO_2 laser, Chinese Phys. Lett. 27 (2010) 24211, https://doi.org/10.1088/0256-307X/27/2/024211.
[42] R.C. Viscovini, J.C.S. Moraes, L.F.L. Costa, F.C. Cruz, D. Pereira, CH_3OH optically pumped by a $13CO_2$ laser: new terahertz laser lines, Appl. Phys. B Lasers Opt. 91 (2008) 517–520, https://doi.org/10.1007/s00340-008-3018-2.
[43] L.-H. Xu, R.M. Lees, E.C.C. Vasconcellos, L.R. Zink, K.M. Evenson, S.C. Zerbetto, A. Predoi, New far-infrared laser lines and assignments for $^{13}CH_3OH$ methanol, J. Opt. Soc. Am. B Opt. Phys. 12 (1995) 2352–2359, https://doi.org/10.1364/JOSAB.12.002352.
[44] K.S. Rao, A.K. Chaudhary, M. Venkatesh, K. Thirupugalmani, S. Brahadeeswaran, DAST crystal based terahertz generation and recording of time resolved photoacoustic spectra of N_2O gas at 0.5 and 1.5 THz bands, Curr. Appl. Phys. 16 (2016) 777–783, https://doi.org/10.1016/j.cap.2016.04.009.
[45] K.S. Rao, A.K. Chaudhary, F. Yehya, A.S. Kumar, Study of acoustic fingerprinting of nitromethane and some triazole derivatives using UV 266 nm pulsed photoacoustic pyrolysis technique, Spectrochim. Acta – Part A Mol. Biomol Spectrosc. 147 (2015) 316–323, https://doi.org/10.1016/j.saa.2015.03.017.
[46] A. Nahata, A.S. Weling, T.F. Heinz, A wideband coherent terahertz spectroscopy system using optical rectification and electro-optic sampling, Appl. Phys. Lett. 69 (1996) 2321–2323.
[47] Y.P. Kalmykov, Recent advances in broadband dielectric spectroscopy, Springer (2012), https://doi.org/10.1007/978-94-007-5012-8_2.
[48] W.D. Taylor, T.D. Allston, M.J. Moscato, G.B. Fazekas, R. Kozlowski, G.A. Takacs, Atmospheric photodissociation lifetimes for nitromethane, methyl nitrite, and methyl nitrate, Int. J. Chem. Kinet. 12 (1980) 231–240, https://doi.org/10.1002/kin.550120404.
[49] K.S. Rao, A.K. Chaudhary, F. Yehya, Investigation of thermal stability and fingerprint spectra of energetic 1,2,3-triazole using pulsed photoacoustic pyrolysis technique, Appl. Phys. B Lasers Opt. 121 (2015), https://doi.org/10.1007/s00340-015-6240-8.
[50] K.S. Rao, A.K. Chaudhary, Evaluation of thermal stability and time resolved acoustic fingerprint spectra of 1-(2-methoxy,-3,5-dinitrophenyl)-1H-1,2,3-triazole, Thermochim. Acta. 638 (2016) 17–24, https://doi.org/10.1016/j.tca.2016.06.009.
[51] http://hyperphysics.phy-astr.gsu.edu/hbase/mod3.html.
[52] Y.Q. Guo, a. Bhattacharya, E.R. Bernstein, Photodissociation dynamics of nitromethane at 226 and 271 nm at both nanosecond and femtosecond time scales, J. Phys. Chem. A 113 (2009) 85–96, https://doi.org/10.1021/jp806230p.
[53] J.F. Arenas, J.C. Otero, D. Peláez, J. Soto, The ground and excited state potential energy surfaces of nitromethane related to its dissociation dynamics after excitation at 193 nm, J. Chem. Phys. 119 (2003) 7814, https://doi.org/10.1063/1.1600436.
[54] S. Zabarnick, J.W. Fleming, a.P. Baronavski, Production of OH from the collision-free photodissociation of nitromethane at 266 nm, J. Chem. Phys. 85 (1986) 3395, https://doi.org/10.1063/1.450961.
[55] L.J. Butler, D. Krajnovich, Y.T. Lee, G.S. Ondrey, R. Bersohn, The photodissociation of nitromethane at 193 nm, J. Chem. Phys. 79 (1983) 1708, https://doi.org/10.1063/1.446015.